



HAL
open science

Collective phenomena at the particle emission thresholds

Jose Pablo Linares Fernandez

► **To cite this version:**

Jose Pablo Linares Fernandez. Collective phenomena at the particle emission thresholds. Physics [physics]. Normandie Université, 2023. English. NNT : 2023NORMC268 . tel-04483932

HAL Id: tel-04483932

<https://theses.hal.science/tel-04483932v1>

Submitted on 29 Feb 2024

HAL is a multi-disciplinary open access archive for the deposit and dissemination of scientific research documents, whether they are published or not. The documents may come from teaching and research institutions in France or abroad, or from public or private research centers.

L'archive ouverte pluridisciplinaire **HAL**, est destinée au dépôt et à la diffusion de documents scientifiques de niveau recherche, publiés ou non, émanant des établissements d'enseignement et de recherche français ou étrangers, des laboratoires publics ou privés.

THÈSE

Pour obtenir le diplôme de doctorat

Spécialité **PHYSIQUE**

Préparée au sein de l'**Université de Caen Normandie**

Collective phenomena at the particle emission thresholds

Présentée et soutenue par
JOSE PABLO LINARES FERNANDEZ

Thèse soutenue le 20/10/2023

devant le jury composé de :

MME MARCELLA GRASSO	Directeur de recherche au CNRS - INSTITUT DE PHYSIQUE NUCLEAIRE D'ORSAY	Rapporteur du jury
M. WITOLD NAZAREWICZ	Professeur - Michigan State University	Rapporteur du jury
M. FRÉDÉRIC NOWACKI	Directeur de recherche au CNRS - UNIVERSITE STRASBOURG	Membre du jury
M. PIETER VAN ISACKER	Chercheur au CEA - 14 GANIL de CAEN	Membre du jury
MME FRANCESCA GULMINELLI	Professeur des universités - Université de Caen Normandie	Président du jury
M. MAREK PLOSZAJCZAK	Directeur de recherche au CEA - 14 GANIL de CAEN	Directeur de thèse

Thèse dirigée par **MAREK PLOSZAJCZAK** (Grand Accélérateur National d'Ions Lourds)

Acknowledgments		v
List of acronyms		vii
Introduction		1
1 The single particle Berggren basis		5
1.1 Gamow states		6
1.2 Scattering states		8
1.3 The S-matrix and Jost functions		9
1.4 The Berggren basis		10
1.4.1 Normalization and regularization of the Berggren basis		14
1.4.2 Numerical calculation of Berggren basis states		16
1.5 Rigged Hilbert space		18
2 Closed versus open quantum systems		21
2.1 Shell Model		22
2.1.1 Diagonalizing the Shell Model interaction: the Lanczos method		23
2.2 No-core Shell Model		24
2.2.1 No-core Shell Model and continuum		25
2.3 Continuum Shell Model		27
2.4 Shell Model Embedded in the Continuum		29
3 Formulation of the Gamow Shell Model		31
3.1 Diagonalizing the Gamow Shell Model Hamiltonian: the Overlap method		32
3.2 Hamiltonian in Cluster Orbital Shell Model coordinates		33
3.3 No-core Gamow Shell Model		36
3.4 Applications of the Gamow Shell Model		37
3.5 Interaction for Gamow Shell Model		37
3.5.1 Optimization of the interaction		39
3.6 Differences with other methods		40
4 Coupled channel representation of Gamow Shell Model		43
4.1 Definition of channels in Gamow Shell Model		44
4.2 Hamiltonian in the coupled channel formalism		45

4.3	Construction of the target and projectile wave functions	46
4.4	Construction of the total many-body wave functions	49
4.5	Orthogonalization of composites with respect to the core.	49
4.6	Calculation of the kernels of the Hill-Wheeler equation	50
4.7	Solution of the Hill-Wheeler equation	53
4.7.1	Transformation to a standard eigenvalue problem	53
4.7.2	Solution in the coordinate space: the equivalent potential method	54
4.7.3	Bound and resonance states: overlap method in the context of coupled channels	56
4.7.4	Scattering states: solution via Green's function method	57
4.7.5	Summary of the numerical methods to solve the coupled channels equation	59
4.8	Calculation of reaction observables	59
4.8.1	Applications of the Gamow Shell Model in coupled channels representation	61
4.9	Differences with other methods	62
5	Multiple mass partitions in Gamow Shell Model Coupled Channel representation	63
5.1	Spectroscopic factors in GSM	64
5.2	Description of ${}^7\text{Be}$ and ${}^7\text{Li}$	66
5.2.1	Model space for ${}^6\text{Li}$, ${}^7\text{Be}$, and ${}^7\text{Li}$	66
5.2.2	Interaction for $A=6,7$ systems	67
5.2.3	Spectra of ${}^7\text{Be}$ and ${}^7\text{Li}$	69
5.2.4	Reaction cross-sections involving ${}^7\text{Be}$ and ${}^7\text{Li}$ as composite systems	73
5.3	Description of ${}^8\text{Be}$	76
5.3.1	Model space for ${}^8\text{Be}$	76
5.3.2	Interaction for $A=7,8$ systems	76
5.3.3	Spectrum of ${}^8\text{Be}$	77
5.4	Description of spectra of ${}^{42}\text{Sc}$, ${}^{42}\text{Ca}$, ${}^{42}\text{Ti}$, and transfer reaction ${}^{40}\text{Ca}(d,p){}^{41}\text{Ca}$	83
5.4.1	Model space for calculations with a ${}^{40}\text{Ca}$ core	83
5.4.2	Interaction for $A = 41, 42$ systems	84
5.4.3	Spectrum and reactions with a ${}^{40}\text{Ca}$ core and valence particles	84
6	Near-threshold effects within the Gamow Shell Model	89
6.1	Wigner cusps in reaction cross-sections and spectroscopic factors	90
6.2	From threshold effects to clusterization	93
6.3	Near threshold effects in the coupled channel framework	96
6.3.1	Near-threshold effects in ${}^7\text{Be}$ and ${}^7\text{Li}$	96
6.3.2	Near-threshold effects in ${}^8\text{Be}$	100
6.3.3	Correlation energy in ${}^{7,8}\text{Be}$ and ${}^7\text{Li}$	103
6.3.4	Near-threshold effects in the spectroscopic factors	108
	Conclusion	115
A	Annexes	119
A.1	On the Slater determinants of the wave function in GSM-CC	119
A.2	The current formula for the calculation of partial widths of channel wave functions	120

Acknowledgments

...¡Alumbra, lumbré de alumbra,
Luzbel de piedralumbra! Como
zumbido de oídos persistía el rumor
de las campanas a la oración,
maldobestar de la luz en la sombra,
de la sombra en la luz. ¡Alumbra,
lumbré de alumbra, Luzbel de
piedralumbra, sobre la podredumbra!
¡Alumbra, lumbré de alumbra, sobre
la podredumbra, Luzbel de
piedralumbra! ¡Alumbra, alumbra,
lumbré de alumbra..., alumbra...,
alumbra..., alumbra, lumbré de
alumbra..., alumbra..., alumbra...,
alumbra, lumbré de alumbra...,
alumbra, alumbra...!

El señor presidente
Miguel Angel Asturias

This is the end of my life as a student. Of course, this acknowledgments encompass only the three years of doctoral studies, otherwise this section would probably be as large as a chapter. I also have tried to be as straightforward as possible, without much nonsensical formality as to let the names of the people to be acknowledged stand a bit more. Of course, there is some funny nonsense but not more than what is necessary. I hope that I did not miss anyone, but in the case I did, and you are reading this, please know that I am thankful for your contribution however big or small it may have been.

First and foremost, I thank the former director of GANIL Navin Alahari, for allowing me to do my thesis in this laboratory. Of course, the acknowledgment is also extended to the current director Patricia Roussel-Chomaz for allowing me to continue my thesis in GANIL. My thanks go also to all the people in the administration who allowed me to work without much problems, particularly Sabrina Lecerf and Virginie Lefebvre.

I am grateful to my referees Witold Nazarewicz and Marcella Grasso, who accepted to take some of their time to referee my thesis. Moreover, I am thankful to my referees and the rest of the members of the jury Francesca Gulminelli, Pieter van Isacker, and Frédéric Nowacki for giving some of their time to read my thesis.

If I have been a student then there has to be a mentor. I am thankful to my Ph.D. supervisor Marek Płoszajczak for mentoring me during this three years, even though he did not have to take me as a student, he still did and I will forever be thankful for such opportunity. I was able to learn a lot from this experience, and these lessons will very likely shape my future in research. By now I can only hope that all the difficulties encountered along the way were serious but not hopeless, with the exception of me writing his name without mistake, which is hopeless but not serious. Next, I would like to thank Yannen Jaganathen who introduced me to GSM calculations and to Nicolas Michel, whose titanic work in the GSM code cannot go unmentioned.

I would like to thank my peers for countless discussions during lunches and breaks. Special mention to those with whom I spent the most time: Alexa DoThat, Thon Geralt of Rivia, Thewinesmells Forrest, Antwuan notaMime and SuisRhum notLejoubioux. Although we may never see each other again, I will consider you my friends, and please, if you are reading this, do not forget to eat your vegetables and to eat enough protein.

Additionally, it should be mentioned that to survive I needed money. Of course, this was given to me by the Region Normandie. To be honest, I have little to no idea of where these funds come from, but I am thankful regardless to whoever contributed to those funds. I apologize in advance for taking whatever is left in my savings and spending/investing it elsewhere, it is totally not stealing.

Even though they are almost 8800 kilometers away, across the Atlantic ocean, their unconditional support has allowed me to endure being away from all I have known for most of my life. Indeed, I am thankful to my parents José Bernardo Linares Ramírez and Claudia María Fernández Vásquez and my sisters Mariandrée Linares Fernández and Krista María Linares Fernández. My gratefulness is of course extended to the rest of my family, to those that live and those that could not see me finish.

Finally, I did not spend this three years alone. I am grateful to my beloved Đinh Thị Hòa, whose continuous support and love allowed me to go through any difficulty on my Ph.D. journey. Particularly her help using her network of Vietnamese people when it came to bureaucratic procedures, which I would probably not have finished on my own and may have been deported or maybe stayed homeless. Additionally the warm (and of course never cold), full of flavor, without chemicals, full of spice and fish sauce, never missing the vegetables, masterchef meals were always able to lift my spirits up.

List of acronyms

BBN	Big Bang Nucleosynthesis
CM	Center-of-mass
CNO	Carbon-Nitrogen-Oxygen
COSM	Cluster Orbital Shell Model
CQS	Closed Quantum System
CSM	Continuum Shell Model
EP	Exceptional point
FHT	Furutani-Horiuchi-Tamagaki
GSM	Gamow Shell Model
GSM-CC	Gamow Shell Model in Coupled Channels representation
HO	Harmonic Oscillator
HO-SM	Shell Model in Harmonic Oscillator Basis
NCGSM	No-core Gamow Shell Model
NCSM	No-core Shell Model
OQS	Open Quantum System
RGM	Resonating Group Method
RHS	Rigged Hilbert Space
S-matrix	Scattering matrix
SF	Spectroscopic factor
SM	Shell Model
SMEC	Shell Model Embedded in the Continuum

More than a century ago, the Rutherford gold foil experiments taught us that the atom had a positive charged nucleus surrounded by electrons. These experiments consisted in scattering alpha particles into a foil of gold. Thus, nuclear physics was born. Indeed, the preponderant idea of nuclear physics that has persisted to this day was to scatter particles to gain knowledge of the atomic nucleus.

One may say that nuclear theory is the perfect laboratory for quantum mechanics. Theoretical nuclear physics involves developing models to understand nuclear phenomena based on the fundamental principles and mathematical formulations. However, nuclear theory faces challenges due to the complexity of the many-body problem in the atomic nucleus. The presence of a large number of particles makes it difficult to solve the problem exactly, and conversely, the presence of not enough particles prevents a simple thermodynamic treatment, except in some nuclear astrophysics contexts such as neutron stars. As a result, there is no standard model of nuclear theory, and instead, different regions of the nuclear chart are treated in their own unique way.

For many decades, studies of the nuclear structure focused on bound states, whereas studies of reactions focused on unbound scattering states. This dichotomy has led to a somewhat artificial division between the theory of nuclear structure and the theory of nuclear reactions. The nuclear Shell Model (SM), pioneered by Goeppert-Mayer [1] and Jensen, Haxel and Suess [2], became the preferred tool for exploring nuclear structure. This model and its subsequent developments treated the nucleus as a closed quantum system (CQS) isolated from the environment of scattering continuum. On the other hand, nuclear reactions relied on various approaches depending on the considered reaction mechanism, range of masses or excitation energies. These approaches oftentimes disregard the internal structure of the nucleus by using effective potentials for solving the scattering problem.

An important step towards the unification of structure and reactions was made by Feshbach [3, 4], whose idea was to break the interaction into two parts: one that describes the bound states and another that describes the scattering states. This gave the foundation for the development of the Continuum Shell Model (CSM) [5, 6]. However, the real motivation to advance the studies of unified theories of structure and reactions was given by the experiments. Indeed, nuclear experimental facilities have evolved over the years to be able to produce more and more exotic nuclei far from the valley of the β -stability. As the drip lines were approached, phenomena like nuclear halo in weakly bound or unbound states, among others, were observed. Nuclei in a vicinity of the drip

lines play a significant role in astrophysical processes, such as, e.g., the nucleosynthesis during stellar evolution and supernova explosions. Ikeda *et al.* [7] noted that there exist α -cluster states close to the α -particle emission thresholds. Later it has been conjectured that this observation is more general and one should find states close to any particle emission thresholds [8, 9]. These phenomena can be studied within unified theories like the Shell Model Embedded in the Continuum (SMEC) [10], the Gamow Shell Model (GSM) [11–15] and its realization in coupled channels [15–17], the *ab initio* approaches of the no-core Shell Model (NCSM) with Resonating Group Method (RGM) [18, 19], the no-core Shell Model with Continuum (NCSMC) [20–22], the no-core Gamow Shell Model (NCGSM) [23, 24] and its coupled-channel representation [25].

In the realm of nuclear structure, resonances play a crucial role. Resonances, which are quasi-bound states, have been of theoretical interest since Gamow’s seminal paper on α -decay [26]. The scattering matrix (S-matrix) formalism developed by Heisenberg [27] and the formulation of resonances by Rosenfeld and Humblet [28] paved the way for a comprehensive theory of nuclear reactions. However, incorporating resonances into a theory of nuclear structure remained challenging.

Resonance states in quantum mechanics are characterized by their decay time and cannot be measured in the same way as bound states. Their characteristics are instead extracted from scattering amplitudes and phase shifts, obtained from the S-matrix [27]. In experimental nuclear physics, resonance widths can be measured via phase shifts and scattering cross-sections of nuclear reactions, where resonances appear as quasi-Lorentzian peaks in the cross-section [28].

To describe quantum systems, one typically uses a complete basis of orthonormal functions. A basis set is considered complete if any quantum state can be expressed as a linear combination of these eigenfunctions. A well known example is the harmonic oscillator (HO) basis. While this basis is complete and orthogonal, it is limited to describing bound states. In the 60s, Newton derived a completeness relation in Hilbert space that included bound states and the non-resonant real-energy continuum but not resonances *per se*. In 1968, Berggren introduced a different completeness relation where bound states, resonances, and non-resonant scattering states are treated symmetrically [29]. The Berggren completeness relation also introduces complex observables, reflecting the interference between continuum and resonance states [29–31]. The main feature of these completeness relations is the inclusion of a continuous spectrum. However, this does not fit into standard Hilbert space quantum mechanics and requires a generalization of Hilbert space into the equipped Hilbert space, the so-called rigged Hilbert space (RHS) [32–34], to include continuous spectra and resonances in quantum mechanics in a consistent way.

The configuration mixing approach based on Gamow states and the Berggren basis is the GSM [11–15]. The GSM is a generalization of the standard SM in HO representation. The symmetric treatment of the one-body resonant states (bound states and resonances) and (complex energy) non-resonant scattering states in the Berggren basis means that the corresponding many-body states are also treated symmetrically. This means that the GSM not only can deal with well-bound nuclear states but is designed to also describe exotic states in nuclei far from the stability. For well-bound states, the GSM and the SM in a harmonic oscillator basis (SM-HO) become indistinguishable.

Nevertheless, the GSM is limited to studies of nuclear structure. This stems from the fact that one cannot describe the asymptotic behavior of reaction channels in the Slater determinant representation. This is remedied by going into the GSM in coupled channel representation (GSM-CC) [15–17]. Although originally formulated for the inclu-

sion of single-nucleon decay channels [16, 17], the GSM-CC has been recently expanded to describe deuteron-decay channels [35]. Further developments on the treatment of the deuteron channels can be found in Ref. [36] and the treatment of heavier cluster channels, namely $A = 3, 4$ clusters, can be found in the present thesis.

One of the objectives of this work is to further the understanding of nuclear structure by doing GSM-CC calculations with many reaction channels corresponding to several mass partitions. Specifically, the aim is to do calculations of nuclear structure and reactions with heavier projectiles in a large network of coupled reaction channels. Another advantage of the method is that treating both cluster-like states and shell model-like states symmetrically in the coupled channels framework provides insight into the competition of both effects. The systems chosen for such calculations are ${}^7,8\text{Be}$ and ${}^7\text{Li}$ because they possess both the low-energy cluster thresholds, and the intricate variation of the structure of many-body states in a narrow range of excitation energies, with coexisting 'shell model-like' states and the 'cluster-like' states. However, to stress the advantage of the GSM-CC over other models, we also present results for ${}^{42}\text{Sc}$, which were carried out with a ${}^{40}\text{Ca}$ core. Let us also mention in passing that the no-core GSM-CC has been recently applied for a study of the first excited 0_2^+ state of ${}^4\text{He}$ [25].

Spectroscopic factors serve as an essential link between cross-sections and nuclear structure, with complex SFs characterizing resonant states. Furthermore, the near-threshold clustering, observed in various nuclei [8, 9], points to a general phenomenon present at different emission thresholds. In this work, we investigate the near-threshold phenomena within the framework of the GSM-CC, providing a comprehensive understanding of near-threshold effects in nuclear reactions and their significance in the study of nuclear structure in various nuclei. These studies are focused on the dependence of reaction channel probabilities and SFs on a distance from the decay thresholds. Furthermore, the definition of the continuum coupling correlation energy in GSM-CC, which could become in the future a convenient theoretical tool to quantify the configuration mixing in resonance states has been proposed in this thesis.

Near-threshold effects are crucial in unraveling the universal behavior of atomic nuclei. The unitarity of the S -matrix ensures the preservation of probability flux, leading to the redistribution of probability when particle emission thresholds are crossed. Wigner cusps [37] play a vital role in understanding these effects. Experimental studies confirmed the existence of cusps in cross-sections, and their implications extend to nuclear structure calculations, particularly when dealing with resonances. Specifically, in this work we expand on previous GSM results of near-threshold effects [38, 39] and further generalize it with clusters in the GSM-CC framework. This analysis provides an insight into the clustering as an emergent near-threshold phenomenon which is a consequence of the alignment of near-threshold shell model states of an OQS with the cluster emission threshold. Indeed, by looking at the distribution of reaction channels probabilities, SFs, and a continuum coupling energy correction, we can analyze those effects in some details. This analysis is done for the light nuclei: ${}^7,8\text{Be}$ and ${}^7\text{Li}$ using a network of the coupled reaction channels constructed with different partitions of the total masses of nucleons.

This thesis is divided as follows. Chapter 1 contains a brief introduction to the scattering theory concepts like the S -matrix and Gamow states. Afterwards, the focus is shifted on introducing the Berggren completeness relation and the RHS.

Chapter 2 contains an introduction to various many-body approaches to nuclear structure. Both OQS and CQS formulations are addressed. Next, in Chapter 3, we introduce the GSM and draw comparisons with other OQS approaches like the SMEC or NCSMC.

The coupled channel formulation of the GSM is presented in Chapter 4 alongside the

comparison with other models. The results of GSM-CC calculations with multiple mass partitions for spectra of ${}^7,8\text{Be}$, ${}^7\text{Li}$, ${}^{42}\text{Sc}$, and the reactions corresponding to the elastic scattering of ${}^3\text{He}$ and triton on ${}^4\text{He}$ target, and the transfer reaction ${}^{40}\text{Ca}(d,p){}^{41}\text{Ca}$, are discussed in Chapter 5.

Chapter 6 is devoted to the study of near-threshold effects. We present the concept of Wigner cusp and then we show results of near-threshold effects in ${}^7,8\text{Be}$ and ${}^7\text{Li}$ by studying the probability weights of different channels, the SFs, and the continuum coupling correlation energy appropriately defined for the GSM-CC. Finally, we summarize and conclude this work in the conclusion. Few technical details are presented in the Appendices A.1 and A.2.

The single particle Berggren basis

Resonances have been of particular theoretical interest since its conception as *quasi-bound* states in the paper of Gamow on α decay [26]. In the late 30s, Siegert [40] utilized complex energies in the context of nuclear scattering to derive a dispersion formula for resonances. These two developments meant that complex eigenvalues could be useful for the description of nuclei. At the same time, the S -matrix formalism has been developed by Heisenberg [27], building up from the work of Wheeler [41]. Although originally formulated for quantum scattering, the S -matrix would later prove to have meaning in nuclear structure. Indeed, the poles of the S -matrix correspond to the resonant states of a system. A few decades later, the concept of resonances has been rigorously formulated by Rosenfeld and Humblet [28] in a comprehensive theory of nuclear reactions. This of course did not address the problems of including resonances in a theory of nuclear structure.

In quantum mechanics, one can expand a solution of the Schrödinger equation using a complete basis set. This of course is generally addressed when one deals with discrete eigenvalues. Problems arise when trying to do so for a basis with continuous eigenvalues, because the elements of such basis are not in the Hilbert space. For a complete theory, we would need both discrete basis elements representing bound states, resonances and continuous basis elements representing the scattering continuum. A method to normalize Gamow vectors was proposed by Zel'dovich [42], hence one last piece was missing: how to put both Gamow vectors and continuum states together? The first one to find a solution was Berggren in 1968 [29], who proved the completeness relation that treats bound, resonance and scattering states symmetrically. Nevertheless, a consistent formulation within quantum mechanics arrived much later with the RHS formalism [32–34, 43]. In this formalism, the resonances find a place naturally alongside bound states and non-resonant continuum states.

In this chapter, we attempt to give all the needed information to not only formulate the Berggren basis but also to be able to build it numerically. We start by giving the definition of Gamow states where we also introduce an important concept that comes recurrently in the theory of resonances which is the complex k -plane with the S -matrix poles. Then we give a refresher on scattering theory, the S -matrix and the Jost functions. Afterwards, we introduce the Berggren completeness relation as originally introduced by Berggren and also other completeness relations like the Newton or the Mittag-Leffler completeness relations. We follow the theory with some practical steps to construct a

Berggren basis for a given one-body interaction. Finally, we end up with some elements of the RHS formalism. The latter part does not provide an extensive description but it is aimed to include the necessary theory to understand resonant expansions.

1.1 Gamow states

In any quantum mechanics experiment, we find a system in either a bound (stationary) state or a scattering state. A resonance or *quasi-stationary state* will decay over time and hence one says that it has a finite lifetime. This means that resonances cannot be measured in the same way as bound states, but should be measured via the characteristics of the scattering states like scattering amplitudes and phase shifts. This information can be extracted from the S-matrix [27].

In the advent of quantum mechanics, Gamow introduced complex energy eigenvalues in his paper about α -decay [26]. The traditional definition of a resonance express it as a solution of the Schrödinger equation $\Psi(\mathbf{r}, t) = \Phi(\mathbf{r}) \exp(-itz/\hbar)$ with a complex energy eigenvalue: $z = E - i\Gamma/2$. This means that the probability amplitude of the wave functions is:

$$|\Psi(\mathbf{r}, t)|^2 = |\Phi(\mathbf{r})|^2 \exp\left(-\frac{\Gamma}{\hbar}t\right), \quad (1.1)$$

where Φ is the complex eigenfunction of this state, which together with the decaying exponential factor is called *quasi-stationary* as Ψ decays exponentially in time.

We follow Humblet and Rosenfeld's [28] definition of the resonant states. Assuming spherical symmetry, we can separate the radial and angular parts of the Schrödinger equation. The angular solutions are the spherical harmonics and will not be discussed in this work as they are already discussed in any elementary quantum mechanics book. The radial Schrödinger equation is:

$$u_\ell''(r, k) = \left[\frac{\ell(\ell+1)}{r^2} + v_\ell(r) - k^2 \right] u_\ell(r, k), \quad (1.2)$$

with boundary conditions:

$$u_\ell(0, k) = 0, \quad (1.3)$$

$$u_\ell(R)u_\ell'(kR) - u_\ell'(R)u_\ell(kR) = 0, \quad (1.4)$$

where u_ℓ is the radial solution for angular momentum ℓ , v_ℓ is the interaction (which for atomic nuclei is nuclear + Coulomb interaction), k is the momentum eigenvalue, R is a radius greater than the range of the nuclear interaction, and u_ℓ^+ is the outgoing solution with $v_\ell(r) = 0$.

The roots of Eq. (1.4) may be complex, hence we define for each eigenfunction $u_{\ell n} \equiv u_\ell(r, k_{\ell n})$ a complex eigenvalue $k_{\ell n}$ as

$$k_{\ell n} = \kappa_{\ell n} - i\gamma_{\ell n}. \quad (1.5)$$

We can relate κ and γ to the well known energy E and widths Γ via the following formulae

$$\frac{\hbar^2}{2m}k_{\ell n} \equiv E_{\ell n} - \frac{1}{2}i\Gamma_{\ell n}, \quad (1.6)$$

with

$$E_{\ell n} = \frac{\hbar^2}{2m}(\kappa_{\ell n}^2 - \gamma_{\ell n}^2), \quad \Gamma_{\ell n} = \frac{\hbar^2}{2m}4\kappa_{\ell n}\gamma_{\ell n}. \quad (1.7)$$

We can categorize eigenstates by their asymptotics as follows:

- if $\kappa_{\ell n} > \gamma_{\ell n} > 0$ then $u_{\ell n}$ is a *decaying narrow resonance state*¹
- if $\gamma_{\ell n} > \kappa_{\ell n} > 0$ then $u_{\ell n}$ is a *decaying subthreshold resonance state*²
- If if $\kappa_{\ell n} > 0 > \gamma_{\ell n}$ the $u_{\ell n}$ is a *capturing resonance state*
- if $\kappa_{\ell n} = 0$ and $\gamma_{\ell n} < 0$ then $u_{\ell n}$ is a *bound state*
- if $\kappa_{\ell n} = 0$ and $\gamma_{\ell n} > 0$ then $u_{\ell n}$ is a *virtual or antibound state*

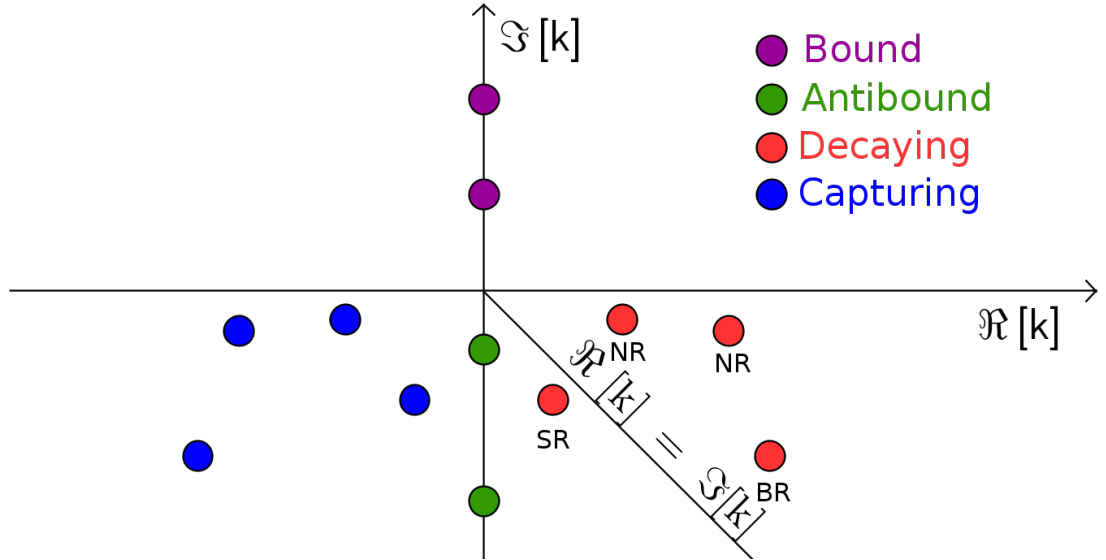


Figure 1.1: Schematic representation of the complex k -plane. Positions of S -matrix poles corresponding to bound states, antibound states, decaying resonances and capturing resonances are shown in magenta, green, blue and red, respectively. Classification of decaying resonances is made explicitly as a subthreshold resonance is denoted SR, a broad resonance BR and narrow resonances as NR. Decaying and capturing resonances are symmetric with respect to the imaginary k axis because of complex conjugation symmetry. The -45° line separates subthreshold resonances from other decaying resonances.

Before we shall discuss the experimental characteristics of resonant states, we stress the difference between a resonance and a decaying particle. A resonance refers to the energy distribution of an outgoing particle in a scattering process and is characterized by its energy and width. Whereas a decaying particle is described in a time-dependent setting by its energy and lifetime τ . Both are related by:

$$\Gamma = \frac{\hbar}{\tau}. \quad (1.8)$$

Experimentally, most systems allow for the measurement of either width or lifetime.

In nuclear physics, we can measure a resonance width via phase shifts/scattering cross-sections of nuclear reactions. Resonances will show up as *quasi*-Lorentzian peaks in the

¹We stress the distinction between the terms *resonant* and *decaying resonance*. A *resonant* state corresponds to a pole of the S -matrix whereas a *resonance* state corresponds to the definition given above. Hence resonance, bound and antibound states are all resonant states.

²Another way to distinguish narrow and subthreshold resonances is that narrow resonances are above the 45° line in the fourth quadrant of the complex k -plane and subthreshold resonances are below the 45° line.

cross-section. The 'quasi' part is very important, because in a Lorentzian distribution the peak would be at the energy of the resonance. However, for a resonance it is not necessarily true. This means that the narrower the resonance is, the more a peak coincides with the resonance energy and is better fitted by a Breit-Wigner distribution³.

Contrary to bound states asymptotics that tend to zero for large distances, antibound states have the following asymptotics:

$$u_\ell(r) \sim e^{\gamma_{\ell n} r}. \quad (1.9)$$

Therefore they grow exponentially at long distances. It is difficult to give a physical interpretation to antibound states. Strictly speaking, antibound states live within the second energy Riemann sheet which is inaccessible to experiments, hence one can say that it is not actually a state but a feature of the system. Low energy antibound states greatly increase the density of real-energy scattering states just above the threshold [44, 45]. This means that antibound states influence the behavior of the scattering cross-sections at low energy. Some classic examples include the $l = 0$ neutron-neutron scattering phase shift [46], the scattering of slow electrons on molecules [47–49], and the eep -Coulomb system [50].

1.2 Scattering states

Before we can introduce the Berggren basis, we need to add one additional final ingredient. A scattering state is also a solution to the Schrödinger equation, however, it is not a pole of the S -matrix contrary to the Gamow states. Physically, it describes the behavior of particles that scatter away from each other and are no longer strongly interacting.

Broadly speaking, in an experiment one sends a projectile with the wave function φ^{in} towards a target. After the collision, φ^{in} becomes an outgoing state φ^{out} . What we measure is the probability of finding a particular projectile state ψ^{out} given by:

$$\langle \psi^{\text{out}} | \varphi^{\text{out}} \rangle = \langle \psi^{\text{out}} | S | \varphi^{\text{in}} \rangle, \quad (1.10)$$

where S stands for the S -matrix. The incoming states are determined by the preparation of the experiment while the outgoing states are determined by both the initial conditions through φ^{in} and by the scattering process through the S -matrix. Finally, ψ^{out} is determined by the final conditions of the detection system.

More importantly, asymptotically the states φ^{in} and ψ^{out} form the so called incoming φ^+ state and outgoing ψ^- state in the remote past and in the distant future, respectively. The probability amplitude (1.10) becomes:

$$\langle \psi^{\text{out}} | \varphi^{\text{out}} \rangle = \langle \psi^+ | \varphi^- \rangle. \quad (1.11)$$

Moreover, the states φ^{in} and ψ^{out} are related to the states φ^+ and ψ^- via the Møller operators:

$$\begin{aligned} \Omega_+ \varphi^{\text{in}} &= \varphi^+ \\ \Omega_- \psi^{\text{out}} &= \psi^-. \end{aligned} \quad (1.12)$$

The physical interpretation of the Møller operators is that they convert the free states φ^{in} and ψ^{out} into the states φ^+ and ψ^- that are equal to them in the remote past and

³Lorentz and Breit-Wigner distribution are the same. However, in physics we typically use the term *Breit-Wigner distribution* when referring to resonance measurements.

remote future, respectively. The theory of quantum scattering is rather broad. For more details on the Møller operators and what follows until the derivation of the cross-sections one can see for example Ref. [51]. For a detailed physical interpretation of preparing an experiment and what is measured by a detector see Ref. [52]. Ultimately, what really matters in quantum scattering is the probability amplitude (1.10), (1.11), so there is focus on the calculation of the incoming and outgoing states and/or the S-matrix.

Solutions to equation (1.2) which can be conveniently categorized as incoming and outgoing, describe the behavior of a particle before and after it interacts with the nuclear potential, respectively. We can do this separation because Eq. (1.2) is a second order differential equation and hence, it has two independent solutions. In order to properly define an incoming and outgoing solution we first consider the asymptotic solutions of Eq. (1.2), which becomes:

$$u_\ell''(r, k) = \left[\frac{\ell(\ell+1)}{r^2} + \frac{2\eta k}{r} - k^2 \right] u_\ell(r, k), \quad (1.13)$$

where η is the Sommerfeld parameter:

$$\eta = \frac{mZ}{\hbar^2 k}. \quad (1.14)$$

The solutions to Eq. (1.13) are the regular $F_{\ell,\eta}(kr)$ and irregular $G_{\ell,\eta}(kr)$ Coulomb wave functions [53]. Moreover, from the asymptotic behavior of the Coulomb wave functions, we can define the incoming and outgoing Coulomb wave functions as:

$$H_{\ell,\eta}^+(kr) = G_{\ell,\eta}(kr) + iF_{\ell,\eta}(kr) \quad (1.15)$$

$$H_{\ell,\eta}^-(kr) = G_{\ell,\eta}(kr) - iF_{\ell,\eta}(kr). \quad (1.16)$$

Thus, we have the following asymptotic solutions:

$$\begin{aligned} u(r, k) &= C_0 r^{l+1} & r \sim 0 \\ u(r, k) &= C^+ H_{\ell,\eta}^+(kr) + C^- H_{\ell,\eta}^-(kr) & r \rightarrow \infty, \end{aligned} \quad (1.17)$$

where $C_0, C^+, C^- \in \mathbb{C}$ are constants to be determined. Now we can define the general outgoing and incoming solutions with the following boundary condition:

$$u^\pm(r, k) = H^\pm(r, k), \quad r \rightarrow \infty. \quad (1.18)$$

Therefore, an arbitrary scattering state is:

$$u(r, k) = C^+ u^+(r, k) + C^- u^-(r, k). \quad (1.19)$$

In comparison, the asymptotics requirements of bound and resonance states require the amplitudes u to vanish when $r \rightarrow \infty$, therefore $C^- = 0$ is necessary for these states.

1.3 The S-matrix and Jost functions

An important concept in scattering theory is the S-matrix. It is a mathematical object that describes the behavior of a quantum system when two or more particles interact. The concept was originally conceived by Wheeler in 1937 [41] and later expanded upon by a series of papers of Heisenberg starting in 1942 [27]. Physically, the scattering matrix relates the initial state with the final state of a quantum mechanical system. This lead

Heisenberg to believe that the S-matrix would replace the Hamiltonian, however, it was not the case [54]. Although the S-matrix theory is very broad and interesting, for the purposes of this work it is better to skip part of the formalism before its description in terms of the Jost functions.

The Jost functions were originally introduced by Res Jost [55]. The concept was conceived as a means to describe the asymptotic behavior of the solutions to the Schrödinger equation. One can define the Jost functions via the Wronskian:

$$J^\pm(k) = W[u(r, k), u^\pm(r, k)] = u(r, k)u'^\pm(r, k) - u'(r, k)u^\pm(r, k), \quad (1.20)$$

where u^\pm are the outgoing and incoming solutions. The Jost function is independent of r . This can be easily proven by taking Eq. (1.2) and the derivative of the Jost function with respect to r . The S-matrix can be defined from the Jost functions as:

$$S_\ell(k) = \frac{J^-(k)}{J^+(k)} = -\frac{C^+}{C^-}. \quad (1.21)$$

Since the S-matrix is unitary, then it can also be defined as:

$$S_\ell(k) = \exp(2i\delta_\ell(k)), \quad (1.22)$$

where $\delta_\ell(k)$ is the phase shift of the scattering state $u(r, k)$. Generally, phase shift refers to the amount by which a phase of wave functions differs from a reference wave. In this case the reference wave is that of a free particle.

1.4 The Berggren basis

One usually uses a complete basis or orthonormal eigenfunctions to describe a quantum system. A basis set $\{|n\rangle\}$ is complete if any quantum state $|\Psi\rangle$ can be expressed as a linear combination of the basis states $|n\rangle$:

$$|\Psi\rangle = \sum_n c_n |n\rangle, \quad (1.23)$$

where $c_n = \langle n|\Psi\rangle$. If the set is complete, then we have the *completeness relation*:

$$\langle\Psi|\Psi\rangle = \sum_n |c_n|^2 = 1, \quad (1.24)$$

and the *closure relation*:

$$\delta(r - r') = \sum_n v_n(r)v_n^*(r'), \quad (1.25)$$

where $v_n(r)/r = \langle r|n\rangle$, which can be written as a *projection operator*:

$$\mathbb{1} = \sum_n |n\rangle\langle n|. \quad (1.26)$$

In the theory of resonant states expansion, it is customary to call Eqs. (1.25) and (1.26) the completeness relations [56].

An example of a complete and orthogonal basis is the HO basis. However, due to the nature of the HO potential one can only describe bound states using this basis. In the 60s, Newton derived the completeness relation in Hilbert space for neutral particles [51]. This completeness relation goes as follows:

$$\sum_n u_{\ell,n}(r)u_{\ell,n}^*(r') + \int_0^\infty dk u_\ell(k, r)u_\ell^*(k, r') = \delta(r - r'), \quad (1.27)$$

where $u_{\ell,n}(r)$ are bound states with positive imaginary momentum k , and $u_{\ell}(k, r)$ scattering states with real momentum. Even though it is possible to use the Newton completeness relation (1.27) to describe resonance phenomena, however its application would be impossible in most cases as it would require a very fine discretization of the integral [15]. Thus if the resonance is narrow, one risks to miss it.

Nevertheless, it was this approach that Berggren used [29] to show the completeness relation that included not only scattering and bound states but also decaying resonance states. Here we show the outline of the proof of the Berggren completeness relation which was based on the Newton completeness relation [51]. Berggren improved upon Newton by instead taking a deformed contour in k -plane that would embed narrow resonances, i.e. the poles in the second Riemann sheet of the S -matrix [29]. The Berggren completeness relation reads:

$$\sum_n u_{\ell,n}(r) \tilde{u}_{\ell,n}^*(r') + \int_{L^+} dk u_{\ell}(k, r) \tilde{u}_{\ell}^*(k, r') = \delta(r - r'). \quad (1.28)$$

The difference with the Newton completeness relation is two-fold. First of all the discrete sum contains not only bound states but also narrow resonances. Second, the contour integral over non-resonant scattering states is deformed into the path L^+ in the fourth quadrant of the complex k -plane embedding all important resonances. This allows for the simultaneous treatment of bound, resonance and non-resonant scattering states.

The idea of the original proof of Berggren was to evaluate the integral:

$$I(r) = \int_C k dk \int_0^{\infty} dr' h(r') G_{\ell}(-k, r, r'), \quad (1.29)$$

where h is at least square integrable, G_{ℓ} is the Green's function associated to Eq. (1.2) and C is a contour to be defined. The contour C that is used for Gamow Shell Model (GSM) applications is a semicircle in the upper k plane and a deformed contour that encloses the resonance poles as shown in Fig. 1.1. The integral can be divided into two parts: the outer semicircle I_R and the deformed L part I_L . It can be shown using the asymptotic properties of the regular and irregular solutions of Eq. (1.2) alongside the properties of the Jost functions that

$$I_R(r) = i\pi h(r). \quad (1.30)$$

On the other hand:

$$I_L(r) = -i\pi \int_0^{\infty} dr' h(r') \int_{L^+} dk u_{\ell}(k, r) \tilde{u}_{\ell}^*(k, r'), \quad (1.31)$$

where u_l are non-resonant solutions of Eq. (1.2) and the tilde refers to time conjugation. Lastly, the integral in Eq. (1.29) can be evaluated using the analytic properties of the Jost functions and the Cauchy residue theorem. It gives:

$$I(r) = i\pi \int_0^{\infty} dr' h(r') \sum_n u_{\ell n}(r) \tilde{u}_{\ell n}^*(r'), \quad (1.32)$$

where u_{ln} are bound or resonant solutions of Eq. (1.2). Using Eqs. (1.30, 1.31, 1.32) we find:

$$\int_0^{\infty} dr' h(r') \delta(r - r') = \int_0^{\infty} dr' h(r') \left[\sum_n u_{\ell n}(r) \tilde{u}_{\ell n}^*(r') + \int_{L^+} dk u_{\ell}(k, r) \tilde{u}_{\ell}^*(k, r') \right]. \quad (1.33)$$

Hence, the Berggren completeness relation is:

$$\delta(r - r') = \sum_n u_{\ell n}(r) \tilde{u}_{\ell n}^*(r') + \int_{L^+} dk u_{\ell}(k, r) \tilde{u}_{\ell}^*(k, r'). \quad (1.34)$$

Here we have skipped the definitions of resonant and non-resonant solutions of Eq. (1.2) in terms of Jost functions and the incoming and outgoing solutions, but details can be found in Refs. [29, 51, 56].

An issue with this proof is that it assumes that the interaction v_l is analytic in the upper complex k -plane. This is not the case for the Coulomb interaction. However, a complete proof has been given by Michel [57] for not only Coulomb interaction but also for non-local potentials. The tilde in Eq. (1.27) and (1.28) corresponds to time reversal. Indeed, differently from standard quantum mechanics where the inner product takes the form $\langle u_f | u_i \rangle = \int dr u_f^*(r) u_i(r)$, the inner product is not the standard one. This requires a reformulation of quantum mechanics in RHS [32–34]. In the theory of RHS the inner product changes and all observables for unbound states are complex.

Eq. (1.28) includes only bound states and few resonances, however it is not unique. Indeed if one were to modify the contour of integration, one can derive relations that include different combinations of poles of the S-matrix [56] which will redistribute the imaginary part from the sum to the integral or vice-versa. To distinguish among the following completeness relations we introduce the labels a, b, c, d for antibound, bound, capturing resonance and decaying resonance, respectively. If we were to use a contour that includes both capturing and decaying resonances, the completeness relation would be:

$$\delta(r - r') = \sum_{n=b} u_{\ell n}(r) \tilde{u}_{\ell n}^*(r') + \frac{1}{2} \sum_{n=c,d} u_{\ell n}(r) \tilde{u}_{\ell n}^*(r') + \int_W dk u_{\ell}(k, r) \tilde{u}_{\ell}^*(k, r'), \quad (1.35)$$

where W is the red contour shown in Fig. 1.2 which includes bound, decaying and capturing resonances. If now we also include the antibound states using contour U from Fig. 1.2 then we would obtain:

$$\delta(r - r') = \frac{1}{2} \sum_{n=a,b,c,d} u_{\ell n}(r) \tilde{u}_{\ell n}^*(r') + \int_U dk u_{\ell}(k, r) \tilde{u}_{\ell}^*(k, r'). \quad (1.36)$$

Moreover, the completeness relation that arises using the Mittag-Leffler theory [58] is:

$$\delta(r - r') = \frac{1}{2} \sum_n u_{\ell n}(r) \tilde{u}_{\ell n}^*(r'), \quad (1.37)$$

where the sum goes over all poles of the S-matrix. The relation (1.37) is valid for a given radius R_c smaller than the range of the potential generating the basis $\{u_{\ell n}\}$.

Eqs. (1.35), (1.36) and (1.37) are called *overcompleteness relations*. This comes from the fact that the basis states are not linearly independent, and this is embodied by the $1/2$ factors. Eq. (1.35) is not useful in practice as we are just double counting the resonances as their contribution is the same due to symmetry under complex conjugation. Eq. (1.36) has a $1/2$ factor that indicates that the antibound states may have a similar contribution as bound states. However, the need of both bound and antibound states may indicate that the eventual difference between them is formally important and not compensated by the integral.

Finally, Eq. (1.37) may seem more practical due to the absence of a contour integral, however it is difficult to deal with the non-orthogonality in numerical application because

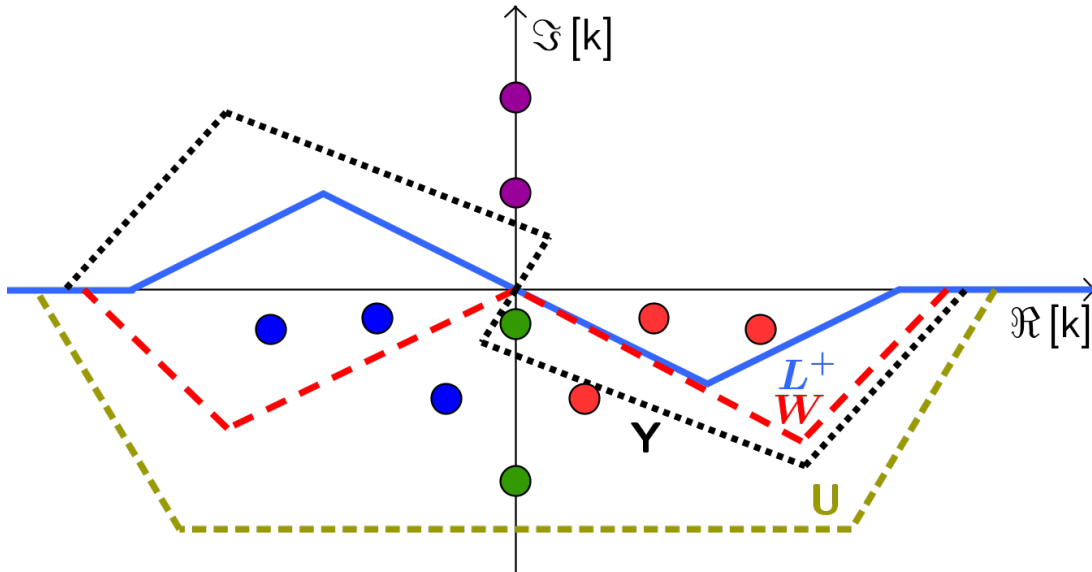


Figure 1.2: Schematic representation of the complex k -plane with different possible contours. Positions of S -matrix poles corresponding to bound states, antibound states, decaying resonances and capturing resonances are shown in magenta, green, blue and red, respectively. Figure inspired from Ref. [56].

one has to solve generalized eigensystems. Additionally, the absence of the integral implies that the contour integral from the other completeness relations is equivalent to the infinite sum of the resonances outside of them. To achieve convergence, one would require a large cut-off radius. Moreover, the amplitude of antibound and resonance states increase exponentially with r , adding instability to any calculation. Hence, even though the Mittag-Leffler completeness relation seem to be more practical at first glance, it is in fact not. This is why we stick to Eq. (1.28).

Another feature of the Berggren basis are complex observables. The mean value of an observable \mathcal{O} is complex and is given by:

$$\langle \mathcal{O} \rangle = \text{Re}[\mathcal{O}] + i\text{Im}[\mathcal{O}], \quad (1.38)$$

where the real part is the measured mean value of this observable and the imaginary part can be interpreted as its uncertainty [29–31, 59] coming from the interference between the continuum states and resonance states.

Lastly, even though the aforementioned completeness relations work for a basis $\{u_\ell\}$ generated by a real potential, they also work for eigenfunctions generated by complex potentials [15]. This can be proven by using a potential:

$$V(\lambda, r) = V_R(r) + \lambda V_I(r), \quad (1.39)$$

where $\lambda \in \mathbb{C}$. If λ is real then the potential is real. One can make it complex by an analytic continuation such that $\lambda = i$. This has to be done cautiously because if one has a spectral singularity (a resonance on the real axis) [60], then nonanalytic points are generated and it is not possible to use a real energy contour. Nevertheless, this is easily avoided by deforming the contour and the spectral singularities can be normalized with complex scaling.

Another case when the analytic continuation does not work for complex potentials corresponds to the exceptional point (EP) [10, 61–64]. EPs appear when two resonances with the same quantum numbers coincide in the complex k -plane. This makes the Berggren

basis incomplete. However one can regain completeness by adding the derivative with respect to k of the wave functions associated to the exceptional states [65]. The latter happens because $u_n(r)$ and $du_n(r)/dk$ are linearly independent.

1.4.1 Normalization and regularization of the Berggren basis

Due to the complex nature of the momentum k , the magnitude of the resonance states oscillations increase exponentially in space. This poses a problem when trying to compute observables and also in the normalization of the basis. Integrals that appear in the calculations for resonant and scattering states have to be regularized. One method of regularization has been proposed by Zel'dovich [42]. This method consisted in adding an exponential factor with a limit:

$$\text{Reg} \int_0^\infty dr u_f(r) \hat{\mathcal{O}}(r) u_i(r) = \lim_{\epsilon \rightarrow 0} \int_0^\infty dr e^{-\epsilon r^2} u_f(r) \hat{\mathcal{O}}(r) u_i(r), \quad (1.40)$$

where $\hat{\mathcal{O}}$ is an arbitrary operator. This method though formally correct, is not useful in practical applications as the convergence requires very large computational resources to obtain stable results [66]. Nevertheless, this allowed Berggren [29] to normalize the Gamow states. A more convenient approach, called external complex scaling, has been proposed by Gyarmati and Vertse [66]. This method relies on the wave functions being regular in the first quadrant of the complex plane. By using the Cauchy Theorem, integrating in the contour given by:

$$z = \begin{cases} r & R \leq r < \infty & \text{on } C_1 \\ |z|e^{i\alpha} & |z| \rightarrow \infty & 0 \leq \alpha \leq \phi & \text{on } C_2 \\ R + \rho e^{i\phi} & \arctan \frac{\gamma}{\kappa} < \phi < \frac{1}{2}\pi & 0 \leq \rho < \infty & \text{on } C_3 \end{cases} \quad (1.41)$$

(see Fig. 1.3) yields zero. Thus, for a radius larger than a given rotation point R we can do a change of the variable.

Since the integrands are regular, the contour integral is zero. This allows for a substitution $r \rightarrow R + \rho e^{i\theta}$, where θ is an angle that is chosen to ensure convergence [13]. In this way, we are able to construct numerically a Berggren basis of normalized single-particle eigenstates. Following Kukulín *et al.* [67], we introduce the functional on $(-\infty, V_{\text{lim}})$:

$$F(V_0) = \frac{\mathcal{O}_{ij}}{N_i N_f}, \quad (1.42)$$

which is just a matrix element where the Gamow vectors are assumed to be not normalized. Using the complex rotation method, the normalization factors are:

$$N_i^2 = \int_0^\infty dr u_i^2(r) + \int_0^\infty d\rho u_i^2(R + \rho e^{i\phi}) e^{i\phi}, \quad (1.43)$$

and the not normalized matrix elements are:

$$\mathcal{O}_{ij} = \int_0^R dr u_f(r) \hat{\mathcal{O}}(r) u_i(r) + \int_0^\infty d\rho u_f(R + \rho e^{i\phi}) \hat{\mathcal{O}}(R + \rho e^{i\phi}) u_i(R + \rho e^{i\phi}) e^{i\phi}. \quad (1.44)$$

In Ref. [67], the analytic continuation of Eq. (1.42) was done using Padé approximants. In contrast, the complex rotation method allows the calculation for potentials with $V_0 > V_{\text{lim}}$. Regardless if u_i and u_f are bound or resonance states, one defines the following angles α_i, α_f from the momenta $k_i = |k_i|e^{i\alpha_i}$ and $k_f = |k_f|e^{i\alpha_f}$. One also knows the asymptotics

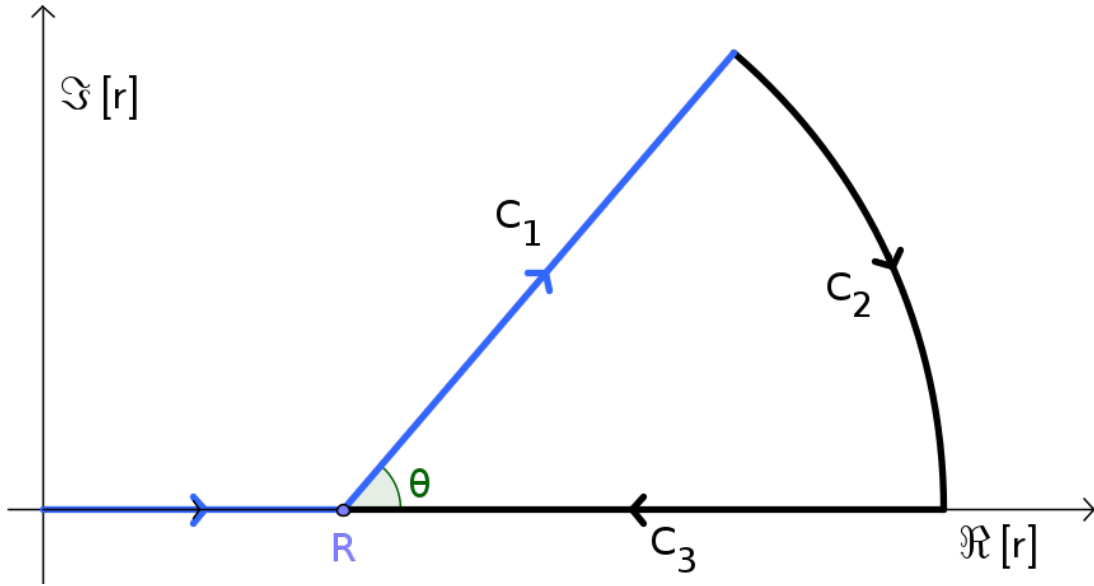


Figure 1.3: The integration path in the complex plane corresponding to the complex rotation technique at a point R with an angle θ . R is large compared to the nuclear radius which means that the nuclear potential is negligible for $r > R$. The blue lines indicate the integration done in practice that is equivalent to integrating on the real axis.

of the radial wave functions $u(r) \rightarrow a(r)e^{ikr}$, where $a(r)$ is an increasing function of polynomial order⁴. Hence, the second integrand in Eq. (1.44) becomes

$$a_f(R + \rho e^{i\phi})\hat{O}(R + \rho e^{i\phi})a_i(R + \rho e^{i\phi})e^{i(k_i+k_f)R}e^{i\phi}e^{i(k_i+k_f)\rho e^{i\phi}}. \quad (1.45)$$

Assuming that \hat{O} is also a function of polynomial order, the only term that can make the integrand equal to zero at the limit $\rho \rightarrow \infty$ is the term $e^{i(k_i+k_f)\rho e^{i\phi}}$. In particular, if we separate the argument of the exponential in real and imaginary parts, only the imaginary part leads to the exponential decay. We have the following inequalities that would allow for convergence

$$\begin{aligned} \text{Im}[(k_i + k_f)\rho e^{i\phi}] &> 0 \\ \text{Im}[(k_i + k_f)e^{i\phi}] &> 0 \\ \text{Im}[|k_i|e^{i(\phi-\alpha_i)} + |k_f|e^{i(\phi-\alpha_f)}] &> 0. \end{aligned} \quad (1.46)$$

Relations (1.46) mean that we need to *rotate* the momenta of resonances in such a way that the sum of both imaginary parts are positive. Additionally, since every other part of the integrand is of polynomial order, the exponential decay will make the integral converge. Therefore, all integrals are properly regularized. The result is independent of the choice of ϕ , however it must follow the condition:

$$2\phi > \alpha_f + \alpha_i. \quad (1.47)$$

Lastly, this method can be used also for the regularization of scattering states but one must consider separately the incoming and outgoing parts of the wavefunction $u(r)$. Contrary to resonances and bound states, the presence of both incoming and outgoing parts in the same integral does not allow to find a unique path in the complex plane along which the integrand decreases exponentially. Hence, the one-body matrix element

⁴By polynomial order we mean that the function increases or decreases as fast as a polynomial function.

for scattering states is:

$$F(k_f) = \int_0^R dr [u_f(r)V(r)u_i(r)] + A_f A_i F_{++}(k_f) + A_f B_i F_{+-}(k_f) + B_f A_i F_{-+}(k_f) + B_f B_i F_{--}(k_f), \quad (1.48)$$

where

- $u_f(r) = A_f u_f^+(r) + B_f u_f^-(r)$
- $u_i(r) = A_i u_i^+(r) + B_i u_i^-(r)$, where k_i in $F(k_f)$ is fixed and $u_i(r)$ can be either bound, resonance, or scattering state
- $F_{s_f, s_i} = \int_0^\infty dx u_f^{s_f}(R+x) \hat{O}(R+x) u_i^{s_i}(R+x)$ with $s_f, s_i \in \{+, -\}$.

Additionally, the normalization of scattering states cannot be done in the traditional sense because the integrals diverge. Therefore the normalization to the Dirac delta function is used:

$$\int_0^\infty dr u(k_a, r) u(k_b, r) = \delta(k_a - k_b), \quad (1.49)$$

which leads to the normalization condition

$$2\pi C^+ C^- = 1, \quad \forall u_k. \quad (1.50)$$

1.4.2 Numerical calculation of Berggren basis states

In this subsection, we shall discuss how to generate a Berggren basis. The outline can be found in Ref. [15] and here we develop from there. There are two problems: first we have to be able to calculate the wave functions u for any $k \in \mathbb{C}$, and second we would like to find where the poles of the S-matrix are, otherwise we would never be able to compute bound and resonance wave functions. From Eq. (1.21), we need to find the zeroes of $J^+(k)$.

We need both boundary conditions in Eq. (1.17). Next we choose a matching radius R_m which is of the order of the nuclear interaction range. Typically if one uses a Woods-Saxon potential, one would set $R_m = R_0$. This is what is done in GSM calculations.

We start by integrating in the interval $r \in [r_i, R_m]$ using the first boundary condition in (1.17) where r_i is a very small initial radius. This allows to obtain $u(R_m, k)$. Next, we integrate in the interval $r \in [R_m, R_{\max}]$ using the second boundary condition in (1.17) where R_{\max} is big enough so that the nuclear interaction is negligible. This allows to obtain $C^+ u_{\ell, \eta}^+(kR_m) + C^- u_{\ell, \eta}^-(kR_m)$. Finally, we end up with the system of equations to solve for C^+ and C^- :

$$\begin{aligned} C^+ u_{\ell, \eta}^+(kR_m) + C^- u_{\ell, \eta}^-(kR_m) &= u(R_m, k) \\ C^+ u_{\ell, \eta}'^+(kR_m) + C^- u_{\ell, \eta}'^-(kR_m) &= u'(R_m, k). \end{aligned} \quad (1.51)$$

This is true for both scattering and resonant states. However, for resonant states $C^- = 0$ and this is what will allow us to find the poles of the S-matrix.

To find the poles of the S-matrix, we use the following algorithm:

1. We start with an initial guess k_{start} which can be from the diagonalization of the potential with a HO basis or may as well be obtained with a bisection method if it is loosely bound, antibound or resonance state.

2. We obtain the wave function for $r \in [r_i, R_m]$, integrate it in the interval $r \in [R_m, R_{\max}]$ where $R_{\max} \gg R_m$, and also set the constants $C^+ = 1$ and $C^- = 0$. C^+ is set to unity for convenience, whereas C^- is zero from the definition of resonant states with outgoing asymptotics.
3. We calculate the Jost function $J^+(k)$. We find the zeroes of this function by means of a Newton-Raphson method calculating new wave functions until convergence.

Afterwards, we just have to normalize the basis as it was discussed in Sect. 1.4.1. Similar figures to Fig. 1.1 are usually shown in the literature to showcase the different S-matrix poles, however, it is quite different for practical cases.

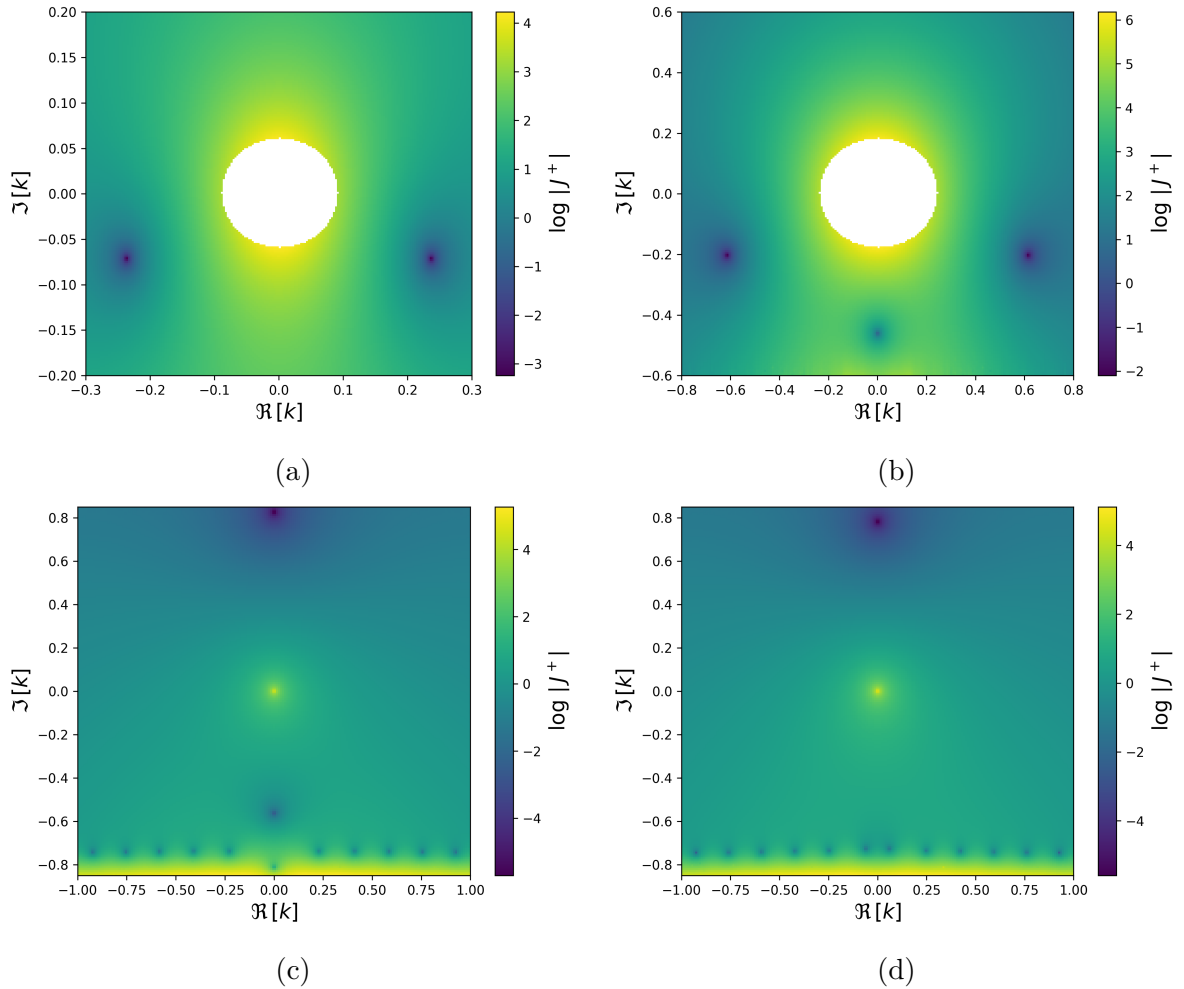


Figure 1.4: Modulus of J^+ for different ℓ_j partial waves in the complex k plane for neutrons. Each calculation was done with the Woods-Saxon parameters (V_0, R_0, d, V_{SO}) and all were done for an $A=4$ core with the exception of (b) which is an $A=16$ core. (a) $p_{3/2}$ (45 MeV, 2 fm, 0.65 fm, 3.8 MeV), (b) $d_{5/2}$ (55 MeV, 2 fm, 0.65 fm, 3.8 MeV) (c) $s_{1/2}$ (53 MeV, 2.2 fm, 0.65 fm, 0 MeV), (d) $s_{1/2}$ (55 MeV, 2 fm, 0.65 fm, 0 MeV). Some values were not included in the figures as they were very large.

Fig. 1.4 shows examples where this algorithm can be employed. Here, we have the logarithm of the modulus of the Jost function. Capturing and decaying resonances mirror each other. This is a consequence of Eq. (1.2) being symmetric under complex conjugation of k . Figs. 1.4a and 1.4b are typical cases that come up in calculations with ${}^4\text{He}$ and

^{16}O cores. A particular difference between them is that Fig. 1.4b has an antibound state. However when one does a GSM calculation one would select the decaying resonance.

On the other hand, Figs. 1.4c and 1.4d showcases particular issues that may arise in GSM calculations and in fact will be mentioned again in Chap. 5. These would be the Jost functions for a ^4He core calculation. The bound state will typically correspond to the frozen core $0s_{1/2}$ shell. Hence, calculations with a ^4He core are generally stable as long as we include only the p -shell. However if one would like to do a ^4He calculation in the psd -shell, one would have to deal with the antibound state in Fig. 1.4c.

Lastly, Figs. 1.4c and 1.4d show how changing the Woods-Saxon parameters change the nature of the S-matrix. For example, the antibound state can become a broad resonance. Moreover, the further one goes away from the real axis, the bigger are the values of the Jost functions. This can lead to numerical inaccuracies and tells us that one must not choose a contour L^+ that extends too deep into the complex plane for the scattering states.

It may happen that the potential needed for a particular calculation gives very unbound poles of the S-matrix. A way to circumvent the numerical limitations is by applying the Berggren completeness relation. One typical application consists of expanding high energy, unbound single-particle states in a more stable basis generated by a binding potential [13]. Such an expansion of a one-body state u_{WS} in a basis generated by another potential $\{u_B\}$ is:

$$u_{WS}(r) = \sum_i c_{k_i} u_B(k_i, r) + \int_{L^+} dk c(k) u_B(k, r), \quad (1.52)$$

where, due to the basis being normalized, the overlap amplitudes follow the condition:

$$\sum_i c_{k_i}^2 + \int_{L^+} dk c^2(k) = 1. \quad (1.53)$$

For certain applications it is useful to use the properties of a HO state. For example, one can expand matrix elements in Berggren basis using the HO basis. This is particularly useful when calculating two-body matrix elements. Another example is the transformation from relative to laboratory coordinates using a Talmi-Brody-Moshinsky [68, 69] transformation. This transformation is straightforward in the HO basis, however it is computationally demanding in any other basis. This difficulty has been circumvented in Berggren basis by expanding the two-body matrix elements with a HO basis truncated to N_{\max} :

$$\langle ab|\hat{V}|cd\rangle = \sum_{\alpha\beta\gamma\delta}^{N_{\max}} \langle\alpha\beta|\hat{V}|\gamma\delta\rangle \langle a|\alpha\rangle \langle b|\beta\rangle \langle c|\delta\rangle \langle d|\delta\rangle, \quad (1.54)$$

where the Latin letters correspond to the Berggren basis, the Greek letters to the HO basis and \hat{V} is a generic interaction [70]. This method is not limited to the Hamiltonian matrix elements but can also be conveniently used for the computation of electromagnetic operators.

1.5 Rigged Hilbert space

We began the discussion of the previous section by defining a completeness relation for a space that has only discrete states and then proceeded to derive the Berggren completeness relation and discuss other overcompleteness relations which are comprised of both a discrete part and a continuous part. In standard quantum mechanics, one would work

with the former as those eigenfunctions would belong to the Hilbert space. We define the Hilbert space for three dimensions as the space of square integrable functions:

$$L^2 = \left\{ f(\mathbf{r}) \mid \int_{\mathbb{R}^3} d\mathbf{r} |f(\mathbf{r})|^2 < \infty, \mathbf{r} \in \mathbb{R}^3 \right\}. \quad (1.55)$$

One can easily prove that a system with a continuous spectrum does not fit in the Hilbert space. Let us take as example the free particle case⁵ of Eq. (1.2) with angular momentum $l = 0$ whose solution is:

$$\Psi_{\text{free}}(r) = A e^{ikr}, \quad (1.56)$$

where A is a normalization constant and its norm is:

$$\|\Psi_{\text{free}}(r)\|^2 = \int_0^\infty dr |\Psi_{\text{free}}(r)|^2 = \int_0^\infty dr A^2 = \infty. \quad (1.57)$$

Hence, Ψ_{free} is not in the Hilbert space.

One can make sense of these cases and also of Dirac's bra-ket notation in the RHS [32–34, 71, 72]. RHS is neither an extension nor an interpretation of the physical principles of quantum mechanics [34]. The main idea of the RHS is to include distributions in the theory in a consistent way. Without too many details⁶, a RHS or Banach-Gelfand triple [43] is a triad of spaces:

$$\Phi \subset \mathcal{H} \subset \Phi^\times, \quad (1.58)$$

where \mathcal{H} is a Hilbert space, Φ is a dense subspace of \mathcal{H} and Φ^\times is the space of antilinear functionals over Φ . Every RHS (1.58) has associated another RHS:

$$\Phi \subset \mathcal{H} \subset \Phi', \quad (1.59)$$

where Φ' contains instead the linear functionals over Φ . Mathematically speaking, Φ can be interpreted as the space of *test functions* while Φ^\times the *space of distributions*. On the other hand, physically, Φ^\times and Φ' will include kets and bras, respectively, that are eigenstates which are not necessarily normalizable in the traditional sense. This is very important, as it will give a *raison d'être* to those *wave functions* that are not square integrable like the Dirac delta [78, 79].

The construction of the space Φ has been discussed for example in Refs. [73, 74] for the Lippmann–Schwinger bras and kets; in Ref. [75] for the Gamow states; and in Ref. [34] for the one-dimensional case with a potential barrier. More interestingly, we can define a ket in the context of RHS. Given a function $f(r)$ and a space of test functions Φ , the antilinear functional F that corresponds to the functions $f(r)$ in an integral operator whose kernel is precisely $f(r)$:

$$F(\varphi) = \int_0^\infty dr \varphi^*(r) f(r). \quad (1.60)$$

Rewriting (1.60) in Dirac's notation, it becomes:

$$\langle \varphi | F \rangle = \int_0^\infty dr \langle \varphi | x \rangle \langle x | f \rangle. \quad (1.61)$$

⁵This may seem like a one dimensional case, however the other two dimensions are within the angular part.

⁶See for example Refs. [32–34, 43, 71–77] for a more rigorous definition.

Let us consider the position \hat{Q} and momentum \hat{P} operator which have continuous spectra:

$$\begin{aligned}\hat{Q}|r\rangle &= r|r\rangle, \quad \|r\|^2 < \infty \\ \hat{P}|p\rangle &= p|p\rangle, \quad \|p\|^2 < \infty,\end{aligned}\tag{1.62}$$

whose wave functions:

$$\begin{aligned}\langle r'|r\rangle &= \delta(r' - r) \\ \langle r|p\rangle &= \frac{1}{(2\pi\hbar)^{3/2}} e^{\frac{i}{\hbar}\mathbf{p}\cdot\mathbf{r}},\end{aligned}\tag{1.63}$$

are not square integrable, hence they do not belong to the Hilbert space. However, if we choose the functional F in Eq. (1.61) to be the position and momentum:

$$\langle\varphi|r\rangle \equiv \int_0^\infty dr \varphi^*(r) \delta(r' - r) \equiv \int_0^\infty dr \langle\varphi|r\rangle \langle r'|r\rangle\tag{1.64}$$

$$\langle\varphi|p\rangle \equiv \int_0^\infty dr \varphi^*(r) \frac{1}{(2\pi\hbar)^{3/2}} e^{\frac{i}{\hbar}\mathbf{p}\cdot\mathbf{r}} \equiv \int_0^\infty dr \langle\varphi|r\rangle \langle r|p\rangle,\tag{1.65}$$

then the fact that the eigenfunctions with continuous spectrum are distributions and are well defined in RHS becomes explicit. Moreover, the definition of a bra can be done analogously to the ket except that they will be defined in a linear space. The completeness relation (1.28) has both a discrete and a continuous part, therefore we need a formalism that allows to properly define normalization for both. Normalization for eigenfunctions with a continuous spectrum is done via the Dirac delta normalization [34].

In conclusion, the RHS allows for the natural inclusion of resonances and non-resonant continuum states in the formulation of quantum mechanics. Here we can include a continuous spectrum part in the completeness relations, unlike standard quantum mechanics that do not allow this because of the requirements of the Hilbert space. Moreover, the normalization of scattering states also makes sense as concepts such as delta normalization make sense within the RHS framework. Thus, making the RHS ideal as the theoretical framework to include the Berggren basis completeness relation (1.28) into quantum mechanics.

Closed versus open quantum systems

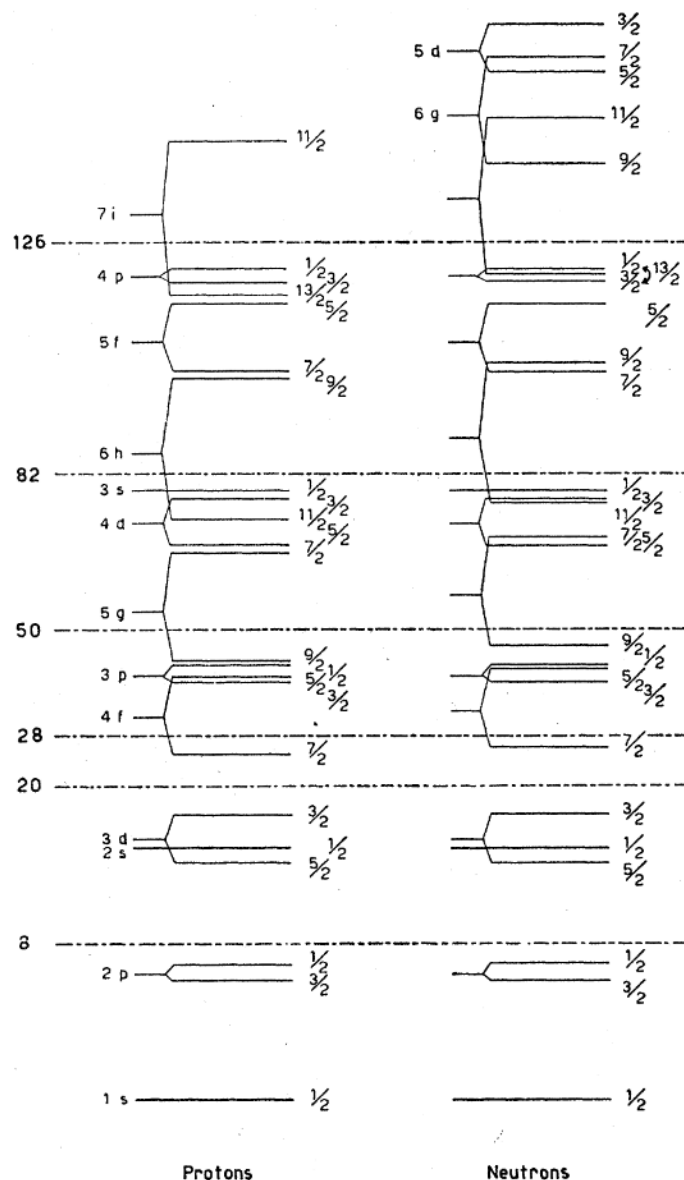
Across different fields in physics, the definition of an OQS varies. In particular, in nuclear physics an OQS is a system A that is coupled to system B , where A is a studied microscopic localized system and B is the environment. In contrast, a CQS is the system A that is decoupled from the environment B . Although many applications exist for an OQS description in other fields like e.g. nanoscience and mesoscopic physics, the focus of this work is in its applications to the atomic nucleus.

In the standard SM [1, 2], one describes the nucleus as completely isolated from the rest of the universe (environment). This approximation is satisfactory for bound states in particle stable nuclei because they are almost decoupled from the environment, as they do not decay and their separation energies are high. However, if we move towards the drip lines far from the valley of stability we encounter a different situation. In this region, we have to deal with weakly bound or unbound nuclei, hence a CQS treatment would be insufficient as the environment of decay channels and scattering states play here an important role. One might argue that it could be possible to treat the continuum perturbatively. However, Fano realized that the perturbative approach is inadequate [80]. Indeed, beyond the drip lines or above the lowest energy reaction threshold, nuclei may decay via the particle emission. This means that the decay channels have to be coupled somehow to the bound and resonance states. Moreover, a SM description of resonances is impossible as it yields real energies (no widths and no information about emission thresholds) and/or no information about scattering (no S -matrix therefore no phase shifts, hence no widths) processes.

In this chapter, we describe some many-body approaches for the description of the atomic nucleus both in CQS and OQS frameworks with the aim to draw comparisons with the GSM in Chaps. 3 and 4. We start first with the SM described originally by Goeppert-Meyer [1] and Haxel, Jensen and Suess [2]. Then we move to the *ab initio* method NCSM [81–83] that treats all particles in the A -body system as active. Afterwards, we move to approaches that include some continuum effects such as the NCSM with RGM [18, 19] approach that treats the atomic nucleus as a pair of clusters and the NCSMC [19, 20]. We end this chapter with the CSM [5, 6] and its recent realization the SMEC [10, 84–89] that are based on the Feshbach projection formalism [3, 4] to define the environment.

2.1 Shell Model

The SM is perhaps the most emblematic tool for studying nuclear structure. In its simplest version, the SM was used for explaining the *magic numbers* of nucleons in a one-body picture. The principal innovation was a spin-orbit coupling that allowed grouping shells in such a way that the magic numbers appeared naturally. The skeleton of the SM is provided by single-particle eigenstates. Each state is labelled by quantum numbers like angular momentum and parity. Improvement of the model consisted of using different two-body interactions in valence space. On one hand, we can find interactions that fit the one- and two-body matrix elements like for example the so-called KB3G interaction [90] and on the other hand, interactions that focus on symmetries like Elliot's SU(3) model [91] and Dufour and Zuker multipole Hamiltonian [92].



that the nucleons in the inert core exert an effective one-body interaction on the valence nucleons. The other is the choice of the nucleon-nucleon interaction.

The A -nucleon Hamiltonian of the SM, restricted to two-body interactions is:

$$H = \sum_{i \in \text{val}} T_i + \sum_{i < j \in \text{val}} V_{ij}, \quad (2.1)$$

where T_i is the kinetic term and V_{ij} is the two-body interaction term. Since in SM we assume an inert core that exerts an effective mean field for the valence particles, we can express Eq. (2.1) as:

$$\begin{aligned} H &= \sum_{i \in \text{val}} [T_i + U(r_i)] + \left[\sum_{i < j \in \text{val}} V_{ij} - \sum_{i \in \text{val}} U(r_i) \right] \\ &= H_0 + H_{\text{res}} = \sum_{i \in \text{val}} h_0(i) + H_{\text{res}}, \end{aligned} \quad (2.2)$$

where H_0 describes the motion of the A nucleons as if they were independent from each other, H_{res} is the so-called residual interaction which generates configuration mixing and $h_0(i)$ is the single particle Hamiltonian for particle i . H_0 term generates the single particle basis that is later used to build the Slater determinants of the A -nucleon wave function. An example of $U(r_i)$ can be a HO potential with a spin-orbit coupling term:

$$U(r_i) = \frac{1}{2} m \omega^2 r_i^2 + V_{SO} (\vec{\ell} \cdot \vec{s}), \quad (2.3)$$

where m is the particle mass and $\vec{\ell}$, \vec{s} are the angular momentum and spin, respectively. Fig. 2.1 shows the splitting of the HO degeneracy by a spin-orbit coupling and how this splitting generates the correct *magic numbers*.

The SM wave function $|\Psi\rangle$ that describes a nucleus is a linear combination of Slater determinants $|\Phi_a\rangle$ such as:

$$|\Psi\rangle = \sum_a b_a |\Phi_a\rangle, \quad (2.4)$$

where b_a is the amplitude of each Slater determinant. The Slater determinants $|\Phi_a\rangle$ are built using the single particle basis eigenstates $|\phi_i\rangle$ generated by H_0 . We should also remember that for a chosen inert core and valence space, we have an effective interaction H_{eff} and, hence, effective wave functions $|\Psi_{\text{eff}}\rangle$. This means that we cannot use the same interaction in different model spaces.

2.1.1 Diagonalizing the Shell Model interaction: the Lanczos method

The Lanczos method [94] is the numerical method of choice to solve the SM [95]. The idea of this method is to express the interaction first as a tridiagonal matrix and then diagonalize. The aforementioned matrix arises from the orthogonalization of the states $H_{\text{eff}}|1\rangle$, where the Hamiltonian H_{eff} is applied repeatedly on a basis state $|1\rangle$, called pivot. This state is a linear combination of Slater determinants. The first step of the Lanczos algorithm is:

$$H_{\text{eff}}|1\rangle = E_{11}|1\rangle + E_{12}|2\rangle, \quad (2.5)$$

where $E_{ij} = \langle i|H_{\text{eff}}|j\rangle$. E_{12} can be obtained by applying $\langle 2|$ to:

$$E_{12}|2\rangle = H_{\text{eff}}|1\rangle - E_{11}|1\rangle = (H_{\text{eff}} - E_{11})|1\rangle. \quad (2.6)$$

The next step is:

$$H_{\text{eff}} |2\rangle = E_{21} |1\rangle + E_{22} |2\rangle + E_{23} |3\rangle, \quad (2.7)$$

where the hermicity of the Hamiltonian implies $E_{12} = E_{21}$, $E_{22} = \langle 2|H_{\text{eff}}|2\rangle$ and E_{23} is obtained by normalization:

$$E_{23} |3\rangle = (H_{\text{eff}} - E_{22}) |2\rangle - E_{21} |1\rangle. \quad (2.8)$$

Finally, we get the recursion relation:

$$H_{\text{eff}} |N\rangle = E_{NN-1} |N-1\rangle + E_{NN} |N\rangle + E_{NN+1} |N+1\rangle, \quad (2.9)$$

where $E_{NN+1} |N+1\rangle = (H - E_{NN}) |N\rangle$. These leads to a tridiagonal matrix:

$$\begin{pmatrix} E_{11} & E_{12} & 0 & 0 & 0 & 0 & \cdots \\ E_{12} & E_{22} & E_{23} & 0 & 0 & 0 & \cdots \\ 0 & E_{23} & E_{33} & E_{34} & 0 & 0 & \cdots \\ 0 & 0 & E_{34} & E_{44} & E_{45} & 0 & \cdots \\ \vdots & \vdots & \ddots & \ddots & \ddots & \ddots & \ddots \end{pmatrix} \quad (2.10)$$

This algorithm has variational properties and the convergence to the lowest eigenvalues is very efficient [96]. However, it slows down if more eigenvalues are calculated since the more eigenvalues we have the greater the number of steps. In the n -th step there is an $n \times n$ matrix to be diagonalized, leading to n eigenvectors, therefore each step becomes increasingly demanding. Eventually, the energy of the first m eigenvectors converges and these are the ones that are kept [95].

2.2 No-core Shell Model

The NCSM is a many-body approach for the description of the atomic nucleus. This method was first used by Navrátil and Barrett [81]. It differs from a standard SM as it does not assume a pre-existing frozen core, instead it treats all A nucleons as active. In this model, one considers an A -body system of point-like non-relativistic nucleons that interact by a realistic interaction that may be NN or $NN + NNN$. Therefore the Hamiltonian is:

$$H = \frac{1}{A} \sum_{i < j} \frac{(\mathbf{p}_i - \mathbf{p}_j)^2}{2m} + \sum_{i < j} V_{NN,ij} + \sum_{i < j < k} V_{NNN,ijk}. \quad (2.11)$$

The NCSM uses a HO basis because it allows for the use of second quantization representation while conserving translational invariance. The many-body wave function $|\Psi_A^{J^\pi T}\rangle$ is therefore expanded over a complete set of antisymmetric A -nucleon HO basis states $|ANiJ^\pi T\rangle$ characterized by a HO length b that contain up to N_{max} HO excitation above the lowest possible configuration:

$$|\Psi_A^{J^\pi T}\rangle = \sum_N \sum_{\alpha}^{N_{\text{max}}} c_{N\alpha} |AN\alpha J^\pi T\rangle, \quad (2.12)$$

where N is the total number of HO excitation above the minimum configuration, J^π is the total angular momentum and parity, T is the isospin and α contains any other quantum

number associated to the HO state. Moreover, Jacobi coordinates are used because the NN and NNN interactions depend on relative coordinates and/or momenta:

$$\begin{aligned}\xi_0 &= \sqrt{\frac{1}{A}} [\mathbf{r}_1 + \mathbf{r}_2 + \dots + \mathbf{r}_A] \\ \xi_1 &= \sqrt{\frac{1}{2}} [\mathbf{r}_1 - \mathbf{r}_2] \\ \xi_2 &= \sqrt{\frac{2}{3}} \left[\frac{1}{2} (\mathbf{r}_1 + \mathbf{r}_2) - \mathbf{r}_3 \right] \\ &\vdots \\ \xi_{A-1} &= \sqrt{\frac{A-1}{A}} \left[\frac{1}{A-1} (\mathbf{r}_1 + \mathbf{r}_2 + \dots + \mathbf{r}_{A-1}) - \mathbf{r}_A \right]\end{aligned}$$

The antisymmetrization procedure of the Jacobi-coordinate HO basis is discussed in Refs. [81–83].

As the number of particles increase, so does the computational resources necessary to antisymmetrize the wave function. A generalization to systems with $A \geq 3$ nucleons can be done with Slater determinants [97, 98]. The Slater determinant basis is constructed from single nucleon HO wave functions such as:

$$\varphi_{n\ell j m m_t}(\vec{r}, \sigma, \tau; b) = R_{n\ell}(r; b) [Y^\ell(\hat{r})\chi(\sigma)]_m^j \chi(\tau)_{m_t}, \quad (2.13)$$

where $R_{n\ell}$ are the radial HO wave function, b the HO length and χ are spinors for spin σ and isospin τ . The wave functions in Eq. (2.13) are eigenstates of a translationally invariant Hamiltonian that can be factorized into a relative part and a CM part. Thus, the HO many-body expansion of the wave function $|\Psi_A^{J^\pi T}\rangle_{SD}$ in the Cartesian coordinate Slater determinant basis is:

$$\langle \mathbf{r}_1 \dots \mathbf{r}_A | \Psi_A^{J^\pi T} \rangle_{SD} = \sum_{N=0}^{N_{\max}} \sum_{\alpha} c_{N\alpha}^{(SD)} \langle \mathbf{r}_1 \dots \mathbf{r}_A | \Phi_A^{J^\pi T} \rangle_{SD}, \quad (2.14)$$

where $|\Phi_A^{J^\pi T}\rangle_{SD}$ corresponds to a HO many-body state. NCSM calculations require a renormalization procedure to facilitate convergence of calculations. Such methods are the Lee-Suzuki or Okubo-Lee-Suzuki schemes [99–101] and the Similarity Renormalization Group [102]. More details can be found for example in Ref. [97].

One of the main difficulties of the NCSM is the rapid increase of the model space as one includes more particles in the calculations. An amelioration to the model has been proposed with the symmetry adapted NCSM. This model reduces the basis by considering only the physically relevant elements considering the $SU(3) \in SO(3)$ subgroup chain [103, 104] or the symplectic $SP(3, \mathbb{R})$ group [105, 106]. Another approaches that allow for all nucleons to be active are the Monte Carlo Shell Model [107–109] and the Green's Function Monte Carlo approach [110, 111].

2.2.1 No-core Shell Model and continuum

Although originally developed for the study of nuclear structure, the NCSM has been extended to include nuclear reactions. The first extension came by combining the NCSM with the RGM [112–116]. The basic idea of the RGM is to describe the nucleus as a collection of clusters rather than a single entity. This allows for the inclusion of cluster effects for example.

In NCSM/RGM [18, 19], the wave function for a scattering process involving a pair of clusters can be cast as:

$$|\Psi^{J\pi T}\rangle = \sum_c \int dr r^2 \frac{u_c^{J\pi T}(r)}{r} \hat{\mathcal{A}}_c |\Phi_{cr}^{J\pi T}\rangle, \quad (2.15)$$

through an expansion over binary-cluster channel states of total angular momentum J , parity π and isospin T . This binary-cluster channel states are:

$$|\Phi_{cr}^{J\pi T}\rangle = [(|A-a \alpha_1 I_1^{\pi_1} T_1\rangle \otimes |a \alpha_2 I_2^{\pi_2} T_2\rangle)^{sT} Y_\ell(\hat{\mathbf{r}}_{A-a,a})]^{J\pi T} \frac{\delta(r - r_{A-a,a})}{r r_{A-a,a}}, \quad (2.16)$$

where clusters 1 and 2 have $A-a$ and a nucleons respectively, angular momentum I_i , parity π_i and additional quantum numbers α_i for $i = 1, 2$. The symbols Y_ℓ and δ correspond to a spherical harmonic and Dirac delta, respectively. The CM of clusters are separated by the relative radius:

$$\mathbf{r}_{A-a,a} = r_{A-a,a} \hat{\mathbf{r}}_{A-a,a} = \frac{1}{A-a} \sum_{i=1}^{A-a} \mathbf{r}_i - \frac{1}{a} \sum_{j=A-a+1}^A \mathbf{r}_j, \quad (2.17)$$

where $\{\mathbf{r}_i, i = 1, 2, \dots, A\}$ are the single particle coordinates. Finally, the channel index c includes the following quantum numbers $c = \{A-a \alpha_1 I_1^\pi T_1; a \alpha_2 I_2^\pi T_2\}$.

The goal of the NCSM/RGM is to solve the Schrödinger equation spanned by the basis states (2.16):

$$\sum_c \int dr r^2 [H_{c'c}^{J\pi T}(r', r) - E N_{c'c}^{J\pi T}(r', r)] \frac{u_c^{J\pi T}(r)}{r} r^2 dr = 0, \quad (2.18)$$

where

$$H_{c'c}^{J\pi T}(r', r) = \langle \Phi_{c'r'}^{J\pi T} | \hat{\mathcal{A}}_c H \hat{\mathcal{A}}_c | \Phi_{cr}^{J\pi T} \rangle \quad (2.19)$$

$$N_{c'c}^{J\pi T}(r', r) = \langle \Phi_{c'r'}^{J\pi T} | \hat{\mathcal{A}}_c \hat{\mathcal{A}}_c | \Phi_{cr}^{J\pi T} \rangle, \quad (2.20)$$

are named the Hamiltonian and norm kernels, respectively, and H is the intrinsic A -nucleon Hamiltonian. Once the relative wave functions $u_c^{J\pi T}(r)$ are determined, one can extract the S -matrix with the asymptotic form for large distances:

$$u_c^{J\pi T}(r) = \frac{i}{2} v_c^{-1/2} [\delta_{ci} H_{\ell,\eta}^-(\kappa_c r) - S_{ci}^{J\pi T} H_{\ell,\eta}^+(\kappa_c r)], \quad (2.21)$$

where $S_{ci}^{J\pi T}$ is the S -matrix for a particular entrance channel i and exit channel c and v_c is the velocity of the projectile.

Another *ab initio* approach is the NCSMC [20–22]. This method assumes that the many-body wave function includes both an A -body square-integrable (from NCSM) and a $(A-a, a)$ binary cluster continuous basis (from NCSM/RGM) as:

$$|\Psi_A^{J\pi T}\rangle = \underbrace{\sum_\lambda c_\lambda |A\lambda J\pi T\rangle}_{\text{NCSM}} + \underbrace{\sum_c \int dr r^2 \frac{u_c^{J\pi T}(r)}{r} \hat{\mathcal{A}}_c |\Phi_{cr}^{J\pi T}\rangle}_{\text{NCSM/RGM}}. \quad (2.22)$$

The NCSM sector of Eq. (2.22) describes the short to medium range A -body structures and the NCSM/RGM sector provides the capability of the theory to handle scattering physics. Thus, Eq. (2.22) is capable of describing both bound and unbound states. The

quantities to determine are the discrete c_λ and the continuous $u_c^{J^\pi T}(r)$. For this end, one solves the coupled equations

$$\begin{bmatrix} H_{\text{NCSM}} & \bar{h} \\ \bar{h} & \bar{\mathcal{H}} \end{bmatrix} \begin{bmatrix} c \\ u \end{bmatrix} = E \begin{bmatrix} 1 & \bar{g} \\ \bar{g} & 1 \end{bmatrix} \begin{bmatrix} c \\ u \end{bmatrix}, \quad (2.23)$$

where H_{NCSM} is the NCSM Hamiltonian, $\bar{\mathcal{H}}$ is the NCSM/RGM Hamiltonian, and \bar{h} and \bar{g} are related to the Hamiltonian and norm kernels from the NCSM/RGM formalism, respectively.

Details of the NCSM/RGM and the NCSMC formalisms are out of the scope of this work. More details can be found for example in Refs. [19, 20]. Moreover, these *ab initio* approaches obtain the widths and any other scattering information from the phase shifts, something that, as will be explained in Chaps. 3 and 4, is done differently in the GSM.

2.3 Continuum Shell Model

The CSM describes the nucleus as an OQS by coupling a continuum space to the SM space via the Feshbach projection formalism [3, 4]. As described in Refs. [5, 6, 10], one can define a set of two Schrödinger equations:

$$[H^{\text{SM}} - E_i^{\text{SM}}] |\phi_i^{\text{SM}}\rangle = 0 \quad (2.24)$$

and

$$\sum_{c'} [H_{cc'} - E] |\xi_E^{c'(+)}\rangle = 0, \quad (2.25)$$

where H^{SM} is the SM Hamiltonian and $H_{cc'} = H_0 + V_{\text{res}}^c$ is the standard Hamiltonian of coupled-channel calculations. In its simplest version, the main idea of the CSM is to partition the A -nucleus wave function into an $A - 1$ part $|\phi_i^{A-1}\rangle$ given by Eq. (2.24), and an unbound particle state $|\zeta_E^c\rangle$ whose relative motion to the residual $(A - 1)$ -nucleus determines the channel c and is given by Eq. (2.25).

The basic idea of the Feshbach projection formalism [3, 4] is to divide the total space into two subspaces such that:

$$\hat{Q} + \hat{P} = \mathbb{1}, \quad (2.26)$$

where \hat{Q} and \hat{P} are projection operators. In the CSM one defines them as:

$$\hat{Q} = \sum_{i=1}^N |\phi_i^{\text{SM}}\rangle \langle \phi_i^{\text{SM}}|, \quad \hat{P} = \sum_{c=1}^{\Lambda} \int_{\epsilon_c}^{\infty} dE |\xi_E^c\rangle \langle \xi_E^c|, \quad (2.27)$$

where N and Λ are the number of shell model states and number of channels, respectively. Moreover, the wave function $|\Psi_E^c\rangle$ of the whole system has its own Schrödinger equation:

$$[H - E] |\Psi_E^c\rangle = 0, \quad (2.28)$$

where the Hamiltonian follows

$$\begin{aligned} H &= (\hat{Q} + \hat{P})H(\hat{Q} + \hat{P}) \\ &= \hat{Q}H\hat{Q} + \hat{P}H\hat{P} + \hat{Q}H\hat{P} + \hat{P}H\hat{Q} \\ &= H_{QQ} + H_{PP} + H_{QP} + H_{PQ}, \end{aligned} \quad (2.29)$$

where we use the convention $\hat{X}H\hat{Y} \equiv H_{XY}$. A third equation can be obtained by solving the coupled-channel equations with a source term:

$$|\omega_i^{(+)}\rangle = G_P^{(+)} H_{PQ} |\phi_j^{\text{SM}}\rangle, \quad (2.30)$$

where

$$G_P^{(+)} = \hat{P} \frac{1}{E - H_{PP}} \hat{P} \quad (2.31)$$

is the Green's function in the P subspace. $|\omega_i^{(+)}\rangle$ can be understood as the continuation of $|\phi_i^{\text{SM}}\rangle$ into the scattering continuum.

Using the three sets of wave functions $\{|\phi_i^{\text{SM}}\rangle\}$, $\{|\xi_E^c\rangle\}$ and $\{|\omega_i^{(+)}\rangle\}$, one can obtain the solution of Eq. (2.28):

$$|\Psi_E^c\rangle = |\xi_E^c\rangle + \sum_{ij} \left(|\phi_i^{\text{SM}}\rangle + |\omega_i^{(+)}\rangle \right) \langle \phi_i^{\text{SM}} | (E - \mathcal{H}_{QQ}(E))^{-1} | \phi_j^{\text{SM}} \rangle \langle \phi_j^{\text{SM}} | H_{QP} | \xi_E^c \rangle, \quad (2.32)$$

where E is the total energy, and $\mathcal{H}_{QQ}(E)$ is the effective Hamiltonian in Q -space given by:

$$\mathcal{H}_{QQ}(E) = H_{QQ} + H_{QP} G_P^{(+)}(E) H_{PQ}. \quad (2.33)$$

The effective Hamiltonian $\mathcal{H}_{QQ}(E)$ is Hermitian for energies below the particle emission threshold and non-Hermitian above the threshold. The effective Hamiltonian can be interpreted as the SM Hamiltonian with a perturbation $H_{QP} G_P^{(+)}(E) H_{PQ}$ that represents the *correction* coming from the coupling to the continuum. Moreover, the wave function Ψ_E^c contains two terms that describe the direct reaction part and the resonance reaction part.

We can describe bound and resonance states via the effective Hamiltonian in Q -space. The A -nucleon system will have a set of discrete states $|\Psi_n\rangle$ following the Schrödinger equation $(H - E)|\Psi\rangle = 0$ and by using the projectors \hat{Q} and \hat{P} we can separate the wave functions as $|\Psi_n\rangle = |\Psi_Q\rangle + |\Psi_P\rangle$. Indeed, the states $|\Psi_Q\rangle$ are eigenstates of the effective Hamiltonian:

$$[E - \mathcal{H}_{QQ}(E)] |\Psi_Q\rangle = 0, \quad (2.34)$$

with complex eigenvalues $E_n(E) - i\Gamma_n(E)/2$. Now we define the extension of the wave function in Q -space into P -space as:

$$|\tilde{\omega}_n^{(+)}\rangle = G_P^{(+)}(E) H_{PQ} |\Psi_Q\rangle. \quad (2.35)$$

Hence, an eigenstate n of the A -nucleon system will be:

$$|\tilde{\Omega}_n^{(+)}\rangle = |\Psi_Q^n\rangle + G_P^{(+)}(E) H_{PQ} |\Psi_Q\rangle = |\Psi_Q^n\rangle + |\tilde{\omega}_n^{(+)}\rangle. \quad (2.36)$$

Additionally, one can expand the states $|\Psi_Q^n\rangle$ and $|\tilde{\omega}_n^{(+)}\rangle$ using the basis sets $\{|\phi_i^{\text{SM}}\rangle\}$ and $|\omega_n^{(+)}\rangle$, and define their completeness relations, respectively as:

$$|\Psi_Q^n\rangle = \sum_i \alpha_i^n |\phi_i^{\text{SM}}\rangle, \quad \sum_n |\Psi_Q^n\rangle \langle \Psi_Q^n| \quad (2.37)$$

$$|\tilde{\omega}_n^{(+)}\rangle = \sum_i \alpha_i^n |\omega_n^{(+)}\rangle, \quad \sum_n |\tilde{\omega}_n^{(+)}\rangle \langle \tilde{\omega}_n^{(+)}|, \quad (2.38)$$

where α_i are normalization constants. Finally, one can write the solution as:

$$|\Psi_c\rangle = |\xi_c\rangle + \sum_n |\tilde{\Omega}_n^{+}\rangle \frac{\gamma_n}{E - \left(E_n(E) - i\frac{\Gamma_n(E)}{2} \right)}, \quad (2.39)$$

where

$$\gamma_n \equiv \langle \Psi_Q^n | H_{QP} | \xi_c \rangle \quad (2.40)$$

represents the coupling between pure scattering states in P -space and pure SM states in Q -space. The states $|\Psi_c\rangle$ and $|\tilde{\Omega}_n^{(+)}\rangle$ are analogous to each other. The former consists of a scattering state corrected for the influence of resonant states whereas the latter consists of a resonant state corrected for the influence of the continuum.

In the CSM, given an entrance channel c_0 and an exit channel c , the S -matrix is given by:

$$S_{cc_0} = S_{cc_0}^{(0)} - i \exp [i(\delta_c^0 + \delta_{c_0}^0)] \sum_n \frac{\tilde{\gamma}_c^n \tilde{\gamma}_{c_0}^n}{E - \left(E_n(E) - i \frac{\Gamma_n(E)}{2} \right)}, \quad (2.41)$$

where $S_{cc_0}^{(0)}$ is the non-resonant part of the S -matrix, δ_c^0 are the phase shifts associated to a scattering channel c and $\tilde{\gamma}_c^n = \langle \xi_c | H_{PQ} | \Psi_Q^n \rangle$.

The CSM allows for the unification of nuclear structure and reactions as we can use it to calculate both spectra and cross-sections with the same Hamiltonian and using the same many-body framework. The cross-section describing the scattering process involving the incoming/entrance channel c_0 and outgoing/exit channel c is given by

$$\frac{d\sigma}{d\Omega}(c_0 \rightarrow c) = \frac{\pi}{k_{c_0}^2} \left| \sum_{\ell, \ell', m'} i^{\ell-\ell'} \sqrt{2\ell+1} Y_{\ell' m'}^{m'}(\theta, \phi) (S_{cc_0} - \delta_{cc_0}) \right|^2, \quad (2.42)$$

where Y_{ℓ}^m are spherical harmonics and k_{c_0} is the momentum of the entrance channel.

2.4 Shell Model Embedded in the Continuum

So far we have not discussed the Hamiltonian H used in the CSM. Generally, in the CSM one uses a schematic phenomenological interaction. In contrast, in SMEC [10, 84–89] one is using a more realistic SM interactions. In SMEC, we identify the Hamiltonian in Q -subspace with the SM Hamiltonian $H^{\text{SM}} = H_{QQ}$ and the P -subspace Hamiltonian as $H_{cc} = H_{PP}$. The coupling between Q and P -subspaces is generated by the residual Wigner-Bartlett contact interaction. In general, the effective Hamiltonian in Q -space is non-Hermitian and energy dependent. Below the lowest decay threshold, eigenvalues of the effective Hamiltonian are real, whereas above the threshold, the eigenenergies become complex.

The main difference between CSM and SMEC corresponds to the construction of Q and P -subspaces. In the CSM/SMEC, Q -subspace contains bound states and localized part of the resonance wave functions, P -subspace contains scattering states and tails of the resonances included in the Q -subspace [6, 10, 117]. The separation between the localized part of the resonance inside the potential and its tail is rather arbitrary in CSM. It is characterized by a cut-off function, like for example a Fermi distribution [118], but the cut-off radius is arbitrary. This induces arbitrariness in the definition of Q and P -subspaces, which has influence on calculated cross-sections and energy spectra. This problem is solved in SMEC with the method of anamneses [119]. The method consists of replacing the resonances wave function by the anamneses, i.e. the quasi-bound state embedded in the real-energy continuum. The anamnesis is constructed by:

1. Projecting the pole of the S -matrix corresponding to the resonance at k_{res} in the complex k -plane, on the real axis $\Re(k) > 0$: $\kappa = \sqrt{\Re(k_{\text{res}}^2)}$.

2. Joining the solution of Eq. (1.2) in the inner region $[0, R]$ with the scattering wave function in the external region $[R, \infty)$ at, yet, an arbitrary matching radius R .

In the external region, we require that the anamnesis of the resonance has the bound state asymptotic behavior corresponding to $k = i\kappa$. The continuity of the resonances anamnesis wave function and its first derivative is fixing the matching radius R . It should be stressed that the so-defined resonance anamneses in Q -subspace and its real-energy scattering wave function tail in P -subspace reproduce exactly the phase-shifts of the original resonance [119].

Formulation of the Gamow Shell Model

The coupling to the scattering continuum and the decay channels change properties of the wave functions. For bound states, virtual scattering to continuum states modifies the nucleon-nucleon interaction. For unbound states, nuclei interact with neighboring nuclei by decays and captures which explicitly modifies the wave functions. The cornerstone of the SM success is the description of the magic numbers of nucleons. However far from stability, one might ask if magic numbers remain unchanged. Indeed, in the case of the nucleon drip lines there are three main components that change the structure of the shell orbits [120, 121]: the tensor interaction which modifies the mean field as orbits are filled [122, 123], the many-body correlations that involve weakly bound and unbound nucleons which become significant when the nucleon (neutron/proton) separation energy is small [10, 14], and the presence of particle emission thresholds [8, 9, 14]. The last two require an OQS description of the nucleus.

In Chap. 2 we briefly introduced the SM. The SM has proven to be an excellent tool for studies of nuclear structure in stable nuclei. Nevertheless, in SM one assumes that the atomic nucleus is decoupled from the environment of scattering states and decay channels. This of course is a good approximation for well bound states in the valley of stability. In Sects. 2.3 and 2.4, we introduced the CSM and the SMEC. These models equip the SM with the coupling to decay channels and allow for the description of resonances and reaction cross-sections with simple projectiles.

An alternative many-body approach, introduced in Refs. [11–15] is based on using the Berggren complete single-particle basis which allows for the symmetric treatment of resonant and scattering single-particle states. The many-body basis based on Berggren single-particle basis is used in the Gamow Shell Model and allows for the description of many-body states in all regimes of bindings. In this chapter, the Gamow Shell Model, which provides the generalization of the standard SM, will be discussed in some details.

Analogously to the standard SM, the many-body antisymmetric states are built with Slater determinants of single-particle basis states. Even though the Berggren basis is complete, an approximation has to be made in the completeness relation. The infinite number of scattering states are approximated by the discretization of the integral in the completeness relation in Eq. (1.28):

$$\int_{L^+} u_\ell(k, r) \tilde{u}_\ell^*(k, r') \approx \sum_i^{N_d} u_{\ell, i}(r) \tilde{u}_{\ell, i}^*(r'), \quad (3.1)$$

where we discretize the contour L^+ with a Gauss-Legendre quadrature for a number N_d of points with momentum $k_i \in L^+$ each [13]. Therefore the Berggren completeness relation becomes:

$$\begin{aligned} \sum_n^N u_{\ell,n}(r) \tilde{u}_{\ell,n}^*(r') + \int_0^\infty dk u_\ell(k, r) \tilde{u}_\ell^*(k, r') &= \sum_n^N u_{\ell,n}(r) \tilde{u}_{\ell,n}^*(r') + \sum_i^{N_d} u_{\ell,i}(r) \tilde{u}_{\ell,i}^*(r') \\ &= \sum_n^{N+N_d} u_{\ell,n}(r) \tilde{u}_{\ell,n}^*(r'), \end{aligned} \quad (3.2)$$

where N is the number of poles to be taken inside the contour. This leaves us with a discrete single-particle Berggren basis $\{u_\ell\}$. Typically in GSM applications, we use a contour as shown in Fig. 3.1 where important resonances lie between the real axis and the triangle defined by k_{peak} and k_{mid} . The choice of k_{max} is generally between 2 and 3 fm⁻¹, where one usually achieves convergence. It is important to stress that there is a contour for each partial wave and they do not necessarily need to be the same.

Using the discretized Berggren basis, we can now build the the many-body completeness relation:

$$\sum_n |\text{SD}_n\rangle \langle \widetilde{\text{SD}}_n| \approx \mathbb{1}; \quad |\text{SD}\rangle = |u_{\ell_1 1} u_{\ell_2 2} \dots u_{\ell_M M}\rangle, \quad (3.3)$$

where different Slater determinants are obtained by occupying bound, resonance and discretized single-particle scattering states. The precision of this relation depends on the achieved precision of the discretized completeness relation (3.1). The tilde in Eq. (3.3) keeps its meaning of time reversal. The many-body completeness relation will be used to expand many-body states that go as $e^{ikr} Y_{ljm}(\theta, \varphi)$, hence its applicability will depend on its domain of k . This limits the value that a width of a resonance can have. Additionally, one must select k_{max} big enough so that it becomes possible to expand the high-energy many-body states [15].

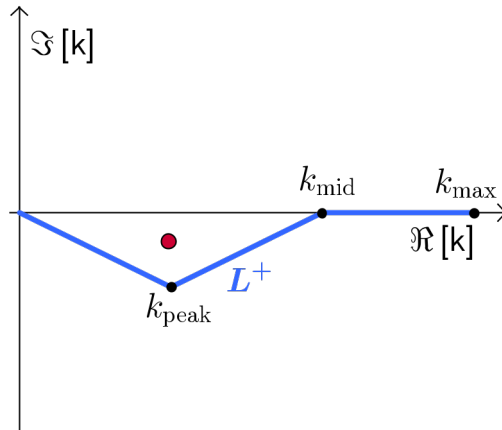


Figure 3.1: Typical contour enclosing the resonance pole for a GSM calculation in the complex k -plane.

3.1 Diagonalizing the Gamow Shell Model Hamiltonian: the Overlap method

An identification of resonances in GSM requires a special procedure. Even though it exists a Lanczos method for complex matrices, it cannot be used in GSM because the Lanczos algorithm yields the lowest energy eigenvalues. However, in GSM, we not only have bound

and resonance states but also scattering states that are eigenstates of the Hamiltonian. This means that resonances are embedded in a discretized continuum of scattering states and the scattering states may have lower energy than the resonance. Fig. 3.2 shows the first states given by a Lanczos algorithm for ${}^6\text{He}$ in GSM. One can clearly see the ground state because it is below the scattering continuum. However, as soon as the state is embedded within the scattering states, it is impossible to differentiate scattering states from a resonance. One way to overcome this difficulty is by doing several calculations with different contours. The eigenvalues corresponding to the scattering states are going to move in the k complex plane, whereas physical resonances will be stationary [12–14].

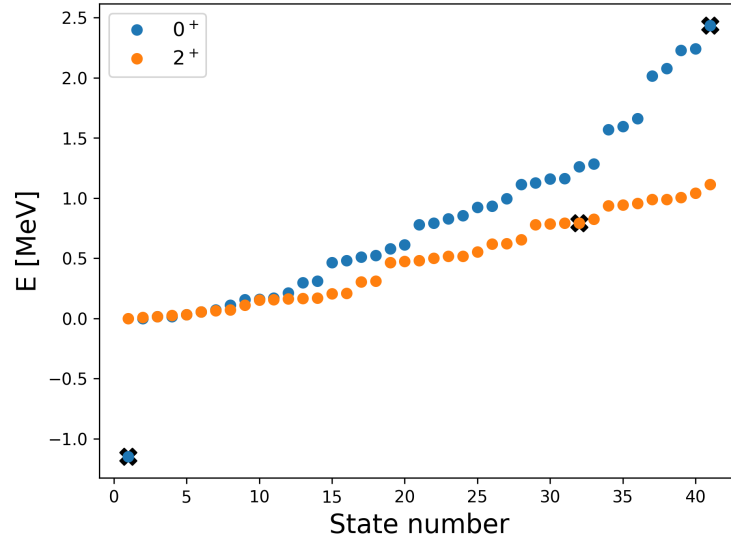


Figure 3.2: First few states with spin 0^+ and 2^+ given by the Lanczos method of a ${}^6\text{He}$ calculation with GSM. The physical states that are obtained via the overlap method are marked with an X.

This is not very practical so a different approach, the so-called overlap method, was developed. This method consist of doing a full diagonalization with an incomplete basis including only poles of the S-matrix (bound and resonance states) to extract a pivot $|\Psi_0\rangle$. Afterwards, one finds the many-body state $|\Psi\rangle$ with the full Berggren basis that maximises the overlap $|\langle\Psi_0|\Psi\rangle|$ [13] using the Jacobi-Davidson method [124].

3.2 Hamiltonian in Cluster Orbital Shell Model coordinates

In a SM calculation, one removes the CM excitations using the Lawson method [125]. This method cannot be applied in the GSM [12–14]. One option is to use Jacobi coordinates, but its application is numerically demanding. In most applications GSM is solved in the core + valence particle approximation. To deal with the problem, we transform the Hamiltonian from the laboratory coordinates to the relative Cluster Orbital Shell Model (COSM) coordinates [126]. The COSM coordinates are defined as:

$$\mathbf{r}_i = \begin{cases} \mathbf{r}_{i,\text{lab}} - \mathbf{R}_{\text{CM,core}} & i \in \text{val} \\ \mathbf{r}_{i,\text{lab}} & i \in \text{core} \end{cases} \quad (3.4)$$

where $\mathbf{r}_{i,\text{lab}}$ is the coordinate of a nucleon in laboratory coordinates and

$$\mathbf{R}_{\text{CM,core}} = \frac{1}{M_{\text{core}}} \sum_{i \in \text{core}} m_i \mathbf{r}_{i,\text{lab}} \quad (3.5)$$

is the coordinate in laboratory of the CM of the core. A schematic representation of COSM valence particle coordinates which are defined relative to the CM of the core is shown in Fig. 3.3.

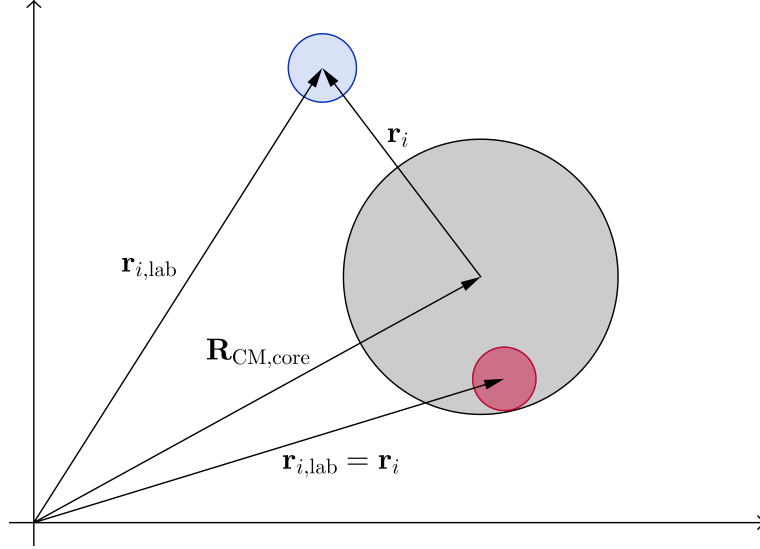


Figure 3.3: Schematic view of COSM coordinates (see Eq. (3.4)). The core is represented by the bigger black circle, and a valence nucleon by the small blue circle. A nucleon inside the core is denoted by a red circle.

Following Ref. [15], let us transform the Hamiltonian in laboratory coordinates to COSM coordinates. First, let us note that the momentum is:

$$\mathbf{p}_i = -i\hbar\nabla_i = -i\hbar\left(\frac{\partial}{\partial x} + \frac{\partial}{\partial y} + \frac{\partial}{\partial z}\right). \quad (3.6)$$

The transformation of the differential operator of coordinates $x_{i,\text{lab}}$ to COSM coordinates reads:

$$\frac{\partial}{\partial x_{i,\text{lab}}} = \begin{cases} \frac{\partial}{\partial x_i} - \sum_{j \in \text{val}} \frac{m_j}{M_{\text{core}}} \frac{\partial}{\partial x_j} & i \in \text{core} \\ \frac{\partial}{\partial x_i} & i \in \text{val} \end{cases} \quad (3.7)$$

The other coordinates are the same, and thus, we obtain the momentum in COSM coordinates

$$\mathbf{p}_{i,\text{lab}} = \begin{cases} \mathbf{p}_i - \sum_{j \in \text{val}} \frac{m_j}{M_{\text{core}}} \mathbf{p}_j & i \in \text{core} \\ \mathbf{p}_i & i \in \text{val} \end{cases} \quad (3.8)$$

On the other hand, the CM linear momentum \mathbf{P}_{lab} in COSM coordinates is a function of core linear momentum only:

$$\mathbf{P}_{\text{lab}} = \sum_{i \in \text{core}} \mathbf{p}_i. \quad (3.9)$$

Moreover, the squared momenta are:

$$\mathbf{p}_{i,\text{lab}}^2 = \begin{cases} \mathbf{p}_i^2 + \sum_{j,j' \in \text{val}} \left(\frac{m_j}{M_{\text{core}}}\right)^2 \mathbf{p}_j \cdot \mathbf{p}_{j'} - 2 \sum_{j \in \text{val}} \frac{m_j}{M_{\text{core}}} \mathbf{p}_i \cdot \mathbf{p}_j & i \in \text{core} \\ \mathbf{p}_i^2 & i \in \text{val} \end{cases} \quad (3.10)$$

for the individual particles, and:

$$\mathbf{P}_{\text{lab}}^2 = \sum_{i \in \text{core}} \mathbf{p}_i^2 + 2 \sum_{i < j \in \text{core}} \mathbf{p}_i \cdot \mathbf{p}_j, \quad (3.11)$$

for the CM linear momentum. Using Eqs. (3.10) and (3.11), one can calculate the kinetic part of the Hamiltonian in COSM coordinates:

$$\begin{aligned} \hat{T} &= \sum_{i=1}^A \frac{\mathbf{p}_{i,\text{lab}}^2}{2m_i} - \frac{\mathbf{P}_{\text{lab}}^2}{2M} = \sum_{i \in \text{val}} \frac{\mathbf{p}_i^2}{2\mu_i} + \frac{1}{M_{\text{core}}} \sum_{i < j \in \text{val}} \mathbf{p}_i \cdot \mathbf{p}_j \\ &+ \sum_{i \in \text{core}} \frac{\mathbf{p}_i^2}{2\mu'_i} - \frac{1}{M} \sum_{i < j \in \text{core}} \mathbf{p}_i \cdot \mathbf{p}_j - \frac{1}{M_{\text{core}}} \sum_{i \in \text{core}} \mathbf{p}_i \cdot \sum_{j \in \text{val}} \mathbf{p}_j, \end{aligned} \quad (3.12)$$

where M is the total mass of the A-system and μ_i, μ'_i are the reduced masses given by:

$$\frac{1}{\mu} = \frac{1}{m_i} + \frac{1}{M_{\text{core}}}; \quad \frac{1}{\mu'_i} = \frac{1}{m_i} - \frac{1}{M}. \quad (3.13)$$

The coupling between core and valence particle will vanish because typically the core will be coupled to 0^+ (e.g. ${}^4\text{He}$, ${}^{16}\text{O}$, ${}^{40}\text{Ca}$, etc.) and $\sum_{i \in \text{core}} \mathbf{p}_i$ is a spherical tensor of rank one.

Two-body matrix elements are straightforward to calculate in COSM coordinates and their calculations will not differ from standard SM methods if they involve either only core states or only valence states. Indeed, from Eqs. (3.4) and (3.8) one obtains

$$\mathbf{r}_{i,\text{lab}} - \mathbf{r}_{j,\text{lab}} = \mathbf{r}_i - \mathbf{r}_j \quad (3.14)$$

$$\mathbf{p}_{i,\text{lab}} - \mathbf{p}_{j,\text{lab}} = \mathbf{p}_i - \mathbf{p}_j, \quad (3.15)$$

so that the result is not different from using relative coordinates. On the other hand, if it involves a core-valence coupling, Eqs. (3.4) and (3.8) yield:

$$\mathbf{r}_{i,\text{lab}} - \mathbf{r}_{j,\text{lab}} = \mathbf{r}_i - \mathbf{r}_j + \mathbf{R}_{\text{CM},\text{core}} \quad (3.16)$$

$$\mathbf{p}_{i,\text{lab}} - \mathbf{p}_{j,\text{lab}} = \mathbf{p}_i - \mathbf{p}_j + \sum_{j' \in \text{val}} \frac{m_j}{M_{\text{core}}} \mathbf{p}_{j'}. \quad (3.17)$$

One would like to avoid working with these extra terms. A solution is to make the core-valence coupling vanish. We can achieve this with a SM treatment of the interaction similar to Eqs. (2.1) and (2.2). We consider an effective Hamiltonian $\hat{H} = \hat{T} + \hat{U} + \hat{V}$, where \hat{U} is the one-body mean field interaction, and \hat{V} is a two-body interaction in laboratory frame. Since the core is inert, it is not considered in the Hamiltonian. Therefore, the effective Hamiltonian in COSM coordinates is:

$$\hat{H} = \sum_{i \in \text{val}} \left(\frac{\mathbf{p}_i^2}{2\mu_i} + \hat{U}_i(\mathbf{r}_i) \right) + \frac{1}{M_{\text{core}}} \sum_{i < j \in \text{val}} \mathbf{p}_i \cdot \mathbf{p}_j + \sum_{i < j \in \text{val}} \hat{V}_{ij}(|\mathbf{r}_i - \mathbf{r}_j|), \quad (3.18)$$

where \hat{V}_{ij} is translationally invariant, therefore laboratory or COSM coordinates lead to the same results. \hat{U}_i in Eq. (3.18) is the one-body operator of the mean field acting on particle i .

We now focus on the mean field term U_i . First we separate U_i in central and spin-orbit terms in laboratory coordinates:

$$\hat{U}_i(\mathbf{r}_{i,\text{lab}}) = \hat{U}_i^{(\text{C})}(\mathbf{r}_{i,\text{lab}}) + \hat{U}_i^{(\text{LS})}(\mathbf{r}_{i,\text{lab}})(\mathbf{l}_{i,\text{lab}} \cdot \mathbf{s}_i). \quad (3.19)$$

In order to transform from laboratory coordinates into COSM coordinates, one expands $\hat{U}_i(\mathbf{r}_{i,\text{lab}})$ in a Taylor series. We begin with the central term:

$$\hat{U}_i^{(C)}(\mathbf{r}_{i,\text{lab}}) = \hat{U}_i^{(C)}(\mathbf{r}_i) + \mathbf{R}_{\text{CM,core}} \cdot \nabla \hat{U}_i^{(C)}(\mathbf{r}_i) + \frac{1}{2} \mathbf{R}_{\text{CM,core}} \cdot \Delta \hat{U}_i^{(C)}(\mathbf{r}_i) \cdot \mathbf{R}_{\text{CM,core}} + \text{h.o.}, \quad (3.20)$$

where $\Delta \hat{U}_i^{(C)}$ is the Hessian matrix associated to $\hat{U}_i^{(C)}$. Higher order terms are neglected. Similarly the spin-orbit part is expanded as:

$$\begin{aligned} \hat{U}_i^{(\text{LS})}(\mathbf{r}_{i,\text{lab}}) &= \hat{U}_i^{(\text{LS})}(\mathbf{r}_{i,\text{lab}}) [(\mathbf{r}_i + \mathbf{R}_{\text{CM,core}}) \times \mathbf{p}_i] \cdot \mathbf{s}_i \\ &= \hat{U}_i^{(\text{LS})}(\mathbf{r}_i) (\mathbf{l}_i \cdot \mathbf{s}_i) + \hat{U}_i^{(\text{LS})}(\mathbf{r}_i) [\mathbf{R}_{\text{CM,core}} \times \mathbf{p}_i] \cdot \mathbf{s}_i \\ &+ \left(\mathbf{R}_{\text{CM,core}} \cdot \nabla \hat{U}_i^{(\text{LS})}(\mathbf{r}_i) \right) (\mathbf{l}_i \cdot \mathbf{s}_i) \\ &+ \left(\mathbf{R}_{\text{CM,core}} \cdot \nabla \hat{U}_i^{(\text{LS})}(\mathbf{r}_i) \right) [\mathbf{R}_{\text{CM,core}} \times \mathbf{p}_i] \cdot \mathbf{s}_i \\ &+ \frac{1}{2} \left(\mathbf{R}_{\text{CM,core}} \cdot \Delta \hat{U}_i^{(\text{LS})}(\mathbf{r}_i) \right) \cdot [\mathbf{R}_{\text{CM,core}} \times \mathbf{p}_i] \cdot \mathbf{s}_i + \text{h.o.} \end{aligned} \quad (3.21)$$

The first order terms of Eqs. (3.20) and (3.21) vanish because the core is coupled to 0^+ and $\mathbf{R}_{\text{CM,core}}$ is a spherical tensor of rank 1. The second order terms involving $\mathbf{R}_{\text{CM,core}}^2$ are of the order of $\Delta U/M_{\text{core}}$. Furthermore, the Laplacian of a Woods-Saxon potential is around five times smaller than the potential itself and the derivative of the LS part is even smaller. However, this means that removing the second- and higher-order terms will induce an error in the calculations. This error is of the order of 5% for the worst case of the lightest core: the ^4He core [127].

3.3 No-core Gamow Shell Model

The Berggren basis applications in nuclear physics is not limited to the SM. Indeed, one can use the Berggren basis in a no-core SM approach, the so called NCGSM [23, 24]. The potential used to generate the Berggren basis is the one-body self-consistent multi-Slater determinant Hartree-Fock potential $U_{\text{MSDHF}}(r)$ [15, 128–130]. Therefore, the one-body Schrödinger equation to solve for generating the single-particle basis is:

$$u_k''(r) = \left[\frac{\ell(\ell+1)}{r^2} + \frac{2m}{\hbar^2} U_{\text{MSDHF}}(r) + V_C(Z, r) - k^2 \right] u_k(r), \quad (3.22)$$

where $V_C(Z, r)$ is the one-body Coulomb potential.

By adopting such a single-particle basis, we describe the nucleus with $3A$ coordinates. However, this breaks translational invariance, where one would need $3A-3$ coordinates instead. In the NCSM approaches with HO bases, it is possible to separate the relative and center-of-mass degrees of freedom $|\psi_{\text{rel}}\rangle \otimes |\psi_{\text{CM}}\rangle$ by using properties of the HO single particle basis in a full $N\hbar\omega$ space. Nonetheless, this limits the application of the method to well-bound systems.

In NCGSM the separation between the relative part and the CM part is not guaranteed. Thus one must check the factorization numerically. Assuming that the relative-CM factorization is valid and also that the wave function of the CM part has a Gaussian shape, one can check the expectation value of the CM Hamiltonian given by:

$$H_{\text{CM}} = \frac{1}{2mA} \mathbf{P}_{\text{CM}}^2 + \frac{mA\omega^2}{2} \mathbf{R}_{\text{CM}}^2 - \frac{3}{2} \hbar\omega, \quad (3.23)$$

where $\hbar\omega$ is the parameter that characterizes the Gaussian wave function [131]. If $\langle H_{\text{CM}} \rangle \sim 0$ then the relative-CM factorization is valid [132]. Nevertheless, this condition works only for bound states. Currently, the elimination of the spurious CM excitations in unbound states is an open problem in the NCGSM [15].

3.4 Applications of the Gamow Shell Model

Since its conception at the turn of this century, the GSM has been applied in the description of the various neutron rich nuclei like $^{18-28}\text{O}$ [12, 13, 87, 133, 134], ^{80}Ni [11, 135], ^{5-10}He [13, 127, 136], ^{5-11}Li [127, 128, 136, 137] and their mirrors [137], $^{51-70}\text{Ca}$ [138], $A=18-22$ proton rich nuclei with a ^{16}O core [139]. In Refs. [134, 136, 137, 140, 141] the Density Matrix Renormalization Group technique [142, 143] has been applied for the diagonalization of the GSM Hamiltonian. Many phenomena that have been investigated in the GSM include, among others, studies of: (i) near-threshold spectroscopic properties in light nuclei associated with the presence of particle emission thresholds [14, 38, 39]; (ii) influence of antibound states [144, 145]; (iii) Thomas-Ehrman shift in light nuclei [137, 146]; (iv) halo nuclei [144, 147, 148]; (v) asymptotic normalization coefficients [149]; and (vi) charge radii and the neutron-neutron correlations [150]. The implementation of Lee-Suzuki regularization method [100] in GSM has been discussed in Ref. [151] for schematic interactions and in Refs. [70, 152, 153] for realistic chiral N^3LO interactions [154]. For some additional applications see Refs. [14, 15].

Similarly to Sect. 2.2, the NCGSM has been proposed for the study of well bound and unbound states of light nuclei with a realistic N^3LO chiral interaction [23]. Studies of NCGSM employ the density matrix renormalization group method [140, 141] to reduce the size of the matrices to be diagonalized without decreasing the accuracy of the calculations. The NCGSM has been applied to study the tetra-neutron hypothesis [155, 156], the unbound isotopes of heavy hydrogen nuclei [23, 24, 156, 157], $A = 4$ $T = 1$ isospin triplet states [156], and heavier light nuclei like ^6Li [158].

3.5 Interaction for Gamow Shell Model

Over the years, the interaction for generating the one-body elements of the Berggren basis for GSM has been the Woods-Saxon (WS) potential with a spin-orbit and a Coulomb parts. The WS potential used is:

$$V(r) = -V_{0,\ell}f(r) - 4V_{\text{SO},\ell}(\vec{\ell} \cdot \vec{s})\frac{1}{r}\frac{df(r)}{dr} + U_C(r), \quad (3.24)$$

where the form factor $f(r)$ of the WS potential is given by:

$$f(r) = \left[1 + \exp\left(\frac{r - R_{0,\ell}}{d_\ell}\right) \right]^{-1}. \quad (3.25)$$

In the equation above, $V_{0,\ell}$ is the potential depth, $V_{\text{SO},\ell}$ is the spin-orbit strength, $R_{0,\ell}$ is the radius of the potential and d_ℓ is the diffuseness and $U_C(r)$ is the Coulomb field. In some applications, the potential for each partial wave ℓ , has different parameters because it can be useful to fit the single particle energies where the shell separation energies may not be correct if the potential is homogeneous in ℓ . The Coulomb field is generated by a spherical Gaussian charge distribution given by

$$U_C(r) = \frac{2e^2}{r} \text{erf}\left(\frac{3\sqrt{\pi}r}{4R_{\text{ch}}}\right), \quad (3.26)$$

where R_{ch} is the charge radius.

On the other hand, the two-body interaction used for GSM has evolved over the years. In one of the first applications of GSM, a surface delta interaction [159] was used [13] for the nucleon-nucleon interaction. Nowadays, it is common to use the Furutani-Horiuchi-Tamagaki (FHT) finite range interaction [160, 161] which consists of a central, spin-orbit and tensor terms with Gaussian form factors. The general form of a nuclear interaction was derived early in the 40s [162] by symmetry arguments.

The central, spin-orbit and tensor terms of the FHT interaction are given by:

$$\tilde{V}_c(r) = \sum_{n=1}^3 V_c^n (W_c^n + B_c^n P_\sigma - H_c^n P_\tau - M_c^n P_\sigma P_\tau) e^{-\beta_c^n r^2} \quad (3.27)$$

$$\tilde{V}_{LS}(r) = \vec{L} \cdot \vec{S} \sum_{n=1}^2 V_{LS}^n (W_{LS}^n - H_{LS}^n P_\tau) e^{-\beta_{LS}^n r^2} \quad (3.28)$$

$$\tilde{V}_T(r) = S_{ij} \sum_{n=1}^3 V_T^n (W_T^n - H_T^n P_\tau) r^2 e^{-\beta_T^n r^2}, \quad (3.29)$$

respectively. Here W , B , H , and M correspond to coefficients of the Wigner, Bartlett, Heisenberg and Majorana forces, respectively; P_σ and P_τ are spin and isospin exchange operators, respectively; \vec{L} is the relative orbital angular momentum; $\vec{S} = (\sigma_i + \sigma_j)/2$; and $S_{ij} = 3(\sigma_i \cdot \tilde{r})(\sigma_j \cdot \tilde{r}) - \sigma_i \cdot \sigma_j$. Each part of the interaction contains a Gaussian distribution with a different range: the first to account for the hard core of the nucleon, the second for mimicking the one-pion exchange potential, and the third for a description of an intermediate range. An exception is done for the spin-orbit part as it will not contain a long-range part [163].

Because we are dealing with a SM problem where the interaction is an effective interaction that depends on the valence space, the interaction listed in Eqs. (3.27), (3.28) and (3.29) should be modified to be easily applicable in a designated model space for a particular GSM calculation. This is achieved by rewriting the FHT interaction in terms of spin-isospin projectors Π_{ST} [164, 165]:

$$V_c(r) = V_c^{11} f_c^{11}(r) \Pi_{11} + V_c^{10} f_c^{10}(r) \Pi_{10} + V_c^{00} f_c^{00}(r) \Pi_{00} + V_c^{01} f_c^{01}(r) \Pi_{01} \quad (3.30)$$

$$V_{LS}(r) = (\vec{L} \cdot \vec{S}) V_{LS}^{11} f_{LS}^{11}(r) \Pi_{11} \quad (3.31)$$

$$V_T(r) = S_{ij} [V_T^{11} f_T^{11}(r) \Pi_{11} + V_T^{10} f_T^{10}(r) \Pi_{10}], \quad (3.32)$$

where the parameters to be optimized are reduced to seven interaction strengths in spin-isospin channels: V_c^{10} , V_c^{10} , V_c^{00} , V_c^{01} , V_{LS}^{11} , V_T^{11} , V_T^{10} . The form factors $f_{c,LS,T}^{ST}$ are linear combinations of the radial form factors of Eqs. (3.27), (3.28) and (3.29). They are normalized to the first parameter $V_{c,LS,T}^1$ for each central, spin-orbit and tensor term so that they are dimensionless. The remaining parameters, namely the Wigner, Bartlett, Heisenberg and Majorana strength, the relative strength of the Gaussian components, and the Gaussians range remain unchanged from Ref. [160] and are listed in Tab. 3.1.

Additionally, one must consider the Coulomb interaction between valence nucleons. We follow the method introduced in Ref. [166]. The Coulomb part of the interaction is $U_C^{Z_{\text{core}}} + V_C$ and because the one-body Coulomb term is additive one can end up with:

$$U_{\text{Coul}} = \underbrace{U_C^{Z-1}}_{\text{Infinite range}} + \underbrace{V_C - U_C^{Z_{\text{val}}-1}}_{\text{Short range}}, \quad (3.33)$$

where we have separated the infinite and short range parts. The short range part can be expanded with a HO basis as:

$$V_C - U_C^{Z_{\text{val}}-1} = \sum_{\alpha\beta\gamma\delta} |\alpha\beta\rangle \langle\alpha\beta| V_C - U_C^{Z_{\text{val}}-1} |\gamma\delta\rangle \langle\gamma\delta|, \quad (3.34)$$

Table 3.1: Parameters of the FHT interaction as given in Ref. [160]. The depths V^n of the central and spin-orbit interaction are given in MeV, whereas the tensor part in MeV fm⁻². The W , B , M and H parameters are dimensionless.

	n	V^n	β^n [fm ⁻²]	W^n	M^n	B^n	H^n
V_c	1	-6.0	0.160	-0.2363	1.1530	0.5972	-0.5139
	2	-546.0	1.127	0.4242	0.4055	0.1404	0.030
	3	1655.0	3.400	0.4474	0.3985	0.1015	0.0526
V_{LS}	1	1918.0	5.0	0.5			-0.5
	2	-1519.0	3.0	0.5			-0.5
V_T	1	-16.96	0.53	0.3277			0.6723
	2	-369.5	1.92	0.4102			0.5898
	3	1688.0	8.95	0.5			0.5

where Eq. (3.34) is reminiscent of Eq. (1.54). The infinite range part of the Coulomb interaction is taken exactly into account. Since GSM involves an inert core, the treatment of the Coulomb interaction is not exact, namely, we neglect the contribution to the exchange term arising from the protons in the core and neglect charge symmetry-breaking electromagnetic terms like the Coulomb spin-orbit interaction [166].

3.5.1 Optimization of the interaction

When we optimize the interaction, we have to assess the statistical uncertainties of the interaction parameters. Following Refs. [127, 167], given a model with N_p parameters $p = \{p_1, \dots, p_{N_p}\}$ to be adjusted to describe N_d observables \mathcal{O}_i ($i = 1, \dots, N_d$), the penalty function to minimize is:

$$\chi^2(\mathbf{p}) = \sum_{i=1}^{N_d} \left(\frac{\mathcal{O}_i(\mathbf{p}) - \mathcal{O}_i^{\text{exp}}}{\delta\mathcal{O}_i} \right)^2, \quad (3.35)$$

where $\mathcal{O}_i(\mathbf{p})$ are calculated observables, $\mathcal{O}_i^{\text{exp}}$ are experimental data used to constrain the model, and $\delta\mathcal{O}_i$ are the adopted errors whose contribution stems from experimental uncertainties, numerical inaccuracies and theoretical errors due to model deficiency.

There is some arbitrariness in the choice for the theoretical error. Part of this arbitrariness can be removed or at least mitigated by adopting errors that are consistent with the distribution of the residuals similarly to a case of a purely statistical distribution [167]. In particular, one can require the penalty function to be normalized to the number of degrees of freedom (dof) $N_{\text{dof}} = N_d - N_p$ at the minimum \mathbf{p}_0 [168]:

$$\frac{\chi^2(\mathbf{p}_0)}{N_{\text{dof}}} \longleftrightarrow 1. \quad (3.36)$$

If there is only a single type of data (e.g. excitation energies) and assuming that experimental and numerical error are negligible, then the condition (3.36) can be achieved by doing a global scaling of the initial adopted errors:

$$\delta\mathcal{O}_i \longrightarrow \delta\mathcal{O}_i \sqrt{\frac{\chi^2(\mathbf{p}_0)}{N_{\text{dof}}}}. \quad (3.37)$$

At the end, one can find the uncertainties of the fitted parameters with the correlation matrix. More details on the treatment of the correlation matrix can be found in Refs. [127, 167].

The probability distribution verified by \mathbf{p} is arbitrary and has to be postulated based on physical grounds. An option is to demand a Gaussian distribution with a dependence on $\chi^2(\mathbf{p})$ [167]:

$$\bar{P}(\mathbf{p}) \propto \exp(-\chi^2(\mathbf{p})), \quad (3.38)$$

where the factor of proportionality is determined by normalization.

The standard procedure to calculate statistical errors in this framework is the Bayesian analysis. For this, a prior probability distribution of parameters is postulated, from which a posterior probability distribution is calculated, which can then confirm or infirm the hypothesis borne by the prior. The theory of Bayesian analysis can be found, for example, in Ref. [169]. The implementation of Bayesian analysis in GSM has not been implemented yet.

3.6 Differences with other methods

Having introduced the theory behind GSM, we can now compare it to other methods for nuclear structure described in Chap. 2. First big difference from methods like SM or CSM is that GSM is formulated in RHS. As depicted in Fig. 3.4a, one can think of CSM/SMEC as taking a subset of the Hilbert space and dividing it into two parts: \mathcal{Q} , the subspace of localized states, and \mathcal{P} , the subspace of non-resonant continuum states. Here our quantum system is represented by \mathcal{Q} and therefore it is modified via couplings to the designated external environment \mathcal{P} . However, in the case of CSM/SMEC one chooses \mathcal{P} , hence one could say that the environment is encapsulated inside the topological sum of \mathcal{Q} and \mathcal{P} which is the closed quantum system. This is why in Fig. 3.4a the outer circle is depicted with a straight outline, and we conclude that the system as a whole $\mathcal{Q} \cup \mathcal{P}$ is closed.

On the other hand, Fig. 3.4b depicts an OQS, like GSM formulated in the RHS. Here we have the resonant states in the subspace \mathcal{D} , and the background part containing complex-energy scattering states in the subspace \mathcal{B} . The OQS here is the combined system $\mathcal{D} \cup \mathcal{B}$ since otherwise the basis would not be complete. In principle, it is an ideal OQS, however in practice we need to do some approximations like the discretization of the continuous part in \mathcal{B} and truncation of a single particle basis by choosing a k_{\max} .

Let us now compare GSM with the traditional SM. From the practical point of view, the GSM basis is going to be significantly larger than that of a SM basis. For SM in m -scheme, given a choice of valence space we will have n_π possible proton basis states and n_ν possible neutron basis states. Let r_π and r_ν denote the number of protons and neutrons in valence space for a given nucleus. The number N_{SM} of possible many-body states is:

$$N_{\text{SM}} = \binom{n_\pi}{r_\pi} \binom{n_\nu}{r_\nu}. \quad (3.39)$$

For GSM, we take n_π and n_ν as the possible pole states and we add m_π and m_ν as the total possible single particle scattering states from the discretized continuum part. Then the number N_{GSM} of possible many-body states is:

$$N_{\text{GSM}} = \binom{n_\pi + m_\pi}{r_\pi} \binom{n_\nu + m_\nu}{r_\nu}. \quad (3.40)$$

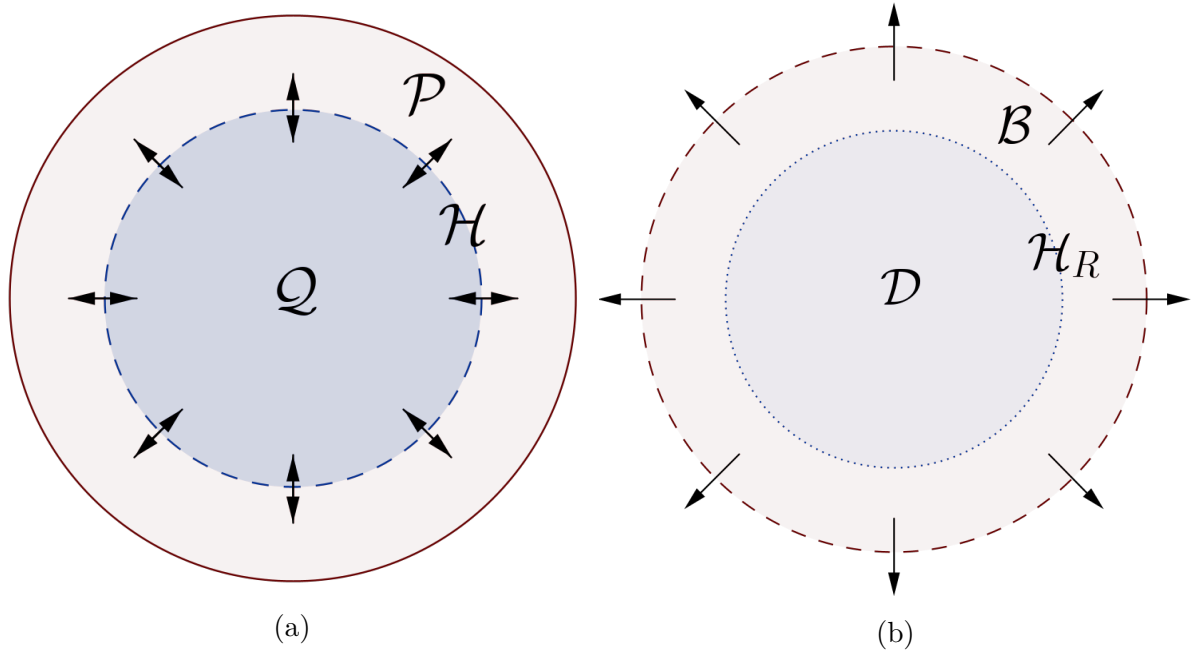


Figure 3.4: Schematic representation of the OQS in (a) Hilbert space and (b) rigged Hilbert space. Figure inspired from Ref. [15].

This limits the number of particles and the size of the model space that we can consider in GSM. To this end we assume that the many-body states become less important as the number of particles in the continuum increases. Therefore if we truncate the basis up to s_π and s_ν particles in the continuum and up to s total particles in the continuum, the number $N_{\text{GSM, truncated}}$ of many-body states becomes:

$$N_{\text{GSM, truncated}} = \sum_{\substack{i,j=0 \\ i+j \leq s}}^{s_\pi, s_\nu} \binom{n_\pi}{r_\pi - i} \binom{m_\pi}{i} \binom{n_\nu}{r_\nu - j} \binom{m_\nu}{j}. \quad (3.41)$$

Let us take a simple example of ^8Be with a ^4He core, i.e. two protons and two neutrons in the valence shells. Taking only $l_j : p_{3/2}, p_{1/2}$ shells in the pole space and 30 shells in the discretized contour for each l_j , we have a staggering 296 012 025 elements in the many-body basis. If we truncate the basis to 2 particles in the continuum it becomes 1 682 325 many-body states. Hence, a reduction of two orders of magnitude is significant from a practical point of view. For the sake of completeness, a SM (or the pole approximation for GSM) calculation with the same valence space would be only 225 many-body states.

Coupled channel representation of Gamow Shell Model

Nuclear reactions should be treated within the formal theory of quantum scattering [170–172]. The reactions of interest in this work are the direct reactions. Direct reactions are defined as those that quickly and directly proceed from initial into final states without forming an intermediate compound state. Indeed, if the initial and final states are unchanged we have *elastic scattering* and if there is some excitation in the final states we have *inelastic scattering*. This happens because the atomic nuclei have internal degrees of freedom which can be excited in a process of collision. Another case is that of *transfer reactions*, where there is an exchange of nucleons between the target and the projectile. The other two cases are the *break-up reactions*, where the projectile breaks into two or more fragments; and the *knock-out reactions*, where a nucleon or cluster is removed from the target after a collision.

In the preceding chapter, we argued that in GSM, which is formulated in the Slater determinant representation, one cannot define reaction channels as the many-body scattering eigenstates in GSM are generally a linear combination of many channels and therefore we cannot describe the asymptotic behavior of a reaction properly. We define a *channel* as the arrangement:

$$A + x \rightarrow B + y, \quad (4.1)$$

where A, B are the initial and final states of the target, respectively, and x, y are the initial and final states of the projectile, respectively¹.

In order to do calculations of cross-sections and phase-shifts, one formulates the GSM in the representation of coupled channels. The GSM-CC formulation, allows the definition of entrance and exit channels with correct asymptotics and hence, allows the calculation of reaction observables. In this representation, we can also calculate spectroscopic observables. This yields a unified theory of nuclear structure and nuclear reactions in Berggren basis.

The asymptotic Hamiltonian for a particular reaction channel between a projectile particle with a nucleons towards a target particle with $A - a$ nucleons is:

$$H_{\text{asymptotic}} = H_{A-a} + V_a + T_a + V_C, \quad (4.2)$$

where H_{A-a} is the full nuclear Hamiltonian of the $(A - a)$ -nucleon system, V_a is the nuclear interaction for the a -nucleon projectile, T_a is the kinetic term of the a -nucleon

¹In here we are disregarding break-up reactions involving three or more particles in the exit channel.

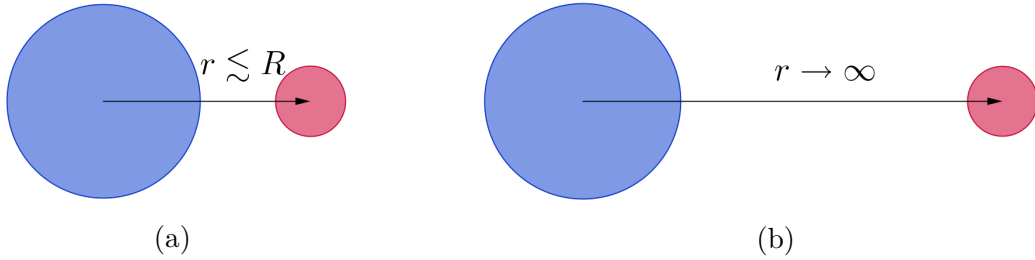


Figure 4.1: Schematic representation of the two asymptotic situations that should be properly addressed for a simultaneous treatment of nuclear structure and reactions. The $(A - a)$ -nucleon target system is depicted with the big blue circle and the a -nucleon projectile system with the small red circle. (a) Is the situation where projectile and target relative distance r is less or similar to the nuclear interaction range R . (b) Is the situation where projectile and target are far from each other and thus decoupled.

system and V_C is the Coulomb interaction. This is the situation depicted in Fig. 4.1b. We can diagonalize such a Hamiltonian but we cannot define an initial and final reaction channels.

This chapter presents the formalism of GSM-CC. We follow closely Ref. [15] and references therein, however clarification and some additional details are given when considered necessary. Particular detail has been given to angular momentum couplings. Sects. 4.1-4.5 deal with the definition of the target and projectile wave functions. Sect. 4.6 deals with the calculation of the kernels of the Hill-Wheeler equation in the context of GSM-CC. Afterwards, the methods to solve the Hill-Wheeler equation are presented in Sect. 4.7. The nuclear reaction solution for the calculation of cross-section is presented in Sect. 4.8. We finish the chapter with the past applications of the GSM-CC formalism in Sect. 4.8.1 and a comparison with other methods that attempt to unify nuclear structure and reactions in Sect. 4.9.

4.1 Definition of channels in Gamow Shell Model

We proceed as in the RGM [113] to define channels with proper asymptotics. We begin with the usual definition of the channel wave functions

$$|c, r\rangle = \mathcal{A} \left\{ |\Psi_T^{J_T}\rangle \otimes |\Psi_P^{J_P}\rangle \right\}_{M_A}^{J_A}, \quad (4.3)$$

where the indices T and P refer to *target* and *projectile*, respectively. The quantum number $c \rightarrow \{Z - z, N - n, J_T; z, n, \ell, J_{\text{int}}, J_P\}$ includes the quantum numbers of both target and projectile which are proton number, neutron number, and spin. In particular, ℓ is the angular momentum of the projectile, and J_{int} is the intrinsic spin of the projectile. The spins are coupled as $\ell + \mathbf{J}_{\text{int}} = \mathbf{J}_P$ and $\mathbf{J}_T + \mathbf{J}_P = \mathbf{J}_A$. Here we can define the channel completeness relation as:

$$\sum_c \int_0^\infty dr r^2 |c, r\rangle \langle c, r| = \mathbf{1}, \quad (4.4)$$

and we can use it to expand the solution of a Hamiltonian for a particular nucleus with $A \equiv Z + N$ nucleons. One obtains:

$$|\Psi\rangle_{M_A}^{J_A} = \sum_c \int_0^\infty dr r^2 \frac{u_c^{J_A}(r)}{r} |c, r\rangle, \quad (4.5)$$

where $u_c^{J_A}$ is the radial amplitude that describes the relative motion of the projectile with respect to the core with a total angular momentum J_A .

With this expansion, the Schrödinger equation:

$$\hat{H} |\Psi\rangle_{M_A}^{J_A} = E |\Psi\rangle_{M_A}^{J_A}, \quad (4.6)$$

can be written as:

$$\sum_c \int_0^\infty [H_{cc'}(r, r') - E N_{cc'}(r, r')] \frac{u_c(r)}{r} r^2 dr = 0, \quad (4.7)$$

where

$$H_{cc'}(r, r') = \langle r, c | \hat{H} | r', c' \rangle \quad (4.8)$$

$$N_{cc'}(r, r') = \langle r, c | r', c' \rangle \quad (4.9)$$

are the interaction matrix elements and the overlap functions, respectively. Eq. (4.7) is called Hill-Wheeler equation. The channel states $|c, r\rangle$ are expanded in a one-body Berggren basis $|c, n\rangle$ to calculate the kernels $H_{cc'}(r, r')$ and $N_{cc'}(r, r')$. The many-body matrix elements $N_{cc'}$ are computed using the Slater determinant expansion of the cluster wave functions $|c, n\rangle$.

4.2 Hamiltonian in the coupled channel formalism

Since we are constructing the total wave function with a product of the target and projectile wave function, one would like to separate the total Hamiltonian into projectile and target parts. Indeed, as the target and projectile at high energy do not interact any longer due to a large difference in momenta, one can express the Hamiltonian \hat{H} as:

$$\hat{H} = \hat{H}_T + \hat{H}_P + \hat{H}_{TP}, \quad (4.10)$$

where \hat{H} is the standard SM Hamiltonian, \hat{H}_T is intrinsic Hamiltonian of the target, \hat{H}_P is the projectile Hamiltonian and $\hat{H}_{TP} = \hat{H} - \hat{H}_T - \hat{H}_P$.

In particular, one would like to separate the CM part from the intrinsic part in the projectile Hamiltonian. To this end, the total Hamiltonian in laboratory coordinates is:

$$\hat{H} = \sum_i \frac{\mathbf{P}_{i,\text{lab}}^2}{2m_i} + \sum_{i<j} \hat{V}_{ij}, \quad (4.11)$$

where i, j goes over all nucleons and \hat{V}_{ij} is the nucleon-nucleon interaction in laboratory coordinates. From the point of view of the projectile, the nucleons in the target will generate a mean field \hat{U}_i^T acting on the projectile nucleons:

$$\sum_{j \in T} \hat{V}_{ij} \longrightarrow \hat{U}_i^T, \quad (4.12)$$

where i is a nucleon in the projectiles and \hat{U}_i^T is assumed to be spherical. Thus, under this approximation, one can write the projectile Hamiltonian as:

$$\hat{H}_P = \underbrace{\sum_{i \in P} \left(\frac{\mathbf{P}_{i,\text{lab}}^2}{2m_i} + \hat{U}_i^T \right)}_{\text{one-body}} + \underbrace{\sum_{i < j \in P} \hat{V}_{ij}}_{\text{two-body}}. \quad (4.13)$$

Now we transform Eq. (4.13) into COSM coordinates [126]:

$$\hat{H}_P = \underbrace{\sum_{i \in P} \frac{(\mathbf{p}_i - \frac{1}{a} \mathbf{P}_{\text{CM}})^2}{2m_i}}_{\text{Intrinsic part}} + \sum_{i < j \in P} \hat{V}_{ij} + \underbrace{\frac{\mathbf{P}_{\text{CM}}^2}{2M_P} + \sum_{i \in P} \hat{U}_i^T}_{\text{CM part}}, \quad (4.14)$$

where $\mathbf{P}_{\text{CM}} = \sum_{i \in P} \mathbf{p}_i$ is the CM momentum of the projectile, m_i is mass of nucleon i , and M_P is the reduced mass of the projectile.

The last step is to define the mean field. Assuming the cluster approximation where $\mathbf{r}_i \approx \mathbf{R}_{\text{CM}}$, the central part of the mean field $\hat{U}_{\text{CM},C}$ created by the nucleons in the target can be approximated by:

$$\hat{U}_{\text{CM},C}^\ell(\mathbf{R}_{\text{CM}}) = z \hat{U}_{\text{p},C}^\ell(\mathbf{R}_{\text{CM}}) + n \hat{U}_{\text{n},C}^\ell(\mathbf{R}_{\text{CM}}), \quad (4.15)$$

where p and n sub-index refer to proton and neutron, respectively; z and n is the number of protons and neutrons in the projectile, respectively; and ℓ is the angular momentum. Moreover, the cluster approximation also implies that $\ell_i \approx \mathbf{L}_{\text{CM}}/a$ and $\sum_{i \in P} \mathbf{s}_i \approx \mathbf{J}_{\text{int}}$, therefore the spin-orbit part of the potential can be expressed as:

$$\hat{U}_{\text{CM},\text{SO}}^\ell(\mathbf{R}_{\text{CM}}) = \frac{z}{a} \hat{U}_{\text{p},\text{SO}}^\ell(\mathbf{R}_{\text{CM}}) + \frac{n}{a} \hat{U}_{\text{n},\text{SO}}^\ell(\mathbf{R}_{\text{CM}}). \quad (4.16)$$

Finally, the mean field potential part reads:

$$\sum_{i \in P} \hat{U}_i^T = \hat{U}_{\text{CM}}^\ell(\mathbf{R}_{\text{CM}}) = \hat{U}_{\text{CM},C}^\ell(\mathbf{R}_{\text{CM}}) + \frac{1}{a} \hat{U}_{\text{CM},\text{SO}}^\ell(\mathbf{R}_{\text{CM}})(\mathbf{L}_{\text{CM}} \cdot \mathbf{J}_{\text{int}}), \quad (4.17)$$

and will be used to generate the $|K_{\text{CM}}, L_{\text{CM}}\rangle$ wave functions.

4.3 Construction of the target and projectile wave functions

Before we can solve the Hill-Wheeler equation, we must define the wave functions of the projectiles and the targets in order to generate the channels. Following from Ref. [15], the target wave functions will be calculated with a GSM calculation, and it will be expressed in Slater determinants:

$$|\Psi_T^{J_T}\rangle = \sum_m d_m |SD_{m,A-a}\rangle, \quad (4.18)$$

where the single-particle basis used can be a Berggren basis or a HO basis. In the case of a nucleon scattering it is possible to use the Berggren ensemble, however, as will be explained later, we use a HO basis if clusters are involved.

On the other hand, projectiles are not calculated in the GSM but within the NCSM framework. Additionally, we can divide the projectile wave function into CM part and intrinsic (int) part:

$$|\Psi_P^{J_P}\rangle = [|K_{\text{CM}} L_{\text{CM}}\rangle \otimes |K_{\text{int}} J_{\text{int}}\rangle]_{M_P}^{J_P}, \quad (4.19)$$

where K_{CM} and L_{CM} are the linear and angular momentum of the CM, respectively, K_{int} is the intrinsic linear momentum, and J_{int} is the intrinsic angular momentum. The two parts couple as $\mathbf{J}_P = \mathbf{J}_{\text{int}} + \mathbf{L}_{\text{CM}}$. One would like to express the projectile wave function in Slater determinants similarly to the target wave function:

$$|\Psi_P^{J_P}\rangle = \sum_n c_n |SD_{n,a}\rangle. \quad (4.20)$$

However, the overlap:

$$\langle \Psi_P^{J_P} | \Psi_{P'}^{J_{P'}} \rangle = \delta(K_{\text{CM}} - K'_{\text{CM}}) \quad (4.21)$$

is difficult to treat numerically [35]. This is because the treatment of the Dirac delta would require a fine discretization of the continuum for the CM/int separation of the projectile wave functions at large distances.

The solution to this is to proceed indirectly and use the properties of the HO basis that the Berggren basis lacks. Hence we define the projectile wave function in the HO basis as:

$$|\Psi_P^{J_P}\rangle^{\text{HO}} = \left[|N_{\text{CM}} L_{\text{CM}}\rangle^{\text{HO}} \otimes |K_{\text{int}} J_{\text{int}}\rangle^{\text{HO}} \right]_{M_P}^{J_P} = \sum_N C_N |SD_{N,a}\rangle^{\text{HO}}, \quad (4.22)$$

where $|N_{\text{CM}} L_{\text{CM}}\rangle^{\text{HO}}$ is a CM HO state, $|K_{\text{int}} J_{\text{int}}\rangle^{\text{HO}}$ is the intrinsic projectile cluster state expanded with a HO basis, $|SD_{N,a}\rangle^{\text{HO}}$ is a Slater determinant made with the one-body HO states.

The intrinsic part $|K_{\text{int}} J_{\text{int}}\rangle$ is constructed by diagonalizing the NN interaction, e.g. the chiral effective interaction, in the intrinsic part of Eq. (4.14). This leaves only the CM part. To this end, one begins by calculating with the Lawson method the ground state of the cluster with a $0s$ CM part:

$$|N_{\text{CM}} = 0, L_{\text{CM}} = 0, M_{\text{CM}} = 0\rangle \otimes |J_{\text{int}} M_{\text{int}}\rangle. \quad (4.23)$$

We introduce the rank-1 spherical tensor ladder operator $A_{\mu,\text{CM}}^\dagger$ ² to calculate the rest of the HO states:

$$\hat{A}_{\mu,\text{CM}}^\dagger = \sqrt{\frac{M\omega}{2\hbar}} \hat{R}_\mu^{(1)} - i \sqrt{\frac{1}{2M\hbar\omega}} \hat{P}_\mu^{(1)}, \quad (4.24)$$

where $R_\mu^{(1)}$ and $P_\mu^{(1)}$ represent the position and momentum of the projectile in CM system:

$$\hat{R}_\mu^{(1)} = \frac{1}{a} \sum_{i=1}^a \hat{r}_{i,\mu}^{(1)}, \quad \hat{P}_\mu^{(1)} = \sum_{i=1}^a \hat{p}_{i,\mu}^{(1)}, \quad (4.25)$$

where $r_{i,\mu}^{(1)}$ and $p_{i,\mu}^{(1)}$ are the position and momentum of nucleon i in the center-of-mass system, respectively. Nevertheless, the action of A^\dagger over $|SD_{N,a}\rangle^{\text{HO}}$ is computed in second quantization using:

$$\hat{R}_\mu^{(1)} = \frac{1}{a} \sum_{\alpha,\beta} \langle \alpha | \hat{r}_\mu^{(1)} | \beta \rangle \hat{c}_\alpha^\dagger \hat{c}_\beta, \quad \hat{P}_\mu^{(1)} = \sum_{\alpha,\beta} \langle \alpha | \hat{p}_\mu^{(1)} | \beta \rangle \hat{c}_\alpha^\dagger \hat{c}_\beta, \quad (4.26)$$

where the kets with greek letters represent one-body HO states, and \hat{c}_α^\dagger , \hat{c}_β are the creation and annihilation operators.

Now we take a look at what happens when applying A^\dagger on a state $|NLM\rangle$. Firstly, applying the A^\dagger tensor increases $2N + L$ by one unit:

$$2N + L \longrightarrow 2N + L + 1 = 2N' + L' \quad (4.27)$$

Afterwards, we couple A^\dagger and $|NL\rangle$ to $L'M'$:

$$[A^\dagger |NL\rangle]_{M'}^{L'} = C_{NL}^{N'L'} |N'L'M'\rangle, \quad (4.28)$$

² $\mu = -1, 0, 1$ for a rank-1 spherical tensor.

where we have suppressed the intrinsic part as it does not play a role in these couplings. The coefficient $C_{NL}^{N'L'}$ can be found as follows:

$$\begin{aligned}
C_{NL}^{N'L'} &= \langle N'L'M' | [A^\dagger | NL] \rangle_{M'}^{L'} \\
&= \sum_{\mu M} \langle LM1\mu | L'M' \rangle \langle N'L'M' | A_\mu^\dagger | NLM \rangle \\
&= \sum_{\mu M} \langle LM1\mu | L'M' \rangle \langle LM1\mu | L'M' \rangle \frac{1}{\sqrt{2L'+1}} \langle N'L' || A^\dagger || NL \rangle \\
&= \frac{1}{\sqrt{2L'+1}} \langle N'L' || A^\dagger || NL \rangle,
\end{aligned} \tag{4.29}$$

where we have used the orthogonality properties of the Clebsch-Gordan coefficients and the Wigner-Eckart theorem.

Now we can build a set of HO states $\{|N_{CM}L_{CM}M_{CM}\rangle \otimes |J_{int}M_{int}\rangle\}$ because the degeneracy induced by A_μ^\dagger is lifted by coupling to L_{CM} . It follows that we can couple the CM part and the intrinsic part to the total angular momentum J_P of the projectile with the appropriate Clebsch-Gordan coefficients $\langle L_{CM}M_{CM}J_{int}M_{int} | J_{int}M_{int} \rangle$. Finally, the coupled states:

$$[|N_{CM}L_{CM}\rangle \otimes |J_{int}\rangle]_{M_P}^{J_P} = \sum_N C_N |SD_{N,a}\rangle^{\text{HO}}, \tag{4.30}$$

can be expanded in the Berggren basis via the many-body completeness relation:

$$\sum_n |SD_{n,a}\rangle \langle SD_{n,a}| = \mathbf{1}, \tag{4.31}$$

as follows:

$$\begin{aligned}
|\Psi_P^{J_P}\rangle &= \sum_N C_N |SD_{N,a}\rangle^{\text{HO}} \\
&= \sum_N C_N \sum_n |SD_{n,a}\rangle \langle SD_{n,a} | SD_{N,a} \rangle^{\text{HO}} \\
&= \sum_n c_n |SD_{n,a}\rangle,
\end{aligned} \tag{4.32}$$

where we identify the constants c_n with

$$c_n = \sum_N C_N \langle SD_{n,a} | SD_{N,a} \rangle^{\text{HO}}. \tag{4.33}$$

Because $|SD_{a,n}\rangle$ and $|SD_{a,n}\rangle^{\text{HO}}$ are built from different one-body bases, the overlap is calculated using the Slater determinant definition as a linear combination of non-antisymmetrized tensor products:

$$\langle SD_{n,a} | SD_{N,a} \rangle^{\text{HO}} = \sum_k (-)^{\varphi_k} \langle s_1 \dots s_a | P_k | \sigma_1 \dots \sigma_a \rangle, \tag{4.34}$$

where P_k is the permutation operator labeled by an index k that goes over all permutations, $|s_i\rangle$ are the single-particle states of the Berggren basis occupied in $|SD_{n,a}\rangle$, $|\sigma_i\rangle$ are the single-particle states of the HO basis occupied in $|SD_{N,a}\rangle^{\text{HO}}$, and $(-)^{\varphi_k}$ is the reordering phase associated with the permutation P_k .

4.4 Construction of the total many-body wave functions

Now that we have derived the projectile and target wave functions, we can proceed to coupling them together in order to generate the A -body wave function. This will yield the A -body wave function $|\Psi\rangle$ that will be used to evaluate the matrix elements in a complete basis of A -body Slater determinants. Defining $A_{[[N_{\text{CM}}L_{\text{CM}}]\otimes|J_{\text{int}}]\}_{M_P}^{J_P}$ as the projectile creation operator, the expansion of the A -body wave function is:

$$|\Psi\rangle_{M_A}^{J_A} = \left[A_{[[N_{\text{CM}}L_{\text{CM}}]\otimes|J_{\text{int}}]\}_{M_P}^{J_P} |\Psi_T^{J_T}\rangle \right]_{M_A}^{J_A} = \sum_{\alpha} C_{\alpha}^A |SD_{\alpha,A}\rangle, \quad (4.35)$$

where $|SD_{\alpha,A}\rangle$ are A -body Slater determinants. To this end, we use the Slater determinant expansions of the projectile and target wave functions as in Eqs. (4.18) and (4.20), which are obtained from the diagonalization of the GSM Hamiltonian:

$$|\Psi_{M_T}^{J_T}\rangle = \sum_{\beta} B_{\beta}^{A-a} |SD_{\beta,A-a}\rangle \quad (4.36)$$

$$[[N_{\text{CM}}L_{\text{CM}}]\otimes|J_{\text{int}}]\}_{M_P}^{J_P} = \sum_{\gamma} B_{\gamma}^a |SD_{\gamma,a}\rangle, \quad (4.37)$$

where we have made explicit the number of nucleons in each of the Slater determinant coefficients. Using Eqs. (4.35), (4.36) and (4.37) one can obtain the uncoupled fully antisymmetrized A -body wave function:

$$\begin{aligned} A_{[[N_{\text{CM}}L_{\text{CM}}]\otimes|J_{\text{int}}]\}_{M_P}^{J_P} |\Psi_T^{J_T}\rangle &= \sum_{\beta} B_{\beta}^{A-a} A_{[[N_{\text{CM}}L_{\text{CM}}]\otimes|J_{\text{int}}]\}_{M_P}^{J_P} |SD_{\beta,A-a}\rangle \\ &= \sum_{\beta\gamma} B_{\beta}^{A-a} B_{\gamma}^a \mathcal{A} [|SD_{\beta,A-a}\rangle \otimes |SD_{\gamma,a}\rangle] \\ &= \sum_{\alpha} B_{\alpha}^A |SD_{\alpha,A}\rangle, \end{aligned} \quad (4.38)$$

where $|SD_{\alpha,A}\rangle = \mathcal{A} [|SD_{\beta,A-a}\rangle \otimes |SD_{\gamma,a}\rangle]$, and $B_{\alpha}^A = (-)^{\varphi_{\alpha}} B_{\beta}^{A-a} B_{\gamma}^a$, with $(-)^{\varphi_{\alpha}}$ a rearrangement phase. In particular, if $|SD_{\beta,A-a}\rangle$ and $|SD_{\gamma,a}\rangle$ share a particle with the same quantum numbers then the corresponding $|SD_{\alpha,A}\rangle$ vanishes. The final step is to couple the result of Eq. (4.38) to a total angular momentum J_A with projection M_A using the appropriate Clebsch-Gordan coefficients. Few more details concerning Eq. (4.38) are discussed in Appendix A.1.

4.5 Orthogonalization of composites with respect to the core.

As stated in Sect. 3.2, all occupied states should be orthogonal to the core. In principle, should the target and projectile satisfy the orthogonalization condition they can be diagonalized with the same Berggren basis, where the occupied core one-body states are removed. An option to ensure the orthogonalization is through the use of a basis of HO states or Jacobi coordinates. However, it is cumbersome to apply [15].

We instead proceed with an alternative method to impose the orthogonalization condition for composite eigenstates with a cluster projectile. Indeed, the cluster wave function

can be factorized into a CM part times a relative part. In order to avoid problems arising from the change between COSM- and CM-relative coordinates, one can define the projectors [3]:

$$\hat{Q}_{\text{CM}} = \sum_{N_{\text{CM}} \leq N_{\text{CM},\text{min}}} |N_{\text{CM}} L_{\text{CM}} J_{\text{int}} J_P M_P\rangle \langle N_{\text{CM}} L_{\text{CM}} J_{\text{int}} J_P M_P| \quad (4.39)$$

$$\hat{P}_{\text{CM}} = \mathbf{1} - \hat{Q}_{\text{CM}}, \quad (4.40)$$

where $N_{\text{CM},\text{min}}$ is chosen so as to include the cluster eigenstates of \hat{H}_P sizably occupying the core. We can now redefine \hat{H}_{CM} as:

$$\hat{H}_{\text{CM}} \rightarrow \hat{P}_{\text{CM}} \hat{H}_{\text{CM}} \hat{P}_{\text{CM}} = \hat{H}_{\text{CM}} - \hat{Q}_{\text{CM}} \hat{H}_{\text{CM}} - \hat{H}_{\text{CM}} \hat{Q}_{\text{CM}} + \hat{Q}_{\text{CM}} \hat{H}_{\text{CM}} \hat{Q}_{\text{CM}}, \quad (4.41)$$

which adds an additional short-range interaction to \hat{H}_P in Eq. (4.13). This also changes the coupling between target and projectile, even though, \hat{H} does not change. This procedure has been checked to be numerically reliable and stable [15].

4.6 Calculation of the kernels of the Hill-Wheeler equation

Repeating from Sect. 4.2, it is convenient to express the Hamiltonian as $\hat{H} = \hat{H}_T + \hat{H}_P + \hat{H}_{TP}$, where \hat{H}_T and \hat{H}_P are the target and projectile Hamiltonians, respectively. Moreover, it was shown that \hat{H}_P can be decomposed as $\hat{H}_P = \hat{H}_{\text{int}} + \hat{H}_{\text{CM}}$, where \hat{H}_{int} describes its intrinsic properties and \hat{H}_{CM} the dynamics of its CM.

The action of the projectile and target Hamiltonians is considered over non-antisymmetrized A -body wavefunctions as:

$$\hat{H}_T [|\Psi_T^{J_T}\rangle \otimes |\Psi_P^{H_P}\rangle]_{M_A}^{J_A} = [\hat{H}_T |\Psi_T^{J_T}\rangle \otimes |\Psi_P^{H_P}\rangle]_{M_A}^{J_A} = E_T [|\Psi_T^{J_T}\rangle \otimes |\Psi_P^{H_P}\rangle]_{M_A}^{J_A} \quad (4.42)$$

$$\hat{H}_P [|\Psi_T^{J_T}\rangle \otimes |\Psi_P^{H_P}\rangle]_{M_A}^{J_A} = [|\Psi_T^{J_T}\rangle \otimes \hat{H}_P |\Psi_P^{H_P}\rangle]_{M_A}^{J_A} = (E_{\text{CM}} + E_{\text{int}}) [|\Psi_T^{J_T}\rangle \otimes |\Psi_P^{H_P}\rangle]_{M_A}^{J_A}, \quad (4.43)$$

where E_T , E_{CM} and E_{int} are the target energy, the projectile CM energy, and the projectile intrinsic energy, respectively. Thus, we now show how to compute the kernels (4.8) and (4.9). First of all, we expand the A -body wave functions with the Berggren basis $\{|N_{\text{CM},L_{\text{CM}}}\rangle\}$ ³ generated with H_{CM} such that we have the completeness relation:

$$\sum_{N_{\text{CM}}} |N_{\text{CM},L_{\text{CM}}}\rangle \langle N_{\text{CM},L_{\text{CM}}}| = \mathbf{1}, \quad (4.44)$$

³Here we are not including the projection of the angular momentum M_{CM} . This only means that the corresponding spherical harmonic is not included in the wave function. The dependence on L_{CM} comes from the angular momentum in the Schrödinger equation used to generate the Berggren basis. Moreover, N_{CM} depicts the number of the discretized states of the Berggren basis and has nothing to do with the HO basis.

and thus

$$\begin{aligned}
|\Psi_{M_A}^{J_A}\rangle &= \mathcal{A} [|\Psi_T^{J_T}\rangle \otimes [|R_{CM} L_{CM}\rangle \otimes |J_{int}\rangle]^{J_p}]_{M_A}^{J_A} \\
&= \mathcal{A} [|\Psi_T^{J_T}\rangle \otimes [|R_{CM, L_{CM}}\rangle \otimes |L_{CM}\rangle \otimes |J_{int}\rangle]^{J_p}]_{M_A}^{J_A} \\
&= \mathcal{A} \left[|\Psi_T^{J_T}\rangle \otimes \left[\sum_{N_{CM}} |N_{CM, L_{CM}}\rangle \langle N_{CM, L_{CM}} | R_{CM, L_{CM}} \rangle \otimes |L_{CM}\rangle \otimes |J_{int}\rangle \right]^{J_p} \right]_{M_A}^{J_A} \\
&= \mathcal{A} \sum_{N_{CM}} \frac{U_{N_{CM}}(R_{CM})}{R_{CM}} [|\Psi_T^{J_T}\rangle \otimes [|N_{CM, L_{CM}}\rangle \otimes |L_{CM}\rangle \otimes |J_{int}\rangle]^{J_p}]_{M_A}^{J_A} \\
&= \mathcal{A} \sum_{N_{CM}} \frac{U_{N_{CM}}(R_{CM})}{R_{CM}} [|\Psi_T^{J_T}\rangle \otimes [|N_{CM}, L_{CM}\rangle \otimes |J_{int}\rangle]^{J_p}]_{M_A}^{J_A}, \tag{4.45}
\end{aligned}$$

where we have defined the wave functions $U_{N_{CM}}(R_{CM})/R_{CM} = \langle N_{CM, L_{CM}} | R_{CM, L_{CM}} \rangle$ and at some point we separated the radial and angular parts of the CM wave function.

We calculate the overlap and Hamiltonian kernels (4.9) and (4.8), respectively, using the results of Eq. (4.45):

$$N_{cc'}^{J_A, M_A}(R_{CM}, R'_{CM}) = \sum_{N_{CM}, N'_{CM}} N_{cc'}^{J_A, M_A}(N_{CM}, N'_{CM}) \frac{U_{N_{CM}}(R_{CM})}{R_{CM}} \frac{U_{N'_{CM}}(R'_{CM})}{R'_{CM}} \tag{4.46}$$

$$H_{cc'}^{J_A, M_A}(R_{CM}, R'_{CM}) = \sum_{N_{CM}, N'_{CM}} H_{cc'}^{J_A, M_A}(N_{CM}, N'_{CM}) \frac{U_{N_{CM}}(R_{CM})}{R_{CM}} \frac{U_{N'_{CM}}(R'_{CM})}{R'_{CM}}, \tag{4.47}$$

where we identify the overlap and Hamiltonian kernels in Berggren basis as:

$$\begin{aligned}
N_{cc'}^{J_A, M_A}(N_{CM}, N'_{CM}) &= \\
& \left[\langle \Psi_T^{J_T} | \otimes [\langle N_{CM}, L_{CM} | \otimes \langle J_{int} |]^{J_p} \right]_{M_A}^{J_A} \mathcal{A} \mathcal{A} \left[|\Psi_{T'}^{J_{T'}}\rangle \otimes [|N'_{CM}, L'_{CM}\rangle \otimes |J'_{int}\rangle]^{J_{p'}} \right]_{M_A}^{J_A} \\
H_{cc'}^{J_A, M_A}(N_{CM}, N'_{CM}) &= \tag{4.48}
\end{aligned}$$

$$\begin{aligned}
& \left[\langle \Psi_T^{J_T} | \otimes [\langle N_{CM}, L_{CM} | \otimes \langle J_{int} |]^{J_p} \right]_{M_A}^{J_A} \mathcal{A} \hat{H} \mathcal{A} \left[|\Psi_{T'}^{J_{T'}}\rangle \otimes [|N'_{CM}, L'_{CM}\rangle \otimes |J'_{int}\rangle]^{J_{p'}} \right]_{M_A}^{J_A}. \tag{4.49}
\end{aligned}$$

The overlap kernels are straightforward to calculate:

$$\begin{aligned}
N_{cc'}^{J_A, M_A}(R_{CM}, R'_{CM}) &= \\
&= \sum_{N_{CM}, N'_{CM}} \frac{U_{N_{CM}}(R_{CM})}{R_{CM}} \frac{U_{N'_{CM}}(R'_{CM})}{R'_{CM}} \langle \Psi_T^{J_t} | A_{[|N_{CM} L_{CM}\rangle \otimes |J_{int}\rangle]_{M_P}^{J_p}} A^\dagger_{[|N_{CM} L_{CM}\rangle \otimes |J_{int}\rangle]_{M_P}^{J_p}} | \Psi_{T'}^{J_t} \rangle \\
&= \sum_{N_{CM}, N'_{CM}} \frac{U_{N_{CM}}(R_{CM})}{R_{CM}} \frac{U_{N'_{CM}}(R'_{CM})}{R'_{CM}} \sum_{\alpha, \alpha'} C_\alpha^A C_{\alpha'}^A \langle SD_{\alpha, A} | SD_{\alpha', A} \rangle. \tag{4.50}
\end{aligned}$$

The targets will consist of bound or resonance states, thus their high-energy components in Berggren basis are extremely small. Therefore, if the projectile momentum is moderate to high, then antisymmetry does not play a role, and thus channels become orthogonal [16].

Afterwards we define a particular N_{\max} whose momentum is large and divide the sum

in Eq. (4.47) into four cases:

$$\begin{aligned}
H_{cc'}^{J_A, M_A}(R_{\text{CM}}, R'_{\text{CM}}) &= \sum_{\substack{N_{\text{CM}} \leq N_{\text{max}} \\ N'_{\text{CM}} \leq N_{\text{max}}}} H_{cc'}^{J_A, M_A}(N_{\text{CM}}, N'_{\text{CM}}) \frac{U_{N_{\text{CM}}}(R_{\text{CM}})}{R_{\text{CM}}} \frac{U_{N'_{\text{CM}}}(R'_{\text{CM}})}{R'_{\text{CM}}} \\
&+ \sum_{\substack{N_{\text{CM}} > N_{\text{max}} \\ N'_{\text{CM}} \leq N_{\text{max}}}} H_{cc'}^{J_A, M_A}(N_{\text{CM}}, N'_{\text{CM}}) \frac{U_{N_{\text{CM}}}(R_{\text{CM}})}{R_{\text{CM}}} \frac{U_{N'_{\text{CM}}}(R'_{\text{CM}})}{R'_{\text{CM}}} \\
&+ \sum_{\substack{N_{\text{CM}} \leq N'_{\text{max}} \\ N_{\text{CM}} > N'_{\text{max}}}} H_{cc'}^{J_A, M_A}(N_{\text{CM}}, N'_{\text{CM}}) \frac{U_{N_{\text{CM}}}(R_{\text{CM}})}{R_{\text{CM}}} \frac{U_{N'_{\text{CM}}}(R'_{\text{CM}})}{R'_{\text{CM}}} \\
&+ \sum_{\substack{N_{\text{CM}} > N_{\text{max}} \\ N'_{\text{CM}} > N_{\text{max}}}} H_{cc'}^{J_A, M_A}(N_{\text{CM}}, N'_{\text{CM}}) \frac{U_{N_{\text{CM}}}(R_{\text{CM}})}{R_{\text{CM}}} \frac{U_{N'_{\text{CM}}}(R'_{\text{CM}})}{R'_{\text{CM}}}. \quad (4.51)
\end{aligned}$$

The first term is finite and thus, can be computed using standard SM formulas. Since antisymmetry can be neglected when $N_{\text{CM}} > N_{\text{max}}$ or $N'_{\text{CM}} > N_{\text{max}}$, the matrix elements in Berggren basis are:

$$\begin{aligned}
H_{cc'}^{J_A, M_A}(N_{\text{CM}}, N'_{\text{CM}}) &= \\
&= [\langle \Psi_T^{J_T} | [\langle N_{\text{CM}}, L_{\text{CM}} | \langle J_{\text{int}} |]^{J_p}]_{M_A}^{J_A} (\hat{H}_T + \hat{H}_P + \mathcal{A} \hat{H}_{TP} \mathcal{A}) [| \Psi_{T'}^{J_{T'}} \rangle [| N'_{\text{CM}}, L'_{\text{CM}} \rangle | J'_{\text{int}} \rangle]^{J_{p'}}]_{M_A}^{J_A} \\
&= [E_T + E_{\text{CM}} + E_{\text{int}}] \delta_{cc'} \delta_{N_{\text{CM}} N'_{\text{CM}}} + \sum_{\alpha \alpha'} C_{\alpha}^A C_{\alpha'}^A \langle SD_{A, \alpha} | \hat{H}_{TP} | SD_{A, \alpha} \rangle \\
&= [E_T + E_{\text{CM}} + E_{\text{int}}] \delta_{cc'} \delta_{N_{\text{CM}} N'_{\text{CM}}} + \sum_{\substack{\alpha \alpha' \\ \alpha \beta \gamma \delta}} \langle \alpha \beta | (\hat{V}_{\text{res}} - \hat{U}_0) | \gamma \delta \rangle \langle SD_{A, \alpha} | a_{\alpha}^{\dagger} a_{\beta}^{\dagger} a_{\delta} a_{\gamma} | SD_{A, \alpha} \rangle.
\end{aligned}$$

It can be proven that the residual matrix elements which involve target-projectile coupling at high energy can be neglected [15, 35]:

$$\langle \alpha \beta | (\hat{V}_{\text{res}} - \hat{U}_0) | \gamma \delta \rangle \approx 0 \text{ if } \exists (i, j) \in \{\alpha, \beta, \gamma, \delta\} \mid k_i \ll k_{\text{max}} \text{ and } k_j \gtrsim k_{\text{max}}, \quad (4.52)$$

where $|\alpha\rangle, |\beta\rangle, |\gamma\rangle, |\delta\rangle$ are Berggren states with momentum $k_{\alpha}, k_{\beta}, k_{\gamma}, k_{\delta}$ and k_{max} is an arbitrarily large one-body momentum corresponding to N_{max} . Therefore, the second and third sums in Eq. (4.51) are zero because $N_{\text{CM}} \neq N'_{\text{CM}}$ and the matrix elements satisfy condition (4.52). Hence, Eq. (4.51) simplifies to:

$$\begin{aligned}
H_{cc'}^{J_A, M_A}(R_{\text{CM}}, R'_{\text{CM}}) &= \sum_{\substack{N_{\text{CM}} \leq N_{\text{max}} \\ N'_{\text{CM}} \leq N_{\text{max}}}} H_{cc'}^{J_A, M_A}(N_{\text{CM}}, N'_{\text{CM}}) \frac{U_{N_{\text{CM}}}(R_{\text{CM}})}{R_{\text{CM}}} \frac{U_{N'_{\text{CM}}}(R'_{\text{CM}})}{R'_{\text{CM}}} \\
&+ \sum_{N_{\text{CM}} > N_{\text{max}}} [E_T + E_{\text{CM}} + E_{\text{int}}] \delta_{cc'} \frac{U_{N_{\text{CM}}}(R_{\text{CM}})}{R_{\text{CM}}} \frac{U_{N_{\text{CM}}}(R'_{\text{CM}})}{R'_{\text{CM}}}. \quad (4.53)
\end{aligned}$$

The second sum in Eq. (4.53) can be written as:

$$\sum_{N_{\text{CM}} > N_{\text{max}}} \longrightarrow \sum_{N_{\text{CM}}} - \sum_{N_{\text{CM}} \leq N_{\text{max}}}, \quad (4.54)$$

where the terms in the first sum can be expressed in terms of Dirac's delta due to the completeness of the $\{U_{N_{\text{CM}}}\}$ basis:

$$\begin{aligned}
&\sum_{N_{\text{CM}}} [E_T + E_{\text{CM}} + E_{\text{int}}] \delta_{cc'} \frac{U_{N_{\text{CM}}}(R_{\text{CM}})}{R_{\text{CM}}} \frac{U_{N_{\text{CM}}}(R'_{\text{CM}})}{R'_{\text{CM}}} \\
&= (E_T + E_{\text{int}}) \frac{\delta(R_{\text{CM}} - R'_{\text{CM}})}{R_{\text{CM}} R'_{\text{CM}}} + \hat{T}_{\text{CM}} \frac{\delta(R_{\text{CM}} - R'_{\text{CM}})}{R_{\text{CM}} R'_{\text{CM}}} + \hat{U}_{\text{CM}}(R_{\text{CM}}, R'_{\text{CM}}), \quad (4.55)
\end{aligned}$$

where \hat{T}_{CM} and \hat{U}_{CM} are the kinetic and potential CM parts in Eq. (4.14). The final result for the Hamiltonian kernels is:

$$\begin{aligned} H_{cc'}^{J_A, M_A}(R_{\text{CM}}, R'_{\text{CM}}) &= \delta_{cc'} \left[-\frac{\hbar^2}{2M_p} \frac{\partial^2}{\partial R_{\text{CM}}^2} + \frac{\hbar^2}{2M_P} \frac{L_{\text{CM}}(L_{\text{CM}} + 1)}{R_{\text{CM}}^2} + E_T + E_{\text{int}} \right] \frac{\delta(R_{\text{CM}} - R'_{\text{CM}})}{R_{\text{CM}} R'_{\text{CM}}} \\ &+ \delta_{cc'} \hat{U}_{\text{CM}}(R_{\text{CM}}, R'_{\text{CM}}) + \tilde{V}_{cc'}(R_{\text{CM}}, R'_{\text{CM}}), \end{aligned} \quad (4.56)$$

where $\tilde{V}_{cc'}$ includes the short-range terms and is given by:

$$\begin{aligned} \tilde{V}_{cc'}(R_{\text{CM}}, R'_{\text{CM}}) &= \sum_{\substack{N_{\text{CM}} \leq N_{\text{max}} \\ N'_{\text{CM}} \leq N_{\text{max}}}} H_{cc'}^{J_A, M_A}(N_{\text{CM}}, N'_{\text{CM}}) \frac{U_{N_{\text{CM}}}(R_{\text{CM}})}{R_{\text{CM}}} \frac{U_{N'_{\text{CM}}}(R'_{\text{CM}})}{R'_{\text{CM}}} \\ &- \sum_{N_{\text{CM}} \leq N_{\text{max}}} [E_T + E_{\text{CM}} + E_{\text{int}}] \delta_{cc'} \frac{U_{N_{\text{CM}}}(R_{\text{CM}})}{R_{\text{CM}}} \frac{U_{N_{\text{CM}}}(R'_{\text{CM}})}{R'_{\text{CM}}}. \end{aligned}$$

$\tilde{V}_{cc'}$ contains the calculation of $\langle \alpha\beta | (\hat{V}_{\text{res}} - \hat{U}_0) | \gamma\delta \rangle$ matrix elements. Since the residual interaction is of short range, then we can use a HO oscillator basis expansion to calculate them. Using the method in Eq. (1.54) allows for a more stable calculation.

4.7 Solution of the Hill-Wheeler equation

The coupled-channel and Slater determinant representations of GSM are mathematically equivalent, however truncations of model spaces in both representations are not. Indeed, in the Slater determinant representation we truncate the number of allowed Slater determinants. On the other hand, the truncation at the level of channels consists of choosing the relevant channels under the assumption that only a few of them contribute to the total wave function. Therefore in practice the solutions of GSM and GSM-CC are going to be different.

So far, we have gathered the necessary tools to begin solving the Hill-Wheeler equation (4.7) in the context of GSM-CC. First, we will transform the generalized eigenvalue problem into a standard eigenvalue problem. Afterwards, we will solve the entrance channel by direct integration. Then, we will solve for the resonant states using a version of the overlap method discussed in Chap. 3. Finally we will solve for the scattering states using a Green's function method.

4.7.1 Transformation to a standard eigenvalue problem

Eq. (4.7) is a generalized eigenvalue problem which is solved by first transforming it into a standard eigenvalue problem. One starts by rewriting it in the matrix form as:

$$\mathcal{H}\mathcal{U} = \mathcal{E}\mathcal{N}\mathcal{U}. \quad (4.57)$$

By defining: $\mathcal{W} = \mathcal{N}^{1/2}\mathcal{U}$ and $\mathcal{H}_m = \mathcal{N}^{-1/2}\mathcal{H}\mathcal{N}^{-1/2}$, where \mathcal{W} is a vector containing the orthogonal channel wave function and \mathcal{H}_m is the modified Hamiltonian [16], Eq. (4.57) becomes:

$$\mathcal{H}_m\mathcal{W} = \mathcal{E}\mathcal{W}. \quad (4.58)$$

One can separate the overlap kernels in their orthogonal part and their short-range target-projectile coupling part $\tilde{\mathcal{N}}$:

$$\mathcal{N} = \mathbb{1} + \tilde{\mathcal{N}}, \quad (4.59)$$

which means that we can express $\mathcal{N}^{-1/2}$ similarly as

$$\mathcal{N}^{-1/2} = \mathbb{1} + \Delta, \quad (4.60)$$

where Δ will carry all contributions from the short-range interaction. In particular, $\mathcal{N}^{-1/2}$ is calculated using the Moore-Penrose pseudo-inverse. The modified Hamiltonian in matrix form becomes:

$$\mathcal{H}_m = \mathcal{H} + \mathcal{H}\Delta + \Delta\mathcal{H} + \Delta\mathcal{H}\Delta. \quad (4.61)$$

This allows to write equation (4.58) as:

$$\mathcal{H}\mathcal{W} + (\mathcal{H}\Delta + \Delta\mathcal{H} + \Delta\mathcal{H}\Delta)\mathcal{W} = \mathcal{H}\mathcal{W} + \mathcal{D}\mathcal{W} = E\mathcal{W}, \quad (4.62)$$

where we identify:

$$\mathcal{D} = \mathcal{H}\Delta + \Delta\mathcal{H} + \Delta\mathcal{H}\Delta, \quad (4.63)$$

and which in non-matricial form is:

$$\begin{aligned} \sum_{c'} \int dR'_{\text{CM}} R'_{\text{CM}}{}^2 H_{cc'}(R_{\text{CM}}, R'_{\text{CM}}) w_{c'}(R'_{\text{CM}}) \\ + \sum_{c'} \int dR'_{\text{CM}} R'_{\text{CM}}{}^2 D_{cc'}(R_{\text{CM}}, R'_{\text{CM}}) w_{c'}(r') = E w_c(R_{\text{CM}}). \end{aligned} \quad (4.64)$$

In this equation, we identify $D_{cc'}(r, r')$ as the matrix element of \mathcal{D} and $w_c(r)$ is the orthogonalized wave function. Plugging Eq. (4.56) in Eq. (4.64) we get:

$$\begin{aligned} \left[\frac{\hbar^2}{2M_P} \left(-\frac{\partial^2}{\partial R_{\text{CM}}^2} + \frac{L_{\text{CM}}(L_{\text{CM}} + 1)}{R_{\text{CM}}^2} \right) + E_T + E_{\text{int}} \right] w_c(R_{\text{CM}}) + U_c^{\text{local}}(R_{\text{CM}}) w_c(R_{\text{CM}}) \\ + \sum_{c'} \int dR'_{\text{CM}} R'_{\text{CM}}{}^2 V_{cc'}^{\text{non-local}}(R_{\text{CM}}, R'_{\text{CM}}) w_{c'}(R'_{\text{CM}}) = E w_c(R_{\text{CM}}). \end{aligned} \quad (4.65)$$

Here we have identified the local potential coming from the mean-field, and the non-local part given by:

$$V_{cc'}^{\text{non-local}}(R_{\text{CM}}, R'_{\text{CM}}) = \tilde{V}_{cc'}(R_{\text{CM}}, R'_{\text{CM}}) + D_{cc'}(R_{\text{CM}}, R'_{\text{CM}}). \quad (4.66)$$

The final missing piece after solving Eq. (4.65) is to recover the non-orthogonal wave functions $u_c(R_{\text{CM}})$. One obtains the physical channel wave functions via:

$$u_c(R_{\text{CM}}) = w_c(R_{\text{CM}}) + \sum_{c'} \int dR'_{\text{CM}} R'_{\text{CM}}{}^2 \Delta_{cc'}(R_{\text{CM}}, R'_{\text{CM}}) w_{c'}(R'_{\text{CM}}), \quad (4.67)$$

where the kernel $\Delta_{cc'}(R_{\text{CM}}, R'_{\text{CM}}) = \langle R_{\text{CM}}, c | \Delta | R'_{\text{CM}}, c' \rangle$.

4.7.2 Solution in the coordinate space: the equivalent potential method

In this section we will describe the method to solve Eq. (4.65). It consist of a generalization of the equivalent potential method described in Ref. [129]. We will express the system of equations with non-local potentials into a system of equations with local potentials and a source term. We define the following equivalent potential:

$$V_{cc'}^{\text{eq}}(R_{\text{CM}}) = \delta_{cc'} U_{c'}(R_{\text{CM}}) + \left(\frac{1 - F_{c'}(R_{\text{CM}})}{w_{c'}(R_{\text{CM}})} \right) \int dR_{\text{CM}} R_{\text{CM}}^2 V_{cc'}^{\text{non-local}}(R_{\text{CM}}, R'_{\text{CM}}) w_{c'}(R'_{\text{CM}}), \quad (4.68)$$

and the following source term:

$$S_c^{\text{eq}} = \sum_{c'} F'_c(R_{\text{CM}}) \int dR'_{\text{CM}} R_{\text{CM}}^2 V_{cc'}^{\text{non-local}}(R_{\text{CM}}, R'_{\text{CM}}) w_{c'}(R'_{\text{CM}}), \quad (4.69)$$

where we have used a smoothing function $F'_c(R_{\text{CM}})$. The job of this function is to remove the singularities due to the zeros of $w_{c'}$. We require that $F'_c \sim 1$ close to the singularities of $w_{c'}$ and zero elsewhere⁴. We also define the following matrix:

$$M_{cc'}^{\text{eq}} = \left[\frac{L_{\text{CM}}(L_{\text{CM}} + 1)}{R_{\text{CM}}^2} - k^2 \right] \delta_{cc'} + \frac{2M_P}{\hbar^2} V_{cc'}^{\text{eq}}(R_{\text{CM}}), \quad (4.70)$$

where $k^2 = (2M_P/\hbar^2)(E_T + E_{\text{int}} + E)$. Finally, the equivalent potential equation in matrix form becomes:

$$\mathcal{W}(R_{\text{CM}}) = M^{\text{eq}}(R_{\text{CM}})\mathcal{W}(R_{\text{CM}}) + S^{\text{eq}}(R_{\text{CM}}), \quad (4.71)$$

and is solved iteratively. As any other iterative method, it is crucial to have a good starting point. It is obtained by diagonalizing Eq. (4.65) with the non-local terms set to zero.

We now move into details of the boundary conditions. In particular, we expand w_c in the forward basis in the interval $r \in [0, R]$ corresponding to the internal region where the nuclear potential is non-negligible:

$$w_c(R_{\text{CM}}) = \sum_b c_b^{(0)} w_{c,b}^{(0)}(R_{\text{CM}}), \quad (4.72)$$

and we expand w_c in the backward basis in the interval $r \in [R, R_{\text{max}}]$ corresponding to the asymptotic region where the nuclear potential is negligible:

$$w_c(R_{\text{CM}}) = \sum_b c_b^{(+)} w_{c,b}^{(+)}(R_{\text{CM}}) + w_e^{(-)}(R_{\text{CM}}). \quad (4.73)$$

Here we have included the entrance channel, which is zero if we are describing a resonant state. The idea of using these bases is that they have a simplified asymptotic behavior, namely:

$$w_{c,b}^{(0)}(R_{\text{CM}} \sim 0) \sim \begin{cases} R_{\text{CM}}^{L_{\text{CM},b+1}} & c = b \\ \mathcal{O}\left(R_{\text{CM}}^{L_{\text{CM},b+1}}\right) & c \neq b \end{cases} \quad (4.74)$$

for the forward basis, and:

$$w_{c,b}^{(+)}(R_{\text{CM}}) \rightarrow \begin{cases} C_b^{(+)} H_{L_{\text{CM},b}\eta_b}^+(k_b R_{\text{CM}}) & c = b \\ 0 & c \neq b \end{cases} \quad (4.75)$$

for the backward basis. In particular, the backward basis is zero for different channels because there is no channel-channel coupling in this region. On the other hand, we cannot ignore the channel-channel coupling in the internal region. Thus we need to find the behavior of $w_{c,b}$ for $c \neq b$.

We can rewrite Eq. (4.71) for small CM distances in the forward basis as:

$$w_{c,b}^{\prime\prime(0)}(R_{\text{CM}}) = \left[\frac{L_{\text{CM}}(L_{\text{CM}} + 1)}{R_{\text{CM}}^2} + a_c \right] w_{c,b}^{(0)}(R_{\text{CM}}) + \sum_{c \neq c'} a_{cc'} w_{c',b}^{(0)}(R_{\text{CM}}), \quad (4.76)$$

⁴In particular, this means that for $R_{\text{CM}} \sim 0$ the source term is zero as the channel wave functions are non-zero in that region.

where we made the identifications:

$$a_c = \frac{2M_p}{\hbar^2} V_{cc}^{\text{eq}}(R_{\text{CM}} \rightarrow 0) - k^2 \quad (4.77)$$

$$a_{cc'} = \frac{2M_p}{\hbar^2} V_{cc'}^{\text{eq}}(R_{\text{CM}} \rightarrow 0). \quad (4.78)$$

If $c \neq b$, then Eq. (4.76) becomes:

$$w_{c,b}^{(0)''}(R_{\text{CM}}) = \frac{L_{\text{CM}}(L_{\text{CM}} + 1)}{R_{\text{CM}}^2} w_{c,b}^{(0)}(R_{\text{CM}}) + a_b R_{\text{CM}}^{L_{\text{CM},b+1}} + \mathcal{O}(R_{\text{CM}}^{L_{\text{CM},b+1}}). \quad (4.79)$$

The terms $\mathcal{O}(R_{\text{CM}}^{L_{\text{CM},b+1}})$ are negligible and thus, Eq. (4.79) becomes a simple differential equation problem, which can be dealt with by the ansatz:

$$w_{c,b}^{(0)''}(R_{\text{CM}}) = \begin{cases} \mathcal{C} R_{\text{CM}}^t & L_{\text{CM},c} \neq L_{\text{CM},b} + 2 \\ \mathcal{D} R_{\text{CM}}^t \ln(R_{\text{CM}}) & L_{\text{CM},c} = L_{\text{CM},b} + 2 \end{cases} \quad (4.80)$$

and solved for the constants $\mathcal{C}, \mathcal{D}, t$. This allows to write the full solution in the internal region for the forward basis:

$$w_{c,b}^{(0)}(R_{\text{CM}}) = \begin{cases} R_{\text{CM}}^{L_{\text{CM},b+1}} & c = b \\ \frac{a_b R_{\text{CM}}^{L_{\text{CM},b+3}}}{(L_{\text{CM},b} + 3)(L_{\text{CM},b} + 2) - L_{\text{CM},c}(L_{\text{CM},c} + 1)} & c \neq b, L_{\text{CM},c} \neq L_{\text{CM},b} + 2 \\ \frac{a_b}{2L_{\text{CM},b} + 5} R_{\text{CM}}^{L_{\text{CM},b+3}} \ln(R_{\text{CM}}) & c \neq b, L_{\text{CM},c} = L_{\text{CM},b} + 2 \end{cases} \quad (4.81)$$

Finally, with both the forward and backward bases properly defined, we move to the determination of the constants $c_b^{(0)}, c_b^{(+)}$. This is straightforward from matching the forward and backward solutions and its derivatives at a matching radius R_m :

$$\sum_b \left[c_b^{(0)} w_{c,b}^{(0)}(R_m) - c_b^{(+)} w_{c,b}^{(+)}(R_m) \right] = w_c^{(-)}(R_m) \quad (4.82)$$

$$\sum_b \left[c_b^{(0)} \frac{dw_{c,b}^{(0)}(R_m)}{dR_{\text{CM}}} - c_b^{(+)} \frac{dw_{c,b}^{(+)}(R_m)}{dR_{\text{CM}}} \right] = w_c^{(-)}(R_m). \quad (4.83)$$

If it is a scattering state, the system to solve is of the form $AX = B$, and thus, straightforward to calculate. However, for a resonant state, it is of the form $AX = 0$ and thus the problem is solved when $\det A = 0$. This allows the interpretation of $\det A$ as a generalization of the Jost functions described in Sect. 1.3. Once the solution for $\det A = 0$ has been found, the constants $c_b^{(0)}$ and $c_b^{(+)}$ are given by the eigenvector X of A of zero eigenvalue.

4.7.3 Bound and resonance states: overlap method in the context of coupled channels

The method presented in the previous section is iterative, and thus it can present instabilities. To calculate spectra, it is more convenient to use a different method. Reminiscent to the GSM, we can also use the overlap method. In order to do this, we expand the channel wave functions in the Berggren basis as in Eq. (4.45) and then use Eq. (4.58)

which yields a complex symmetric matrix for the modified Hamiltonian. However, it can be casted using orthogonal channels defined as:

$${}_o\langle c', r' | c, r \rangle_o = \frac{\delta(r - r')}{rr'} \delta_{cc'}, \quad (4.84)$$

where the transformation from the non-orthogonal channel basis $\{|c, r\rangle\}$ to the orthogonal basis $\{|c, r\rangle_o\}$ is given by $|c, r\rangle = \mathcal{N}^{1/2} |c, r\rangle_o$. This allows to write Eq. (4.58) as:

$$\sum_{c'} \int dR'_{\text{CM}} R'_{\text{CM}} \left({}_o\langle c', R'_{\text{CM}} | \hat{H} | c, R_{\text{CM}} \rangle_o - E \frac{\delta(R_{\text{CM}} - R'_{\text{CM}})}{R_{\text{CM}} R'_{\text{CM}}} \delta_{cc'} \right) {}_o\langle c', R'_{\text{CM}} | \Phi_{M_A}^{J_A} \rangle_o = 0 \quad (4.85)$$

where $|\Phi_{M_A}^{J_A}\rangle_o = \mathcal{N}^{1/2} |\Psi_{M_A}^{J_A}\rangle$, and we do the following identifications:

$${}_o\langle c', R'_{\text{CM}} | \hat{H} | c, R_{\text{CM}} \rangle_o \equiv \langle c', R'_{\text{CM}} | \mathcal{H}_m | c, R_{\text{CM}} \rangle \quad (4.86)$$

$${}_o\langle c', R'_{\text{CM}} | \Phi_{M_A}^{J_A} \rangle_o \equiv \frac{w_c(R_{\text{CM}})}{R_{\text{CM}}}. \quad (4.87)$$

Diagonalizing this matrix yields eigenstates consisting of bound, resonance and scattering states. The resonances are embedded among the scattering states, which is the same situation as in the GSM, and thus it is possible to use the overlap method to find the resonances. In the context of coupled-channels, the pole approximation consists of building channels only with the pole states of the Berggren basis coming from the projectile CM Hamiltonian. Finally, the overlap is maximized in the same fashion as described in Sect. 3.1.

4.7.4 Scattering states: solution via Green's function method

We need an alternative and more stable method to calculate the scattering states. This is done with the Green's function method [35] to get the scattering solutions of Eq. (4.65). The idea is to proceed perturbatively, so we define the zeroth-order Hamiltonian $\hat{H}^{(0)}$ and its eigenvector $|\Psi^{(0)}\rangle$:

$$\hat{H}^{(0)} = \begin{cases} \hat{t} + \hat{U}_{\text{basis}} & (\text{nucleon}) \\ \hat{T}_{\text{CM}} + \hat{U}_{\text{CM}} & (\text{cluster}) \end{cases} \quad (4.88)$$

$$\hat{H}^{(0)} |\Psi^{(0)}\rangle = E |\Psi^{(0)}\rangle. \quad (4.89)$$

To be more specific, $\hat{H}^{(0)}$ is a matrix whose off-diagonal elements are zero due to the absence of channel-channel coupling, and only one nonzero diagonal term corresponding to the entrance channel c_0 that is activated. Hence, Eq. (4.89) is a one-dimensional differential equation.

We now separate the total Hamiltonian \hat{H} and the total wave function $|\Psi_{M_A}^{J_A}\rangle$ into their zeroth order parts and the rest:

$$\hat{H} = \hat{H}^{(0)} + \hat{H}_{\text{rest}} \quad (4.90)$$

$$|\Psi_{M_A}^{J_A}\rangle = |\Psi^{(0)}\rangle + |\Psi_{\text{rest}}\rangle. \quad (4.91)$$

Using Eqs. (4.6),(4.89),(4.90), and (4.91), one obtains:

$$(\hat{H} - E) |\Psi_{\text{rest}}\rangle = -\hat{H}_{\text{rest}} |\Psi^{(0)}\rangle = |\Psi_S\rangle, \quad (4.92)$$

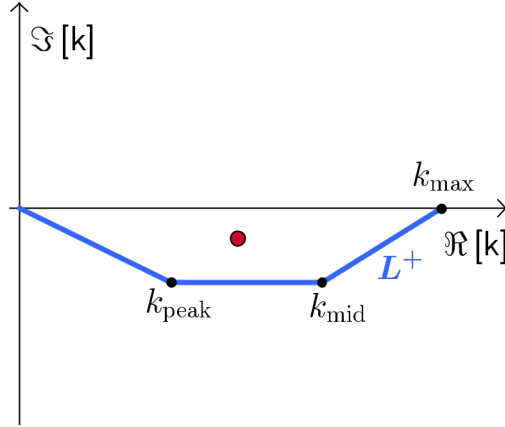


Figure 4.2: Typical contour enclosing the resonance pole for a GSM-CC calculation in the complex k -plane.

where we have introduced a source term $|\Psi_S\rangle$. Eq. (4.92) implies that the asymptotic behavior of the source term is $\lim_{r \rightarrow \infty} \Psi_S(r) = 0$ because \hat{H}_{rest} is of finite range. This means that the source term can be expanded in the Berggren basis generated by \hat{H}_0 , so that Eq. (4.92) becomes a linear system:

$$[\Psi_{\text{rest}}]_{n,c} = \langle n, c | \Psi_{\text{rest}} \rangle \quad (4.93)$$

$$[M_E]_{n,c;n',c'} = \langle n', c' | \hat{H} - E | n, c \rangle \quad (4.94)$$

$$[\Psi_S]_{n,c} = \langle n, c | \Psi_S \rangle \quad (4.95)$$

$$M_E \Psi_{\text{rest}} = \Psi_S, \quad (4.96)$$

where $|n, c\rangle$ is a Berggren basis state with index n and of the channel c . The matrix elements of \hat{H} are calculated with the complex scaling method.

To solve Eq. (4.96) one has to invert the matrix M_E . However, similarly to the Lippmann-Schwinger equation, M_E is not invertible on the real axis. Thus, the solution is to impose a small imaginary part $\varepsilon \rightarrow 0^+$ such that $E \rightarrow E + i\varepsilon$. Additionally, since channels other than the entrance channel consist only of outgoing wave function parts, one can impose an outgoing wave function condition for $u_c(r)$ when $c \neq c_0$. Nevertheless, this method becomes unstable for small ε .

This instabilities are mended by defining the contour of the discretized part of the Berggren basis differently than what was shown in Fig. 3.1. Instead we choose a contour like the trapezoid shown in Fig. 4.2, where the contour points have non-zero imaginary part. Additionally, the outgoing wave function behavior for Ψ_{rest} is guaranteed in a Berggren basis representation. Indeed, from the Parseval equality:

$$\|\Psi_{\text{rest}}\|^2 = \sum_n |c_n|^2 \|u_c^{(n)}\|^2, \quad (4.97)$$

it can be deduced that the $|\Psi_{\text{rest}}\rangle$ is a localized state when complex rotation is applied because the Berggren basis states are.

This method offers a numerical advantage over the method of equivalent potential for the solution of the GSM-CC. It is sufficient to compute one representation of the Hamiltonian \hat{H} in the Berggren basis, and then solve for different energies. Nevertheless, it has been checked that both the equivalent potential method and the Green's function method yields the same solution for $|\Psi_{MA}^{JA}\rangle$ [15, 35]. Additionally, due to the increased numerical cost of solving the GSM-CC as compared to the GSM, the matrix \hat{H} is first transformed into a diagonal or tridiagonal form.

4.7.5 Summary of the numerical methods to solve the coupled channels equation

In the previous subsections, we have described different methods used to solve the GSM-CC equations (4.6). However, it is fair to ask why the equivalent potential method has been introduced in this work if it can be replaced with the overlap method and the Green's function method. Indeed, current GSM-CC calculations for spectra and spectrum related calculations are done with the overlap + Green's function method. However, the calculations for reaction observables need the equivalent potential method as the S -matrix elements are constructed via the $c^{(0)}$ and $c^{(+)}$ constants in Eqs. (4.82) and (4.83).

4.8 Calculation of reaction observables

After calculating the scattering and resonant solutions of the GSM-CC equation (4.6), we can now move on to calculate reaction observables from standard scattering theory formulas. In order to do this, one has to build the many-body scattering wave functions with the correct asymptotics. Indeed, as we build these wave functions we obtain information about the S -matrix and hence, the phase shifts. Finally, we can extract the scattering amplitude from the scattering wave functions, which allows for the calculation of cross-sections.

We rewrite Eq. (4.5) as:

$$|\Psi_{M_A}^{e,J_A}\rangle = \sum_c \int_0^\infty dR_{\text{CM}} R_{\text{CM}}^2 \frac{u_c^{e,J_A}(R_{\text{CM}})}{R_{\text{CM}}} |c, R_{\text{CM}}\rangle, \quad (4.98)$$

where the entrance channel e has been made explicit and the channels c indicate all possible exit channels. We repeat the definition of the channels wave functions:

$$|c, R_{\text{CM}}\rangle = \mathcal{A} [|\psi_T^{J_T}\rangle \otimes [|R_{\text{CM}} L_{\text{CM}}\rangle \otimes |J_{\text{int}}\rangle]^{J_P}]_{M_A}^{J_A}, \quad (4.99)$$

where we use the angular momentum coupling scheme:

$$\mathbf{L}_{\text{CM}} + \mathbf{J}_{\text{int}} = \mathbf{J}_P \quad (4.100)$$

$$\mathbf{J}_P + \mathbf{J}_T = \mathbf{J}_A. \quad (4.101)$$

Ultimately, the choice of coupling scheme does not matter as there exists the unitary transformation using angular momentum algebra that relates one coupling scheme with another.

In the presence of a spherically symmetric short range potential, the asymptotic behavior of the radial amplitude associated to the channel c is given by:

$$\begin{aligned} u_c^{e,J_A}(R_{\text{CM}}) &\longrightarrow -\frac{1}{2i} \left[\delta_{ec} H_{L_{\text{CM}}^e \eta_e}^- (K_{\text{CM}}^e R_{\text{CM}}) - S_{ec}^{J_A} H_{L_{\text{CM}}^c \eta_c}^+ (K_{\text{CM}}^c R_{\text{CM}}) \right] \\ &= \delta_{ec} F_{L_{\text{CM}}^e \eta_e} (K_{\text{CM}}^e R_{\text{CM}}) + T_{ec}^{J_A} H_{L_{\text{CM}}^c \eta_c}^+ (K_{\text{CM}}^c R_{\text{CM}}), \end{aligned} \quad (4.102)$$

where $F_{L_{\text{CM}}^e \eta_e}$ and $H_{L_{\text{CM}}^c \eta_c}^\pm$ are the regular and outgoing/incoming Coulomb wave functions, respectively. $S_{ec}^{J_A}$ is the S -matrix element representing the scattering to the channel c with $T_{ec}^{J_A}$ the T -matrix element and they are related by:

$$T_{ec}^{J_A} = \frac{S_{ec}^{J_A} - \delta_{ec}}{2i}. \quad (4.103)$$

In a reaction, the magnetic number is to be conserved. Therefore, the physical scattering state must contain this information. Additionally, since the Schrödinger equation is a linear, a linear combination of solutions is also a solution. Moreover, light projectiles, particularly those that have four or less nucleons, can be assumed to be not excited in the reaction. Given these assumptions, the physical scattering state⁵ is:

$$|\varphi_{M_P^{\tilde{e}} M_T^{\tilde{e}}}^{\tilde{e}}\rangle = \sum_{L_{\text{CM}}^e J_P^e J_A} \frac{A_{M_P^{\tilde{e}} M_T^{\tilde{e}}}^{J_P^e(L_{\text{CM}}^e J_{\text{int}}) J_T^{\tilde{e}} J_A}}{K_{\text{CM}}^{\tilde{e}}} |\Psi_{M_P^{\tilde{e}} M_T^{\tilde{e}}}^{J_P^e(L_{\text{CM}}^e J_{\text{int}}) J_T^{\tilde{e}} J_A}\rangle, \quad (4.104)$$

where we separate the channel set of quantum number c into the set $(\tilde{c}, L_{\text{CM}}^e, J_P^e)$ and thus \tilde{c} is the set of quantum number that completely defines a target state. Moreover, we have made explicit the angular momentum coupling scheme with the superscripts.

The factors $A_{M_P^{\tilde{e}} M_T^{\tilde{e}}}^{J_P^e(L_{\text{CM}}^e J_{\text{int}}) J_T^{\tilde{e}} J_A}$ have to be chosen such that we obtain the correct asymptotic behavior for the scattering state $|\varphi_{M_P^{\tilde{e}} M_T^{\tilde{e}}}^{\tilde{e}}\rangle$. The idea is that if there was no short-range potential, we could recover the asymptotic of a Coulomb scattering. The appropriate coefficients are therefore:

$$A_{M_P^{\tilde{e}} M_T^{\tilde{e}}}^{J_P^e(L_{\text{CM}}^e J_{\text{int}}) J_T^{\tilde{e}} J_A} = \langle L_{\text{CM}}^e 0 J_{\text{int}} M_{\text{int}} | J_P^e M_P^{\tilde{e}} \rangle \langle J_P^e M_P^{\tilde{e}} J_T^e M_T^{\tilde{e}} | J_A M_A \rangle i^{L_{\text{CM}}^e} \sqrt{4\pi(2L_{\text{CM}}^e + 1)} e^{i\sigma_{L_{\text{CM}}^e}}, \quad (4.105)$$

where $\sigma_\ell = \arg[\Gamma(\ell + 1 + i\eta)]$ is the Coulomb phase shifts. The first Clebsch-Gordan coefficient in equation (4.105) contains a zero term for the projection of the CM angular momentum L_{CM}^e . This is a consequence of assuming that the incoming beam is aligned with the z -axis. This allows to use the properties like [173]:

$$\sum_\ell i^\ell \sqrt{4\pi(2\ell + 1)} e^{i\sigma_\ell} \frac{F_{\ell, \eta}(kr)}{kr} Y_0^\ell(\theta) \xrightarrow{r \rightarrow \infty} e^{i[kz + \eta \ln(k(r-z))]} + f_C(\theta) \frac{e^{i(kr - \eta \ln(2kr))}}{r}. \quad (4.106)$$

It can be shown that the scattering state defined in Eq. (4.104) using the coefficients in (4.105) gives the correct asymptotic behavior. That is to say:

$$\begin{aligned} \langle \vec{R}_{\text{CM}} | \varphi_{M_P^{\tilde{e}} M_T^{\tilde{e}}}^{\tilde{e}} \rangle &\xrightarrow{r \rightarrow \infty} e^{i[K_{\text{CM}}^{\tilde{e}} z + \eta \ln(K_{\text{CM}}^{\tilde{e}}(R_{\text{CM}} - z))]} |J_{\text{int}} M_P\rangle \otimes |\psi_{M_T}^{\tilde{e}, J_T}\rangle \\ &+ \sum_{\tilde{c} M_P^{\tilde{e}} M_T^{\tilde{e}}} f_{\tilde{c} M_P^{\tilde{e}} M_T^{\tilde{e}} \rightarrow \tilde{c} M_P^{\tilde{e}} M_T^{\tilde{e}}}(\theta, \phi) \frac{e^{i(K_{\text{CM}}^{\tilde{e}} R_{\text{CM}} - \eta \ln(2K_{\text{CM}}^{\tilde{e}} R_{\text{CM}}))}}{R_{\text{CM}}} |J_{\text{int}} M_P\rangle \otimes |\psi_{M_T}^{\tilde{e}, J_T}\rangle, \end{aligned} \quad (4.107)$$

where the scattering amplitude has the expected behavior $f_C(\theta) + f'(\theta, \phi)$ due to the inclusion of the nuclear potential:

$$\begin{aligned} f_{\tilde{c} M_P^{\tilde{e}} M_T^{\tilde{e}} \rightarrow \tilde{c} M_P^{\tilde{e}} M_T^{\tilde{e}}}(\theta, \phi) &= \delta_{\tilde{c} \tilde{c}} \delta_{M_P^{\tilde{e}} M_P^{\tilde{e}}} \delta_{M_T^{\tilde{e}} M_T^{\tilde{e}}} f_C(\theta) \\ &+ \sum_{L_{\text{CM}}^e J_P^e L_{\text{CM}}^e J_P^e J_A} \frac{C_{M_P^{\tilde{e}} M_T^{\tilde{e}} M_P^{\tilde{e}} M_T^{\tilde{e}}}^{J_P^e(L_{\text{CM}}^e J_{\text{int}}) J_T^{\tilde{e}} J_P^e(L_{\text{CM}}^e J_{\text{int}}) J_T^{\tilde{e}}}}{K_{\text{CM}}^{\tilde{e}}} T_{\tilde{c} L_{\text{CM}}^e J_P^e, \tilde{c} L_{\text{CM}}^e J_P^e}^{J_A} Y_{M_P^{\tilde{e}} + M_T^{\tilde{e}} - M_P^{\tilde{e}} - M_T^{\tilde{e}}}^{L_{\text{CM}}^e}(\theta, \phi), \end{aligned} \quad (4.108)$$

⁵This is not to be confused with a scattering solution pertaining to the complex contour in the k -plane in the Berggren basis.

where:

$$\begin{aligned}
& C_{M_P^{\tilde{e}} M_T^{\tilde{e}} M_P^{\tilde{c}} M_T^{\tilde{c}}}^{J_P^e(L_{\text{CM}}^e J_{\text{int}}) J_T^{\tilde{e}} J_P^c(L_{\text{CM}}^c J_{\text{int}}) J_T^{\tilde{c}}} \\
&= \langle L_{\text{CM}}^e 0 J_{\text{int}} M_P^{\tilde{e}} | J_P^e M_P^{\tilde{e}} \rangle \langle L_{\text{CM}}^c (M_P^{\tilde{e}} + M_T^{\tilde{e}} - M_P^{\tilde{c}} - M_T^{\tilde{c}}) J_{\text{int}} M_P^{\tilde{c}} | J_P^c (M_P^{\tilde{e}} + M_T^{\tilde{e}} - M_T^{\tilde{c}}) \rangle \\
&\times \langle J_P^e M_P^{\tilde{e}} J_T^{\tilde{e}} M_P^{\tilde{c}} | J_A (M_P^{\tilde{e}} + M_T^{\tilde{e}}) \rangle \langle J_P^c (M_P^{\tilde{e}} + M_T^{\tilde{e}} - M_T^{\tilde{c}}) | J_A (M_P^{\tilde{e}} + M_T^{\tilde{e}}) \rangle \\
&\times i^{L_{\text{CM}}^e - L_{\text{CM}}^c} \sqrt{4\pi (2L_{\text{CM}}^e + 1)} e^{i(\sigma_{L_{\text{CM}}^e} + \sigma_{L_{\text{CM}}^c})}. \tag{4.109}
\end{aligned}$$

Thus, the cross-section follows as:

$$\frac{d\sigma_{\tilde{e}M_P^{\tilde{e}}M_T^{\tilde{e}} \rightarrow \tilde{c}M_P^{\tilde{c}}M_T^{\tilde{c}}}(\theta, \phi)}{d\Omega} = \frac{K_{\text{CM}}^{\tilde{c}}}{K_{\text{CM}}^{\tilde{e}}} \left| f_{\tilde{e}M_P^{\tilde{e}}M_T^{\tilde{e}} \rightarrow \tilde{c}M_P^{\tilde{c}}M_T^{\tilde{c}}}(\theta, \phi) \right|^2. \tag{4.110}$$

However, generally a scattering process involves non-polarized beams, so the cross-section is the average of all possible random configurations of magnetic numbers:

$$\frac{d\sigma_{\tilde{e} \rightarrow \tilde{c}}(\theta, \phi)}{d\Omega} = \frac{1}{(2J_{\text{int}} + 1)(2J_T^{\tilde{e}} + 1)} \sum_{M_P^{\tilde{e}} M_T^{\tilde{e}} M_P^{\tilde{c}} M_T^{\tilde{c}}} \frac{K_{\text{CM}}^{\tilde{c}}}{K_{\text{CM}}^{\tilde{e}}} \left| f_{\tilde{e}M_P^{\tilde{e}}M_T^{\tilde{e}} \rightarrow \tilde{c}M_P^{\tilde{c}}M_T^{\tilde{c}}}(\theta, \phi) \right|^2. \tag{4.111}$$

The sum in the amplitude (4.108) goes over infinite partial waves J_A and the angular momentum L_{CM} . However, in practice one has to do truncations in the calculation of cross-sections, i.e. selecting relevant partial waves for a particular studied process. Moreover, we also truncate the maximum allowed angular momentum L_{CM} . Additionally, we are neglecting, for convenience of notation, the parity tag so that all previous formulae goes as $J_A \rightarrow J_A^\pi$.

Since we start from a SM calculation, the construction of certain partial waves may sometimes prove to be difficult due to the choice of valence space. The S-matrix elements are calculated with the equivalent potential method described in Sect. 4.7.2 and in this form is currently used for such calculations in the GSM-CC scheme. Since we know that the equivalent potential method is unstable for purely scattering states, trying to construct a partial wave with scattering states can lead to unstable results.

4.8.1 Applications of the Gamow Shell Model in coupled channels representation

The GSM-CC formalism was applied first for the description of proton scattering on ^{18}Ne [16]. Soon after, it was extended to the studies of radiative capture [17] of nucleons. These studies include the reactions $^{18}\text{Ne}(p,p)$ [16]; $^{15}\text{O}(p,p)$ and the spectra of ^{16}F and ^{16}N [174]; $^7\text{Be}(p,\gamma)^8\text{B}$ and $^7\text{Li}(n,\gamma)^8\text{Li}$ [17]; $^6\text{Li}(p,\gamma)^7\text{Be}$ and $^6\text{Li}(n,\gamma)^7\text{Li}$ [175]; $^8\text{Li}(n,\gamma)^9\text{Li}$ [176]; and $^8\text{Be}(n,\gamma)^9\text{B}$ [177]. The previously mentioned studies involve reactions with nucleon projectiles only. However, the GSM-CC formalism was extended to clusters and first tested with the elastic scattering reaction $^4\text{He}(d,d)$ [35]. The GSM-CC with clusters has been used to study the transfer reaction $^{40}\text{Ca}(d,p)^{41}\text{Ca}$ [36], which will be presented in Chap. 5. Additionally, it has been used to describe ^7Li and ^7Be and the evolution of spectroscopic factors and probability weights as a function of the distance to the emission thresholds [178]. This will be presented in both Chaps. 5 and 6. Recently, the coupled-channels version of the NCGSM has been developed and applied to study the 0_2^+ resonance of ^4He [25].

4.9 Differences with other methods

Having introduced the theory behind GSM, we can now compare it to other methods for nuclear structure described in Chap. 2. In the case of the no-core approaches and the continuum shell model approaches, focus is on the calculation of phase shifts. From the phase shifts one extracts the widths. On the contrary, in GSM-CC the focus is on the S -matrix. Additionally, the width arises naturally in the diagonalization of the Hamiltonian because of the inclusion of the Berggren basis. Moreover, in GSM-CC we do not have divergent wave functions for resonances as we can regularize them with complex scaling.

Nevertheless, the biggest difference between the GSM-CC and the no-core approaches discussed in Sect. 2.2 is the inclusion of a core. This, of course, presents advantages and disadvantages. The main advantage is that we are not bound to light systems and we can instead use heavier cores to do calculations in heavier nuclei. Of course, the disadvantage is that the effect of nucleons in the inert core is reduced to a mean field effect and the excitation energies are restricted to those below the threshold of inelastic channel corresponding to the core excitation. Another advantage is that the interaction is an effective interaction that can be fitted depending on the chosen model space. And again, paired to this is the disadvantage of not using the interaction derived from first principles. This difference is of course no longer valid for comparing SMEC and GSM-CC results. The difference here is similar to GSM as was discussed in Sect. 3.6. Hence we do not repeat the arguments related to the difference in the respective definition of OQS in both approaches.

One may notice that the coupled channels approach is very similar to the RGM [113]. However the difference between both methods lies in the calculation of the wave functions of the components of the target-projectile system. Indeed, in GSM-CC one uses Slater determinants similarly to no-core approaches to build the wave functions, whereas in RGM one constructs the wave function as a linear combination of many different basis functions, where each basis function represents a possible configuration of the nucleus. These basis functions are constructed by treating the nucleus as a collection of clusters or groups of nucleons, and then taking linear combinations of these cluster wave functions to construct the total wave function of the nucleus. This means that the RGM includes clustering in a more phenomenological manner and GSM-CC in a more mathematically rigorous manner.

Multiple mass partitions in Gamow Shell Model Coupled Channel representation

Low energy nuclear reactions are of great importance in nuclear astrophysics, particularly in the study of stellar nucleosynthesis. By examining reaction rates, scientists can gain a valuable insight into essential processes of the nucleosynthesis such as the proton-proton chain of reactions and the CNO cycle. These reactions provide a deeper understanding of the birth, evolution, and energy production of stars. Additionally, they play a vital role in unraveling the mechanisms behind supernova explosions, neutron star formation, and the synthesis of heavy elements in the Universe. Moreover, the investigation of low energy nuclear reactions enables to probe fundamental properties of the matter under extreme conditions, paving the way for conceptual advances in both nuclear physics and astrophysics.

The conventional method in reaction theory involves constructing few-body nuclear systems using uncorrelated cluster wave functions. Cross sections are then calculated by employing coupling potentials, which are directly adjusted to match experimental data. One popular framework for such calculations is the R-matrix theory, as discussed by Descouvemont and Baye [179]. In Chap. 4 we have described the GSM-CC approach for a unified description of structure and reactions. Moreover, in Chap. 2 we have discussed other approaches for a description of nuclear reactions and nuclear structure like the NCSMC and SMEC. Particularly, the ${}^7\text{Be}$ and ${}^7\text{Li}$ nuclei have been studied in the NCSMC approach [180, 181] where up to two mass partitions were studied. Unlike in the GSM-CC, these two mass partitions have not been coupled. ${}^7\text{Be}$ and ${}^7\text{Li}$ have also been studied within the GSM-CC framework [175], however this was done with one mass partition involving nucleons. Recently, ${}^8\text{Be}$ was also studied in the multiple mass partition NCSMC framework [182].

${}^7\text{Be}$ and ${}^7\text{Li}$ offer particular conditions that make them ideal candidates for pioneering studies of GSM-CC with multiple mass partitions. Unlike heavier nuclei, they have a small density of states, which means that calculations of cross-sections do not need a suppression of any important partial wave. One can see that by adding one more valence particle, the density of states around and above the proton and neutron thresholds increase significantly, like in ${}^8\text{Be}$. Moreover, we do not need to worry about core excitations, as the first excited state of ${}^4\text{He}$ is more than 20 MeV above the ground state. On the other hand, the advantage of the GSM-CC over *ab initio* approaches is the possibility to do

calculations with heavier systems because it uses an inert core approach. Hence, the calculations with several valence nucleons outside of the cores: ^{12}C , ^{16}O , ^{40}Ca , etc. are possible.

In this chapter, we present results of GSM-CC studies with the multiple mass partitions. We begin with the definition of spectroscopic factors in Sect. 5.1. In Sect. 5.2 we present the spectra of ^7Be and ^7Li and cross-sections of elastic scattering of clusters and protons. Afterwards, in Sect. 5.3, we show results for the spectrum of ^8Be . Finally, in Sect. 5.4 we present results of the deuteron transfer reaction $^{40}\text{Ca}(d,p)^{41}\text{Ca}$ and the spectra of $A = 42$ nuclei calculated with a ^{40}Ca core.

5.1 Spectroscopic factors in GSM

Experimentally, the SF is given by the proportionality coefficient between the cross-section in a single-particle model and the measured cross-section in a given channel:

$$\sigma_{nljm} = S_{nljm} \sigma_{s.p.}^{nljm}. \quad (5.1)$$

In this expression, S_{nljm} is the SF associated to the state with quantum numbers $nljm$ and $\sigma_{s.p.}^{nljm}$ is the cross-section containing all the kinetic dependence related to the transfer of the nucleon of the projectile and without the nucleon-nucleon interaction [170, 183]. To get the total cross-section σ , one sums over all quantum numbers ($nljm$)

$$\sigma = \sum_{nljm} \sigma_{nljm}. \quad (5.2)$$

The SF can be interpreted as a measure of the occupancy of a particular j -shell. The information about internucleon correlations is contained in the SF.

Theoretical calculations of SF are based on some configuration interaction approach like the SM. Usually, in standard SM calculations, one takes only one major HO shell. Such a space is incomplete, which creates a spurious basis dependence of the calculated SFs [184–188].

In SM calculations, the one-nucleon spectroscopic factor \mathcal{S}^2 is given by:

$$\mathcal{S}^2 = \frac{1}{2J_A + 1} \langle \Phi_A^{J_A} \| a_{\ell j}^\dagger \| \Phi_{A-1}^{J_{A-1}} \rangle^2. \quad (5.3)$$

$\Phi_A^{J_A}$ and $\Phi_{A-1}^{J_{A-1}}$ in this expression are the wave functions of nuclei with A and $A - 1$ nucleons, and $a_{\ell j}^\dagger$ is the creation operator related to the oscillator shell (ℓ, j) . Eq. (5.3) is approximately valid for states that are well bound, and should not be applied for near-threshold and unbound states.

A consistent definition of the theoretical SFs can be obtained in the Berggren basis, extending Eq. (5.3) to OQS. We can define the SF as the norm of the radial overlap function $I_{\ell j}(r)$ [170, 171, 183]:

$$I_{\ell j}(r) = \langle \Psi_A^{J_A} | [|\Psi_{A-1}^{J_{A-1}} \rangle \otimes | \ell, j \rangle]^{J_A}, \quad (5.4)$$

where $\Psi_A^{J_A}$ and $\Psi_{A-1}^{J_{A-1}}$ are the wave functions of nuclei with A and $A - 1$ nucleons, respectively, and $| \ell, j \rangle$ is the angular-spin part of the channel functions. The radial overlap functions can be expanded using a complete Berggren basis as:

$$I_{\ell j}(r) = \int_{\mathcal{B}} \langle \tilde{\Psi}_A^{J_A} \| a_{\ell j}^\dagger(\mathcal{B}) \| \Psi_{A-1}^{J_{A-1}} \rangle \langle r \ell j | \mathcal{B} \rangle, \quad (5.5)$$

where \mathcal{B} runs over all Berggren basis states $|\mathcal{B}\rangle$, including resonant and discretized continuum states with quantum numbers (ℓ, j) . $a_{\ell j}^\dagger(\mathcal{B})$ in Eq. (5.5) is the creation operator associated to the state $|\mathcal{B}\rangle$. Finally, the one-nucleon spectroscopic factor \mathcal{S}^2 is given by:

$$\mathcal{S}^2 = \frac{1}{2J_A + 1} \oint_{\mathcal{B}} \langle \tilde{\Psi}_A^{J_A} \| a_{\ell j}^\dagger(\mathcal{B}) \| \Psi_{A-1}^{J_{A-1}} \rangle^2. \quad (5.6)$$

Since the SF in Eq. (5.6) is defined in a complete basis, therefore it is basis independent. As such, it is useful in any regime of binding energies: for well bound states, weakly bound states or for resonances in the continuum.

In GSM-CC, the spectroscopic factor is calculated in the following way :

$$\begin{aligned} \mathcal{S}_{L_{CM}J_P}^2 &= \int_0^{+\infty} u_c(r)^2 dr \\ &+ \left[\sum_{N_{CM}} \mathcal{A}_{L_{CM}J_P}^2(N_{CM}) - \int_0^{+\infty} u_c(r)^2 dr \right]^{(\text{HO})}, \end{aligned} \quad (5.7)$$

where c is the non-orthogonalized channel associated to the L_{CM} and J_P quantum numbers (see Chap. 4), the superscript (HO) indicates that one projects wave functions on a basis of HO states, and $\mathcal{A}_{L_{CM}J_P}(N_{CM})$ is the k -particle spectroscopic amplitude :

$$\mathcal{A}_{L_{CM}J_P}(N_{CM}) = \frac{\langle \Psi_A \| A_{N_{CM}L_{CM}J_P}^\dagger \| \Psi_{A-k} \rangle}{\sqrt{2J_A + 1}}. \quad (5.8)$$

In Eq. (5.8), Ψ_A and Ψ_{A-k} are the wave functions of the systems with A and $A - k$ nucleons, respectively. J_A is the total angular momentum of the system with A nucleons, and $A_{N_{CM}L_{CM}J_P}^\dagger$ is a creation operator associated with the HO projectile basis state $|N_{CM} L_{CM} J_{\text{int}} J_P\rangle$. Integral of the $u_c(r)^2$ in Eq. (5.7) is the GSM-CC spectroscopic factor where asymptotic properties are included exactly but antisymmetry between target and projectile is neglected. As antisymmetry is localized inside the nuclear region, it is restored by adding the GSM spectroscopic factor projected in a HO basis, where antisymmetry is exactly taken into account via the use of Slater determinants, and by removing the HO projected $u_c(r)^2$ function.

One should stress that the SFs are not observables [189, 190]. On the contrary, the radial overlap function is an observable, at least its asymptotic behavior. Indeed, for a particular process $a \rightarrow b + c$, the radial overlap function I_{bc}^a in the asymptotic region is:

$$I_{bc;\ell j}^a(r) = \frac{1}{r} C_{\ell j} W_{-\eta, \ell+1/2}(2\kappa r), \quad (5.9)$$

where $W_{-\eta, \ell+1/2}$ is the Whittaker function, $C_{\ell j}$ is the asymptotic normalization coefficient (ANC), and r is the relative distance between particles b and c . In this expression:

$$\kappa = \sqrt{2\mu S_c^{(a)} / \hbar^2}, \quad (5.10)$$

where μ is the reduced mass of $b + c$ and $S_c^{(a)}$ the separation energy of particle c in the nucleus a . The ANCs being measured directly [191, 192] makes the radial overlap function an observable.

Let us consider the case that either the A -nucleus or the $(A-1)$ -nucleus is unbound. In this case the corresponding radial overlap integral is complex and its asymptotic behavior:

$$I_{ij}(r) \sim e^{\kappa r}, \quad (5.11)$$

is determined by the complex one-nucleon separation energy [39]:

$$\tilde{S}_{1n} \equiv E(A-1) - E(A) = S_{1n} - \frac{i}{2} [\Gamma(A-1) - \Gamma(A)]. \quad (5.12)$$

In this expression, $S_{1n} = \mathcal{R}e[E(A-1)] - \mathcal{R}e[E(A)]$ is the standard, real one-nucleon separation energy [38].

5.2 Description of ${}^7\text{Be}$ and ${}^7\text{Li}$

${}^7\text{Li}$ and ${}^7\text{Be}$ hold significant importance in nuclear astrophysics, particularly concerning the Big Bang Nucleosynthesis (BBN). The radiative capture reaction ${}^3\text{H}({}^4\text{He}, \gamma){}^7\text{Li}$ plays a crucial role in determining the primordial abundance of ${}^7\text{Li}$. The intriguing abundance of ${}^6\text{Li}$ and ${}^7\text{Li}$ has sparked a substantial interest within the field of nuclear astrophysics. The origin of ${}^7\text{Li}$ in hot, low-metallicity stars is believed to stem from BBN, while ${}^6\text{Li}$ is thought to originate from spallation and fusion reactions in the interstellar medium [193]. Consequently, the abundance ratio of ${}^6\text{Li}$ and ${}^7\text{Li}$ can serve as an effective time scale for stellar evolution [194].

In the determination of the fraction of branches in the pp -chain resulting in ${}^7\text{Be}$ and ${}^8\text{B}$ neutrinos, the radiative capture reaction ${}^3\text{He}({}^4\text{He}, \gamma){}^7\text{Be}$ plays a pivotal role [195, 196]. Considerable attention has been devoted to the study of reactions that can produce ${}^7\text{Be}$ in stellar environments, with particular emphasis on the ${}^6\text{Li}(p, \gamma){}^7\text{Be}$ reaction, which is essential for the removal of ${}^6\text{Li}$ and the formation of ${}^7\text{Be}$. Recent experimental investigations of this reaction have suggested a potential resonant enhancement of the ${}^6\text{Li}(p, \gamma){}^7\text{Be}$ cross section near the threshold [197].

Calculations of ${}^7\text{Be}$ and ${}^7\text{Li}$ were done using two different mass partitions. For ${}^7\text{Be}$ we use the partitions: ${}^4\text{He} + {}^3\text{He}$ and ${}^6\text{Li} + p$, which represent the two lowest particle emission threshold. Similarly, for ${}^7\text{Li}$ we use the partitions: ${}^4\text{He} + {}^3\text{H}$ and ${}^6\text{Li} + n$. The theoretical framework for the calculations of spectra and reaction cross-sections is the GSM-CC, described in Chap. 4. Both partitions are treated symmetrically in each calculation. In Sect. 5.2.1 we define our model space and in Sect. 5.2.2 we obtain an effective interaction to reproduce experimental spectra of ${}^6, {}^7\text{Li}$ and ${}^7\text{Be}$.

5.2.1 Model space for ${}^6\text{Li}$, ${}^7\text{Be}$, and ${}^7\text{Li}$

The GSM calculations of the ${}^6\text{Li}$ targets are performed using a ${}^4\text{He}$ core with two valence nucleons (one proton and one neutron). This means that the $0s_{1/2}$ HO shells are fully occupied and inert. The valence space consists of two resonant-like HO shells $0p_{3/2}$, $0p_{1/2}$ and several scattering-like subdominant HO shells in $\{s_{1/2}\}$, $\{p_{3/2}\}$, $\{p_{1/2}\}$, $\{d_{5/2}\}$, $\{d_{3/2}\}$, $\{f_{7/2}\}$, $\{f_{5/2}\}$ partial waves, with $n \in [1 : 4]$ in s, p waves and $n \in [0 : 4]$ in other partial waves. The small number of scattering-like HO states approximate the non-resonant continuum, and additionally, this approximation reduces the size of the GSM matrix. Moreover, the basis of Slater determinants is truncated by limiting the excitation energy to $8\hbar\omega$.

The internal structure of ${}^3\text{He}$ and ${}^3\text{H}$ projectiles is calculated using the N^3LO interactions [198] without the three-body contribution, fitted on phase shifts properties of proton-neutron elastic scattering reactions. The N^3LO realistic interaction is diagonalized in six HO shells to generate the intrinsic states of ${}^3\text{He}$ and ${}^3\text{H}$. The oscillator length in this calculation is $b = 1.65$ fm. With this space and oscillator length, the calculated energy of the ground state $1/2_1^+$ of ${}^3\text{He}$ is -6.35 MeV, whereas the experimental value is -7.71 MeV.

A similar discrepancy is found in ${}^3\text{H}$, where the calculated ground state $1/2_1^+$ energy is -7.14 MeV, compared to -8.48 MeV experimentally. These modifications of binding energy add no significant changes to the structure of the wave functions. In the coupled-channel equations of GSM-CC, we use the experimental binding energies of ${}^3\text{He}$, ${}^3\text{H}$ to assure correct ${}^4\text{He} + {}^3\text{He}$ and ${}^4\text{He} + {}^3\text{H}$ thresholds .

Antisymmetric eigenstates of the GSM-CC are expanded in the basis of channels: $[{}^4\text{He}(0_1^+) \otimes {}^3\text{He}(L_{\text{CM}} J_{\text{int}} J_{\text{P}})]^{J^\pi}$ and $[{}^6\text{Li}(K_i^\pi) \otimes \text{p}(\ell j)]^{J^\pi}$ for ${}^7\text{Be}$, and $[{}^4\text{He}(0_1^+) \otimes {}^3\text{H}(L_{\text{CM}} J_{\text{int}} J_{\text{P}})]^{J^\pi}$ and $[{}^6\text{Li}(K_i^\pi) \otimes \text{n}(\ell j)]^{J^\pi}$ for ${}^7\text{Li}$. Here, the considered ${}^6\text{Li}$ target states are: $K_i^\pi = 1_1^+$, 3_1^+ , 0_1^+ , 2_1^+ , 2_2^+ and 1_2^+ . Of course, the formalism discussed in Chap. 4 applies for projectiles in a single J^π states, hence we only consider the ground state $1/2_1^+$ of ${}^3\text{He}/{}^3\text{H}$.

The relative motion of the ${}^3\text{He}$ and ${}^3\text{H}$ and the ${}^4\text{He}$ target is calculated in the Berggren basis generated by proton and neutron Woods-Saxon potentials. For the clusters, this Berggren basis includes different $L_{\text{CM}} = 0, 1, 2, 3$ partial waves with 3, 3, 2, 2 pole states, respectively, which are included along with the respective contours. On the other hand, for protons and neutrons we take only the poles for the $0p_{3/2}$ and $0p_{1/2}$ shells but we include contours up to $\ell = 3$ shells. All contours consist of three segments, defined by the origin of the K_{CM} complex plane and the complex points K_{CM} : $0.2-i0.1 \text{ fm}^{-1}$, $1.0-i0.1 \text{ fm}^{-1}$ and 2 fm^{-1} . Each segment is discretized with 15 points, so that each contour possesses 45 points. All unbound pole states lie below the Berggren basis contours, so that they do not belong to the considered Berggren bases. The CM parts of ${}^3\text{He}$ and ${}^3\text{H}$ projectiles bear $L_{\text{CM}} \leq 3$, therefore the total angular momentum of ${}^3\text{He}$ and ${}^3\text{H}$ projectiles satisfies $J_{\text{P}} \leq 7/2$.

The use of two different interactions to deal with the structure of ${}^7\text{Be}$ and ${}^7\text{Li}$ and the elastic scattering of ${}^3\text{He}$ and ${}^3\text{H}$ on α -particle is necessary as we have two different pictures in the GSM-CC. Before and after the reaction occurs, cluster properties of the projectiles are prominent, whereas during the reaction, properties of the composite nuclei ${}^7\text{Be}$ and ${}^7\text{Li}$ are decisive. The FHT interaction is defined from properties of the ${}^6\text{Li}$, ${}^7\text{Be}$ and ${}^7\text{Li}$ nuclei, therefore, it cannot describe the cluster behavior of the projectiles at large distances. Conversely, the N^3LO interaction cannot be used in a core and valence particles approximation. Added to that, the N^3LO interaction generating ${}^3\text{He}$ and ${}^3\text{H}$ projectiles makes use of laboratory coordinates, which are directly replaced by COSM coordinates when building channels.

It is cumbersome to transform from laboratory to COSM coordinates and its effect is also much smaller than the other assumptions of the model, such as a restricted number of reaction channels, truncated model spaces, etc. Moreover, as the N^3LO interaction enters only the basis construction of ${}^3\text{He}$ and ${}^3\text{H}$, it is not explicitly present in the Hamiltonian but just insures that the projectiles ${}^3\text{He}$ and ${}^3\text{H}$ have correct both the wave function (binding energy) and the asymptotic behavior. This also implies that the use of both laboratory and COSM coordinates is consistent therein, as they coincide asymptotically. Indeed, cross sections are always calculated in the asymptotic region, whereby $\mathbf{r}_{\text{lab}} - \mathbf{R}_{\text{CM}}^{(\text{core})} \simeq \mathbf{r}_{\text{lab}}$ as $r_{\text{lab}} \rightarrow +\infty$ therein and $\langle R_{\text{CM}}^{(\text{core})} \rangle$ equals a few fm. As a consequence, the use of both realistic interaction for projectiles and effective Hamiltonian for composites induces no problem in the GSM-CC framework.

5.2.2 Interaction for $A=6,7$ systems

We remind ourselves that as in any other SM, we are working with an effective interaction in an effective model space. This means that we cannot directly use interactions like those of Ref. [127] (see Sec. 3.5). However, since we are working with the same core in a similar

Table 5.1: Parameters of the one-body potential for protons and neutrons optimized to describe spectra of ${}^6\text{Li}$, ${}^7\text{Be}$, ${}^7\text{Li}$ in GSM. From top to bottom: central potential depth, spin-orbit strength, radius, diffuseness and charge radius. The numbers in parentheses correspond to the statistical uncertainties given by the fitting procedure.

Parameter	Neutrons	Protons
V_0 (MeV)	52.9(0.9)	52.2(0.7)
$V_{\ell s}$ (MeV fm ²)	3.39(1.04)	3.77 (1.38)
R_0 (fm)	2.0	2.0
d (fm)	0.65	0.65
R_{ch} (fm)	–	2.5

space it can give us a fair initial point for fitting the spectra of $A = 6, 7$ nuclei. In this work, we use the optimization scheme outlined in Sect. 3.5.1.

The systems that we optimize are ${}^6\text{Li}$ (for the target), ${}^7\text{Be}$ and ${}^7\text{Li}$ (for the combined systems). The basis of channels used for a GSM-CC calculation is not complete because channels made of non-resonant continuum states of the target nucleus are not included. Nevertheless, the GSM and GSM-CC results should be similar if all relevant channels are taken into account in the GSM-CC. Moreover, for bound states, like the ground states of ${}^7\text{Be}$ and ${}^7\text{Li}$, the SM calculation in HO representation (HO-SM) is a good approximation of the GSM calculation. Therefore, the optimization of the interaction is done within a HO-SM framework. Furthermore, the matrix elements of the microscopically calculated channel-channel coupling potentials will be modified by tiny corrective factors to reproduce the experimental particle emission thresholds.

For ${}^6\text{Li}$ we take the following states: $K_i^\pi = 1_1^+, 0_1^+, 2_1^+$ and 2_2^+ . Out of all these states, the most important is the ground state 1_1^+ , because it gives the position of the one neutron and one proton thresholds for ${}^7\text{Li}$ and ${}^7\text{Be}$, respectively. We do neglect the 3_1^+ state because it is close to the deuteron emission threshold and we cannot account for deuteron correlations in a Slater determinant formulation. The remaining 0_1^+ , 2_1^+ and 2_2^+ states are fitted to obtain the correct order of states. The 1_2^+ state is excluded from the fit and its energy will be used as a check of the validity of the fitting procedure. We are not including other states as the next known state of ${}^6\text{Li}$ is the 2_1^- state with an excitation energy of 17.98 MeV, which has too large particle emission width for the HO-SM approximation to be justified.

For ${}^7\text{Li}$ and ${}^7\text{Be}$ we take the states: $J_i^\pi = 3/2_1^-, 1/2_1^-, 7/2_1^-, 5/2_1^-, 5/2_2^-, 3/2_2^-, 7/2_2^-$, and $1/2_2^-$ (${}^7\text{Li}$ only ¹). The most important states are the ground state and the first four excited states. Particularly $7/2_1^-$ and $5/2_1^-$ show up in experimental cross-sections of ${}^3\text{He}$ and ${}^3\text{H}$ scattering on ${}^4\text{He}$. Moreover, $5/2_2^-$ shows up in the elastic scattering of protons over a ${}^6\text{Li}$ target. Furthermore, the $3/2_2^-$, $7/2_2^-$, and $1/2_2^-$ (${}^7\text{Li}$ only) states are included because one risks obtaining these states too close in energy to other states, what would contaminate the calculated cross-section.

Parameters of the optimized one-body potential which imitates the effect of ${}^4\text{He}$ core on valence nucleons are shown in Tab. 5.1. Only the potential depth V_0 and the spin-orbit term $V_{\ell s}$ were fitted, whereas standard values were taken for the radius R_0 , the diffuseness d and the charge radius R_{ch} . The statistical properties of the FHT interaction parameters for p -shell nuclei have been analyzed in Ref. [127], where it has been noticed that they

¹The $1/2_2^-$ state for ${}^7\text{Be}$ has not been observed.

Table 5.2: Parameters of the FHT interaction used in this study to describe ${}^7\text{Be}$, ${}^7\text{Li}$ and ${}^8\text{Be}$ nuclei are compared to the FHT parameters reported in Ref.[127] for p -shell nuclei. The statistical uncertainties of the calculated parameters are given in parentheses.

Parameter	FHT [127]	FHT (this work)	FHT(${}^8\text{Be}$)
V_c^{11}	-3.2 (220)	13.8 (232)	11.5 (26.4)
V_c^{10}	-5.1 (10)	-5.38 (0.24)	-6.16 (0.47)
V_c^{00}	-21.3 (66)	-31.5 (145)	-12.5 (9.3)
V_c^{01}	-5.6 (5)	-5.3 (0.33)	-5.19 (0.33)
V_{LS}^{11}	-540 (1240)	-249.2 (2.7)	-202.3 (0.3)
V_T^{11}	-12.1 (795)	-11.1 (29)	-19.4 (14.2)
V_T^{10}	-14.2 (71)	-0.05 (4.7)	0.05 (6.68)

bear a sizable statistical error. Because the effective space used in Ref. [127] is different than the effective space used in our work, we expect that these two interactions will be different. Nevertheless, we find that they are rather similar.

Table 5.2 compares parameters of the FHT interaction optimized in this work with those given in Ref.[127]. One can see that the parameters of the interaction obtained in the present optimization agree with those of Ref.[127] within the statistical errors.

5.2.3 Spectra of ${}^7\text{Be}$ and ${}^7\text{Li}$

The lowest particle emission thresholds in ${}^7\text{Be}$ and ${}^7\text{Li}$ are ${}^4\text{He} + {}^3\text{He}$ and ${}^4\text{He} + {}^3\text{H}$, respectively. Therefore, the description of low-energy states in ${}^7\text{Be}$ and ${}^7\text{Li}$ requires the inclusion of the coupling to ${}^3\text{He}$ and ${}^3\text{H}$ continua in ${}^7\text{Be}$ and ${}^7\text{Li}$, respectively. In this section, we shall discuss the spectra of mirror nuclei ${}^7\text{Be}$ and ${}^7\text{Li}$ in the channel basis comprising $[{}^4\text{He}(0_1^+) \otimes {}^3\text{He}(L_{\text{CM}} J_{\text{int}} J_{\text{P}})]^{J^\pi}$, $[{}^6\text{Li}(K_i^\pi) \otimes p(\ell j)]^{J^\pi}$ in ${}^7\text{Be}$, and $[{}^4\text{He}(0_1^+) \otimes {}^3\text{H}(L_{\text{CM}} J_{\text{int}} J_{\text{P}})]^{J^\pi}$, $[{}^6\text{Li}(K_i^\pi) \otimes n(\ell j)]^{J^\pi}$ in ${}^7\text{Li}$.

Figure 5.1 shows the GSM spectrum of ${}^6\text{Li}$ and the GSM-CC spectrum of ${}^7\text{Li}$ and ${}^7\text{Be}$. Wave functions of ${}^6\text{Li}$ states shown in this figure are used to build channel states in ${}^7\text{Li}$ and ${}^7\text{Be}$. To correct for missing channels in the model space, the matrix elements of the channel-channel coupling potentials involving nucleon-projectile channels have been multiplied by the tiny real factors $c(J^\pi)$ for $3/2_1^-$, $1/2_1^-$, $7/2_1^-$, and $5/2_2^-$ states. These scaling factors are: $c(3/2^-) = 1.0092$, $c(1/2^-) = 1.0156$, $c(7/2^-) = 1.0173$, $c(5/2^-) = 0.9955$.

The agreement with experimental data for resonance energies is excellent. The calculated widths are smaller than found experimentally. One may notice a change in the order of higher lying levels $1/2_2^-$, $3/2_2^-$, $7/2_2^-$ between ${}^7\text{Be}$ and ${}^7\text{Li}$ due to different threshold energies and Coulomb energies. All energies of the states are given relative to the energy of ${}^4\text{He}$ core. Calculated particle emission thresholds: ${}^4\text{He} + {}^3\text{He}$ and ${}^6\text{Li} + p$ in ${}^7\text{Be}$ and ${}^4\text{He} + {}^3\text{H}$ and ${}^6\text{Li} + n$ in ${}^7\text{Li}$, are corrected in the coupled-channel equations so that the threshold energies correspond exactly to the experimental values.

The channels $[{}^6\text{Li}(K_i^\pi) \otimes p(\ell j)]^{J^\pi}$ ($[{}^6\text{Li}(K_i^\pi) \otimes n(\ell j)]^{J^\pi}$) in ${}^7\text{Be}$ (${}^7\text{Li}$), are built by coupling the ${}^6\text{Li}$ wave functions with $K_i^\pi = 1_1^+$, 1_2^+ , 3_1^+ , 0_1^+ , 2_1^+ , 2_2^+ with the proton (neutron) wave functions in the partial waves ℓj : $s_{1/2}$, $p_{1/2}$, $p_{3/2}$, $d_{3/2}$, $d_{5/2}$, $f_{5/2}$, $f_{7/2}$. The cluster channels $[{}^4\text{He}(0_1^+) \otimes {}^3\text{He}(L_{\text{CM}} J_{\text{int}} J_{\text{P}})]^{J^\pi}$ ($[{}^4\text{He}(0_1^+) \otimes {}^3\text{H}(L_{\text{CM}} J_{\text{int}} J_{\text{P}})]^{J^\pi}$) are constructed by coupling ${}^3\text{He}$ (${}^3\text{H}$) wave function in partial waves: ${}^2S_{1/2}$, ${}^2P_{1/2}$, ${}^2P_{3/2}$, ${}^2D_{3/2}$, ${}^2D_{5/2}$, ${}^2F_{5/2}$, ${}^2F_{7/2}$, with the inert ${}^4\text{He}$ core in $J_i^\pi = 0_1^+$ state. Detailed information about the wave functions of low-energy ${}^7\text{Be}$ and ${}^7\text{Li}$ states can be seen in Tabs. 5.3, 5.4.

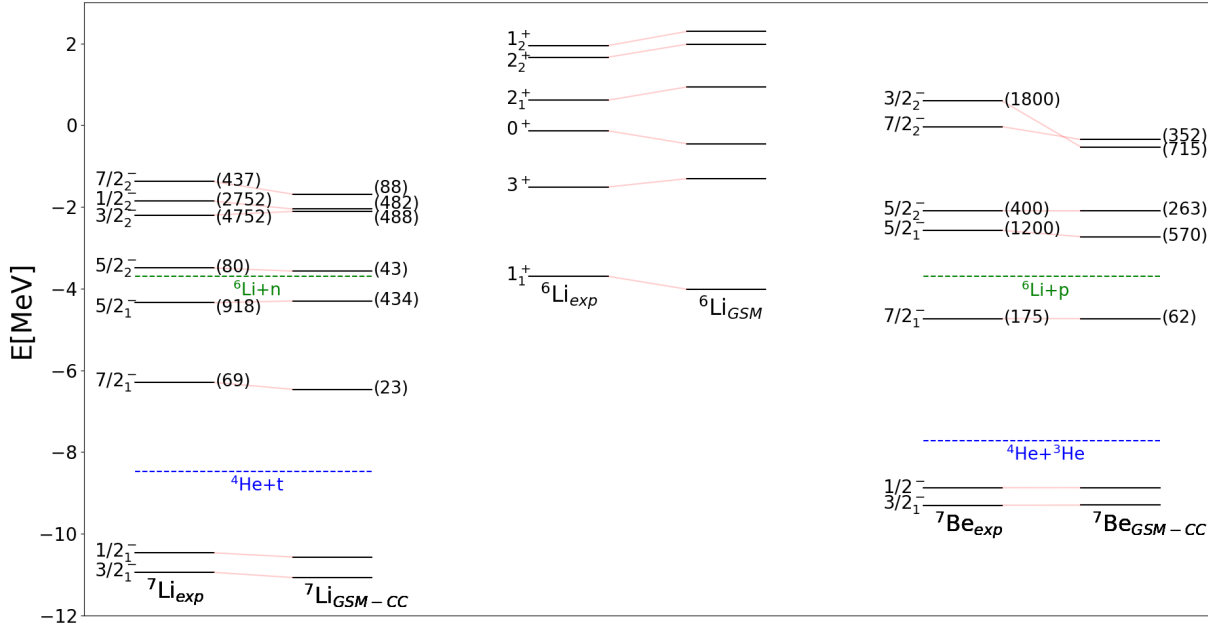


Figure 5.1: (Color online) The calculated energy spectra of ${}^6,{}^7\text{Li}$ and ${}^7\text{Be}$, are compared with experimental data [199]. ${}^7\text{Li}$ and ${}^7\text{Be}$ are calculated in GSM-CC using the channel basis with two mass partitions: ${}^4\text{He} + {}^3\text{He}$, ${}^6\text{Li} + \text{p}$ and ${}^4\text{He} + {}^3\text{H}$, ${}^6\text{Li} + \text{n}$, respectively. The spectrum of ${}^6\text{Li}$ is calculated in GSM and wave functions are expanded in the HO basis. Numbers in the brackets indicate the resonance width in keV.

Fig. 5.2 shows the information about proton and ${}^3\text{He}$ channels in ${}^7\text{Be}$. As it can be deduced from Tab. 5.3, the mirror system ${}^7\text{Li}$ shares a very similar channel decomposition of the states as seen in ${}^7\text{Be}$. The definition of orthogonal channel probability weights is given by:

$$\langle \Psi | \Psi \rangle = \sum_c |\langle w_c | w_c \rangle|^2 = \sum_c b_c^2 = 1 + 0i. \quad (5.13)$$

The sum over all channels of the real parts of channel weights $\mathcal{R}e[b_c^2]$ is normalized to 1, whereas the sum of imaginary parts $\mathcal{I}m[b_c^2]$ is equal to 0. Additional information is provided by the spectroscopic factors \mathcal{S}^2 and by the occupancies of single-particle shells for dominant configurations in the considered states (see Tab. 5.4).

Major amplitudes of channels $[{}^4\text{He}(0_1^+) \otimes {}^3\text{He}(L_{\text{CM}} J_{\text{int}} J_{\text{P}})]^{J^\pi}$, $[{}^6\text{Li}(K_i^\pi) \otimes \text{p}(\ell_j)]^{J^\pi}$ in ${}^7\text{Be}$ are given in Tab. 5.3. A significant probability of the channel wave function $[{}^4\text{He}(0_1^+) \otimes {}^3\text{He}(L_{\text{CM}} J_{\text{int}} J_{\text{P}})]^{J^\pi}$ is seen only in low-energy states: $J_i^\pi = 3/2_1^-, 1/2_1^-, 7/2_1^-, 5/2_1^-$, which are close to the ${}^4\text{He} + {}^3\text{He}$ threshold. In higher lying states, the probability of this cluster channel drops below 1%.

The ground state $3/2_1^-$ and the first excited state $1/2_1^-$ are influenced mainly by the channels $[{}^4\text{He}(0_1^+) \otimes {}^3\text{He}(L_{\text{CM}} J_{\text{int}} J_{\text{P}})]^{J^\pi}$ and $[{}^6\text{Li}(1_1^+) \otimes \text{p}(p_{1/2})]^{J^\pi}$. In the $7/2_1^-$ resonance, the dominant contribution to the resonance wave function comes from the closed proton channels: $[{}^6\text{Li}(3_1^+) \otimes \text{p}(p_{3/2,1/2})]^{7/2^-}$, $[{}^6\text{Li}(2_2^+) \otimes \text{p}(p_{3/2})]^{7/2^-}$, and the open ${}^3\text{He}$ channel: $[{}^4\text{He}(0_1^+) \otimes {}^3\text{He}(2F_{7/2})]^{7/2^-}$.

The $5/2_1^-$ resonance has still a significant component of the open channel $[{}^4\text{He}(0_1^+) \otimes {}^3\text{He}(2F_{5/2})]^{5/2^-}$. However, the dominant contribution in the wave function of this resonance comes from the closed proton channels: $[{}^6\text{Li}(2_1^+) \otimes \text{p}(p_{3/2,1/2})]^{5/2^-}$, $[{}^6\text{Li}(1_2^+) \otimes \text{p}(p_{3/2})]^{5/2^-}$. The contribution of the open proton channel $[{}^6\text{Li}(1_1^+) \otimes \text{p}(p_{3/2})]^{5/2^-}$ amounts to about 2%.

Table 5.3: Major GSM-CC probabilities of channels $[{}^6\text{Li}(K_i^\pi) \otimes \text{p}(\ell j)]^{J^\pi}$ and $[{}^4\text{He}(0_1^+) \otimes {}^3\text{He}(L_{\text{CM}} J_{\text{int}} J_{\text{P}})]^{J^\pi}$ for ${}^7\text{Be}$, and $[{}^6\text{Li}(K_i^\pi) \otimes \text{n}(\ell j)]^{J^\pi}$ and $[{}^4\text{He}(0_1^+) \otimes {}^3\text{H}(L_{\text{CM}} J_{\text{int}} J_{\text{P}})]^{J^\pi}$ for ${}^7\text{Li}$. $\mathcal{Re}[b_c^2]$ denotes the real part of the channel probability $\langle \tilde{w}_c | w_c \rangle^2$. \mathcal{S}^2 corresponds to the GSM-CC spectroscopic factor. The imaginary parts smaller than 0.01 have been suppressed.

${}^7\text{Be}; J^\pi$	${}^6\text{Li}; K^\pi$	${}^3\text{He}$	p	$\mathcal{Re}[b_c^2]$	\mathcal{S}^2	${}^7\text{Li}; J^\pi$	${}^6\text{Li}; K^\pi$	${}^3\text{H}$	p	$\mathcal{Re}[b_c^2]$	\mathcal{S}^2
$3/2_1^-$	${}^2P_{3/2}$			0.31	0.04	$3/2_1^-$	${}^2P_{3/2}$			0.28	0.04
		1_1^+	$p_{3/2}$	0.22	0.43			1_1^+	$p_{3/2}$	0.23	0.44
		1_1^+	$p_{1/2}$	0.10	0.20			1_1^+	$p_{1/2}$	0.11	0.22
		3_1^+	$p_{3/2}$	0.18	0.41			3_1^+	$p_{3/2}$	0.18	0.43
		0_1^+	$p_{3/2}$	0.10	0.22			0_1^+	$p_{3/2}$	0.10	0.22
		2_1^+	$p_{1/2}$	0.02	0.05			2_1^+	$p_{1/2}$	0.03	0.08
		2_2^+	$p_{3/2}$	0.03	0.07			2_2^+	$p_{3/2}$	0.03	0.07
		2_2^+	$p_{1/2}$	0.03	0.08			2_2^+	$p_{1/2}$	0.02	0.07
$1/2_1^-$	${}^2P_{1/2}$			0.33	0.04	$1/2_1^-$	${}^2P_{1/2}$			0.31	0.03
		1_1^+	$p_{3/2}$	0.31	0.64			1_1^+	$p_{3/2}$	0.33	0.67
		1_1^+	$p_{1/2}$	0.06	0.05			1_1^+	$p_{1/2}$	0.03	0.06
		0_1^+	$p_{1/2}$	0.07	0.17			0_1^+	$p_{1/2}$	0.08	0.19
		2_1^+	$p_{3/2}$	0.12	0.27			2_1^+	$p_{3/2}$	0.11	0.23
		2_2^+	$p_{3/2}$	0.06	0.14			2_2^+	$p_{3/2}$	0.08	0.19
		1_2^+	$p_{1/2}$	0.06	0.12			1_2^+	$p_{1/2}$	0.06	0.13
$7/2_1^-$	${}^2F_{7/2}$			0.22	0.03+0.02i	$7/2_1^-$	${}^2F_{7/2}$			0.21	0.03+0.01i
		3_1^+	$p_{3/2}$	0.33	0.70			3_1^+	$p_{3/2}$	0.32	0.68
		3_1^+	$p_{1/2}$	0.18	0.37			3_1^+	$p_{1/2}$	0.19	0.40
		2_1^+	$p_{3/2}$	0.07	0.16			2_1^+	$p_{3/2}$	0.11	0.23
		2_2^+	$p_{3/2}$	0.19	0.43			2_2^+	$p_{3/2}$	0.17	0.38
$5/2_1^-$	${}^2F_{5/2}$			0.24	-0.15+0.06i	$5/2_1^-$	${}^2F_{5/2}$			0.26	-0.09+0.08i
		1_1^+	$p_{3/2}$	0.02	0.02-0.02i			1_1^+	$p_{3/2}$	0.01	0.01-0.02i
		3_1^+	$p_{3/2}$	0.05	0.11-0.07i			3_1^+	$p_{3/2}$	0.05	0.11-0.04i
		2_1^+	$p_{3/2}$	0.22	0.45-0.11i			2_1^+	$p_{3/2}$	0.19	0.40-0.08i
		2_1^+	$p_{1/2}$	0.09	0.19-0.06i			2_1^+	$p_{1/2}$	0.08	0.14-0.03i
		2_2^+	$p_{3/2}$	0.05	0.09-0.04i			2_2^+	$p_{3/2}$	0.07	0.13-0.04i
		2_2^+	$p_{1/2}$	0.10	0.23-0.06i			2_2^+	$p_{1/2}$	0.11	0.27-0.06i
		1_2^+	$p_{3/2}$	0.23	0.47-0.12i			1_2^+	$p_{3/2}$	0.23	0.47-0.10i
$5/2_2^-$	${}^2F_{5/2}$			0.01	-0.01+0.01i	$5/2_2^-$	${}^2F_{5/2}$			0.01	-0.004+0.006i
		1_1^+	$p_{3/2}$	0.46	0.61+0.06i			1_1^+	$p_{3/2}$	0.54	0.67+0.04i
		3_1^+	$p_{3/2}$	0.18	0.27+0.02i			3_1^+	$p_{3/2}$	0.15	0.24+0.01i
		3_1^+	$p_{1/2}$	0.27	0.40-0.04i			3_1^+	$p_{1/2}$	0.25	0.37-0.04i
		2_1^+	$p_{3/2}$	0.06	0.10-0.07i			2_1^+	$p_{3/2}$	0.05	0.08-0.05i
		2_2^+	$p_{3/2}$	0.01	0.03+0.01i			2_2^+	$p_{3/2}$	0.01	0.02+0.01i
		2_2^+	$p_{1/2}$	0.01	0.03-0.03i			2_2^+	$p_{1/2}$	0.01	0.02-0.02i
$3/2_2^-$	${}^2P_{3/2}$			0.12	0.16+0.02i	$3/2_2^-$	${}^2P_{3/2}$			0.13	0.17+0.02i
		1_1^+	$p_{1/2}$	0.35	0.46+0.01i			1_1^+	$p_{1/2}$	0.35	0.46+0.02i
		3_1^+	$p_{3/2}$	0.04	0.05+0.02i			3_1^+	$p_{3/2}$	0.04	0.05
		2_1^+	$p_{3/2}$	0.28	0.42-0.05i			2_1^+	$p_{3/2}$	0.27	0.41-0.06i
		2_1^+	$p_{1/2}$	0.09	0.14-0.01i			2_1^+	$p_{1/2}$	0.09	0.15-0.02i
		1_2^+	$p_{3/2}$	0.12	0.18-0.03i			1_2^+	$p_{3/2}$	0.10	0.16-0.03i
		1_2^+	$p_{1/2}$	0.01	0.02			1_2^+	$p_{1/2}$	0.01	0.01
		1_2^+	$p_{3/2}$	0.02	0.03+0.01i			1_2^+	$p_{3/2}$	0.03	0.03+0.01i
$1/2_2^-$	${}^2P_{1/2}$			0.45	0.61+0.02i	$1/2_2^-$	${}^2P_{1/2}$			0.46	0.60+0.04i
		1_1^+	$p_{1/2}$	0.45	0.61+0.02i			1_1^+	$p_{1/2}$	0.46	0.60+0.04i
		2_1^+	$p_{3/2}$	0.11	0.16			2_1^+	$p_{3/2}$	0.11	0.17-0.01i
		1_2^+	$p_{3/2}$	0.39	0.60-0.07i			1_2^+	$p_{3/2}$	0.37	0.59-0.08i
		1_2^+	$p_{1/2}$	0.02	0.03			1_2^+	$p_{1/2}$	0.02	0.04-0.01i
$7/2_2^-$	${}^2F_{7/2}$			0.45	0.61+0.05i	$7/2_2^-$	${}^2F_{7/2}$			0.48	0.66+0.06i
		3_1^+	$p_{1/2}$	0.40	0.53-0.06i			3_1^+	$p_{1/2}$	0.36	0.50-0.04i
		2_1^+	$p_{3/2}$	0.16	0.23-0.07i			2_1^+	$p_{3/2}$	0.16	0.24-0.02i
		2_2^+	$p_{3/2}$	0.01	0.001+0.003i			2_2^+	$p_{3/2}$	0.01	0.01+0.01i

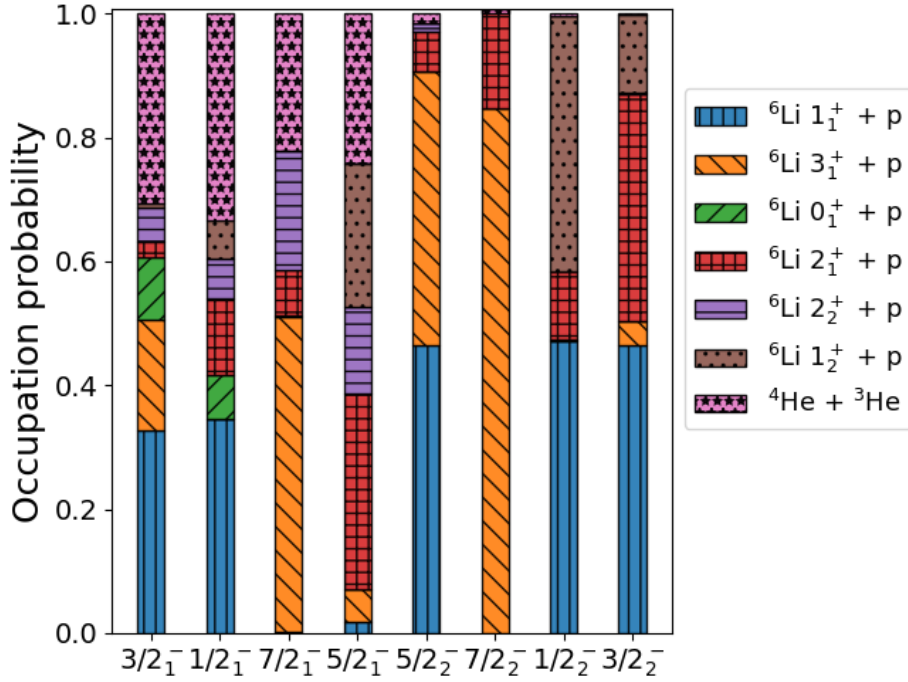


Figure 5.2: The channel decomposition for selected states of ${}^7\text{Be}$. In different colors, we show the summed GSM-CC probabilities of p and ${}^3\text{He}$ channels. Detailed information about major GSM-CC channel probabilities and spectroscopic factors in individual states of ${}^7\text{Be}$ can be found in Tab. 5.3. Information about the number of protons and neutrons in different shells is given in Tab. 5.4.

The close lying $5/2_2^-$ resonance has a completely different structure than the $5/2_1^-$ resonance. The amplitude of ${}^3\text{He}$ channel: $[{}^4\text{He}(0_1^+) \otimes {}^3\text{He}(2F_{5/2})]^{5/2^-}$, is close to 1% and the wave function is influenced mainly by the open proton channel: $[{}^6\text{Li}(1_1^+) \otimes p(p_{3/2})]^{5/2^-}$, and the closed proton channels: $[{}^6\text{Li}(3_1^+) \otimes p(p_{3/2,1/2})]^{5/2^-}$. Hence, we predict that $5/2_1^-$ resonance is excited mainly in ${}^4\text{He} + {}^3\text{He}$ reaction and decays mostly by the emission of ${}^3\text{He}$, whereas $5/2_2^-$ resonance is excited mainly in ${}^6\text{Li} + p$ reaction and decays predominantly by the proton emission.

In the $7/2_2^-$ resonance, the summed probability of $[{}^6\text{Li}(3_1^+) \otimes p(p_{3/2,1/2})]^{7/2^-}$ channels is 85% and the weight of the cluster channel $[{}^4\text{He}(0_1^+) \otimes {}^3\text{He}(2F_{7/2})]^{7/2^-}$ is negligible. In the resonances $3/2_2^-$ and $1/2_2^-$, the channels $[{}^6\text{Li}(1_1^+) \otimes p(p_{3/2,1/2})]^{J^\pi}$ dominate with a summed probability of 47%. Slightly smaller contributions come from the channels $[{}^6\text{Li}(1_2^+) \otimes p(p_{3/2,1/2})]^{1/2^-}$, $[{}^6\text{Li}(2_1^+) \otimes p(p_{3/2,1/2})]^{3/2^-}$ for $1/2_2^-$ and $3/2_2^-$, respectively. Other channel wave functions, including the $[{}^4\text{He}(0_1^+) \otimes {}^3\text{He}(L_{\text{CM}} J_{\text{int}} J_{\text{P}})]^{J^\pi}$ channel, have a negligible weight in these states.

Major amplitudes of the channels $[{}^4\text{He}(0_1^+) \otimes {}^3\text{H}(L_{\text{CM}} J_{\text{int}} J_{\text{P}})]^{J^\pi}$ and $[{}^6\text{Li}(K_i^\pi) \otimes n(\ell j)]^{J^\pi}$ in ${}^7\text{Li}$ can be found in Tab. 5.3. As in ${}^7\text{Be}$, a significant probability of the channel wave function $[{}^4\text{He}(0_1^+) \otimes {}^3\text{H}(L_{\text{CM}} J_{\text{int}} J_{\text{P}})]^{J^\pi}$ is seen only in the low-energy states: $J_i^\pi = 3/2_1^-, 1/2_1^-, 7/2_1^-, 5/2_1^-$, which are close to the ${}^4\text{He} + {}^3\text{H}$ threshold. At higher excitation energies, the probability of the $[{}^4\text{He}(0_1^+) \otimes {}^3\text{H}(L_{\text{CM}} J_{\text{int}} J_{\text{P}})]^{J^\pi}$ channel diminishes rapidly below 1%.

In general, mirror symmetry between low-energy wave functions in ${}^7\text{Be}$ and ${}^7\text{Li}$ is satisfied very well. Major probabilities are close in higher energy resonances $3/2_2^-$, $5/2_2^-$, and $7/2_2^-$ states. For example, the probability of channels: $[{}^6\text{Li}(1_1^+) \otimes p(p_{3/2})]^{5/2^-}$ and $[{}^6\text{Li}(3_1^+) \otimes p(p_{3/2,1/2})]^{5/2^-}$ in ${}^7\text{Be}$ are 0.46 and 0.45, respectively, whereas the mirror channels

Table 5.4: Number of protons (neutrons) in resonant shells: $\ell = 1$ (p) and non-resonant shells of the scattering continuum: $\ell = 0$ ({s}), $\ell = 1$ ({p}), $\ell = 2$ ({d}) are shown for the largest configurations in different GSM eigenfunctions of ${}^7\text{Be}$ (${}^7\text{Li}$). $\mathcal{R}e[a_c^2]$ denote real parts of the studied squared configuration amplitudes. Only occupancies higher than 5% are shown.

	J^π	p	{p}	{d}	{s}	$\mathcal{R}e[a_c^2]$		J^π	p	{p}	{d}	{s}	$\mathcal{R}e[a_c^2]$
${}^7\text{Be}$	$3/2_1^-$	2p1n	0	0	0	0.83	${}^7\text{Li}$	$3/2_1^-$	1p2n	0	0	0	0.83
		1p	0	1p1n	0	0.06			1p	0	1p1n	0	0.07
	$1/2_1^-$	2p1n	0	0	0	0.82		$1/2_1^-$	1p2n	0	0	0	0.83
	$7/2_1^-$	2p1n	0	0	0	0.84		$7/2_1^-$	1p2n	0	0	0	0.85
	$5/2_1^-$	2p1n	0	0	0	0.83		$5/2_1^-$	1p2n	0	0	0	0.83
	$5/2_2^-$	2p1n	0	0	0	0.77		$5/2_2^-$	2p1n	0	0	0	0.78
		1p1n	1p	0	0	0.09			1p1n	1n	0	0	0.09
		1p	0	1p1n	0	0.05			1n	0	1p1n	0	0.06
	$3/2_2^-$	2p1n	0	0	0	0.75		$3/2_2^-$	1p2n	0	0	0	0.76
		1p1n	1p	0	0	0.12			1p1n	1n	0	0	0.11
		1p	0	1p1n	0	0.05			1n	0	1p1n	0	0.05
	$1/2_2^-$	2p1n	0	0	0	0.75		$1/2_2^-$	1p2n	0	0	0	0.77
		1p1n	1p	0	0	0.11			1n	0	1p1n	0	0.05
		1p	0	1p1n	0	0.06			1n	0	1p1n	0	0.05
	$7/2_2^-$	2p1n	0	0	0	0.77		$7/2_2^-$	1p2n	0	0	0	0.78
1p1n		1p	0	0	0.13	1p1n	1n		0	0	0.11		

in ${}^7\text{Li}$ have the weights 0.54 and 0.40.

Occupancies of single-particle shells in the GSM wave functions of ${}^7\text{Be}$ and ${}^7\text{Li}$ are very similar in all considered many-body states. The probability of occupying the scattering continuum shells in ${}^7\text{Be}$ and ${}^7\text{Li}$ is small and does not exceed 15% (see Tab. 5.4). However, even in low-lying states: $J_i^\pi = 3/2_1^-, 1/2_1^-, 7/2_1^-, 5/2_1^-$, the occupation of shells in the scattering continuum, i.e. the complement of the resonant-shell probability (proton only in Tab. 5.4), amounts to about 17% and increases to $\sim 25\%$ for higher lying states.

Table 5.3 shows also the real part of GSM spectroscopic factors for different states of ${}^7\text{Be}$ and ${}^6\text{Li}$. One may notice a good qualitative agreement between the real part of the one-proton channel weights and their corresponding SFs, i.e. large probabilities of channels: $[{}^6\text{Li}(K_i^\pi) \otimes \text{p}(\ell j)]^{J^\pi}$, are closely related with the large SFs: ${}^7\text{Be}(J^\pi) \rightarrow \text{p}(\ell j) \oplus {}^6\text{Li}(K_i^\pi)$. Similarly for ${}^7\text{Li}$, there is a close qualitative relation between the magnitude of the channel amplitudes: $[{}^6\text{Li}(K_i^\pi) \otimes \text{n}(\ell j)]^{J^\pi}$ and SFs: ${}^7\text{Li}(J^\pi) \rightarrow \text{n}(\ell j) \oplus {}^6\text{Li}(K_i^\pi)$. Hence the channel amplitudes and the SFs, both independent of the choice of the single-particle basis, provide useful information about the structure of many-body states. One may also notice the negative SFs for the cluster wave functions. These require a different analysis to give an interpretation and will be discussed in Chap. 6.

5.2.4 Reaction cross-sections involving ${}^7\text{Be}$ and ${}^7\text{Li}$ as composite systems

In this section, we shall discuss the reaction cross-sections ${}^4\text{He}({}^3\text{He}, {}^3\text{He})$, ${}^4\text{He}({}^3\text{H}, {}^3\text{H})$, and ${}^6\text{Li}(\text{p}, \text{p})$. The GSM-CC cross sections are calculated by coupling the real-energy incoming partial waves to the states of ${}^4\text{He}$ or ${}^6\text{Li}$ given by the Hermitian Hamiltonian. GSM-CC calculations are performed using COSM coordinates [126] but the reaction cross sections will be expressed in the CM reference frame. The initial en-

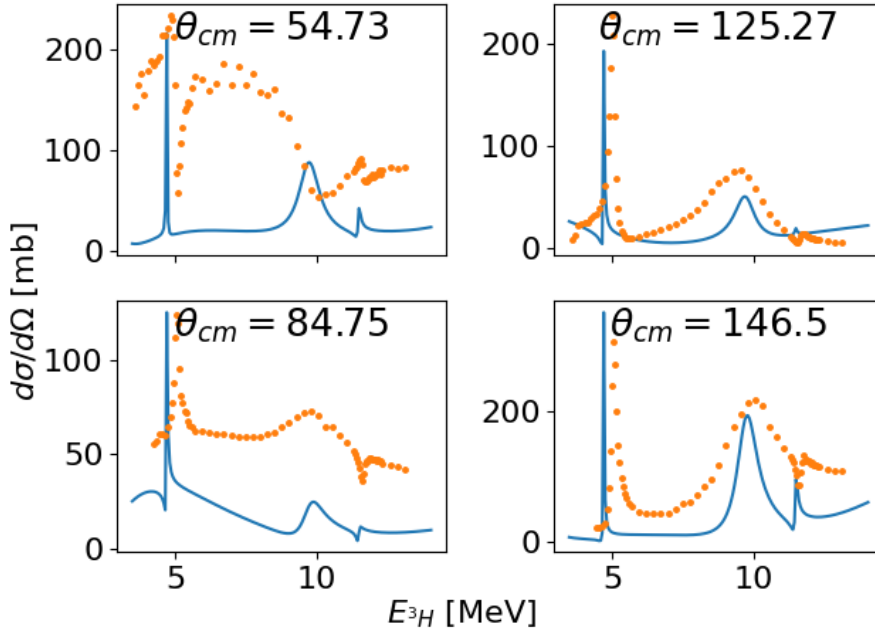


Figure 5.3: (Color online) The GSM-CC elastic differential cross sections of the reaction ${}^4\text{He}({}^3\text{H}, {}^3\text{H}){}^4\text{He}$, calculated at four different CM angles, are compared with the experimental data (in dots) [199]. ${}^3\text{H}$ bombarding energy is given in the laboratory frame.

ergy is $E^{(\text{COSM})} = E_{\text{proj}}^{(\text{COSM})} + E_{\text{T}}^{(\text{COSM})}$, where $E^{(\text{COSM})}$, $E_{\text{proj}}^{(\text{COSM})}$, and $E_{\text{T}}^{(\text{COSM})}$ are the total energy, the projectile energy, and the GSM target binding energy, respectively. One has $E_{\text{proj}}^{(\text{lab})} \simeq 1.25 E_{\text{proj}}^{(\text{COSM})}$ for ${}^4\text{He}({}^3\text{H}, {}^3\text{H}){}^4\text{He}$ and ${}^4\text{He}({}^3\text{He}, {}^3\text{He}){}^4\text{He}$ reactions and $E_{\text{proj}}^{(\text{c.m.})} \simeq 1.07 E_{\text{proj}}^{(\text{COSM})}$ for the ${}^6\text{Li}(\text{p}, \text{p}){}^6\text{Li}$ reaction [15].

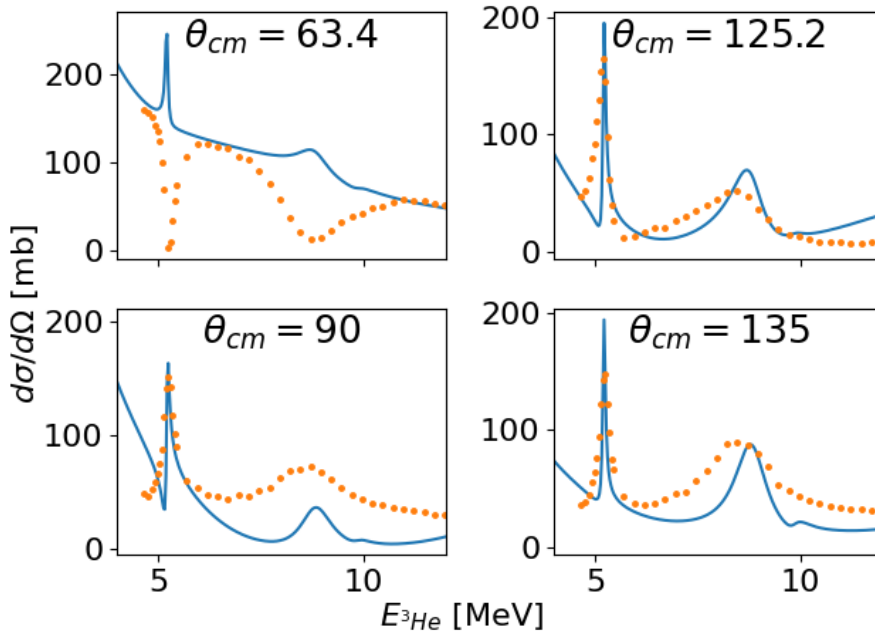


Figure 5.4: The same as in Fig. 5.3 but for the reaction ${}^4\text{He}({}^3\text{He}, {}^3\text{He}){}^4\text{He}$. Experimental data (in dots) are from Ref.[199].

Figure 5.3 shows the ${}^4\text{He}({}^3\text{H}, {}^3\text{H}){}^4\text{He}$ differential cross section calculated in GSM-CC (solid line). Triton bombarding energy is given in the laboratory frame. The calculation is performed using the same Hamiltonian and the same model space as used in the calculation of the spectra of ${}^6, {}^7\text{Li}$. ${}^3\text{H}$ energies in Fig. 5.3 are in the CM reference frame. The estimated error on experimental results varies with the ${}^3\text{H}$ bombarding energy and amounts to about 10% [199]. Peaks in the calculated cross section correspond to $7/2_1^-$, $5/2_1^-$, and $5/2_2^-$ resonances (see Fig. 5.1). The agreement between theory and experiment is satisfactory at backward angles whereas at forward angles the GSM-CC approach underestimates experimental cross-sections.

Similarly, Fig. 5.4 shows the ${}^4\text{He}({}^3\text{He}, {}^3\text{He}){}^4\text{He}$ elastic differential cross section calculated in GSM-CC (solid line) at different CM angles. The GSM-CC cross section provides a good description of experimental cross-sections at large angles. At $\Theta_{\text{CM}} \leq 90$ deg, the calculated cross sections underestimate the experimental ones. The situation seems to be similar to the analogous reaction ${}^4\text{He}({}^3\text{H}, {}^3\text{H}){}^4\text{He}$. However there is a subtle difference in the $5/2_2^-$ peak. Indeed, in the reaction with the triton projectile the peak is more pronounced than with a ${}^3\text{He}$ analogue peak. This agrees with what is observed in experimental data. The discrepancies observed at low angles may be attributed to the absence of cancelations arising from missing partial waves.

Figure 5.5 shows the proton elastic differential cross section ${}^6\text{Li}(p, p){}^6\text{Li}$ calculated in GSM-CC (solid line) at different CM angles. The reproduction of the experimental data is decent. The width of the $5/2_2^-$ state is narrower than observed experimentally. The $5/2_1^-$ state does not show up in the proton scattering cross-section. This correlates with the small probability of the $[{}^6\text{Li}(1_1^+) \otimes p(p_{3/2})]^{5/2^-}$ channel in the spectrum calculations.

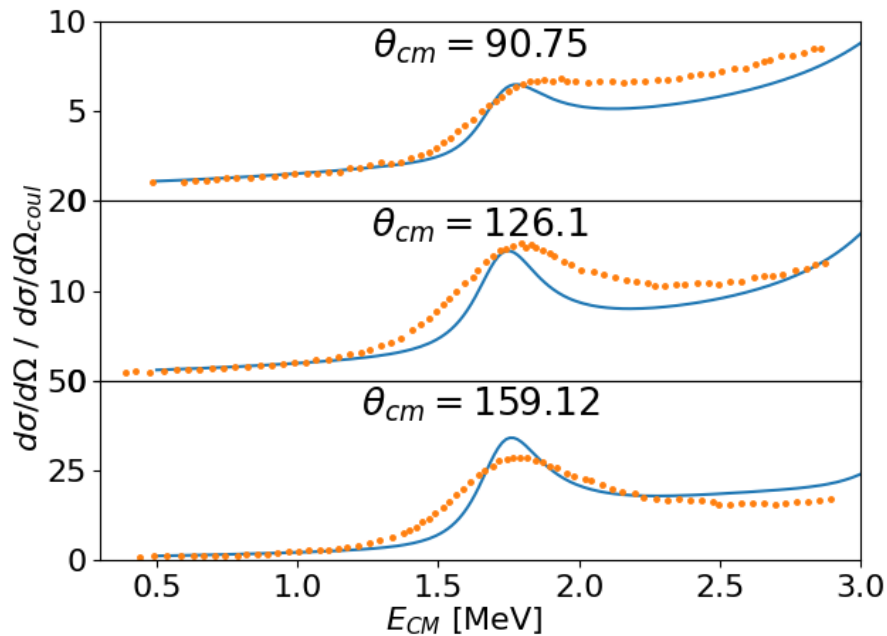


Figure 5.5: The GSM-CC elastic differential cross sections of the reaction ${}^6\text{Li}(p, p){}^6\text{Li}$ at three different CM angles are plotted as a function of proton energy and compared with experimental data (in dots) [200]. Proton bombarding energy is given in the c.m. frame. Both GSM-CC and experimental cross sections are divided by the Rutherford cross section.

5.3 Description of ^8Be

The ^8Be nucleus plays a crucial role in the He-burning process, particularly in the formation of the Hoyle state in ^{12}C , which ultimately leads to the production of ^{16}O . A fundamental aspect underlying the production of ^{12}C , ^{16}O , and heavier elements through the He-burning process is the presence of α -clustering, which consistently emerges near the threshold for α -cluster decay in these nuclei. The α -clustering phenomenon plays a key role in understanding the synthesis of these elements.

The lowest particle emission threshold in ^8Be is $^4\text{He} + ^4\text{He}$. Hence, the description of low-energy states in ^8Be demands the inclusion of the coupling to ^4He continuum. In addition, we use the partitions: $^7\text{Be} + \text{n}$, $^7\text{Li} + \text{p}$, and $^6\text{Li} + \text{d}$. Hence, we shall discuss the spectrum of ^8Be in the channel basis comprising four partitions calculated in the GSM-CC formalism.

5.3.1 Model space for ^8Be

Similarly to Sect. 5.2.1, the GSM calculations of $^6,7\text{Li}$ and ^7Be are done with a ^4He core and two or three valence nucleons (one proton and one neutron for ^6Li , and two protons(neutrons) and one neutron(proton) for $^7\text{Be}(^7\text{Li})$). Hence, the $0s_{1/2}$ HO shells are fully occupied and inert. The valence space is the same as described in Sect. 5.2.1 with an added set of shells $\{g_{9/2}\}$ and $\{g_{7/2}\}$ in the scattering continuum to account for $\ell = 4$ interactions.

On the other hand, the internal structure of ^4He -projectiles is calculated using the N^3LO interaction [198] without a three-body contribution. The N^3LO realistic interaction is diagonalized in eight HO shells to generate intrinsic states of ^4He . The oscillator length chosen for this calculations is $b = 1.70$ fm. With this space and oscillator length, the calculated energy of the ground state 0^+ of ^4He is -26.32 MeV, whereas the experimental value is -28.30 MeV. Using the same parameters and interaction, we can also calculate the internal structure of deuteron projectiles. This yields an energy of -1.95 MeV for the 1^+ ground state of deuteron, whereas the experimental value is -2.2 MeV. Similarly to the calculations done with the ^7Be and ^7Li systems, we use the experimental binding energy of ^4He to assure the correct energy of the $^4\text{He} + ^4\text{He}$ threshold.

Channels with one-proton (one-neutron) projectile are built by coupling the ^7Li (^7Be) wave functions having $K_i^\pi = 3/2_1^-, 1/2_1^-, 7/2_1^-, 5/2_1^-, 5/2_2^-, 3/2_2^-, 1/2_2^-, 7/2_2^-$ with the proton (neutron) wave functions in the partial waves ℓj : $s_{1/2}, p_{1/2}, p_{3/2}, d_{3/2}, d_{5/2}, f_{5/2}, f_{7/2}, g_{7/2}, g_{9/2}$. The cluster channels $[^4\text{He}(0_1^+) \otimes ^4\text{He}(L_{\text{CM}} J_{\text{int}} J_{\text{P}})]^{J^\pi}$ are constructed by coupling ^4He wave function in partial waves: $^1S_0, ^1P_1, ^1D_2, ^1F_3, ^1G_4$ with the ^4He core in $K_i^\pi = 0_1^+$ state. The deuteron channels $[^6\text{Li}(K_i^\pi) \otimes ^2\text{H}(L_{\text{CM}} J_{\text{int}} J_{\text{P}})]^{J^\pi}$ are constructed by coupling the deuteron wave function in partial waves: $^3S_1, ^3P_0, ^3P_1, ^3P_2, ^3D_1, ^3D_2, ^3D_3$, with the ^6Li target in $K_i^\pi = 1_1^+, 3_1^+, 0_1^+, 2_1^+, 2_2^+, 1_2^+$ states.

5.3.2 Interaction for $A=7,8$ systems

Because the model space differs slightly from what was used in the previous example for $A = 6, 7$ nuclei (we include also the g -shells), we expect that the effective interaction will change as well. Nevertheless, the interaction for $^6,7\text{Li}$ and ^7Be should provide a good starting point for constructing the interaction in ^8Be . We do not change the optimization scheme from the previous calculations, so we keep the one outlined in Sect. 3.5.1. The systems that we optimize are ^7Li and ^7Be (for the targets), and ^8Be (for the compound

Table 5.5: Parameters of the one-body potential optimized to describe the GSM spectrum of ${}^8\text{Be}$. From top to bottom: central potential depth, spin-orbit potential depth, radius, diffuseness and charge radius. The statistical uncertainties of optimized parameters are given in parentheses.

Parameter	Neutrons	Protons
V_0 (MeV)	50.0(1.6)	49.8(1.6)
$V_{\ell s}$ (MeV fm 2)	4.78(1.65)	5.02(1.74)
R_0 (fm)	2.0	2.0
a (fm)	0.65	0.65
R_{ch} (fm)	–	2.5

system). The same argument to justify a fit with a HO-SM calculation given in the $A = 6, 7$ case is valid for this calculation. Hence, the optimization of the interactions is done also within a HO-SM framework.

In the optimization procedure for ${}^7\text{Li}$ and ${}^7\text{Be}$, we take the following states: $K_i^\pi = 3/2_1^-$, $1/2_1^-$, $7/2_1^-$, $5/2_1^-$, $5/2_2^-$. The $5/2_1^-$ and $5/2_2^-$ states of ${}^7\text{Li}$ are close to the neutron emission threshold, therefore we expect that near-threshold correlations can be important. Thus, the HO-SM will not give an appropriate result for these particular states. Nevertheless, we choose to include the $5/2^-$ doublets of ${}^7\text{Li}$ to treat both $A = 7$ nuclei symmetrically in the optimization. The higher lying $3/2_2^-$, $1/2_2^-$ (${}^7\text{Li}$ only) and $7/2_2^-$ states are used to check the fitted interaction. For ${}^8\text{Be}$, we do not take the 0_1^+ , 2_1^+ and 4_1^+ states in the fit because they may have strong α -particle correlations that the GSM and HO-SM cannot take into account. We instead focus on fitting states that are closer to the proton and neutron thresholds. We choose the states: $J_i^\pi = 2_2^+$, 2_3^+ , 1_1^+ , 1_2^+ , 3_1^+ , 3_2^+ , 4_2^+ , 0_2^+ , and 3_3^+ . The most important states for this case are the doublets with spin 1^+ and 3^+ as they are supposed to be close to each other and close to the thresholds. This means that if we want to see the near-threshold effects in the structure of ${}^8\text{Be}$, these states are ideal for that purpose.

The parameters of the optimized one-body potential which simulate the effect of ${}^4\text{He}$ core are shown in Tab. 5.5. The parameters of the FHT interaction are shown in Tab. 5.2. The statistical errors are considerably smaller for V_c^{11} and V_c^{00} . The reason for this reduction may be related to the larger number of states included in the fit as compared to the studies presented in Sect. 5.2 and in Ref. [127].

Detailed information about the wave functions of low-energy ${}^8\text{Be}$ states can be seen in Fig. 5.7 and Tabs. 5.7 and 5.6. The decomposition of low-energy wave functions in the channel probabilities is shown in Tab. 5.6. Additional information is provided by the occupancies of single-particle shells for dominant configurations in the considered states (see Tab. 5.7).

5.3.3 Spectrum of ${}^8\text{Be}$

The ground state of ${}^8\text{Be}$ is unbound and slightly above the α -particle emission threshold. Therefore, the description of the ground state and the first few excited states requires the inclusion of couplings to the ${}^4\text{He}$ continuum. In this section, we shall discuss the spectrum of ${}^8\text{Be}$ in the channel basis comprising the $[{}^4\text{He}(0_1^+) \otimes {}^4\text{He}(L_{\text{CM}} J_{\text{int}} J_{\text{P}})]^{J^\pi}$, $[{}^6\text{Li}(K_i^\pi) \otimes {}^2\text{H}(L_{\text{CM}} J_{\text{int}} J_{\text{P}})]^{J^\pi}$, $[{}^7\text{Li}(K_i^\pi) \otimes \text{p}(\ell j)]^{J^\pi}$, and $[{}^7\text{Be}(K_i^\pi) \otimes \text{n}(\ell j)]^{J^\pi}$ channels.

Fig 5.6 shows the GSM-CC spectrum of ${}^8\text{Be}$. The interaction matrix elements entering the microscopic channel-channel coupling potentials for one-nucleon reaction channels

Table 5.6: Major probabilities of channels $[{}^7\text{Li}(K_i^\pi) \otimes p\ell j]^{J^\pi}$, $[{}^7\text{Be}(K_i^\pi) \otimes n\ell j]^{J^\pi}$, $[{}^6\text{Li}(K_i^\pi) \otimes {}^2\text{H}(L_{\text{CM}} J_{\text{int}} J_P)]^{J^\pi}$, and $[{}^4\text{He}(0_1^+) \otimes {}^4\text{He}(L_{\text{CM}} J_{\text{int}} J_P)]^{J^\pi}$ for selected states in ${}^8\text{Be}$. $\mathcal{R}e[b_c^2]$ and \mathcal{S}^2 denote the real part of the orthogonal channel probability $\langle \tilde{w}_c | w_c \rangle^2$ and the GSM-CC spectroscopic factor, respectively.

${}^8\text{Be}; J^\pi$	${}^7\text{Li}; K^\pi$	${}^7\text{Be}; K^\pi$	${}^6\text{Li}; K^\pi$	${}^4\text{He}$	p/n	d	$\mathcal{R}e[b_c^2]$	\mathcal{S}^2	
0_1^+	$3/2_1^-$	$3/2_1^-$		1S_0	$p_{3/2}$		0.27	1.21	
					$p_{3/2}$		0.26	1.19	
	$1/2_1^-$	$1/2_1^-$			$p_{1/2}$		0.15	0.37	
					$p_{1/2}$		0.09	0.41	
			1_1^+			3S_1		0.09	0.41
								0.07	0.33
2_1^+	$3/2_1^-$	$3/2_1^-$		1D_2	$p_{3/2}$		0.11	0.46-0.03i	
					$p_{3/2}$		0.11	0.46-0.03i	
	$1/2_1^-$	$1/2_1^-$			$p_{3/2}$		0.10	0.30+0.16i	
					$p_{3/2}$		0.09	0.41-0.03i	
	$3/2_1^-$	$3/2_1^-$			$p_{3/2}$		0.09	0.31-0.02i	
					$p_{1/2}$		0.07	0.31-0.02i	
		$3/2_1^-$		$p_{1/2}$		0.07	0.31-0.02i		
2_2^+	$3/2_1^-$	$5/2_1^-$		3D_3	$p_{3/2}$		0.26	0.61	
					$p_{3/2}$		0.12	0.47	
	$1/2_1^-$	$3/2_1^-$			$p_{3/2}$		0.11	0.23	
					$p_{3/2}$		0.08	0.19	
			2_2^+					0.07	0.31
2_3^+	$5/2_1^-$	$3/2_1^-$		3S_1	$p_{3/2}$		0.18	0.76	
					$p_{3/2}$		0.14	0.37	
	$1/2_1^-$	$5/2_1^-$	1_1^+		$p_{3/2}$		0.08	0.37	
					$p_{3/2}$		0.08	0.37	
	$3/2_1^-$	$1/2_1^-$			$p_{3/2}$		0.05	0.14	
					$p_{1/2}$		0.05	0.22	
		3_1^+		3S_1		0.05	0.01		
						0.05	0.24		
1_1^+	$1/2_1^-$	$1/2_1^-$		3S_1	$p_{3/2}$		0.19	0.43	
					$p_{3/2}$		0.15	0.33	
	$3/2_1^-$	$5/2_1^-$			$p_{1/2}$		0.12	0.25	
					$p_{3/2}$		0.10	0.33	
	$5/2_1^-$	$3/2_1^-$			$p_{3/2}$		0.08	0.26	
					$p_{1/2}$		0.08	0.16	
1_2^+	$3/2_1^-$	$3/2_1^-$		3D_2	$p_{1/2}$		0.16	0.34-0.01i	
					$p_{1/2}$		0.13	0.29+0.01i	
	$1/2_1^-$	$1/2_1^-$	3_1^+		$p_{3/2}$		0.12	0.38-0.01i	
					$p_{3/2}$		0.11	0.24+0.01i	
	$5/2_1^-$	2_1^+			$p_{3/2}$		0.10	0.16	
					$p_{3/2}$		0.07	0.14-0.01i	
						0.06	0.23		
						0.06	0.22		
						0.06	0.21-0.01i		
3_1^+	$7/2_1^-$	$3/2_1^-$		3D_3	$p_{3/2}$		0.18	0.50-0.01i	
					$p_{3/2}$		0.13	0.29+0.01i	
	$3/2_1^-$	$5/2_1^-$			$p_{3/2}$		0.11	0.36	
					$p_{3/2}$		0.11	0.28-0.01i	
	$7/2_1^-$	$7/2_1^-$			$p_{1/2}$		0.07	0.21+0.01i	
					$p_{1/2}$		0.07	0.21	
		$5/2_1^-$							
3_2^+	$5/2_1^-$	$3/2_1^-$		3D_3	$p_{3/2}$		0.13	0.32+0.01i	
					$p_{1/2}$		0.13	0.40	
	$1/2_1^-$	$7/2_1^-$			$p_{3/2}$		0.09	0.27	
					$p_{3/2}$		0.07	0.21+0.01i	
	$7/2_1^-$	$7/2_1^-$	1_1^+		$p_{3/2}$		0.06	0.26-0.01i	
					$p_{3/2}$		0.06	0.29-0.01i	
		3_1^+		3S_1		0.06	0.17		
						0.05	0.19-0.01i		
4_1^+	$7/2_1^-$	$7/2_1^-$		1G_4	$p_{3/2}$		0.14	0.62+0.03i	
					$p_{3/2}$		0.13	0.60+0.03i	
	$5/2_1^-$	$5/2_2^-$			$p_{3/2}$		0.12	0.58+0.01i	
					$p_{3/2}$		0.12	0.55+0.01i	
	$7/2_1^-$	$7/2_1^-$			$p_{1/2}$		0.10	0.46	
					$p_{1/2}$		0.10	0.47	
						0.03	0.09+0.15i		

Table 5.7: Number of protons and neutrons in resonant shells: $\ell = 1$ (p) and non-resonant shells of the scattering continuum: $\ell = 0$ ({s}), $\ell = 1$ ({p}), $\ell = 2$ ({d}) for largest configurations in different GSM eigenfunctions of ${}^8\text{Be}$. $\mathcal{Re}[a_c^2]$ denote the real parts of the squared configuration amplitude.

	J^π	p	{p}	{d}	{s}	$\mathcal{Re}[a_c^2]$
${}^8\text{Be}$	0_1^+	2p2n	0	0	0	0.82
	2_1^+	2p2n	0	0	0	0.82
	2_2^+	2p2n	0	0	0	0.83
	2_3^+	2p2n	0	0	0	0.81
		1p1n	0	1p1n	0	0.05
	1_1^+	2p2n	0	0	0	0.80
		1p1n	0	1p1n	0	0.05
	1_2^+	2p2n	0	0	0	0.80
	1_3^+	2p2n	0	0	0	0.79
	3_1^+	2p2n	0	0	0	0.81
	3_2^+	2p2n	0	0	0	0.81
		1p1n	0	1p1n	0	0.05
	3_3^+	2p2n	0	0	0	0.80

have been rescaled by the tiny complex multiplicative corrective factors $c(J^\pi)$: $c(0^+) = 1.022$, $c(2^+) = 1.034 + 0.0015i$, $c(4^+) = 1.036 + 0.02i$, $c(1^+) = 1.022 + 0.00013i$, $c(3^+) = 1.019 + 0.0035i$ to correct for missing channels in the model space.² Additionally, the channel-channel coupling potentials for α channels have been rescaled by the corrective factors $c_\alpha(2^+) = 1.0 + 0.06i$ and $c_\alpha(4^+) = 1.0 + 0.2i$. The channel-channel coupling potentials associated to deuteron channels are left unchanged.

Figure 5.6 shows the spectrum of ${}^8\text{Be}$ calculated with and without the deuteron channel. One may notice that the agreement with the experimental data for resonance energies and widths is good, especially if the deuteron channels are included. In contrast to the calculation of $A = 7$ nuclei, where real correction factors were used, the studies of ${}^8\text{Be}$ have been done with complex corrective factors to correct for missing reaction channels. The energy spacing of resonances in the $(1_1^+; 1_2^+)$ doublet is somewhat larger in GSM-CC calculation than in the data. The inclusion of the deuteron channel helps to close the gaps between states of each doublet: $(1_1^+; 1_2^+)$, $(2_2^+; 2_3^+)$, $(3_1^+; 3_2^+)$. In the description of the ground state 0_1^+ , and excited states 2_1^+ , 4_1^+ , inclusion of the deuteron channel does not improve the agreement between the GSM-CC calculation and the data.

Fig. 5.7 shows the relative probability of channels $[{}^7\text{Li}(K_i^\pi) \otimes \text{p}(\ell j)]^{J^\pi}$, $[{}^7\text{Be}(K_i^\pi) \otimes \text{n}(\ell j)]^{J^\pi}$, $[{}^6\text{Li}(K_i^\pi) \otimes {}^2\text{H}(L_{\text{CM}} J_{\text{int}} J_{\text{P}})]^{J^\pi}$, and $[{}^4\text{He}(0_1^+) \otimes {}^4\text{He}(L_{\text{CM}} J_{\text{int}} J_{\text{P}})]^{J^\pi}$ in different states of ${}^8\text{Be}$ for a full calculation and a calculation without the deuteron channel. One may notice that the $[{}^4\text{He}(0_1^+) \otimes {}^4\text{He}(L_{\text{CM}} J_{\text{int}} J_{\text{P}})]^{J^\pi}$ channels play a role only in the two lowest states: 0_1^+ , 2_1^+ . The contribution of α -cluster channels is small in 4_1^+ resonance, and disappears whatsoever in higher-lying states.

The weight of proton and neutron channels in these states is roughly identical (see Tab. 5.8) whether the deuteron channels are included or not. This is not the case in higher energy doublets: $(1_1^+; 1_2^+)$, $(2_2^+; 2_3^+)$, $(3_1^+; 3_2^+)$. Independently on whether we include the deuteron channels or not, the lower-energy member in each of those doublets car-

²The calculation without deuteron channels uses the corrective factors: $c(J^\pi)$: $c(0^+) = 1.024$, $c(2^+) = 1.034 + 0.0015i$, $c(4^+) = 1.033 + 0.02i$, $c(1^+) = 1.023 + 0.00016i$, $c(3^+) = 1.018 + 0.004i$. The corrective factors for the alpha channels are $c_\alpha(2^+) = 1.0 + 0.06i$ and $c_\alpha(4^+) = 1.0 + 0.2i$.

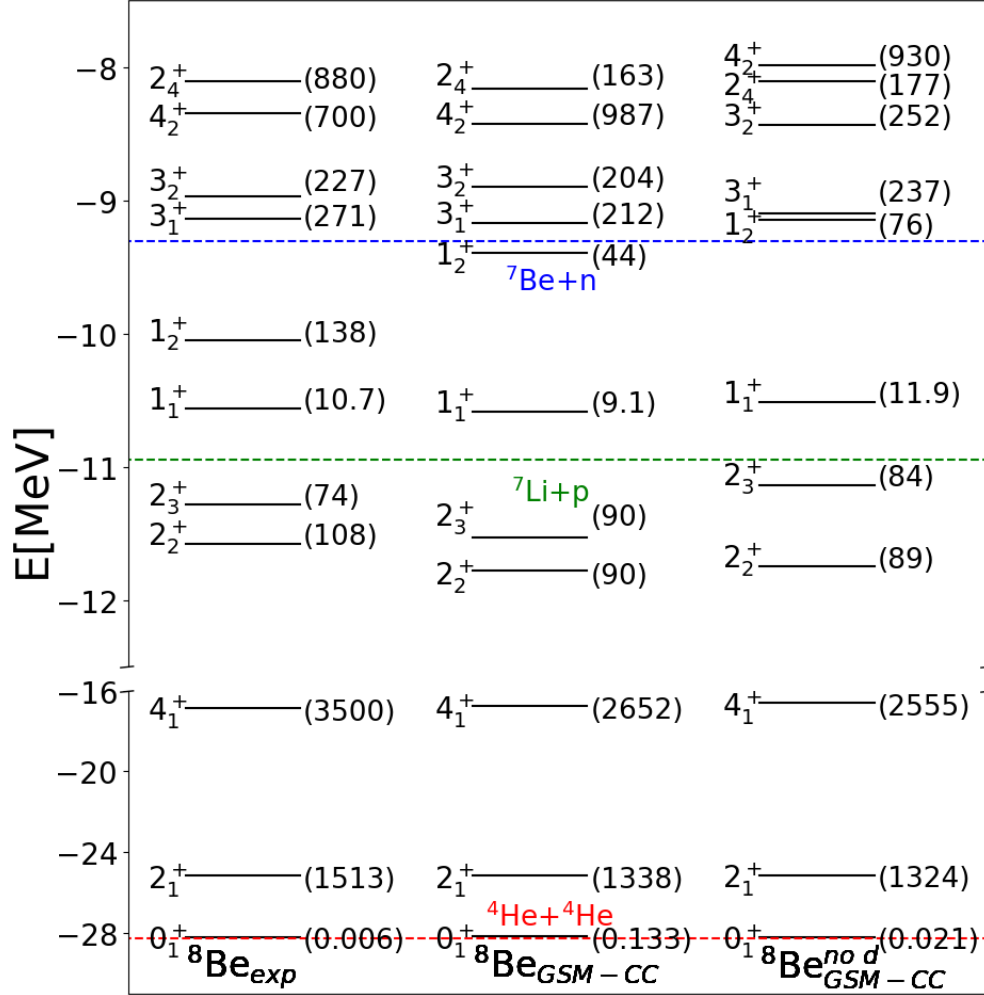


Figure 5.6: Energy spectrum of ${}^8\text{Be}$ calculated in GSM-CC using the channel basis with four mass partitions: $[{}^4\text{He}(0_1^+) \otimes {}^4\text{He}(L_{CM} J_{int} J_P)]^{J^\pi}$, $[{}^6\text{Li}(K_i^\pi) \otimes {}^2\text{H}(L_{CM} J_{int} J_P)]^{J^\pi}$, $[{}^7\text{Li}(K_i^\pi) \otimes p(\ell j)]^{J^\pi}$, and $[{}^7\text{Be}(K_i^\pi) \otimes n(\ell j)]^{J^\pi}$ is compared with the experimental spectrum and a spectrum calculated without the deuteron channels. Numbers in the brackets indicate the resonance widths in keV. All energies of the states are given relative to the energy of ${}^4\text{He}$ core. Experimental particle emission thresholds: ${}^4\text{He} + {}^4\text{He}$ and ${}^7\text{Li} + p$, and ${}^7\text{Be} + n$ are given in dashed lines in the figure.

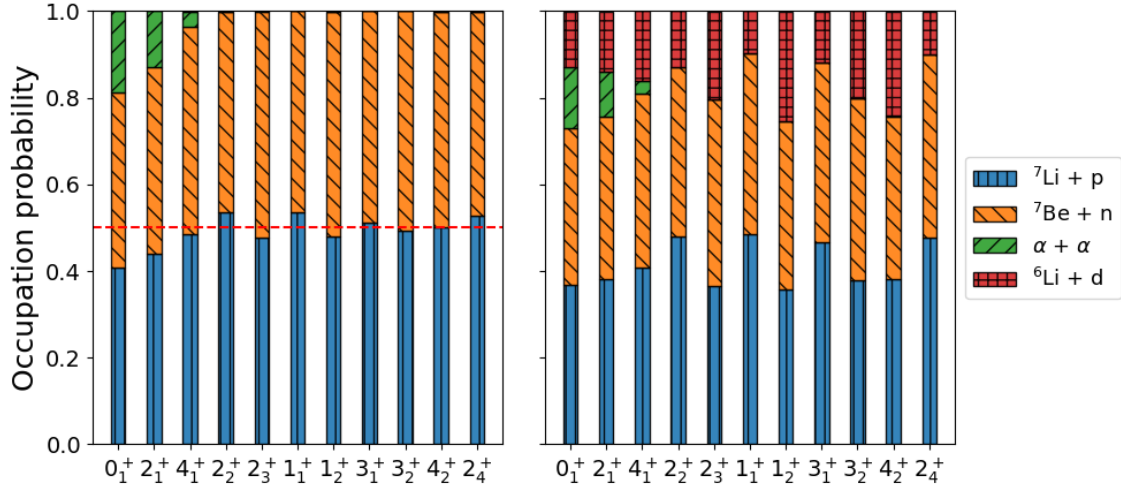


Figure 5.7: The channel decomposition for selected states of ${}^8\text{Be}$. In different colors, we show the summed GSM-CC probabilities of p, n, ${}^4\text{He}$, and d channels. On the left panel we show the distribution where the deuteron channels are absent, and on the right panel we show the calculation with all channels. The dashed horizontal line at 0.5 in the left panel is drawn to facilitate analysis of the symmetry between proton and neutron channels in the doublet states. Detailed information about major GSM-CC channel probabilities and SFs in individual states of ${}^8\text{Be}$ can be found in Tab. 5.6. Information about the number of protons and neutrons in different shells is given in Tab. 5.7.

ries a larger weight of $[{}^7\text{Li}(K_i^\pi) \otimes \text{p}(\ell_j)]^{J^\pi}$ proton channels, whereas in the higher-energy partner the neutron channels $[{}^7\text{Be}(K_i^\pi) \otimes \text{n}(\ell_j)]^{J^\pi}$ are more important. In particular, this effect is attenuated in the doublet $(3_1^+; 3_2^+)$ which is seen slightly above the neutron channel $[{}^7\text{Be}(K_i^\pi) \otimes \text{n}(\ell_j)]^{J^\pi}$. The lower-energy member still carries a larger weight of the $[{}^7\text{Be}(K_i^\pi) \otimes \text{p}(\ell_j)]^{J^\pi}$ proton channels, whereas its higher-energy partner the neutron channels $[{}^7\text{Li}(K_i^\pi) \otimes \text{n}(\ell_j)]^{J^\pi}$ play a slightly larger role. The isospin structure of states in the doublets cannot be calculated in GSM-CC. The main difficulty of the calculation of T^2 comes from the fact that it would require all channels, like those with mass partitions core + p/n, core + 2p/2n/d, core + 3p/3n/ ${}^3\text{He}/{}^3\text{H}$, etc., which require 2/3/4-body asymptotics, etc. Moreover, for an exact treatment of T^2 , the wave functions of protons and neutrons need to be the same and this is not the case in GSM-CC.

The deuteron channels play an important role in the considered wave functions. The probability of these reaction channels surpass even the channels $[{}^4\text{He}(0_1^+) \otimes {}^4\text{He}(L_{\text{CM}} J_{\text{int}} J_P)]^{J^\pi}$ in 2_1^+ , 4_1^+ resonances. The uneven distribution of the deuteron channels in the doublets $(1_1^+; 1_2^+)$, $(2_2^+; 2_3^+)$, and $(3_1^+; 3_2^+)$ allows to understand why the energy gap between members of the doublet changes when this channel is included. As seen in Tab. 5.8, the inclusion of the deuteron channels does not change qualitatively the relative importance of proton $[{}^7\text{Li}(K_i^\pi) \otimes \text{p}(\ell_j)]^{J^\pi}$ and neutron $[{}^7\text{Be}(K_i^\pi) \otimes \text{n}(\ell_j)]^{J^\pi}$ channels in the partner state of each doublet. Therefore, it does not correct the interplay between the other partitions, but its uneven contribution between doublet states corrects the energy gaps that are otherwise bigger. Generally, the contribution of the deuteron channels is in the range from $\sim 10\%$ to $\sim 25\%$. The higher lying 4_2^+ state contains no α -channel component and is symmetric in the contribution of proton and neutron channel functions. The probability of the deuteron channel in this state is very important and equals $\sim 16\%$. However, this probability is distributed equally among all deuteron channels with small individual probabilities up to

Table 5.8: The summed real parts of the channel probabilities for each mass partition in a GSM-CC calculation of ${}^8\text{Be}$. On the left, the calculation without the ${}^6\text{Li} + \text{d}$ mass partition. On the right, the calculation with all four mass partitions.

state	No deuteron included			Full calculation			
	${}^7\text{Li} + \text{p}$	${}^7\text{Be} + \text{n}$	${}^4\text{He} + {}^4\text{He}$	${}^7\text{Li} + \text{p}$	${}^7\text{Be} + \text{n}$	${}^4\text{He} + {}^4\text{He}$	${}^6\text{Li} + \text{d}$
0_1^+	0.409	0.404	0.186	0.368	0.363	0.139	0.130
2_1^+	0.439	0.433	0.128	0.381	0.375	0.104	0.139
4_1^+	0.486	0.478	0.036	0.409	0.402	0.029	0.160
2_2^+	0.535	0.465	0.000	0.479	0.391	0.000	0.130
2_3^+	0.479	0.521	0.000	0.364	0.432	0.000	0.204
1_1^+	0.537	0.463	0.000	0.486	0.417	0.000	0.096
1_2^+	0.479	0.521	0.000	0.358	0.388	0.000	0.254
3_1^+	0.513	0.487	0.000	0.467	0.413	0.000	0.119
3_2^+	0.494	0.506	0.000	0.378	0.421	0.000	0.201
4_2^+	0.501	0.498	0.001	0.380	0.377	0.001	0.242
2_4^+	0.529	0.471	0.000	0.477	0.422	0.000	0.100
0_2^+	0.522	0.478	0.000	0.472	0.461	0.000	0.067

$\sim 3\%$.

The probability of an open cluster channel $[{}^4\text{He}(0_1^+) \otimes {}^4\text{He}(1S_0)]^{0^+}$ in the ground state 0_1^+ amounts to 15% if the deuteron channels are included. This cluster component contributes in the first excited state 2_1^+ as well, with a contribution of 10%. The total contribution of closed channels in this 2_1^+ state is spread over many proton and neutron channels. The second excited state 4_1^+ contains only a small contribution of the channel function $[{}^4\text{He}(0_1^+) \otimes {}^4\text{He}(1G_4)]^{4^+}$: $\mathcal{R}e[b_c^2]=3\%$. The major contributions to the wave function are given by closed proton channels: $[{}^7\text{Li}(7/2_1^-) \otimes \text{p}(p_{3/2}, p_{1/2})]^{4^+}$, $[{}^7\text{Li}(5/2_2^-) \otimes \text{p}(p_{3/2})]^{4^+}$, and neutron channels: $[{}^7\text{Be}(7/2_1^-) \otimes \text{n}(p_{3/2}, p_{1/2})]^{4^+}$, $[{}^7\text{Be}(5/2_2^-) \otimes \text{n}(p_{3/2}, p_{1/2})]^{4^+}$, $[{}^7\text{Be}(5/2_2^-) \otimes \text{n}(p_{3/2})]^{4^+}$.

The real parts of the channel weights $\mathcal{R}e[b_c^2]$ and spectroscopic factors \mathcal{S}^2 in different eigenstates of ${}^8\text{Be}$ follow a similar qualitative tendency, namely large channel probabilities are associated with large spectroscopic factors (see Tab. 5.6). In a GSM calculation, major occupation of single-particle shells in different states of ${}^8\text{Be}$ is seen for resonant shells $p_{3/2}$, $p_{1/2}$. The occupation of non-resonant shells in the scattering continuum is not negligible only in higher-energy eigenstates, such as 2_3^+ , 1_1^+ or 3_2^+ , but the real part of the squared configuration amplitude in these cases is rather small and does not exceed around 5% (see Tab. 5.7).

As can be seen in Tab. 5.6, the states of the doublet ($2_2^+; 2_3^+$) do not show the presence of the same dominant deuteron channels in the decomposition of their wave function. Significant differences in deuteron channels composition are also seen among the states of the doublets ($1_1^+; 1_2^+$), ($3_1^+; 3_2^+$). The asymmetry of the deuteron contributions in the doublets ($1_1^+; 1_2^+$), ($2_2^+; 2_3^+$), ($3_1^+; 3_2^+$) can be attributed to the orthogonality of these states rather than to the deuteron threshold effect, which is too high in energy to be of any importance.

5.4 Description of spectra of ^{42}Sc , ^{42}Ca , ^{42}Ti , and transfer reaction $^{40}\text{Ca}(\text{d,p})^{41}\text{Ca}$

In this section, we shall discuss in GSM-CC the reactions: $^{40}\text{Ca}(\text{p,p})^{40}\text{Ca}$, $^{40}\text{Ca}(\text{n,n})^{40}\text{Ca}$, $^{40}\text{Ca}(\text{d,p})^{41}\text{Ca}$, and spectra of $A = 41, 42$ nuclei using a ^{40}Ca with valence nucleons.

Measuring the cross sections directly at stellar energies poses significant challenges, particularly when dealing with charged particles. Consequently, indirect methods such as transfer reactions are employed to determine the desired reaction rates relevant to astrophysics [201, 202]. Specifically, (d,p) reactions have been extensively studied to extract SFs for isotopes of astrophysical importance, enabling the constraint of neutron-capture rates [203–207]. These one-nucleon transfer reactions are particularly valuable in the investigation of nuclear response to nucleon addition (single-particle strength) across various energy, angular momentum, and parity conditions. Traditionally, one-nucleon transfer reactions to bound states provide insights into direct capture, while those populating the continuum are employed to extract information about resonant and/or compound capture.

Calculations with a ^{40}Ca core were done for: ^{42}Ca , ^{42}Sc and ^{42}Ti . A single mass partition was used for ^{42}Ca and ^{42}Ti consisting of $^{41}\text{Ca} + \text{n}$ and $^{41}\text{Sc} + \text{p}$, respectively. For ^{42}Sc we use three different partitions: $^{41}\text{Ca} + \text{p}$, $^{41}\text{Sc} + \text{n}$ and $^{40}\text{Ca} + \text{d}$. In this section we shall discuss the spectra and reactions associated to these systems, with particular emphasis in the $^{40}\text{Ca}(\text{d,p})^{41}\text{Ca}$ transfer reaction.

5.4.1 Model space for calculations with a ^{40}Ca core

The GSM calculation of the $A = 41$ targets: ^{41}Ca and ^{41}Sc , are performed with a ^{40}Ca core with one valence neutron and proton, respectively. This means that the $0s_{1/2}$, $0p_{3/2}$, $0p_{1/2}$, $0d_{5/2}$, $1s_{1/2}$ and $0d_{3/2}$ shells are fully occupied and inert. The valence space consist of four main resonant-like HO shells $0f_{7/2}$, $0f_{5/2}$, $1p_{3/2}$, $1p_{1/2}$ and several scattering-like subdominant HO shells in $\{s_{1/2}\}$, $\{p_{3/2}\}$, $\{p_{1/2}\}$, $\{d_{5/2}\}$, $\{d_{3/2}\}$, $\{f_{7/2}\}$, $\{f_{5/2}\}$, $\{g_{9/2}\}$, $\{g_{7/2}\}$ partial waves, which verify $n \leq 5$. Similarly to the studies with a ^4He core presented above, the scattering-like HO states approximate the non-resonant continuum, and additionally, reduce the size of the GSM matrix. In this case, we truncate the basis of Slater determinants by limiting the excitation energy to $14\hbar\omega$.

The internal structure of the deuteron projectiles is calculated using the N^3LO interactions without the three-body contribution [198]. The N^3LO realistic interaction is diagonalized in ten HO shells to generate the intrinsic states of deuteron. The oscillator length chosen for this calculations is $b = 1.88$ fm. With this space and oscillator length the calculated energy of the ground state 1^+ of deuteron is -1.95 MeV, whereas the experimental value is -2.22 MeV. Contrary to the examples shown in previous sections, we set the binding energy of the deuteron to -2.1 MeV to reproduce better the calculated spectra and reactions.

Channels with one-nucleon projectile are built by coupling the $^{41}\text{Ca} (^{41}\text{Sc})$ wave functions with $(K_i^\pi = 7/2_1^-, 3/2_1^-, 5/2_1^-, 1/2_1^-)$ and a proton or a neutron wave function in the partial waves ℓj : $s_{1/2}$, $p_{1/2}$, $p_{3/2}$, $d_{3/2}$, $d_{5/2}$, $f_{5/2}$, $f_{7/2}$, $g_{7/2}$, $g_{9/2}$. The deuteron channels $[^{40}\text{Ca}(0_1^+) \otimes {}^2\text{H}(L_{\text{CM}} J_{\text{int}} J_{\text{P}})]^{J^\pi}$ are constructed by coupling the deuteron wave function in partial waves: 3S_1 , 3P_0 , 3P_1 , 3P_2 , 3D_1 , 3D_2 , 3D_3 , with the inert ^{40}Ca core in $K_i^\pi = 0_1^+$ state. The break-up of deuteron can be taken into account by including the scattering deuteron eigenstates arising from a Berggren basis diagonalization [35]. However, for the study of the (d,p) reaction, we only consider a small deuteron projectile energy of about 1.8 MeV, hence deuteron break-up cannot occur. Finally, the HO composite states have

Table 5.9: Parameters of the one-body potential for protons and neutrons optimized to describe the spectra of $^{41,42}\text{Ca}$ and ^{42}Sc . From top to bottom: central potential depth for protons, spin-orbit strength for protons, central potential depth for neutrons and spin-orbit strength for neutrons for partial waves $\ell = 0, 1, 2, 3, 4$.

Parameter	$\ell = 0$	$\ell = 1$	$\ell = 2$	$\ell = 3$	$\ell = 4$
$V_0(p)$	50	55.142	62	56.601	56.5
$V_{ls}(p)$	—	6.012	5	2.884	7
$V_0(n)$	60.5	54.302	59.5	54.204	40
$V_{ls}(n)$	—	5.007	2	2.850	2

Table 5.10: Parameters of the FHT interaction used in this study to describe $^{41,42}\text{Ca}$ and ^{42}Sc nuclei.

Parameter	FHT
V_c^{11}	17.745
V_c^{10}	-4.516
V_c^{00}	-0.210
V_c^{01}	-7.386
V_{LS}^{10}	-2509
V_{LS}^{11}	1000
V_T^{11}	-4.102
V_T^{10}	-1.257

their energy truncated at $E_{\text{max}}^{\text{HO}} = 8\hbar\omega$.

5.4.2 Interaction for $A = 41, 42$ systems

Parameters of the optimized one-body potential which simulates the effect of ^{40}Ca core are shown in Tab. 5.9. Both the WS potentials for protons and neutron use a standard value for diffuseness $d = 0.65$ fm and a radius $R_0 = 1.27A^{1/3} = 4.34$ fm and they are the same for all partial waves. Parameters of the WS potential for $\ell = 1, 3$ have been fitted to reproduce the single-particle states of ^{41}Ca and ^{41}Sc : $K_i^\pi = 7/2_1^-, 3/2_1^-, 5/2_1^-,$ and $1/2_1^-$. The core potentials for $\ell = 0, 2, 4$ partial waves do not play a significant role in the structure of $A = 41, 42$ nuclei. Their values were instead fitted to reproduce the reaction cross-sections that will be presented in Sect. 5.4.3.

The parameters of the FHT interaction are shown in Tab. 5.10. The FHT interaction is fitted to reproduce the low lying spectra of $A = 42$ nuclei. For ^{41}Ca and ^{41}Sc only the ground state 0_1^+ and the first excited state 2_1^+ were fitted, whereas for ^{42}Sc the states: $J_i^\pi = 0_1^+, 1_1^+, 7_1^+, 3_1^+, 5_1^+$ and 2_1^+ were taken into account.

5.4.3 Spectrum and reactions with a ^{40}Ca core and valence particles

Let us now discuss the spectra of ^{42}Ca , ^{42}Ti and ^{42}Sc . ^{42}Ca and ^{42}Ti use a single mass partition consisting of $^{41}\text{Ca} + n$ and $^{41}\text{Sc} + p$, respectively. Whereas ^{42}Sc is described with three mass partitions: $^{41}\text{Ca} + p$, $^{41}\text{Sc} + n$ and $^{40}\text{Ca} + d$. This allows to study the (d,p) transfer reaction within the GSM-CC framework.

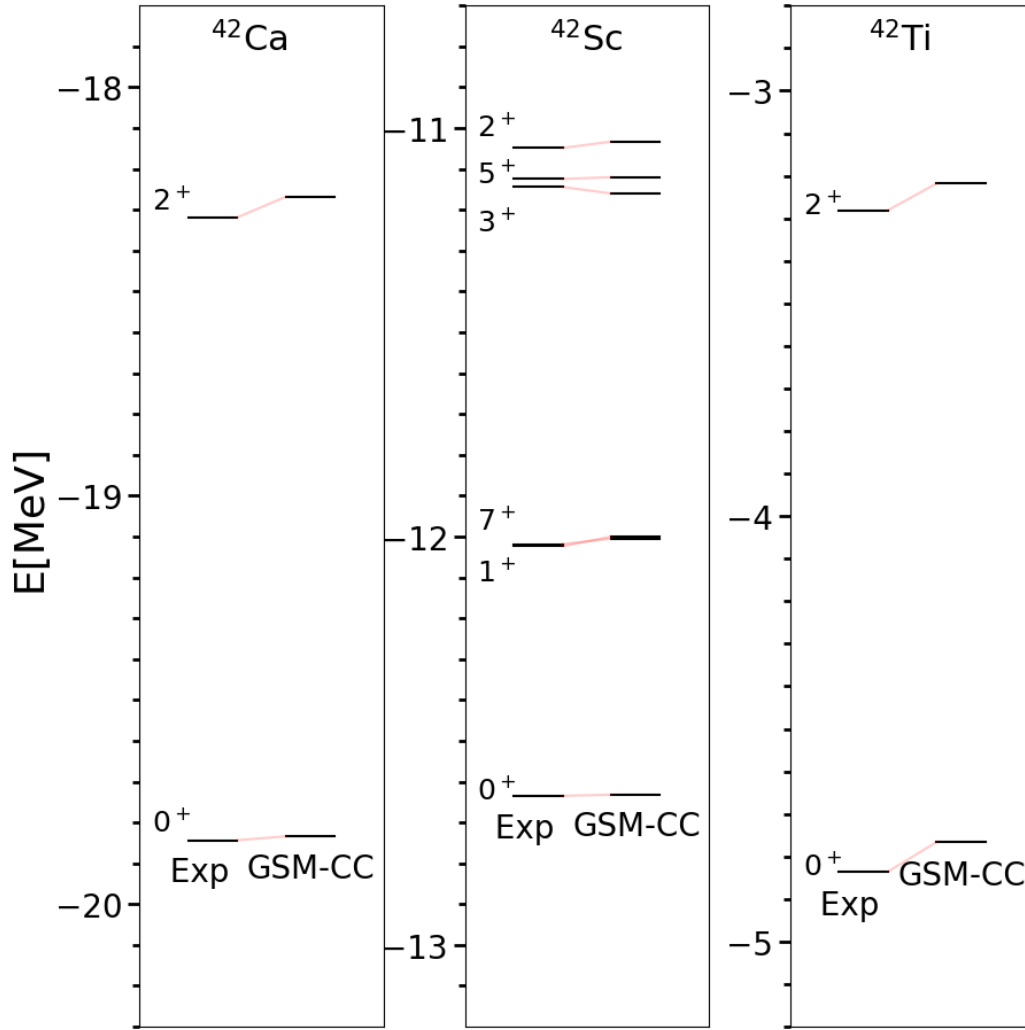


Figure 5.8: GSM-CC low energy spectra of ^{42}Ca , ^{42}Sn , and ^{42}Ti nuclei are compared to the experimental data [208].

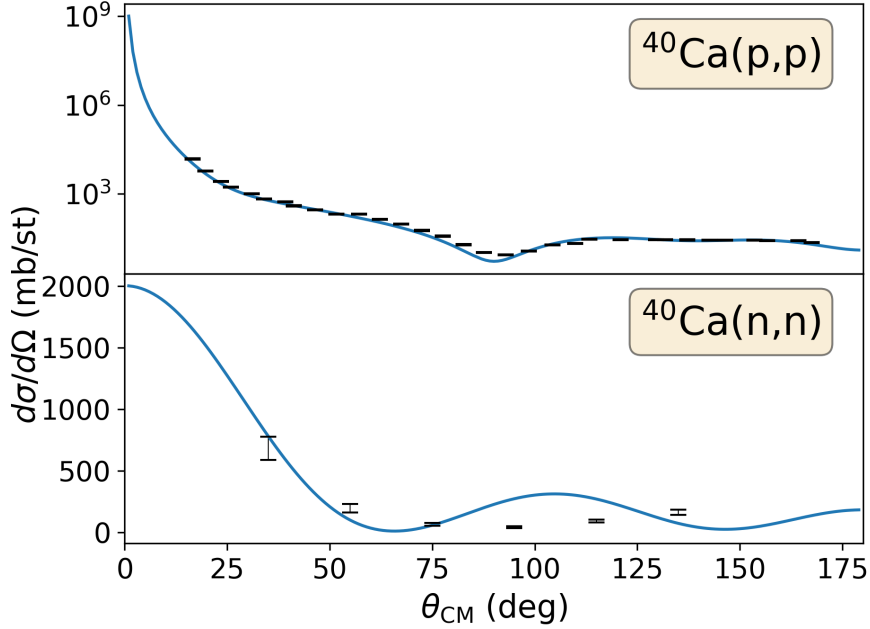
Fig. 5.8 shows the GSM-CC spectrum of ^{42}Ca , ^{42}Sn , and ^{42}Ti . The real scaling factors in this case are: $c(0^+) = 1.14$, $c(1^+) = 0.99$, $c(2^+) = 1.08$, $c(3^+) = 1.04$, $c(5^+) = 1.1$, and $c(7^+) = 1.12$. The large corrective factors for 0^+ , 5^+ , and 7^+ channels may be attributed to the absence of 0_2^+ , 3_1^- , and 2_1^+ low-energy core excitation states in ^{40}Ca . One- and two-nucleon separation energies $S_{n/p}$ and $S_{2n/2p}$, respectively, and the deuteron separation energy S_d calculated in GSM-CC for $A = 41, 42$ nuclei are shown in Tab. 5.11 and are compared to the data.

Fig. 5.9 shows the cross-section for the elastic scattering reactions $^{40}\text{Ca}(\text{p,p})^{40}\text{Ca}$ and $^{40}\text{Ca}(\text{n,n})^{40}\text{Ca}$ at CM energies of 9.71 MeV and 2.69 MeV, respectively. Similarly to what was presented in Sect. 5.2.4, the same Hamiltonian was used for reactions and structure. As only nucleon projectiles are present in these reactions, the reaction channels $[^{40}\text{Ca}(0_1^+) \otimes \text{p}(\ell j)]^{J^\pi}$ and $[^{40}\text{Ca}(0_1^+) \otimes \text{n}(\ell j)]^{J^\pi}$ are defined directly in the Berggren basis. The calculated cross-section reproduce the experimental data quite well, nevertheless, there are small oscillation at large angles θ_{CM} for the neutron scattering.

Fig. 5.10 shows the cross-section of the transfer reaction $^{40}\text{Ca}(\text{d,p})^{41}\text{Ca}$ at a CM energy of 2.69 MeV. This cross-section can be reproduced only by fine-tuning the parameters

Table 5.11: Comparison of theoretical separation energies $S_{n/p}$, $S_{2n/2p}$ and S_d with experimental values. Energies are given in units of MeV.

Nucleus	$S_{n/p}^{\text{th}}$	$S_{n/p}^{\text{exp}}$	$S_{2n/2p}^{\text{th}}$	$S_{2n/2p}^{\text{exp}}$	S_d^{th}	S_d^{exp}
^{41}Ca	8.38/—	8.363/—	—	—	—	—
^{42}Ca	11.36/—	11.48/—	19.74/—	19.8/—	—	—
^{42}Sc	11.42/4.15	11.48/4.27	—	—	12.53	12.48
^{41}Sc	—/1.11	—/1.09	—	—	—	—
^{42}Ti	—/3.57	—/3.75	—/12.53	—/12.48	—	—

Figure 5.9: Cross-sections for the reactions: $^{40}\text{Ca}(p,p)^{40}\text{Ca}$ (top panel) at CM energy of 9.71 MeV and $^{40}\text{Ca}(n,n)^{40}\text{Ca}$ (bottom panel) at CM energy of 2.69 MeV. Proton and neutron experimental cross-sections are taken from Refs. [209, 210], respectively.

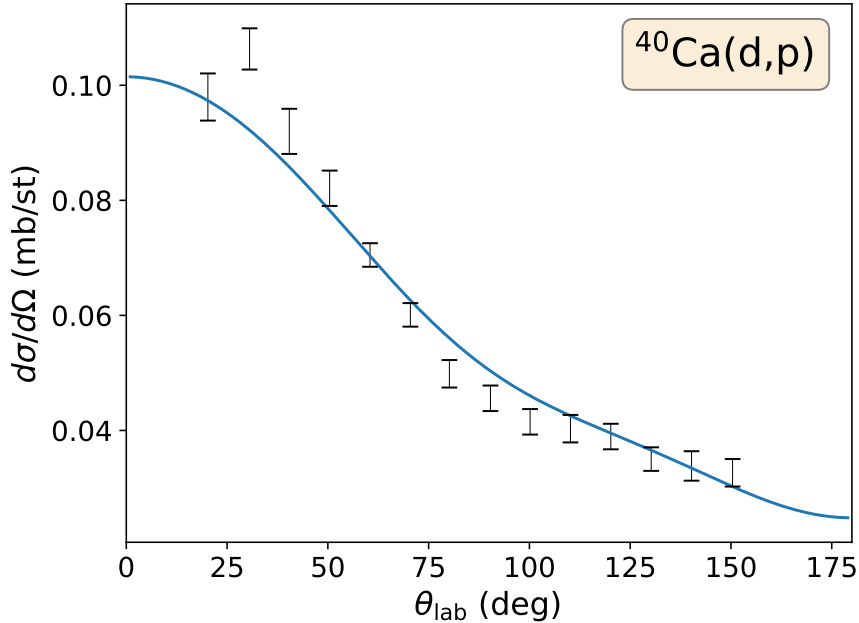


Figure 5.10: Cross-section for the transfer reaction $^{40}\text{Ca}(d,p)^{41}\text{Ca}$ at CM energy of 1.853 MeV. The cross-section and angle are given in laboratory coordinates. The experimental data has been taken from Ref. [211].

of both the Hamiltonian and the WS basis-generating potential describing the continuum wave functions and their asymptotic behavior [212]. In this example, the GSM-CC approach provides a good reproduction of the cross-sections, except for neutron scattering at large angles. However, the price to pay is the fine tuning of the Hamiltonian as well as the Berggren basis parameters. Consequently, it remains difficult to study systematically the transfer reactions in the GSM-CC framework. Although not presented in this thesis, the calculation of transfer reaction $^4\text{He}(^3\text{He},p)^6\text{Li}$ yields cross-sections which are one order of magnitude smaller than reported experimentally in Ref. [199]. The GSM-CC approach for nuclear reactions requires further development and systematic studies to improve its predictive power.

Near-threshold effects within the Gamow Shell Model

We still have not addressed the unitarity of the S-matrix in the context of nuclear reactions. The unitarity means conservation of the probability flux. This leads to the question: what happens with the probability flux at the opening of a particle emission threshold? Indeed as the threshold is crossed the probability flux bifurcates and is distributed into other channels. The theory of the near-threshold effects began with an analysis of the asymptotic behavior of the wave functions [37] and later with the R -matrix theory [213]. For neutral particles, this led to the identification of the so-called Wigner cusps [37] in the cross-sections. This theoretical result has been verified experimentally in various systems (see for example Refs. [214–216]). Nevertheless, one could ask which aspects of this nuclear reaction phenomenon can be found in the nuclear structure.

One way to connect cross-sections to nuclear structure is via the SFs. If nuclear structure and reactions are described in an OQS framework, then the threshold effect in the cross-section might cause an analogous effect in the SFs. GSM studies [38, 39, 166] have shown that the coupling to the continuum is necessary to obtain Wigner cusps in nuclear structure calculations.

Another near-threshold effect, this time related to clustering, has been noted by Ikeda *et al.* in 1968 [7]. They remarked that α -cluster states exist close to the α -particle emission threshold in many ' $N\alpha$ -nuclei'. There is no particular argument that this finding should be limited exclusively to the α -clustering in $N\alpha$ -nuclei. In Refs. [8, 9], it was conjectured that the near-threshold clustering is a general OQS phenomenon which might exist at any particle emission-threshold, even the one where the emitted particle is unbound, like the dineutron [217] or diproton [218, 219]. In the R -matrix framework, this phenomenon has been related to an enhancement in the density of states close to the particle emission threshold [213]. A recent experimental observation of a very narrow $1/2_1^-$ resonance in the vicinity of the $2p$ -threshold in ^{15}F confirms this hypothesis [220]. However, this case is not special as narrow near-threshold resonances are omnipresent in many nuclei. Extensive literature on nuclear clustering and cluster modeling can be found in Ref. [221].

In SMEC, studies of the near-threshold effects that may lead to clusterization, have been done using the continuum-coupling correlation energy [222, 223]. Particle emission thresholds considered in this theoretical framework were restricted to at most two nucleons [88, 89, 218]. This limitation has been avoided in the coupled-channel formulation of the GSM. In the GSM framework, one can define a similar, albeit not the same,

continuum-coupling correlation energy, where the role of different reaction channels can be investigated. The goal of this chapter is to lay ground for these studies in the GSM-CC.

In this chapter, we will briefly describe the theory of Wigner cusps and then follow with a discussion of the structure of many-body wave functions, with the focus on reaction channels probabilities. In particular, in Sects. 6.3.1 and 6.3.2 we will discuss variations of the channel weights depending on the distance from different particle/cluster emission thresholds, and the emergence of aligned, cluster-like configurations, in the vicinity of the cluster threshold. In Sect. 6.3.3 we will present results of calculations regarding the dependence of the continuum-coupling correlation energy on the distance of the particle emission thresholds. As shown in SMEC studies [8, 9, 224–230], the continuum-coupling correlation energy is a useful tool to quantify the configuration mixing of SM states in the vicinity of the particle emission threshold. Finally, in Sect. 6.3.4 we will discuss the features of the SFs in many-body states and their changes depending on the distance from the decay thresholds.

6.1 Wigner cusps in reaction cross-sections and spectroscopic factors

In 1948, Wigner derived the threshold law for cross-sections [37] by analyzing the asymptotic behavior of the wave functions. Indeed, an anomaly shows up at the decay threshold due to different asymptotic conditions above and below the threshold. This law explained the appearance of cusps near the particle emission threshold cross-sections as well as their properties. A decade later, discussion of the Wigner cusps was done in the R -matrix theory [231–237].

Wigner cusps in cross-sections for neutral particles show a rather intriguing behavior.

- For endoergic reactions (e.g. production of slow neutral particles) one finds:

$$\sigma(i \rightarrow j) \sim k_j^{2\ell_j+1} \sim E_j^{\ell_j+1/2}. \quad (6.1)$$

- For exoergic reactions (e.g. absorption of slow neutral particles) one obtains:

$$\sigma(i \rightarrow j) \sim k_i^{2\ell_i-1} \sim E_i^{\ell_i-1/2}. \quad (6.2)$$

The best example for the relation (6.2) is the absorption of slow neutrons where the cross section is inversely proportional to the velocity ($\sigma_{\text{absorption}} \propto 1/v$). This law was developed, earlier than the R -matrix formalism [238–240]. From Eq. (6.1) and (6.2), one can see that there is a discontinuity, which is shaped as a cusp for $\ell = 0, 1$. For higher ℓ values, the cross-section is smooth and the discontinuity shows up in the $(\ell - 1)$ th derivative of the cross-section with respect to the energy of the system.

For charged particles the dependence of the cross-section near threshold is more complicated:

- For endoergic reactions is:

$$\sigma(i \rightarrow j) \sim e^{-2\pi\eta_j}. \quad (6.3)$$

- For an exoergic reactions one finds:

$$\sigma(i \rightarrow j) \sim k_i^2 e^{-2\pi\eta_i}, \quad (6.4)$$

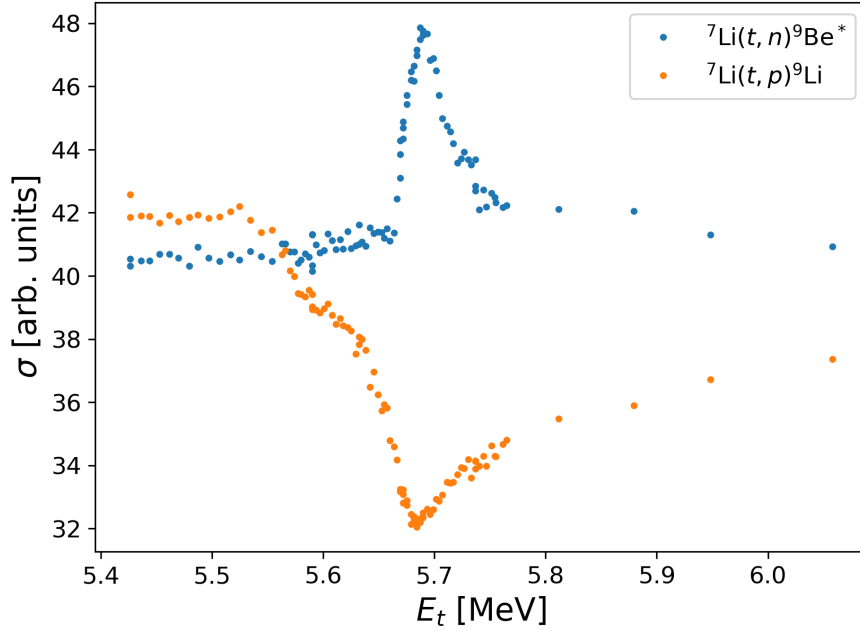


Figure 6.1: Cross-section in arbitrary units for the reactions ${}^7\text{Li}(t, n){}^9\text{Be}^*$ and ${}^7\text{Li}(t, p){}^9\text{Li}$ is shown as a function of the energy of the triton projectile in laboratory coordinates. One can clearly see the opening of the channel ${}^7\text{Li}(t, n){}^9\text{Be}^*$ at ~ 5.68 MeV. Experimental data is taken from Ref. [249].

where η is the Sommerfeld parameter (see Eq. (1.14)). Eqs. (6.3) and (6.4) provide useful relations to extrapolate cross-sections for charged particles to low bombarding energies [237].

The conservation of particle flux is a consequence of the unitarity of the S-matrix. Consequently, the appearance of a Wigner cusp in a vicinity of the channel threshold will modify the cross-section in other channels. Indeed, the opening of a new reaction channel removes some of the flux from other reaction channels. Transfer of the particle flux among open reaction channels at the threshold of a new channel can be conveniently studied in a multichannel framework, like the GSM-CC [15, 16, 35, 36].

Wigner cusps are not related to any particular physical system or interaction among its constituents. They have been found experimentally not only in nuclear physics, but also in condensed matter in studies of carbon nanotubes [241, 242], in atomic physics in scattering of positrons by He atoms [243], in electron photodetachment and in collisions of ultracold atoms [244, 245], in hadronic physics in the $\pi^-p \rightarrow \pi^0n$ reaction at the opening of the η channel [246], and in many other systems (see Refs. [247, 248]).

More relevant to this work, there have been observations of Wigner cusps in nuclear reactions. For example, a Wigner cusp was found in the excitation functions in ${}^{90}\text{Zn}(d, p){}^{91}\text{Zn}$ ($d_{5/2}$, g.s.) and ${}^{90}\text{Zn}(d, p){}^{91}\text{Zn}$ ($s_{1/2}$, $E_x=1.21$ MeV) at the thresholds of the analogue states, namely the ${}^{90}\text{Zn}(d, n){}^{91}\text{Nb}$ ($d_{5/2}$, $E_x=9.48$ MeV) and ${}^{90}\text{Zn}(d, p){}^{91}\text{Zn}$ ($s_{1/2}$, $E_x=1.69$ MeV) channels, respectively [215]. Another examples of cusps in the cross-sections were found in the study of the ${}^{65}\text{Cu}(p, \gamma){}^{66}\text{Zn}$ and ${}^{65}\text{Cu}(p, \alpha_0){}^{62}\text{Ni}$ reactions, where at the opening of the ${}^{65}\text{Cu}(p, n){}^{65}\text{Zn}$ reaction threshold at $E_{CM}=2.13$ MeV there is a clear depletion of the cross-section at the threshold which is shaped as a cusp [216].

Reaction studies in light nuclei have also reported the observation of Wigner cusps. For example, the reactions ${}^7\text{Li}(t, n){}^9\text{Be}$ and ${}^7\text{Li}(t, p){}^9\text{Li}$ show a cusp in the cross-section

of both reactions at the threshold of the latter. Cusps in the excitation function of the ${}^7\text{Li}({}^3\text{He},p){}^9\text{Be}$ reaction were also reported as a consequence of interference with $T = 2$, ${}^{10}\text{B}$ states, which were corroborated with the cross-sections of the ${}^7\text{Li}({}^3\text{He},n){}^9\text{B}$ reaction [214, 249–251]. For further discussion and reactions reporting the existence of Wigner cusps in light nuclei see Ref. [214] and references therein. Other examples of nuclear reactions that show Wigner cusps as a consequence of the opening of reaction thresholds are given in Refs. [248, 252–256].

Fig. 6.1 shows an example of the flux transfer among different reaction channels in the case of triton induced reactions: ${}^7\text{Li}(t,n){}^9\text{Be}^*$ and ${}^7\text{Li}(t,p){}^9\text{Li}$ [249]. In this case, the opening of the ${}^7\text{Li}(t,n){}^9\text{Be}^*$ threshold removes some flux from the ${}^7\text{Li}(t,p){}^9\text{Li}$ reaction channel, resulting in a very clear Wigner cusp. The conclusion of experimental studies is that multichannel coupling manifests itself in salient changes of the cross-sections at various reaction thresholds. These changes have a counterpart in the modifications of many-body states, as will be discussed in the following sections.

Discrepancies between theory and experiment regarding SFs are well known. For example in studies of $(e,e'p)$ reactions there is a difference of about 35% with respect to a standard SM approach [257]. This discrepancy has been attributed to many diverse effects, like the coupling to high-momentum states, long-range, short-range, or tensor correlations [258–261].

More recently, it has been observed that the ratio between experimental and theoretical cross-sections depends on the asymmetry of neutron (S_{1n}) and proton (S_{1p}) separation energies [262–264]. The physical interpretation of the origin of discrepancies arising from the asymmetry between S_{1p} and S_{1n} remains debated [264]. One explanation was put forward in Ref. [230] where SMEC and GSM calculations indicated that the SF of well-bound orbits are strongly suppressed, whereas SFs of weakly bound states are less impacted. This non-intuitive result has been explained by the coupling to the non-resonant continuum. When a minority species nucleon (nucleon from the well bound fluid) is removed, the daughter nucleus moves in the direction of the dripline which leads to significant changes in the configuration of weakly-bound nucleons that are impacted by continuum effects. As a consequence, the SF is reduced. On the contrary, when a majority species nucleon (nucleon from the weakly bound nucleon fluid) is removed, the daughter nucleus moves away from the dripline and stays close to the core of the parent system. In this case, one expects that the SF is large [230]. The isospin dependence of spectroscopic factors has been discussed in Refs. [265–275]. Further discussion of the SFs can be found in Ref. [261].

The theoretical study of $|S_{1n} - S_{1p}|$ -dependence of the SFs can be conveniently studied in the OQS framework of the continuum shell models, such as the SMEC or the GSM. By an appropriate adjustment of the Hamiltonian parameters, one can tune the separation energies in such a way that it is possible to verify what happens close to the particle emission threshold or, in other words, when the one nucleon separation energy tends to zero. This was done in GSM first for ${}^6,7\text{He}$ nuclei in Ref. [38] where it was shown that Wigner cusps in the SFs: $\langle {}^6\text{He}(0_1^+) | [{}^5\text{He}(3/2_1^-) \otimes n(p_{3/2})]^{0^+} \rangle^2$ and $\langle {}^7\text{He}(3/2_1^-) | [{}^6\text{He}(0_1^+) \otimes n(p_{3/2})]^{0^+} \rangle^2$, are noticeable at the particle emission thresholds. In this study, the SFs calculated in GSM have been compared to the SFs calculated in the SM to see the effect of the continuum coupling. It was found that the coupling between discrete states and the non-resonant continuum is necessary to account for the Wigner threshold effect because both the SM calculations and the GSM calculations in the pole approximation did not show any Wigner cusp behavior while the full GSM calculations did. Hence the cusps in the SF can be interpreted as the interference between the non-resonant continuum and resonant states at

the particle emission threshold.

The Wigner cusp in SFs is a consequence of the unitarity which is rigorously respected in the GSM approach. At the particle emission threshold, some of the probability flux goes to the new channel(s) that in turn changes the occupancy of single-particle shells. In Ref. [39] a calculation for $\ell = 2$ waves was done in ^{18}O for the SF $\langle ^{18}\text{O}(0_3^+) | [^{17}\text{O}(3/2_1^+) \otimes n(d_{3/2})]^{0+} \rangle^2$, where the cusp was reported in the first derivative of the SF with respect to the neutron separation energy. Moreover, in Ref. [166] the SFs: $\langle ^6\text{He}(0_1^+) | [^5\text{He}(3/2_1^-) \otimes n(p_{3/2})]^{0+} \rangle^2$ and $\langle ^6\text{Be}(0_1^+) | [^5\text{Li}(3/2_1^-) \otimes p(p_{3/2})]^{0+} \rangle^2$, were analysed by setting both proton and neutron emission threshold at the same energy with respect to the threshold. Different dependencies on energy distance from the decay threshold in $\langle ^6\text{He}(0_1^+) | [^5\text{He}(3/2_1^-) \otimes n(p_{3/2})]^{0+} \rangle^2$ and $\langle ^6\text{Be}(0_1^+) | [^5\text{Li}(3/2_1^-) \otimes p(p_{3/2})]^{0+} \rangle^2$ imply that the mirror many-body systems at the respective neutron and proton dripline will, in general, have different SFs. From this study it was concluded that the coupling to the continuum could cause isospin and mirror symmetry breaking.

6.2 From threshold effects to clusterization

Ikeda diagram [7] for $N\alpha$ nuclei, where N is the number of α -clusters systematize the appearance of molecular like nuclear states close to the alpha particle emission thresholds. Later, Ikeda diagram was extended to include neutrons in the molecular-like states close to the particle emission thresholds [276–279]. Near-threshold states have been modeled with either *a priori* models like the SM or *a posteriori* models like the cluster models [280–282]. In the former models, degrees of freedom are those of the valence nucleons moving in selected single-particle levels, whereas the latter models, based on a molecular viewpoint, use cluster building blocks, such as α -particles. Near-threshold cluster states or cluster correlations are present in several systems like the ground state of the Borromean nucleus ^{11}Li which resembles the configuration $[^9\text{Li} \otimes 2n]$ rather than $[^{10}\text{Li} \otimes n]$ [283], with a similar situation in its mirror ^{11}O being a 2p emitter [284]. Further examples include ^9He , ^6Li , ^7Be , ^7Li , ^{11}C , ^{17}O , ^{20}Ne , ^{26}O , etc.

The observation of Ikeda *et al.* has been extended to any cluster-like structure including unstable systems like dineutron or ^8Be [8, 9]. Let us consider ^{11}Li , as an example. This Borromean nucleus has a well known halo structure [285–287]. Indeed, the two-neutron separation energy is very close to the ground state, which, assuming that the conjecture of Refs. [8, 9] is correct, would explain the appearance of the two neutron correlations in the ground state of ^{11}Li . An even more famous example is 0_2^+ state of ^{12}C , the so-called Hoyle state [288]. This state, however, is expected to be dominated by the $^8\text{Be} + \alpha$ correlations rather than 3α correlations because the $^8\text{Be} + \alpha$ threshold is closer in energy to the Hoyle state than the 3α threshold. Another recent example comes from an observation of the $1/2_1^-$ resonance in ^{15}F about 4.5 MeV above the $^{16}\text{O} + p$ threshold and close to the $^{13}\text{N} + 2p$ threshold. Indeed, this state was found to be narrow because of the strong coupling to the two proton threshold and a very small Q -value for the 2p-decay ($Q_{2p} = 129$ keV) [220]. Structure of the near-threshold states cannot be the consequence of a specific feature of the nuclear interaction because then the nucleon-nucleon correlations or clustering correlations in near-threshold states would appear at random. The experimental data are telling us the contrary, by providing countless examples of the close relation between the structure of a near-threshold state and the nature of a nearby channel.

Universality of the clustering phenomenon is motivated by the basic properties of the S -matrix in a multichannel framework [236]. Each threshold is a branching point (a non-

analytic point) of the S -matrix. So for example, below any particle emission threshold we have one scattering solution, which is regular in the whole space. As the first reaction threshold opens at energy E_1 we obtain the particle emission solution in addition to the regular solution. As we keep opening new decay channels, we obtain a regular scattering solution that coexists with a set of different decay channels, forming together the coupled multichannel representation of the OQS. Hence, going to higher excitation energies, the complexity in the wave function gradually builds up.

In the OQS approach, different SM states with the same quantum numbers couple to a given decay channel. This induces a mixing among them, which may lead to the formation of the collective eigenstate, the so-called *aligned* eigenstate, which couples strongly to the decay channel and carries an imprint of its features. This is a generic feature of the OQS which is absent in the standard SM.

An indication for the enhanced probability of near-threshold states comes from the R -matrix approach [213]. In this approach, a near-threshold resonance could appear because of the increased density of levels with large reduced widths [213, 237, 289]. The density of states is given by:

$$\rho(E) = \frac{\frac{1}{2}\Gamma_\lambda}{(E_\lambda + \Delta_\lambda - E)^2 + (\frac{1}{2}\Gamma_\lambda)^2}, \quad (6.5)$$

where E_λ and Γ_λ are the energy and width of a level λ , respectively, and Δ_λ are the level shifts. In this formalism, the resonance energy is defined as $E_r = E_\lambda + \Delta_\lambda$, which corresponds to the maximum of the function $\rho(E)$ in Eq. (6.5)¹. Using Eq. (6.5), Barker [213] showed that there is an enhancement of the level density close to the particle emission thresholds and that this enhancement is strongest for low potential barriers or lack thereof. This means that $\ell = 0$ neutrons should show the strongest effect. Moreover, the maximum of the enhancement is shifted from the thresholds according to how high the potential barrier is.

A more intuitive form of the level density is associated to the phase shifts [290, 291]:

$$\rho_\ell(E) = \frac{1}{\pi} \frac{d\delta_\ell(E)}{dE}. \quad (6.6)$$

This relation suggests the connection between the Wigner cusp phenomenon in cross-sections and the appearance of near threshold states, as one would expect a sharp change in phase shifts close to the resonance [292]. This sharp change of the phase shift and associated enhancement of the level density is not limited to resonances, but one also expects a similar result for antibound states [292].

The key question is how to characterize the configuration mixing in OQSSs. This mixing is directly or indirectly responsible for resonance trapping [293–297], and super-radiance phenomenon [298, 299], modification of spectral fluctuations [300], clustering and exceptional points [8, 301], violation of orthogonal invariance and channel equivalence [297], pairing anti-halo effect [86], anti-odd-even staggering of separation energies [302], etc.

One way of analyzing the configuration mixing is to study the avoided crossing of resonances that are associated with a nearby EP. EPs [62], exist in non-Hermitian Hamiltonians. The basic idea of how an EP is formed can be grasped by considering a 2×2 matrix with real or complex energies E_1 and E_2 at the diagonal, and complex off-diagonal matrix elements. By a suitable choice of real and imaginary parts of the off-diagonal mixing matrix elements, the energies and the wave functions of the two levels may coalesce

¹This means that the narrower the resonance, the closer the resonance and level energies are.

forming an EP. The EP is a singular point in the Hilbert space which locally, at the energy of the EP, has one linearly independent vector less, i.e. the Hilbert space has locally one dimension less.

A more convenient way to look into effects of configuration mixing in near-threshold states is to calculate the suitably defined correlation energy. In SMEC, one defines a continuum-coupling correlation energy as the difference between the effective Hamiltonian \mathcal{H}_{QQ} , which includes effects of the coupling to the scattering continuum on discrete SM states (see Eq. (2.33)), and the CQS SM Hamiltonian $H_{\text{SM}} \equiv H_{QQ}$, in a certain OQS eigenvector $|\Psi_i\rangle$ of the \mathcal{H}_{QQ} :

$$E_{\text{corr},i}^{(\ell)}(E) = \langle \Psi_i | \mathcal{H}_{QQ}(E) - H_{QQ} | \Psi_i \rangle. \quad (6.7)$$

Here, $E_{\text{corr},i}^{(\ell)}$ is the correlation energy in the OQS eigenstate i with angular momentum ℓ [8, 229, 303]. As seen in the above expression, the idea is that the continuum-coupling correlation energy (6.7) captures the influence of coupling between discrete and continuum states and provides an account of the interplay between the continuum-coupling induced configuration mixing and the effects of the Coulomb and centrifugal potentials. Indeed, it was found that the maximum of the correlation energy is at the threshold for $\ell = 0$ neutrons. For protons the effect is shifted above the threshold due to the Coulomb barrier [8]. Moreover, the minimum of the correlation energy $E_{\text{corr},\text{min}}$ indicates the optimal energy where the coupling to the decay channel is the strongest one [8, 9]. The optimal energy is also a centroid of the opportunity window where the appearance of the aligned state is most probable. The magnitude of the correlation energy is of the same order as the pairing correlation energy which greatly modifies the nucleon-nucleon correlations in the vicinity of the Fermi surface [304].

To see the effects of configuration mixing, we can express the eigenstates of the effective Hamiltonian $|\Psi_i\rangle$ as a mixture of SM eigenstates $|\phi_i^{\text{SM}}\rangle$ [10]:

$$|\phi_i^{\text{SM}}\rangle \rightarrow |\Psi_i\rangle = \sum_j d_{ji} |\phi_j^{\text{SM}}\rangle, \quad (6.8)$$

where the $[d_{ji}]$ is an orthonormal transformation matrix. The square of the matrix element $d_{ji}^2 \in \mathbb{C}$ is the weight of the SM eigenstate $|\phi_i^{\text{SM}}\rangle$ in the correlated OQS eigenstate $|\Psi_i\rangle$, so it follows:

$$\sum_i \text{Re}[d_{ji}^2] = 1, \quad \sum_i \text{Im}[d_{ji}^2] = 0. \quad (6.9)$$

Mixing matrix elements between different SM states are strongest at the minimum of the continuum-coupling correlation energy and decrease with increasing distance between SM states and the studied threshold. Consequently, the strength of the optimal correlation energy decreases with increasing distance to the threshold. This optimal distance depends on the competition between the attractive continuum-coupling and the repulsive Coulomb and centrifugal interactions. Indeed, the continuum coupling effects for heavier nuclei will be negligible at the charged particle thresholds [8, 9].

In GSM, one cannot define the correlation energy in the same way as in SMEC because there is no projection of continuum-coupling effects on discrete eigenvalues which would generate the energy dependence in the Hamiltonian. Contrary to SMEC, where one defines the open quantum subsystem of the CQS by the projection technique [3, 4], in GSM the whole system can be either open or close (see Fig. 3.4). The discrete part of the spectrum in GSM is embedded in the background of complex energy scattering states.

A possible solution is to reformulate GSM in a reaction channel representation, i.e. the GSM-CC. In a vicinity of a threshold of a certain channel c , one can define the

continuum-coupling correlation energy in a given many-body GSM-CC eigenstate $|\Psi^{J^\pi}\rangle$ by a difference of energies:

$$E_{\text{corr},c}^{J^\pi} = \langle \Psi^{J^\pi} | H | \Psi^{J^\pi} \rangle - \langle \Psi_\phi^{J^\pi} | H | \Psi_\phi^{J^\pi} \rangle = E_{\text{full}}^{J^\pi} - E_\phi^{J^\pi}, \quad (6.10)$$

where $|\Psi^{J^\pi}\rangle$ is the full GSM-CC solution defined in Eq. (4.5) as an expansion in terms of reaction channels, and $|\Psi_\phi^{J^\pi}\rangle$ is the wave function expansion without the channel c . $E_{\text{full}}^{J^\pi}$ and $E_\phi^{J^\pi}$ in Eq. (6.10) are the energy eigenvalues corresponding to the eigenfunctions $|\Psi^{J^\pi}\rangle$ and $|\Psi_\phi^{J^\pi}\rangle$, respectively.

6.3 Near threshold effects in the coupled channel framework

In this section we will present the application of the GSM-CC in the multi-mass partition formulation to study consequences of the continuum-coupling on the structure of near-threshold states in ${}^7,8\text{Be}$ and ${}^7\text{Li}$. First, we will address features of the wave function expressed in a basis of reaction channels. Second, we will analyze near-threshold effects in the continuum coupling correlation energy defined in Eq. (6.10). Third, we will study the spectroscopic factors for resonances and compare them with the reaction channel probabilities.

6.3.1 Near-threshold effects in ${}^7\text{Be}$ and ${}^7\text{Li}$

To study the near-threshold effects, we proceed as follows. We take the same model space and effective interaction as described in Sect. 5.2. Afterwards, to vary the distance of a state to the threshold we change the depth V_0 of the Woods-Saxon potential. V_0 is kept the same for all ℓ partial waves. The one-body potential generating the single-particle basis remains unchanged when the depth of a core potential varies. The states of ${}^6,7\text{Li}$ and ${}^7\text{Be}$ are calculated with the same effective interaction. This means that the energy of ${}^6\text{Li}$ moves alongside with the energy of ${}^7\text{Li}$ and ${}^7\text{Be}$. However, the binding energy of ${}^3\text{H}$ and ${}^3\text{He}$ remains unchanged.

We focus on the reaction channel distribution to study effects of the particle emission thresholds in the wave function. As discussed previously and seen in Fig. 5.1, the lowest decay threshold in ${}^7\text{Li}$ is the ${}^4\text{He} + {}^3\text{H}$ threshold. Neutron decay thresholds $[{}^6\text{Li}(K_i^\pi) \otimes n(\ell j)]^{J^\pi}$ open at higher excitation energies. Proton decay thresholds are not considered in the case of ${}^7\text{Li}$.

Figure 6.2 presents the dependence of the orthogonal channel weights b_c^2 and partial widths Γ_c in the $5/2_2^-$ state on the energy difference with respect to the lowest one-neutron decay threshold $[{}^6\text{Li}(1_1^+) \otimes n(\ell j)]^{5/2^-}$. It should be noticed that in the complex-energy framework of the GSM-CC, the squared wave-function amplitude (channel weight) $\mathcal{R}e[b_c^2]$ can be negative [14]. At the leading order, the statistical uncertainty of the $\mathcal{R}e[b_c^2]$ is associated with its imaginary part $\mathcal{I}m[b_c^2]$ [15]. $\mathcal{R}e[b_c^2]$ is the average value of the corresponding channel probability in different measurements, while $\mathcal{I}m[b_c^2]$ can be related to the dispersion rate over time in the measurement, and hence represents its statistical uncertainty [15]. The partial widths are calculated using the current formula [15, 305]. For details of the current formula, see App. A.2. The energy difference between the $5/2_2^-$ state and neutron-threshold energy is varied by changing the depth V_0 of the ${}^4\text{He}$ core potential.

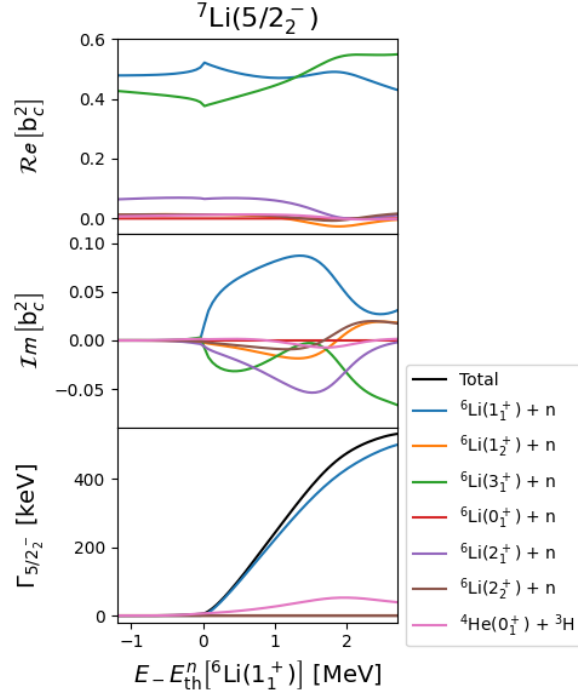


Figure 6.2: From top to bottom: the real and imaginary parts of the channel probability weights $b_c^2 = \langle \tilde{w}_c | w_c \rangle^2$, and the partial widths of each reaction channel in the $5/2_2^-$ state of ${}^7\text{Li}$. Contributions of all partial waves ℓj in reaction channels $[{}^6\text{Li}(1_1^+) \otimes n(\ell j)]^{5/2^-}$ are summed and everything is plotted as a function of the distance of the state to the neutron threshold. The meaning of curves for different channels is explained in the attached insert. Each curve represents the sum of all reaction channels built on the same many-body state of ${}^6\text{Li}$.

Both real and imaginary parts of the channel weights are shown in Fig. 6.2. Below the neutron emission threshold at $E - E_{\text{th}}^n[{}^6\text{Li}(1_1^+)] < 0$, all neutron reaction channels are closed, i.e. the state $5/2_2^-$ is bound with respect to the emission of neutron. At $E - E_{\text{th}}^n[{}^6\text{Li}(1_1^+)] \simeq -0.8$ MeV, the triton channel $[{}^4\text{He}(0_1^+) \otimes {}^3\text{H}(2F_{5/2})]^{5/2^-}$ opens. This opening has no visible consequences on the wave function $5/2_2^-$. This is consistent with the results in Sect. 5.2, where the $5/2_2^-$ state has a small component of cluster in the wave function. At $E - E_{\text{th}}^n[{}^6\text{Li}(1_1^+)] = 0$, the energy of the $5/2_2^-$ GSM-CC state coincides with the energy of the decay threshold in the channel $[{}^6\text{Li}(1_1^+) \otimes n(\ell j)]^{5/2^-}$, and for $E - E_{\text{th}}^n[{}^6\text{Li}(1_1^+)] > 0$, neutron and triton can be emitted.

The contribution of the reaction channel $[{}^6\text{Li}(1_1^+) \otimes n(\ell j)]^{5/2^-}$ dominates below the neutron emission threshold. The second largest probability corresponds to the channel $[{}^6\text{Li}(3_1^+) \otimes n(\ell j)]^{5/2^-}$. In the vicinity of the lowest neutron threshold, the probability of a channel $[{}^6\text{Li}(1_1^+) \otimes n(\ell j)]^{5/2^-}$ in the wave function of $5/2_2^-$ state promptly increases, what is a manifestation of the alignment of the GSM-CC state $5/2_2^-$ with the neutron decay channel. One may notice a cusp in the energy dependence of probability of the channel $[{}^6\text{Li}(1_1^+) \otimes n(\ell j)]^{5/2^-}$. The increased probability of this channel is associated with the opposite effect in other channels, mainly in the channel $[{}^6\text{Li}(3_1^+) \otimes n(\ell j)]^{5/2^-}$.

At higher energies, below opening of the next neutron channel $[{}^6\text{Li}(3_1^+) \otimes n(\ell j)]^{5/2^-}$, the probability of this closed channels increases gradually. The $5/2_2^-$ state in this example changes the nature depending on the embedding continuum. For $E - E_{\text{th}}^n[{}^6\text{Li}(1_1^+)] \sim 0$, the structure of the $5/2_2^-$ state is dominated by the coupling to the reaction channel $[{}^6\text{Li}(1_1^+) \otimes$

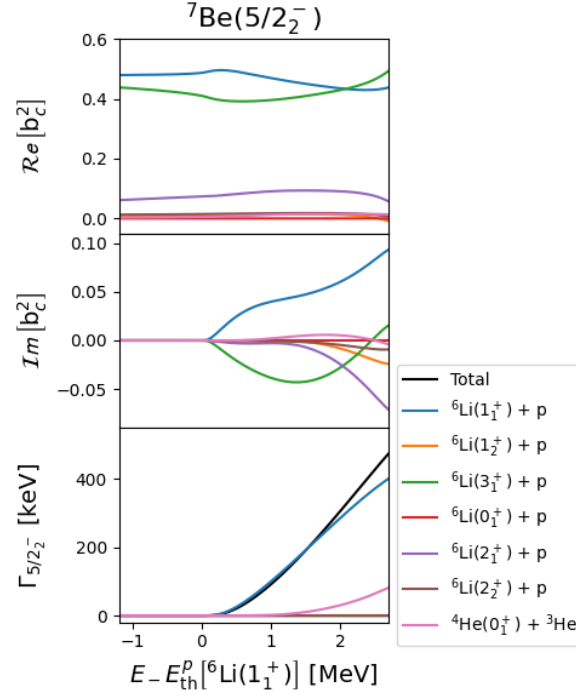


Figure 6.3: The same as in Fig. 6.2 but for the mirror state $5/2^-$ in ${}^7\text{Be}$. All quantities are plotted as a function of the distance of the state to the proton threshold $[{}^6\text{Li}(1_1^+) \otimes p(\ell j)]^{5/2^-}$.

$n(\ell j)^{5/2^-}$ and the weight of this channel dominates the $5/2_2^-$ wave function. However, at higher energies for $E - E_{\text{th}}^n[{}^6\text{Li}(1_1^+)] \geq 1.5$ MeV, close to the threshold of the channel $[{}^6\text{Li}(3_1^+) \otimes n(\ell j)]^{5/2^-}$, the $5/2_2^-$ state changes its nature and becomes strongly influenced by the channel $[{}^6\text{Li}(1_1^+) \otimes n(\ell j)]^{5/2^-}$. Hence, the $5/2_2^-$ behaves like a 'chameleon state', changing its nature depending on the surrounding environment, i.e. on the scattering states and nearby decay channels in the case of the nuclear chameleon state.

The imaginary parts of channel weights b_c^2 are zero below the neutron emission threshold and show a complicate behavior above it. Above the decay threshold $[{}^6\text{Li}(1_1^+) \otimes n(\ell j)]^{J^\pi}$ and below the next threshold $[{}^6\text{Li}(3_1^+) \otimes n(\ell j)]^{J^\pi}$, the major contribution comes from the open reaction channel $[{}^6\text{Li}(1_1^+) \otimes n(\ell j)]^{5/2^-}$. The magnitude of this contribution decreases when we approach the threshold of the channel $[{}^6\text{Li}(3_1^+) \otimes n(\ell j)]^{5/2^-}$ whereas the magnitude of the (negative) contribution of the channel $[{}^6\text{Li}(3_1^+) \otimes n(\ell j)]^{5/2^-}$ strongly increases. The interplay between these two reaction channels continues to dominate the evolution pattern of imaginary parts above this threshold. The dependence of the partial neutron decay width on energy with respect to the lowest neutron-energy threshold is plotted in the lowest part of Fig. 6.2. One may see a gradual increase of the width with increasing excitation energy.

Figure 6.3 shows results of calculations of the channel weights and partial widths of the in the $5/2_2^-$ state of the mirror nucleus ${}^7\text{Be}$. As expected, the mirror system preserves the main features seen for the $5/2_2^-$ state of ${}^7\text{Li}$, namely roughly the same wave function composition. Moreover, the chameleon-like features in the proximity of the $[{}^6\text{Li}(3_1^+) \otimes n(\ell j)]^{J^\pi}$ threshold are also preserved. The opening of the ${}^3\text{He}$ channel $[{}^4\text{He}(0_1^+) \otimes {}^3\text{H}(2F_{5/2})]^{5/2^-}$ does not have any appreciable effects. In the vicinity of the proton emission threshold, there is an increase of the weight of the channel $[{}^6\text{Li}(1_1^+) \otimes p(\ell j)]^{5/2^-}$ which similarly to the neutron case $[{}^6\text{Li}(1_1^+) \otimes n(\ell j)]^{5/2^-}$ in ${}^7\text{Li}$, is a manifestation

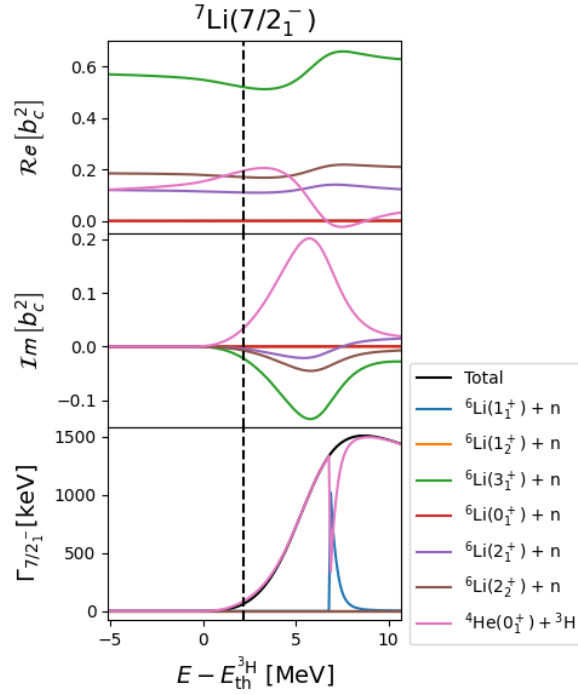


Figure 6.4: The real and imaginary parts of the channel probability weights $b_c^2 = \langle \tilde{w}_c | w_c \rangle^2$ and the partial decay widths in various reaction channels of the $7/2_1^-$ state in ${}^7\text{Li}$ are shown as a function of the distance with respect to the lowest decay threshold ${}^4\text{He} + {}^3\text{H}$. The dashed vertical line shows the GSM-CC energy of the $7/2_1^-$ resonance. Each curve represents the sum of all reaction channels built of the same state of ${}^6\text{Li}$.

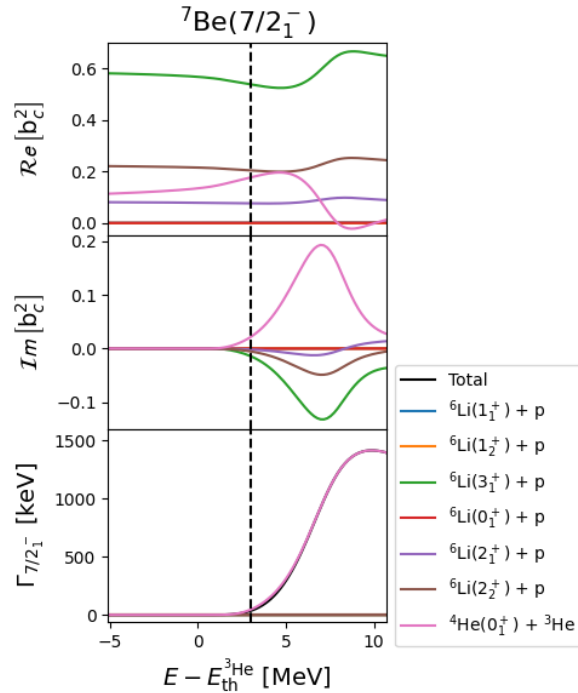


Figure 6.5: The same as in Fig. 6.4 but for the mirror state $7/2^-$ in ${}^7\text{Be}$. All quantities are plotted with respect to the lowest decay threshold ${}^4\text{He} + {}^3\text{He}$. The dashed vertical line gives the GSM-CC energy for the $7/2_1^-$ resonance.

of the alignment with the proton decay channel. Differences between proton and neutron cases (see Figs. 6.2 and 6.3) are mainly the delayed and smoothed effects at the $[{}^6\text{Li}(1_1^+) \otimes \text{p}(\ell j)]^{5/2^-}$ threshold due to the Coulomb interaction. Indeed, in the proton case there is no cusp but a smooth bump after crossing the threshold.

Figure 6.4 presents the dependence of channel weights and partial widths Γ_c in the $7/2_1^-$ state of ${}^7\text{Li}$ on the energy difference with respect to the lowest decay threshold $[{}^4\text{He}(0_1^+) \otimes {}^3\text{H}(L_{\text{CM}} J_{\text{int}} J_{\text{P}})]^{J^\pi}$. This state has a pronounced ${}^3\text{H}$ -cluster structure (see Table 5.3). However, in the whole interval of energies, neutron reaction channel $[{}^6\text{Li}(3_1^+) \otimes \text{n}(\ell j)]^{7/2^-}$ provides the major contribution. The probability of the triton channel $[{}^4\text{He}(0_1^+) \otimes {}^3\text{H}(2F_{7/2})]^{7/2^-}$ grows when approaching the emission threshold and has a maximum close to 3.3 MeV above the threshold energy $E_{\text{th}}^{3\text{H}}$. The maximum of the imaginary part of ${}^3\text{H}$ probability is shifted to slightly higher energy with respect to the maximum of the real part.

The alignment of $7/2_1^-$ state with the channel $[{}^4\text{He}(0_1^+) \otimes {}^3\text{H}(2F_{7/2})]^{7/2^-}$ arises at a higher energy than seen in $5/2^-$ state (see Fig. 6.2) due to both the Coulomb interaction and the angular momentum involved in this reaction channel. At $E - E_{\text{th}}^{3\text{H}} \simeq 6.8$ MeV, at the opening of the channel $[{}^6\text{Li}(1_1^+) \otimes \text{n}(\ell j)]^{7/2^-}$ whose weight is barely visible in Fig. 6.4, the partial width of the ${}^3\text{H}$ decay channel strongly diminishes and the channel $[{}^6\text{Li}(1_1^+) \otimes \text{n}(\ell j)]^{7/2^-}$ becomes dominant. Above the threshold of $[{}^6\text{Li}(1_1^+) \otimes \text{n}(\ell j)]^{7/2^-}$ channel, the triton partial width dominates again. This radical change of the $7/2_1^-$ eigenstate in the vicinity of the neutron threshold $[{}^6\text{Li}(1_1^+) \otimes \text{n}(\ell j)]^{7/2^-}$ is seen only in the singular energy dependence of decay partial widths. This singularity is a threshold effect due to an interplay between neutron and triton channels in a narrow range of energies around the neutrons decay threshold.

Figure 6.5 presents the dependence of channel weights and partial widths in the $7/2_1^-$ state of the mirror nucleus ${}^7\text{Be}$ on the energy difference with respect to the lowest decay threshold ${}^4\text{He} + {}^3\text{He}$. The effects due to the ${}^3\text{He}$ emission threshold appears at slightly higher energies than seen in the mirror system because of a stronger Coulomb interaction. One may notice that the singular variation of partial widths, seen at the neutron threshold $[{}^6\text{Li}(1_1^+) \otimes \text{n}(\ell j)]^{7/2^-}$ in ${}^7\text{Li}$, is absent at the proton threshold $[{}^6\text{Li}(1_1^+) \otimes \text{p}(\ell j)]^{7/2^-}$ in ${}^7\text{Be}$.

6.3.2 Near-threshold effects in ${}^8\text{Be}$

Low-lying states in this nucleus exhibit a presence of α -correlations (see Table 5.6). In the following, we shall discuss the evolution of orthogonal reaction channel probabilities and α -emission decay width as a function of the energy distance $E - E_{\text{th}}^{4\text{He}}[{}^4\text{He}(0_1^+)]$ from the α -decay threshold. In all calculations presented in this section we used three mass partitions, leaving out the ${}^6\text{Li} + \text{d}$ channels. Therefore there are differences compared to results presented in Sect. 5.3. We then proceed in a similar fashion as in the previous section where we use the same interaction described in Sect. 5.3 and vary the depth V_0 of the core potential.

Figure 6.6 shows the energy variation of channel weights for the ground state 0_1^+ . The dashed vertical line corresponds to the experimental energy of the 0_1^+ state. The real part of the channel weights $\mathcal{R}e[b_c^2]$ in the channel $[{}^4\text{He}(0_1^+) \otimes {}^4\text{He}(1S_0)]^{0^+}$ has a maximum at energy $E - E_{\text{th}}^{4\text{He}}[{}^4\text{He}(0_1^+)] \simeq 0.7$ MeV, above the ${}^4\text{He} + {}^4\text{He}$ threshold energy. Therefore, at the GSM-CC energy of the resonance 0_1^+ , the value of $\mathcal{R}e[b_c^2]$ is significantly lower than at the optimal energy for ${}^4\text{He}$ clusterization. The maximum of the imaginary part of the channel weight $\mathcal{I}m[b_c^2]$ at $E - E_{\text{th}}^{4\text{He}}[{}^4\text{He}(0_1^+)] \simeq 1$ MeV is shifted slightly above the maximum of the real part. At energies $E - E_{\text{th}}^{4\text{He}}[{}^4\text{He}(0_1^+)] \geq 1$ MeV, both real and imaginary parts of the α -channel probability drop rapidly, approaching nearly a constant

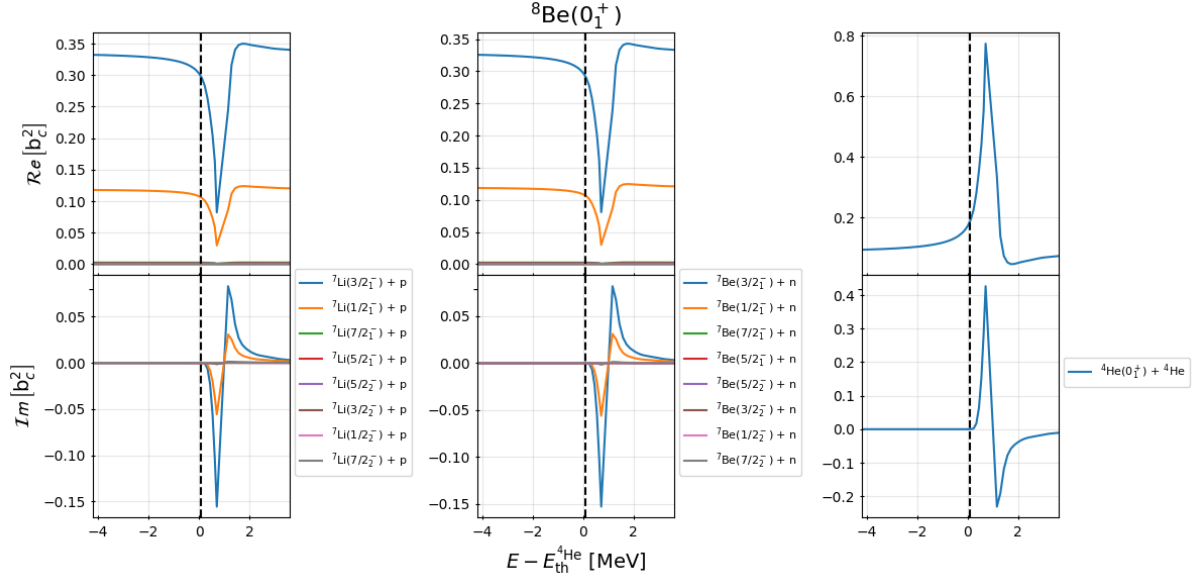


Figure 6.6: From top to bottom: the real and imaginary parts of the channel probability weights $b_c^2 = \langle \tilde{w}_c | w_c \rangle^2$ in the 0_1^+ state of ${}^8\text{Be}$. Different ${}^7\text{Li}+p$, ${}^7\text{Be}+n$, and ${}^4\text{He}+{}^4\text{He}$ reaction channels are shown in the left, middle and right column, respectively. The meaning of different curves is given in the insert attached to each column. Each curve for proton and neutron channels represents the sum of all channels which are built on the same many-body state of ${}^7\text{Li}$ and ${}^7\text{Be}$, respectively. The dashed vertical line gives the GSM-CC energy of the 0_1^+ resonance (see Fig. 5.6).

value.

The maximum in the α -channel $[{}^4\text{He}(0_1^+) \otimes {}^4\text{He}(1S_0)]^{0+}$ probability is associated with the opposite behavior in both proton $[{}^7\text{Li}(3/2_1^-) \otimes p(\ell j)]^{0+}$, $[{}^7\text{Li}(1/2_1^-) \otimes p(\ell j)]^{0+}$ and neutron $[{}^7\text{Be}(3/2_1^-) \otimes n(\ell j)]^{0+}$, $[{}^7\text{Be}(1/2_1^-) \otimes n(\ell j)]^{0+}$ channels. Other proton and neutron channels do not play any role in this phenomenon. In fact, both, proton (${}^7\text{Li} + p$) and neutron (${}^7\text{Be} + n$) parts of the ${}^8\text{Be}$ wave function collapse in the vicinity of the α -channel threshold. It should be noticed that, away from the α -threshold, the 0_1^+ state appears to a large extent as the SM-like state which is composed mainly by ${}^7\text{Li}+p$ and ${}^7\text{Be}+n$ reaction channels. Thus, the α -clustering appears as the OQS threshold phenomenon resulting from the coupling of SM states to the $[{}^4\text{He}(0_1^+) \otimes {}^4\text{He}(1S_0)]^{0+}$ decay channel.

Figure 6.7 shows the energy variation of channel probability weights for 2_1^+ , the first excited state of ${}^8\text{Be}$. At low energies, $E - E_{\text{th}}^{{}^4\text{He}}[{}^4\text{He}(0_1^+)] \simeq +1.7$ MeV, above the decay threshold in the channel $[{}^4\text{He}(0_1^+) \otimes {}^4\text{He}(1D_2)]^{2+}$, the 2_1^+ state has some features of α -clustering and the corresponding α -channel weight is: $\mathcal{R}e[b_c^2] \simeq 0.11$. The maximum of the imaginary part $\mathcal{I}m[b_c^2]$ is found at higher energy $E - E_{\text{th}}^{{}^4\text{He}}[{}^4\text{He}(0_1^+)] \sim 2.5$ MeV. Within an interval of about 4 MeV, the α -clustering is strongly reduced and the probability of the channel $[{}^4\text{He}(0_1^+) \otimes {}^4\text{He}(1D_2)]^{2+}$ decreases from 11% to about 5% and stabilizes at higher energies. The maximum of $\mathcal{R}e[b_c^2]$ is at lower energy than the calculated GSM-CC energy of this state (see Fig. 5.6). The fall-off of the α -clustering at higher energies is accompanied by the raise of probabilities of the one-nucleon channels built on the ground state $3/2_1^-$ and excited states $1/2_1^-$, $7/2_1^-$ and $5/2_1^-$ of ${}^7\text{Be}$ and ${}^7\text{Li}$. Within an interval of ~ 4 MeV, the 2_1^+ state changes its nature from a SM-like state with some α -cluster features to essentially a pure SM state. The significant decrease of the α -cluster weight going from the ground state 0_1^+ to the first excited 2_1^+ state could be caused by three factors: (i) the

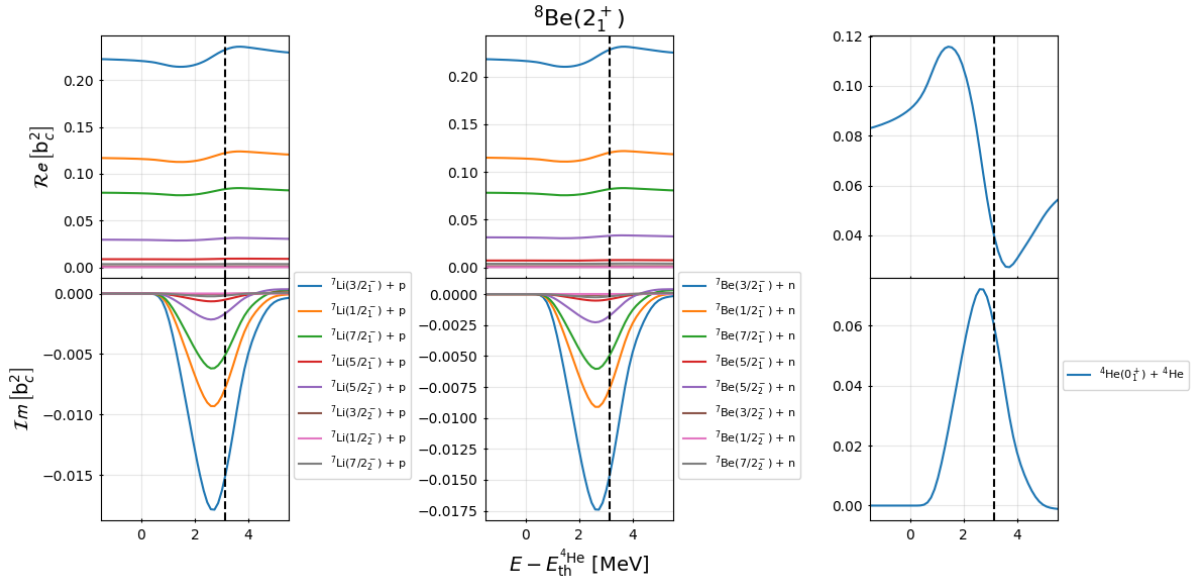


Figure 6.7: The same as in Fig. 6.6 but for the 2_1^+ state of ^8Be . The dashed vertical line gives the GSM-CC energy of the 2_1^+ resonance.

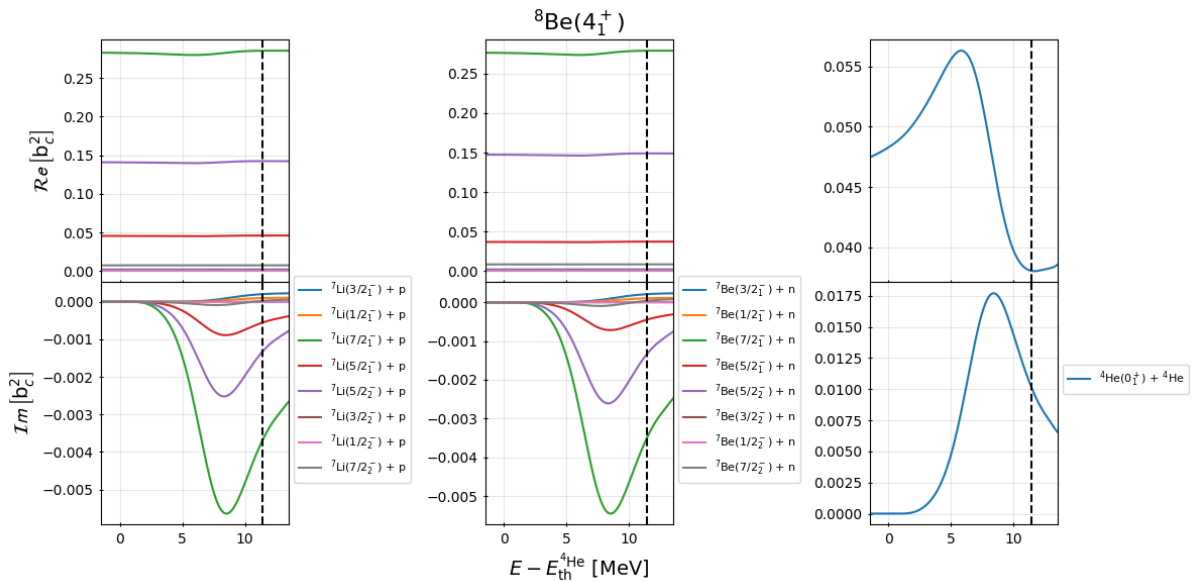


Figure 6.8: The same as in Fig. 6.6 but for the 4_1^+ state of ^8Be . The dashed vertical line gives the GSM-CC energy of the 4_1^+ resonance.

increased separation of the 2_1^+ resonance from the α -decay threshold, (ii) the centrifugal barrier, and (iii) the large width of the 2_1^+ resonance at its experimental energy.

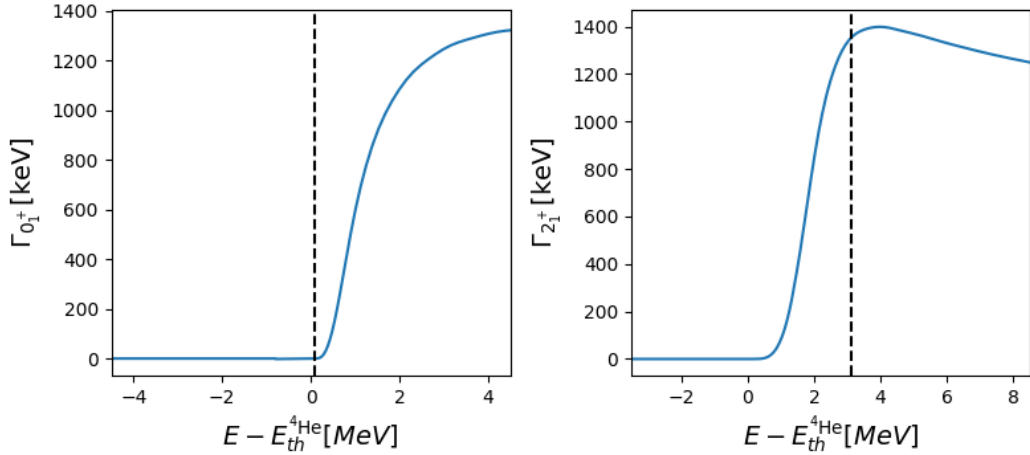


Figure 6.9: The dependence of α -decay width on energy distance $E - E_{\text{th}}^{4\text{He}}[{}^4\text{He}(0_1^+)]$ from the α -threshold for 0_1^+ (left panel) and 2_1^+ (right panel) states in ${}^8\text{Be}$. The vertical dashed line in both panels shows the corresponding energy of 0_1^+ and 2_1^+ states.

Figure 6.8 shows the energy variation of channel weights for the second excited state 4_1^+ . The patterns of the channel weights is similar to the preceding case of the 2_1^+ resonance (see Fig. 6.7). The maximum of $\mathcal{R}e[b_c^2]$ for the channel $[{}^4\text{He}(0_1^+) \otimes {}^4\text{He}(1G_2)]^{4+}$ lies below the calculated energy of the 4_1^+ of this state (see Fig. 6.8). The cluster probability in 4^+ state reaches its maximum at ~ 6 MeV above the threshold. Further away from that point it becomes a SM state. The maximum of $\mathcal{I}m[b_c^2]$ is shifted by ~ 3 MeV with respect to the maximum of $\mathcal{R}e[b_c^2]$. This energy shift is larger than what can be seen for the 2_1^+ resonance.

Figure 6.9 shows the energy dependence of the decay width for the ground state 0_1^+ and the first excited state 2_1^+ in ${}^8\text{Be}$. Contrary to the 0_1^+ state, the α -decay width of the 2_1^+ state is close to maximal at its experimental energy. One may notice that the maximum of the α -clustering in this state (see Fig. 6.7) corresponds to the excitation energy where the α decay width is relatively small.

6.3.3 Correlation energy in ${}^7,8\text{Be}$ and ${}^7\text{Li}$

In this section we shall discuss results for the continuum-coupling correlation energy (6.10) in GSM-CC calculations. For ${}^7\text{Li}$ and ${}^7\text{Be}$ we use the same method as before in Sect. 6.3.1, i.e. we vary the distance of a state to the threshold by changing the Woods-Saxon depth V_0 . For ${}^8\text{Be}$ we keep the depth of the Woods-Saxon potential constant and change the distance to the threshold manually. In the following calculations we use $E_{\text{CM}_{\text{max}}} = 8$.

An example is shown in Fig. 6.10 for the $5/2_2^-$ state in ${}^7\text{Li}$. Here the orthogonal channel probability weights for the states $|\Psi^{5/2_2^-}\rangle$, $|\Psi_{\phi}^{5/2_2^-}\rangle$ and the correlation energy $E_{\text{corr}}^{5/2_2^-}$, are shown as a function of the energy distance from the lowest one-neutron decay threshold $[{}^6\text{Li}(1_1^+) \otimes n(\ell j)]^{5/2^-}$. In the state $|\Psi_{\phi}^{5/2_2^-}\rangle$, the channel $[{}^6\text{Li}(1_1^+) \otimes p(\ell j)]^{5/2^-}$ is absent. Probability of the neutron channel $[{}^6\text{Li}(1_1^+) \otimes n(\ell j)]^{5/2^-}$ in the state $|\Psi^{5/2_2^-}\rangle$ grows while approaching the channel threshold and exhibits a cusp slightly above the neutron threshold. The minimum of the correlation energy associated with this channel is shifted by about 0.35 MeV above the threshold. This shift between the maximum of the real part

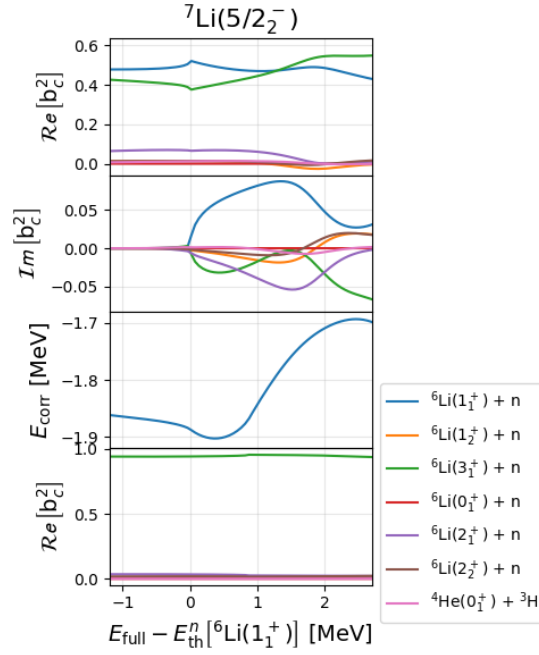


Figure 6.10: From top to bottom: (i) the real part of the channel weights $\mathcal{R}e[b_c^2]$ for the state $|\Psi^{5/2_2^-}\rangle$, (ii) the imaginary part of the channel weights $\mathcal{I}m[b_c^2]$ for the state $|\Psi^{5/2_2^-}\rangle$, (iii) the correlation energy $E_{\text{corr}}^{5/2_2^-}$, and (iv) the real part of the channel weights $\mathcal{R}e[b_c^2]$ for the state $|\Psi_{\phi}^{5/2_2^-}\rangle$, are shown as a function of the distance with respect to the one-neutron decay threshold $[{}^6\text{Li}(1_1^+) \otimes n(\ell j)]^{5/2^-}$.

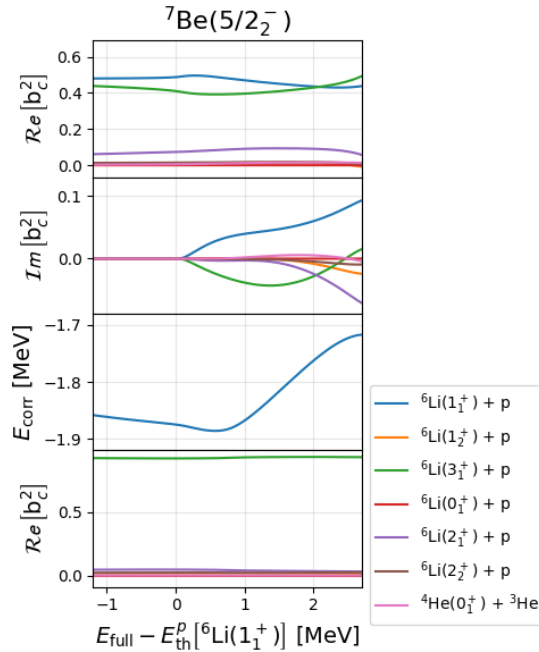


Figure 6.11: The same as in Fig. 6.10 but in a mirror nucleus ${}^7\text{Be}$. All quantities are plotted as a function of the distance from the one-proton decay threshold $[{}^6\text{Be}(1_1^+) \otimes p(\ell j)]^{5/2^-}$.

of the channel weight and the minimum of the corresponding correlation energy which is seen in Fig. 6.10, might be related to a different behavior of the imaginary part of the channel weight which has a maximum shifted to higher energies with respect to the maximum of the real part.

Figure 6.11 shows the GSM-CC results for $5/2_2^-$ state of ${}^7\text{Be}$, a mirror of the state $5/2_2^-$ in ${}^7\text{Li}$. One can see that indeed the mirror symmetry is well satisfied and Figs. 6.10 and 6.11 are quite similar. The minima of the correlation energy in the mirror states differ by about ~ 0.2 MeV. This is consistent with the observation done in the $7/2_1^-$ states (see Figs. 6.12 and 6.13).

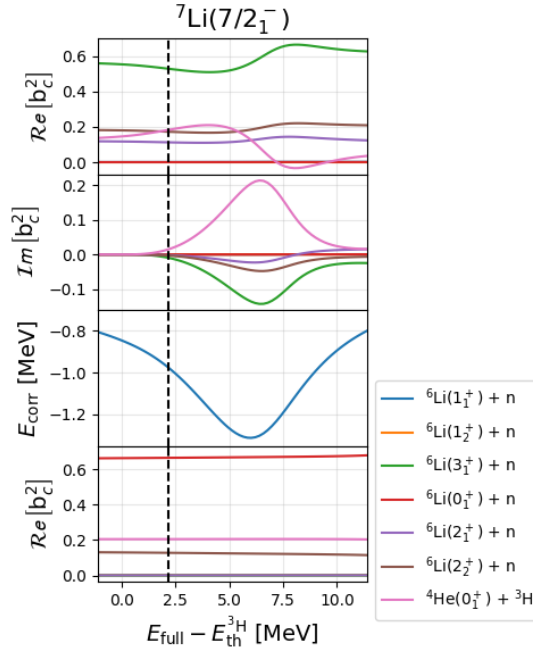


Figure 6.12: From top to bottom: (i) the real part of the channel weights $\mathcal{R}e[b_c^2]$ for the state $|\Psi^{7/2_1^-}\rangle$, (ii) the imaginary part of the channel weights $\mathcal{I}m[b_c^2]$ for the state $|\Psi^{7/2_1^-}\rangle$, (iii) the correlation energy $E_{\text{corr}}^{7/2_1^-}$, and (iv) the real part of the channel weights $\mathcal{R}e[b_c^2]$ for the state $|\Psi_\phi^{7/2_1^-}\rangle$, are shown as a function of the distance with respect to the triton decay threshold ${}^4\text{He} + {}^3\text{H}$. The dashed vertical line gives the GSM-CC energy for the $7/2_1^-$ resonance.

Figure 6.12 presents dependence on the energy difference with respect to the lowest decay threshold ${}^4\text{He} + {}^3\text{H}$ of the real and imaginary parts of the channel weights b_c^2 in the state $|\Psi^{7/2_1^-}\rangle$ of ${}^7\text{Li}$, the real part of the channel weights b_c^2 in the state $|\Psi_\phi^{7/2_1^-}\rangle$ calculated without the triton channel $[{}^4\text{He}(0_1^+) \otimes {}^3\text{H}(L_{\text{CM}} J_{\text{int}} J_{\text{P}})]^{7/2^-}$, and the correlation energy $E_{\text{corr}}^{7/2_1^-}$ (see Eq. (6.10)). As discussed previously, the state $7/2_1^-$ has a pronounced ${}^3\text{H}$ -cluster structure. In the whole interval of energies, neutron reaction channel $[{}^6\text{Li}(3_1^+) \otimes n(\ell j)]^{7/2^-}$ provides a smaller contribution to the wave function $7/2_1^-$. Probability of the ${}^3\text{H}$ channel $[{}^4\text{He}(0_1^+) \otimes {}^3\text{H}(2F_{7/2})]^{7/2^-}$ in $|\Psi^{7/2_1^-}\rangle$ grows when approaching the emission threshold and has a maximum ~ 4.5 MeV above the threshold energy $E_{\text{th}}^{{}^3\text{H}}$. The minimum of the correlation energy is seen at ~ 6 MeV above the cluster emission threshold, which is intermediate between the maxima of $\mathcal{R}e[b_c^2]$ and $\mathcal{I}m[b_c^2]$ for the channel ${}^4\text{He} + {}^3\text{H}$. Removal of the triton channel $[{}^4\text{He}(0_1^+) \otimes {}^3\text{H}(2F_{7/2})]^{7/2^-}$ in $|\Psi_\phi^{7/2_1^-}\rangle$ leaves the real part of the wave function nearly unchanged, bearing a small increase towards ~ 9 MeV where we approach the

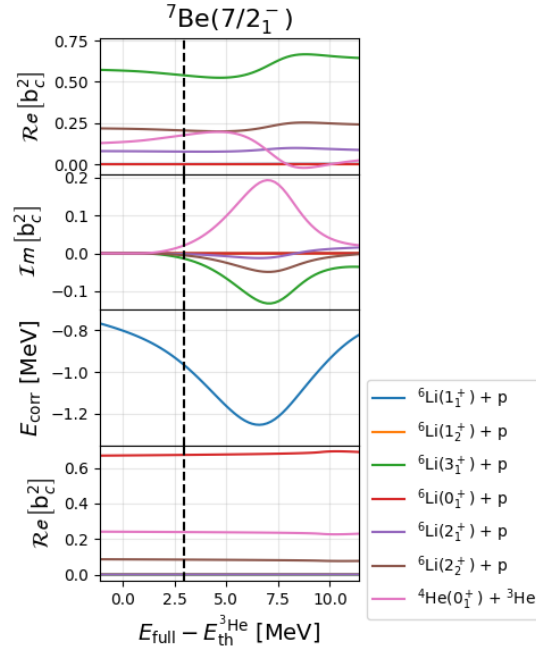


Figure 6.13: The same as in Fig. 6.12 but for a $7/2_1^-$ state in the mirror nucleus ${}^7\text{Be}$. All quantities are plotted as a function of the distance with respect to the ${}^3\text{He}$ decay threshold ${}^4\text{He} + {}^3\text{He}$. The dashed vertical line gives the GSM-CC energy for the $7/2_1^-$ resonance.

proton emission threshold. However, this effect is small and should not interfere with the minimum of the correlation energy.

Results for the mirror state are shown in Fig. 6.13. This figure shows a dependence of the real and imaginary parts of the channel weights b_c^2 in the state $|\Psi^{7/2_1^-}\rangle$, the real part of the channel weights b_c^2 in the state $|\Psi_\phi^{7/2_1^-}\rangle$ without the ${}^3\text{He}$ channel $[{}^4\text{He}(0_1^+) \otimes {}^3\text{He}(2F_{7/2})]^{7/2^-}$, and the correlation energy $E_{\text{corr}}^{7/2_1^-}$, on the energy difference with respect to the ${}^3\text{He}$ decay threshold ${}^4\text{He} + {}^3\text{He}$ in ${}^7\text{Be}$. One can see that the mirror symmetry in $7/2_1^-$ states of ${}^7\text{Li}$ and ${}^7\text{Be}$ is obeyed and the dependence on energy difference from the respective thresholds in ${}^7\text{Li}$ and ${}^7\text{Be}$ is qualitatively the same. There is in fact a small deviation of ~ 0.3 MeV of the minima of ${}^7\text{Li}$ and ${}^7\text{Be}$. This can be attributed to a stronger Coulomb interaction in the channel $[{}^4\text{He}(0_1^+) \otimes {}^3\text{He}(2F_{7/2})]^{7/2^-}$.

Figure 6.14 shows the dependence of real and imaginary parts of the channel weights b_c^2 in the state $|\Psi^{0_1^+}\rangle$ of ${}^8\text{Be}$, the real part of the channel weights b_c^2 for the state $|\Psi_\phi^{0_1^+}\rangle$ without the α -cluster channel, and the correlation energy $E_{\text{corr}}^{0_1^+}$, on the energy difference with respect to the lowest decay threshold $[{}^4\text{He}(0_1^+) \otimes {}^4\text{He}(L_{\text{CM}} J_{\text{int}} J_{\text{P}})]^{J^\pi}$. The ${}^4\text{He}$ -channel does not dominate the structure of this state. The real part of b_c^2 in the channel $[{}^4\text{He}(0_1^+) \otimes {}^4\text{He}(1S_0)]^{0^+}$ has a maximum at energy $E - E_{\text{th}}^{4\text{He}}[{}^4\text{He}(0_1^+)] \simeq 0.7$ MeV, above the ${}^4\text{He}$ threshold energy and approximately coincides with the minimum of $E_{\text{corr}}^{0_1^+}$.

It should be noticed that the 0_1^+ state in this GSM-CC study appears as the SM-like state which is composed mainly by ${}^7\text{Li}+p$ and ${}^7\text{Be}+n$ reaction channels. Slightly above the decay threshold of the channel $[{}^4\text{He}(0_1^+) \otimes {}^4\text{He}(1S_0)]^{0^+}$, a very strong ${}^4\text{He}$ clustering appears in a relatively narrow range of energies and disappears at still higher energies. Hence, α -clustering in the state 0_1^+ is an emerging threshold phenomenon resulting from the interplay between the attractive coupling to the α -decay channel and the repulsive Coulomb interaction.

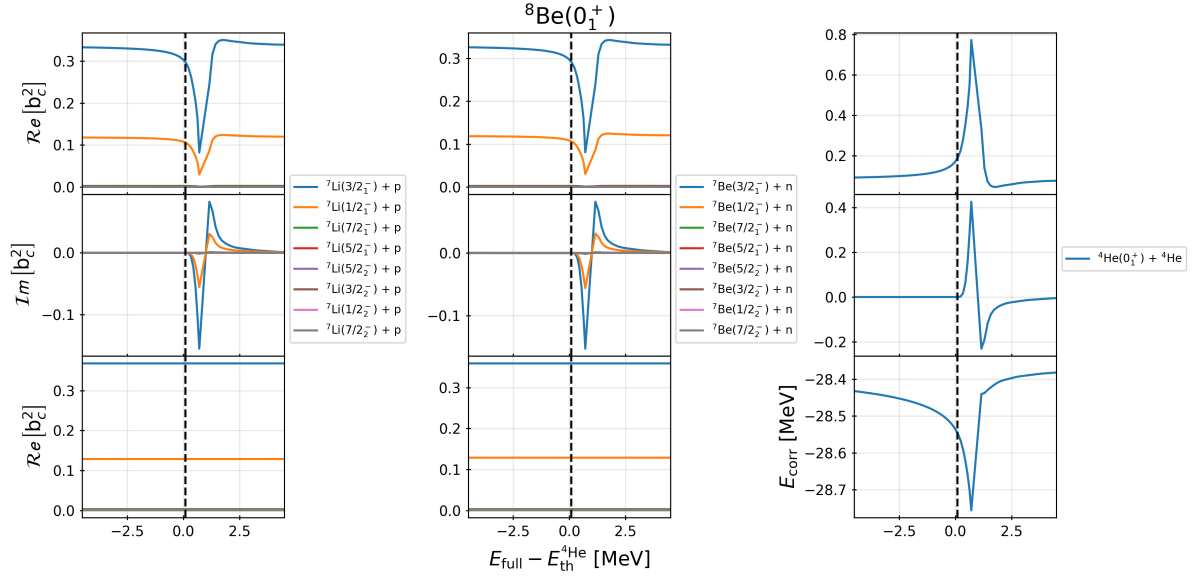


Figure 6.14: The top and the middle panels show respectively the real and imaginary parts of the channel weights b_c^2 in the 0_1^+ state of ^8Be . Different $^7\text{Li}+p$, $^7\text{Be}+n$, and $^4\text{He}+^4\text{He}$ reaction channels are shown in the left, middle and right column, respectively. Each curve for proton and neutron channels represents the sum of all channels which are built on the same many-body state of ^7Li and ^7Be , respectively. On the bottom panels, the left and middle column show the real parts of the channel weights of the proton and neutron channels in the calculation without the channel $[^4\text{He}(0_1^+) \otimes ^4\text{He}(L_{\text{CM}} J_{\text{int}} J_{\text{P}})]^{0+}$, respectively, and the right column shows the continuum-coupling correlation energy. The dashed vertical line gives the GSM-CC energy of the 0_1^+ resonance (see Fig. 5.6).

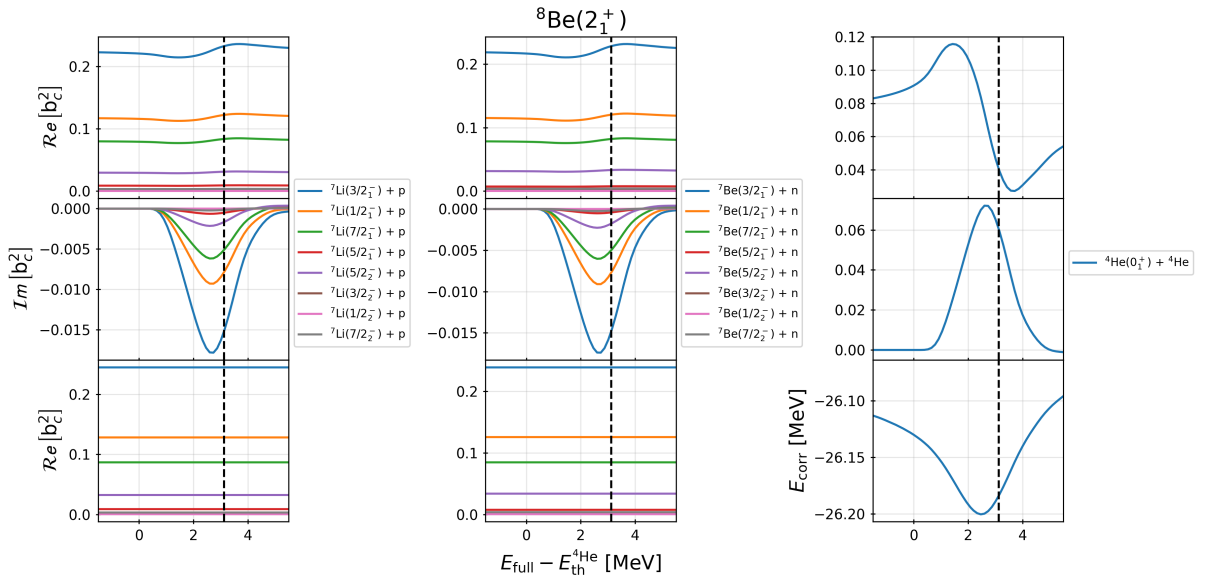


Figure 6.15: The same as in Fig. 6.14 but for a first excited state 2_1^+ of ^8Be . All quantities are plotted as a function of the distance with respect to the $^4\text{He} + ^4\text{He}$ decay threshold.

Figure 6.15 presents the dependence on the energy difference with respect to the lowest decay threshold $[^4\text{He}(0_1^+) \otimes ^4\text{He}(L_{\text{CM}} J_{\text{int}} J_{\text{P}})]^{J^\pi}$ of the real and imaginary parts of the channel weights for $|\Psi^{2_1^+}\rangle$ of ^8Be , the real part of the channel weights b_c^2 for the state

$|\Psi_\phi^{2_1^+}\rangle$ without the α -cluster channel, and the correlation energy $E_{\text{corr}}^{2_1^+}$. As compared to Fig. 6.14 for 0_1^+ resonance, one may notice an energy shift of the maximum of $\mathcal{R}e[b_c^2]$ for the α -cluster channel with respect to the minimum of $E_{\text{corr}}^{2_1^+}$. Since the Coulomb repulsion in 0_1^+ and 2_1^+ states of ${}^8\text{Be}$ is similar, this energy shift has to be related to the effect of the centrifugal barrier in the 2_1^+ state. One may notice that a decrease of the magnitude of $\mathcal{R}e[b_c^2]$ in the 2_1^+ state is connected with a decrease in the magnitude of $E_{\text{corr}}^{2_1^+}$ as compared to $E_{\text{corr}}^{0_1^+}$.

Figure 6.16 presents similar quantities for the 4_1^+ state of ${}^8\text{Be}$. One can see a decreasing magnitude of both α -clustering and $E_{\text{corr}}^{4_1^+}$, and an increased energy shift between the maximum of $\mathcal{R}e[b_c^2]$ for the α -cluster channel and the minimum of $E_{\text{corr}}^{4_1^+}$. The same tendency has been found for the 2_1^+ resonance (see Fig. 6.15).

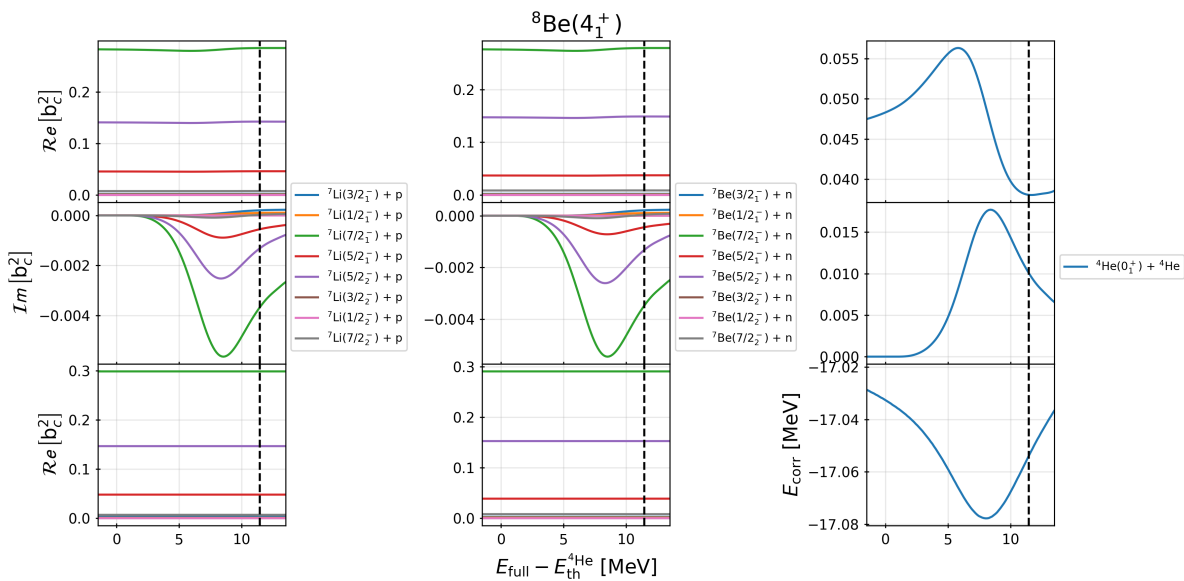


Figure 6.16: The same as in Fig. 6.14 but for the second excited state 4_1^+ of ${}^8\text{Be}$. All quantities are plotted as a function of the distance with respect to the ${}^4\text{He} + {}^4\text{He}$ decay threshold.

We can see in Figs. 6.15 and 6.16 that the effect of continuum-induced α -clusterization in these broad resonances is relatively small. However, it is most interesting to notice the angular momentum effect on the minimum of the correlation energy. Indeed, if we look back to Figs. 6.13 and 6.12, one may notice that the minima of the correlation energy for f -wave clusters are closer to the decay threshold than seen for g -wave clusters (Fig. 6.16) and further away from the threshold than seen for d -wave clusters (Fig. 6.15). This indicates that the angular momentum is an important factor in shifting the optimal energy for clustering away from the cluster decay threshold. In light nuclei studied here, the angular momentum effects seem to be even more pronounced than the effect of the Coulomb interaction.

6.3.4 Near-threshold effects in the spectroscopic factors

In this section we shall discuss the near-threshold effects in the SFs calculated using the GSM-CC wave functions. We calculate SFs in the formalism presented in Sect. 5.1. The number of calculated SFs is limited to just a few relevant ones chosen from Tabs. 5.3

and 5.6. The difference between SFs and channel probabilities is that the calculation of SFs use non-orthogonal channels whereas the channel probabilities b_c^2 correspond to the orthogonalized channels.

First of all, we would like to reproduce the Wigner cusp-like behavior expected for neutrons and protons. Figs. 6.17 and 6.18 show the dependence of the real and imaginary parts of the SFs with respect to the neutron/proton threshold $[{}^6\text{Li}(1_1^+) \otimes \text{n/p}(\ell j)]^{5/2^-}$, respectively. One can immediately notice the Wigner cusp for the neutron case and the delayed, smooth effect for the proton case. This is a proof of consistency of the method. Additionally, as it can be seen in Fig. 6.17, the 'anti-cusp' effect of the closed $[{}^6\text{Li}(3_1^+) \otimes \text{n/p}(\ell j)]^{5/2^-}$ channel is also seen for the SF associated to this channel. Similarly to the channel probabilities b_c^2 discussed in Sect. 6.3.1, the imaginary parts of the SFs present a complicated behavior above the nucleon emission threshold. Approaching the $[{}^6\text{Li}(3_1^+) \otimes \text{n/p}(\ell j)]^{5/2^-}$ threshold, we see a significant variation of the SFs $\langle {}^7\text{Li}(5/2_2^-) | [{}^6\text{Li}(1_1^+ 3_1^+) \otimes \text{n}(p_{3/2})]^{5/2^-} \rangle^2$.

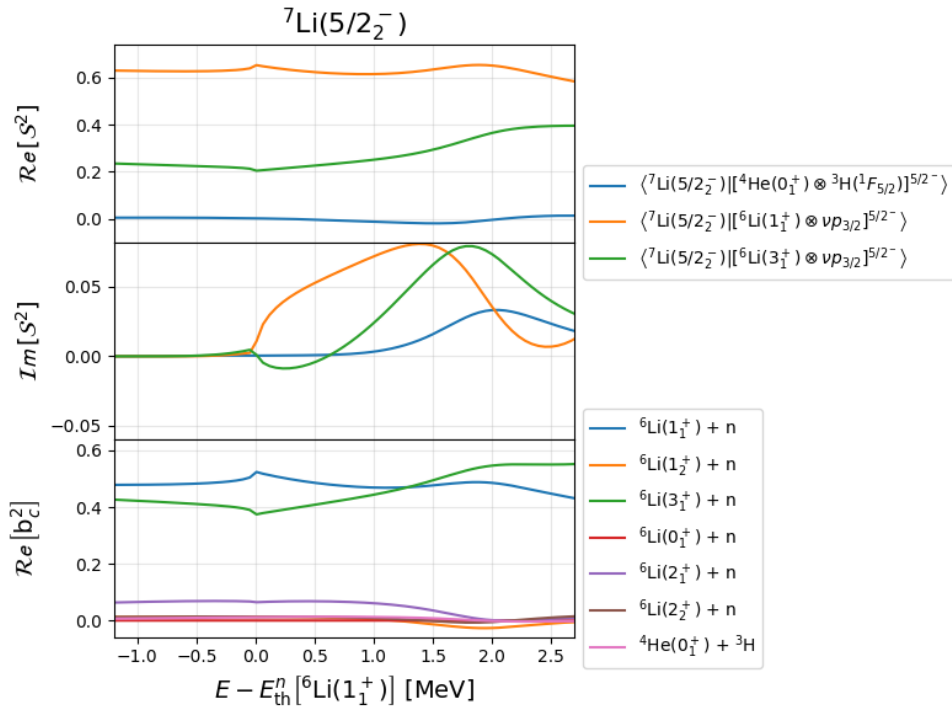


Figure 6.17: From top to bottom: (i) the real part $\text{Re}[\mathcal{S}^2]$ of the SFs (ii) the imaginary part $\text{Im}[\mathcal{S}^2]$ of the SFs and (iii) the real part $\text{Re}[b_c^2]$ of the channel probability are given for the state $|\Psi^{5/2_2^-}\rangle$. The SFs and the channel probabilities are shown as a function of the distance with respect to the one-neutron decay threshold $[{}^6\text{Li}(1_1^+) \otimes \text{n}(\ell j)]^{5/2^-}$.

Figure 6.19 shows the behavior of the real and imaginary parts of the SFs with respect to the $[{}^4\text{He}(0_1^+) \otimes {}^3\text{H}(L_{\text{CM}} J_{\text{int}} J_{\text{P}})]^{J^\pi}$ triton decay threshold in $7/2_1^-$ resonance of ${}^7\text{Li}$. The real part of the SFs behave similarly to the channel weights. Indeed, the minimum of the triton SF is ~ 1 MeV below the minimum of the triton channel weight. Nevertheless, the physical distance to the threshold correspond to ~ 2.2 MeV, which explains why we found such a small cluster SF in Tab. 5.3. Moreover, the minimum of the real part of the triton SF is negative, with a large uncertainty associated with the imaginary part $\text{Im}[\mathcal{S}^2]$. The triton SF increases again after 'recovering' from the effects of the emission threshold. This may mean that even though their presence in the wave function is small, it does not necessarily mean that their contribution to physical phenomena is small.

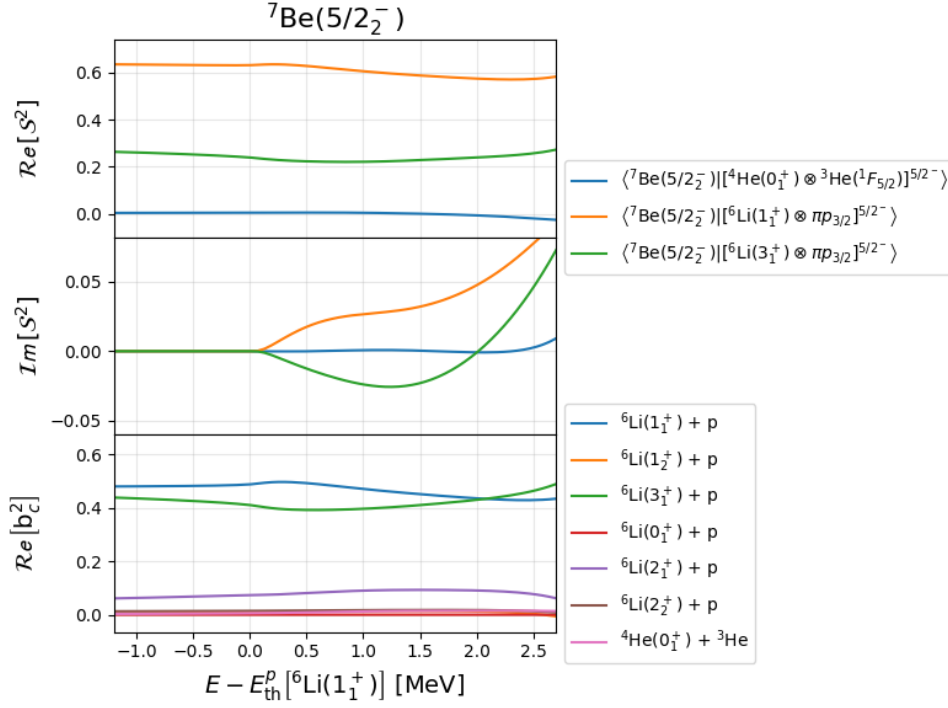


Figure 6.18: Same as Fig. 6.17 but in a mirror nucleus ${}^7\text{Be}$. The SFs and the channel weights are shown as a function of the distance with respect to the one-proton decay threshold $[{}^6\text{Li}(1_1^+) \otimes p(\ell j)]^{5/2^-}$.

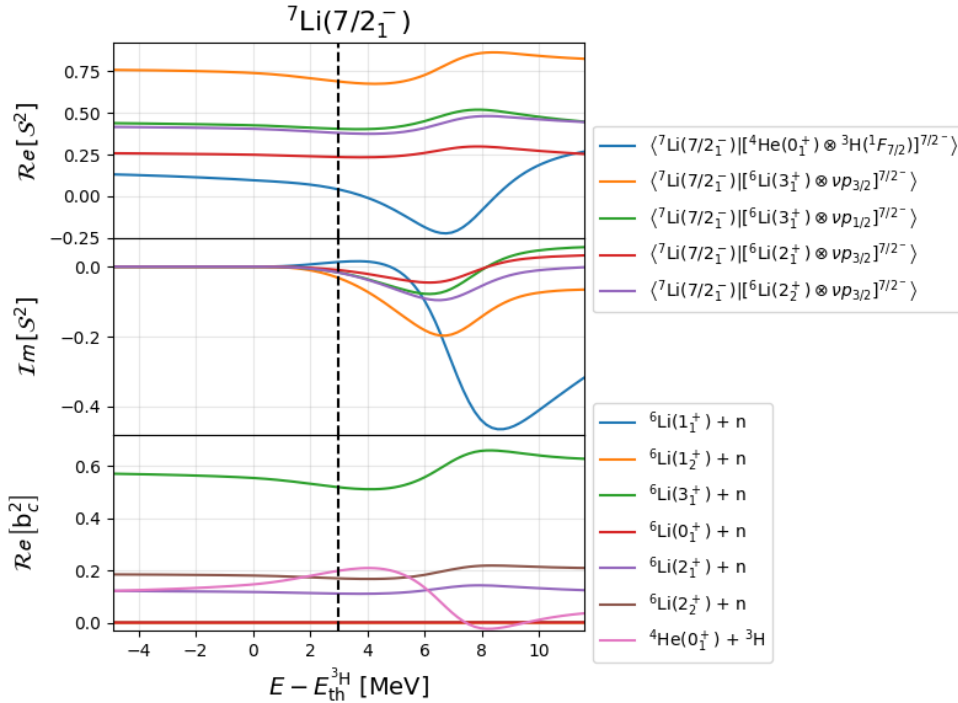


Figure 6.19: Same as Fig. 6.17 but for the state $|\Psi^{7/2_1^-}\rangle$ of ${}^7\text{Li}$. The SFs and the channel weights are shown as a function of the distance with respect to the ${}^4\text{He} + {}^3\text{H}$ decay threshold.

Similarly, Fig. 6.20 shows the behavior of the real and imaginary parts of the SFs with

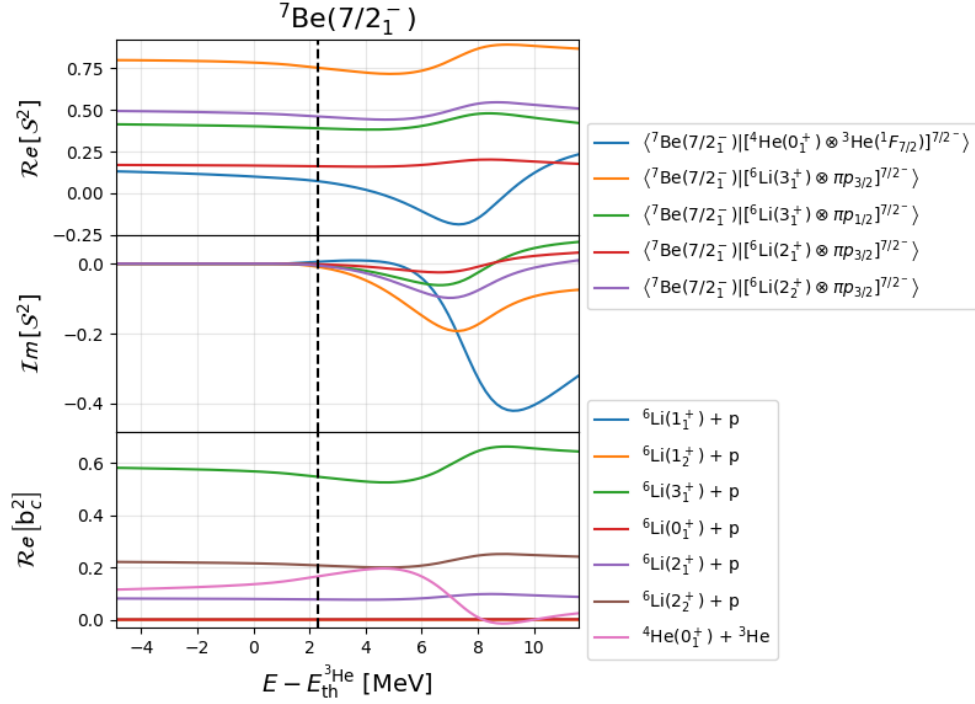


Figure 6.20: Same as Fig. 6.17 but for the state $|\Psi^{7/2_1^-}\rangle$ and the mirror system. The SFs and the channel weights are shown as a function of the distance with respect to the ${}^4\text{He} + {}^3\text{He}$ decay threshold.

respect to the $[{}^4\text{He}(0_1^+) \otimes {}^3\text{He}(L_{\text{CM}} J_{\text{int}} J_P)]^{J^\pi}$, ${}^3\text{He}$ -decay threshold. The effects of the continuum do not differ from previous analysis of the correlation energy and the channel weights. Indeed, the minimum of the real and imaginary parts of the SFs in ${}^7\text{Be}$ is found shifted by ~ 0.5 MeV with respect to the minimum in ${}^7\text{Li}$.

Figs. 6.21, 6.22, and 6.23 show the dependence of the SFs in ${}^8\text{Be}$ as a function of the distance to the threshold of channels $[{}^4\text{He}(0_1^+) \otimes {}^4\text{He}(1S_0)]^{0^+}$, $[{}^4\text{He}(0_1^+) \otimes {}^4\text{He}(1D_0)]^{2^+}$, and $[{}^4\text{He}(0_1^+) \otimes {}^4\text{He}(1G_0)]^{4^+}$. Similarly to the orthogonal channel weights, the effect of continuum induced α -clusterization in the cluster SFs is small. Nevertheless, the maximum of the real part of the cluster SF associated to the ${}^8\text{Be}(0^+)$ state is at ~ 0.8 MeV, the one for the ${}^8\text{Be}(2^+)$ state is at ~ 2.2 MeV, and the one associated to the ${}^8\text{Be}(4^+)$ state is at ~ 7.6 MeV. This is consistent with the expected shift of the near-threshold effects as a function of the strength of the centrifugal barrier discussed in previous sections.

The case of ${}^8\text{Be}$ with the SF associated to the channels $[{}^4\text{He}(0_1^+) \otimes {}^4\text{He}(1S_0)]^{0^+}$, $[{}^4\text{He}(0_1^+) \otimes {}^4\text{He}(1D_0)]^{2^+}$, and $[{}^4\text{He}(0_1^+) \otimes {}^4\text{He}(1G_0)]^{4^+}$ shows the opposite behavior as those associated to triton (see Fig. 6.19). As one moves away from the maximum effect due to the crossing of the emission threshold, the SFs are smaller than before crossing the threshold. In general, the behavior far away from the particle emission threshold is complicated and hence, not easy to interpret. Whereas in the vicinity of the particle emission threshold, behavior of SFs or channel probabilities is to a large extent universal, determined by the singularity of the branching point, far away from it the dependencies of those quantities are not universal. They depend on the specific features of the model and the NN interactions. Therefore, even though in this regime the open reaction channels still play a very important role, their effects cannot be easily disentangled from specific features of the model.

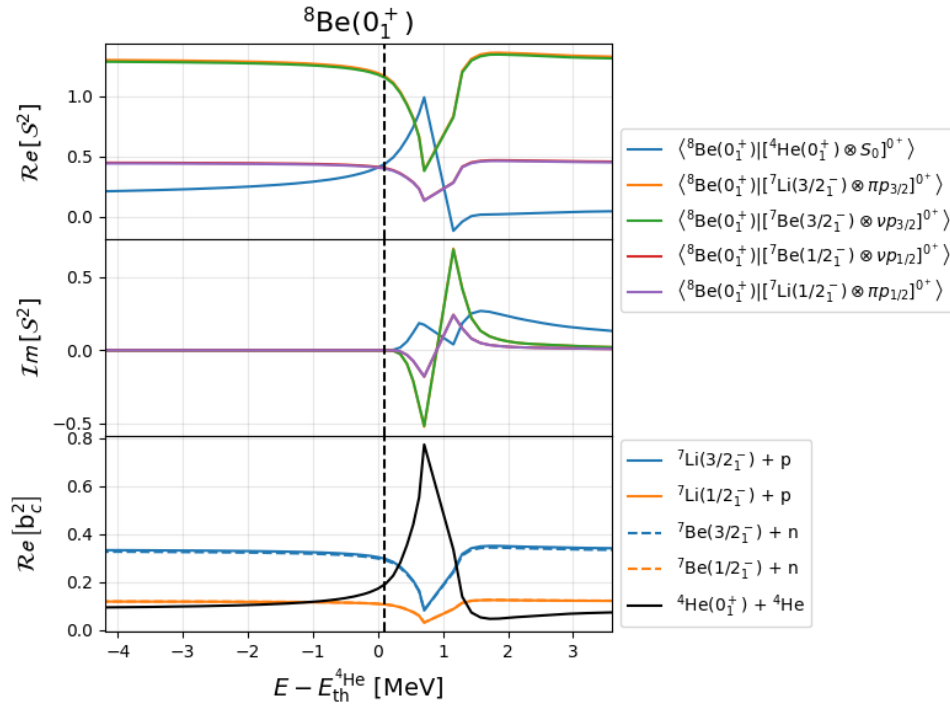


Figure 6.21: Same as Fig. 6.17 but for the state $|\Psi^{0_1^+}\rangle$ of ${}^8\text{Be}$. Only the channel weights associated to the shown SFs are plotted. The SFs and the channel weights are shown as a function for the distance with respect to the ${}^4\text{He} + {}^4\text{He}$ decay threshold.

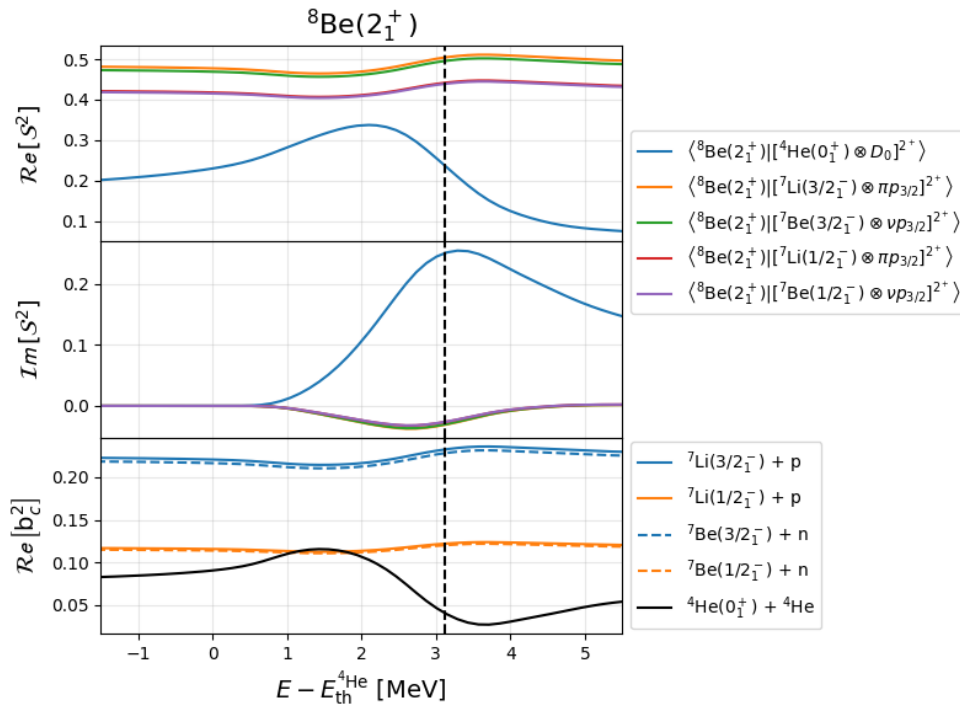


Figure 6.22: Same as Fig. 6.21 but for the state $|\Psi^{2_1^+}\rangle$ of ${}^8\text{Be}$. Only the channel weights associated to the shown SFs are plotted. The SFs and the channel weights are shown as a function for the distance with respect to the ${}^4\text{He} + {}^4\text{He}$ decay threshold.

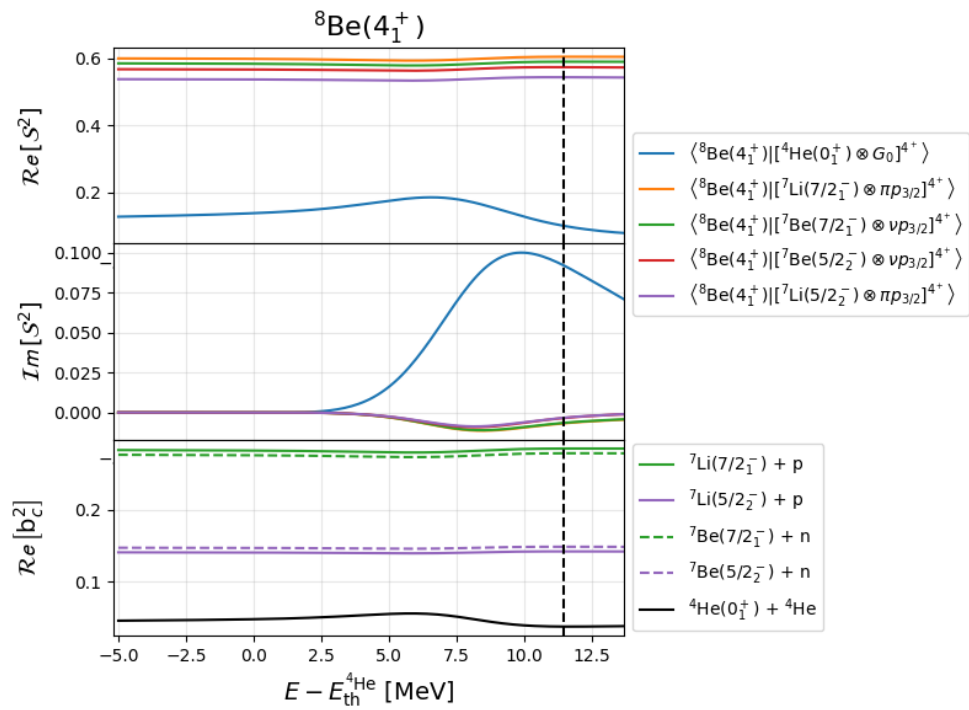


Figure 6.23: Same as Fig. 6.21 but for the state $|\Psi^{4+}_1\rangle$ of ${}^8\text{Be}$. Only the channel weights associated to the shown SFs are plotted. The SFs and the channel weights are shown as a function of the distance with respect to the ${}^4\text{He} + {}^4\text{He}$ decay threshold.

The present work has addressed two main objectives. The first one is related to the applicability of the GSM-CC model to describe the structure and reactions in a multi-channel framework with different mass partitions, whereby the nuclei ${}^7,8\text{Be}$, ${}^7\text{Li}$ and ${}^{42}\text{Sc}$ have been described. This paves the way for future studies with heavier and more complex nuclei. The second objective is to address the near-threshold effects with focus on clustering within a multi-channel framework which allows for the analysis of the competition between clustering and shell model-like effects.

In recent decades, tremendous efforts have been made to formulate and apply *ab initio* methods for a description of the structure of atomic nuclei. Applications of those novel microscopic approaches depend heavily on the parallel enhancement of computational resources available to run such sophisticated calculations. Nevertheless, one may ask a question if we are still gaining new insights by just running the same model with more sophisticated interactions and/or a bigger basis that requires more computation resources. In this work we have attempted to follow a different strategy. Instead of joining the *ab initio* efforts for the description of light nuclei, we have chosen to use an inert core and valence particles, just as in the original SM. As a result, all calculations discussed in this thesis can be done, in principle, using a commercial laptop.

Chapter 5 was devoted to GSM-CC calculations for structure and reactions. We began with successful GSM-CC calculations for ${}^7\text{Be}$ and ${}^7\text{Li}$, using two mass partitions: [6,1] (${}^6\text{Li}$ and a nucleon) and [4,3] (${}^4\text{He}$ core and ${}^3\text{H}/{}^3\text{He}$ cluster). The major result of these studies was the observation of strong clustering in the wave function for states that are close to the cluster emission threshold. Out of these, the most interesting is the $5/2^-$ doublet of states. The lowest state in the doublet, the $5/2_1^-$ state, is not observed in the scattering of low energy protons on ${}^6\text{Li}$, whereas it is most pronounced in the scattering of ${}^3\text{He}$ on ${}^4\text{He}$. On the contrary its partner, the $5/2_2^-$ state, appears most pronounced in the scattering of low energy protons, but it is seen only as a small signal in the scattering of ${}^3\text{H}/{}^3\text{He}$. In Chap. 5 we have explained this by the microscopic structure of $5/2_1^-$ and $5/2_2^-$ states in ${}^7\text{Be}$. A similar features are predicted in the reactions ${}^6\text{Li}(n,n)$ and ${}^4\text{He}({}^3\text{H},{}^3\text{H})$. Differences between experimental and calculated cross-sections are seen for small CM scattering angles. This may be in part attributed to an insufficient number of partial waves in the calculated of cross-section what might have prevented certain interference effects.

Following the calculations of $A = 7$ systems, we have done GSM-CC calculations for ${}^8\text{Be}$ including either three mass partitions ([7,1]: ${}^7\text{Li} + p$, ${}^7\text{Be} + n$, and [4,4]: ${}^4\text{He} + {}^4\text{He}$)

or four mass partitions ($[7,1]$: ${}^7\text{Li} + \text{p}$, ${}^7\text{Be} + \text{n}$, $[6,2]$: ${}^6\text{Li} + \text{d}$, and $[4,4]$: ${}^4\text{He} + {}^4\text{He}$). In the latter case, the energy spectrum was well reproduced by GSM-CC calculations with very small complex corrective factors to account for the missing scattering channels. It was found that the closed ${}^6\text{Li} + \text{d}$ channel was not negligible in all studied states.

The GSM-CC calculation in ${}^8\text{Be}$ was focused on the structure of this nucleus. In the GSM-CC calculation without the ${}^6\text{Li} + \text{d}$ channel we have observed that in the proximity of neutron and proton decay channels, the symmetry of the distribution of proton and neutron projectile channels is broken in the $(1_1^+; 1_2^+)$ and $(3_1^+; 3_2^+)$ doublets. This shows importance of the threshold effects on the composition of the wave function. In the ground state, ${}^8\text{Be}$ is slightly unbound with respect to the α -particle emission. Hence, we might expect α -clustering to be important in the ground state. This is indeed what we observed in our calculations. α -clustering was found only in the lowest states 0_1^+ , 2_1^+ and 4_1^+ of ${}^8\text{Be}$. On the contrary, deuteron clustering is more robust and appears in all low energy states with characteristic variations of the deuteron channel probability in the doublets $(1_1^+; 1_2^+)$, $(2_2^+; 2_3^+)$, and $(3_1^+; 3_2^+)$ namely, the larger probability of the deuteron channel is always in the higher energy member of the doublet. Moreover, the inclusion of deuteron channels $[{}^6\text{Li}(K_i^\pi) \otimes {}^2\text{H}(L_{\text{CM}} J_{\text{int}} J_{\text{P}})]^{J^\pi}$ allows a better description of the $(1_1^+; 1_2^+)$, $(2_2^+; 2_3^+)$ and $(3_1^+; 3_2^+)$ energy doublets by closing the energy distance between members in each doublet. One may note that in all low-energy states of ${}^8\text{Be}$, major contributions to the wave functions are provided by the neutron $[{}^7\text{Be}(K_i^\pi) \otimes \text{n}(\ell j)]^{J^\pi}$ and proton $[{}^7\text{Li}(K_i^\pi) \otimes \text{p}(\ell j)]^{J^\pi}$ channels.

At the end of Chap. 5 we presented the calculations of spectra in ${}^{41,42}\text{Ca}$, ${}^{41,42}\text{Sc}$, ${}^{42}\text{Ti}$, as well as the proton/neutron elastic scattering ${}^{40}\text{Ca}(\text{p/n}, \text{p/n})$ and the transfer reaction ${}^{40}\text{Ca}(\text{d}, \text{p}){}^{41}\text{Ca}$. The GSM-CC description of ${}^{42}\text{Sc}$ has been done using three mass partitions: $[41,1]$: ${}^{41}\text{Ca} + \text{p}$, ${}^{41}\text{Sc} + \text{n}$, and $[40,2]$: ${}^{40}\text{Ca} + \text{d}$. The spectra of ${}^{42}\text{Ca}$ and ${}^{42}\text{Ti}$ have been successfully described by considering only proton and neutron channels ($[41,1]$). Using the same interaction, it was possible to describe the cross-section for the elastic scattering reactions ${}^{40}\text{Ca}(\text{p}, \text{p})$ and ${}^{40}\text{Ca}(\text{n}, \text{n})$ simultaneously with the transfer reaction ${}^{40}\text{Ca}(\text{d}, \text{p}){}^{41}\text{Ca}$. The correct reproduction of these cross-sections depends on the fine tuning of the interaction to find a compromise between the satisfactory description of $A = 42$ spectra on one side and the considered cross-sections, on the other side.

The extensive studies in SMEC [8, 9] have shown that the coexistence of cluster-like and SM-like configurations at low energies can be reconciled in the OQS approach to the SM. This intriguing phenomenon arises due to the presence of the branching point at the particle emission threshold, which leads to a collective mixing of SM states and the formation of the aligned state of an OQS which shares many properties of the nearby particle-emission threshold. The OQS nature of the alignment phenomenon was investigated using GSM-CC for the first time. The presence of cluster states near their corresponding cluster emission thresholds serves as a significant indicator of a profound change in the near-threshold SM wave function and the direct manifestation of the correlations induced in SM wave functions by the continuum-coupling.

Near-threshold effects investigated in Chap. 6 have been inspired by the GSM studies of SFs. [38, 39]. We have extended these studies by analyzing the dependence on the energy distance to the particle emission thresholds of the wave function expanded in reaction channels. In addition to the reaction channel probabilities, we have studied partial decay widths of various channels, continuum coupling correlation energy and SFs. Thus, this is the first time that the phenomena of clusterization in near-threshold states have been studied with GSM-CC. When looking at the change of the properties of ${}^8\text{Be}$ as a function to the energy distance to the α -decay threshold, we found a shift in the maximum effect of the threshold effects associated to the angular momentum. The presence of

chameleon features for states, such as the $5/2^-$ resonances in ${}^7\text{Be}$ and ${}^7\text{Li}$, suggest that the nature of the states changes depending on their environment of reaction channels and scattering continuum states.

The continuum-coupling correlation energy defined in this work measures the effect of the decay thresholds in the configuration mixing. We found that properties of the correlation energy mirror the properties of the channel probability weights. Moreover, the effects of the Coulomb interaction and the centrifugal barrier in the continuum-coupling correlation energy are similar to what is observed in the channel probabilities. In the studied nuclei with $A = 7, 8$, the effects of the Coulomb interaction was small as compared to the effects of angular momentum.

We concluded Chap. 6 with the studies on the SFs for nucleons and ${}^3\text{H}$, ${}^{3,4}\text{He}$ clusters. We found that the alignment effects are carried over from the channel weights to the SFs. The maxima/minima of the SFs do not correspond to those of the channel probabilities, but they are close to each other.

In summary, the effect of the particle emission thresholds on SM states are important. The calculations presented in this work are the first GSM-CC calculations done in a multiple mass-partition framework. These calculations provide evidence for the importance of not only one-nucleon decay thresholds, but also of ${}^3\text{H}$, ${}^3\text{He}$, or ${}^4\text{He}$ more complex emission thresholds for the structure of SM states. We have shown that the near-threshold α -clustering is an emergent OQS phenomenon due to the alignment of the SM eigenstate with the nearby α -decay channel. In the future, similar calculations should be carried for heavier nuclei using a different core, like ${}^{12}\text{C}$ or ${}^{16}\text{O}$ cores. Additionally, further exploration of mass partitions whose decay thresholds are not necessarily at low energies is required, as demonstrated on the example of ${}^6\text{Li} + \text{d}$ partition in low energy states of ${}^8\text{Be}$. The GSM-CC approach formulated in the inert core + valence particles approximation, should be completed by the no-core GSM-CC calculation. Such studies are certainly possible in nuclei with $A \leq 6$ [25].

My contribution to the results presented in this work is contained mainly in Chaps. 5 and 6. These include the application, testing, and correction of numerical codes of the GSM-CC approach with the reaction channels corresponding to the multiple-mass partitions. These studies comprise the development of the interaction for $A = 7, 8$, and 9 nuclei. Results for $A = 9$ nuclei have not been included in the written document. Next, in Chap. 6, I defined the correlation energy which provides a synthesized information about the continuum-coupling correlations calculated in GSM-CC. This quantity is now ready to be applied in many nuclei. Extensive studies were done to define the correlation energy for GSM (not included in this manuscript), however the results obtained were not satisfactory. I have also developed scripts that allow for several consecutive GSM and GSM-CC calculations and also that extract important data from the output files of a calculation. Although the calculations presented in the thesis can be done in a commercial laptop, scripts that allows to take advantage of a computer cluster have been developed that parallelize multiple GSM calculations. Finally, the threshold effects calculations for probabilities of orthogonal reaction channels, the spectroscopic factors and the correlation energy were prepared and ran by me using the GSM-CC computer code.

A.1 On the Slater determinants of the wave function in GSM-CC

In this Appendix we give details about the construction of the total wave function in GSM-CC in terms of Slater determinants. We begin with the projectile wave function:

$$|\Psi_{M_P}^{J_P}\rangle = A^\dagger_{[[N_{\text{CM}}L_{\text{CM}}]\otimes|J_{\text{int}}]\}_{M_P}^{J_P}} |0\rangle, \quad (\text{A.1})$$

where $|0\rangle$ is the Fock space. We can express the projectile creation operator in single-particle creation operators a^\dagger as:

$$A^\dagger_{[[N_{\text{CM}}L_{\text{CM}}]\otimes|J_{\text{int}}]\}_{M_P}^{J_P}} \rightarrow \sum_{\gamma} B_{\gamma}^a \prod_{i=1}^a a_{\gamma_i}^\dagger, \quad (\text{A.2})$$

where $\gamma_i = (\tau_i, s_i, \ell_i)$ is the set of quantum numbers that characterizes a particular nucleon i of isospin τ_i , spin s_i and angular momentum ℓ_i . Additionally, we can make the identifications $a\vec{\ell}_i = \vec{L}_{\text{CM}}$ and $\sum_{i \in \text{core}} \vec{\ell}_i + \vec{s}_i = \vec{J}_{\text{int}}$. By considering the angular momentum couplings, the projectile wave function is:

$$|\Psi_{M_P}^{J_P}\rangle = \sum_{M_{\text{CM}}M_{\text{int}}} \langle L_{\text{CM}}M_{\text{CM}}J_{\text{int}}M_{\text{int}}|J_P M_P\rangle \sum_{\gamma} B_{\gamma}^a \prod_{i=1}^a a_{\gamma_i}^\dagger |0\rangle. \quad (\text{A.3})$$

Similarly, the target wave function can be expressed as:

$$|\Psi_{M_T}^{J_T}\rangle = A^\dagger_{|\Psi_{M_T}^{J_T}\rangle} |0\rangle = \sum_{\beta} B_{\beta}^{A-a} \prod_{j=g}^{A-a} a_{\beta_j}^\dagger |0\rangle, \quad (\text{A.4})$$

where g is the number of particles in the core plus one unit. Finally, we can couple both projectile and target wave functions of Eqs. (A.3) and (A.4) into the full wave function as:

$$\begin{aligned} |\Psi_{M_A}^{J_A}\rangle &= \mathcal{K} \sum_{\substack{M_P M_T \\ M_{\text{CM}} M_{\text{int}}}} \langle L_{\text{CM}}M_{\text{CM}}J_{\text{int}}M_{\text{int}}|J_P M_P\rangle \langle J_P M_P J_T M_T|J_A M_A\rangle \\ &\times \sum_{\beta\gamma} B_{\beta}^{A-a} B_{\gamma}^a \left(\prod_{i=1}^a a_{\gamma_i}^\dagger \right) \left(\prod_{j=g}^{A-a} a_{\beta_j}^\dagger \right) |0\rangle, \end{aligned} \quad (\text{A.5})$$

where \mathcal{K} is a normalization constant.

If we want to define a proper Slater determinant for the full wave function, we have to set a convention in the order of the creation operators. This order however, means a rearrangement of the single particle creation operators in equation (A.5). This is the origin of rearrangement phase factors $(-)^{\varphi}$. Thus the sum of creation operators in the total wave function can be expressed as

$$\sum_{\beta\gamma} B_{\beta}^{A-a} B_{\gamma}^a \left(\prod_{i=1}^a a_{\gamma_i}^{\dagger} \right) \left(\prod_{j=g}^{A-a} a_{\beta_j}^{\dagger} \right) \rightarrow \sum_{\alpha} B_{\alpha}^A \prod_{i=g}^A a_{\alpha_i}^{\dagger}, \quad (\text{A.6})$$

where $B_{\alpha}^A = (-)^{\varphi_{\alpha}} B_{\beta}^{A-a} B_{\gamma}^a$.

A.2 The current formula for the calculation of partial widths of channel wave functions

We emulate [28, 306] to derive the so-called current formula for the calculation of partial widths for channel wave functions. In the following we simplify the notation by removing the CM tag from the equations. For large CM distances, the coupling between channels is negligible and thus, using Eqs. (4.50) and (4.56) the Hill-Wheeler Eq. (4.7) becomes:

$$\left[\frac{\partial^2}{\partial r^2} + \frac{\ell(\ell+1)}{r^2} + \frac{2m_p}{\hbar^2} (E_{\text{T}} + E_{\text{int}}) - \frac{2m_p}{\hbar} E \right] u_c(r) + \sum_{c'} V_{cc'} u_{c'}(r) = 0. \quad (\text{A.7})$$

The usual trick is to multiply by the conjugate $u_c^*(r)$ and then subtract the complex conjugate of the whole equation (A.7) to yield:

$$u_c^*(r) u_c''(r) - u_c(r) u_c''^*(r) + \frac{2m_p}{\hbar^2} i\Gamma + \sum_{c'} V_{cc'}(r) [u_c^*(r) u_{c'}(r) - u_c(r) u_{c'}^*(r)] = 0, \quad (\text{A.8})$$

where the energy E is assumed complex such that $E = \mathcal{R}e[E] - i\Gamma/2$. If we now notice that

$$\int_0^r dr' [u_c^*(r) u_c''(r) - u_c(r) u_c''^*(r)] = u_c^*(r) u_c'(r) - u_c(r) u_c'^*(r), \quad (\text{A.9})$$

and that

$$\sum_{cc'} V_{cc'}(r) [u_c^*(r) u_{c'}(r) - u_c(r) u_{c'}^*(r)] = 0. \quad (\text{A.10})$$

So by applying the operators $\int_0^r dr$ and $\sum_{c'}$ we derive the current formula:

$$\Gamma(r) = i \frac{\hbar^2}{2m_p} \frac{\sum_c [u_c^*(r) u_c'(r) - u_c(r) u_c'^*(r)]}{\sum_{c'} \int_0^r dr' |u_{c'}(r')|^2}. \quad (\text{A.11})$$

Thus, since the width can be expressed as the sum of partial widths $\Gamma = \sum_c \Gamma_c$, then, the expression for the partial width for a specific channel c is simply:

$$\Gamma_c(r) = i \frac{\hbar^2}{2m_p} \frac{u_c^*(r) u_c'(r) - u_c(r) u_c'^*(r)}{\sum_{c'} \int_0^r dr' |u_{c'}(r')|^2}. \quad (\text{A.12})$$

References

- [1] M. Goeppert-Mayer, *Physical Review* **75**, 1969 (1949).
- [2] O. Haxel, J. H. D. Jensen, and H. E. Suess, *Physical Review* **75**, 1766 (1949).
- [3] H. Feshbach, *Annals of Physics* **5**, 357 (1958).
- [4] H. Feshbach, *Annals of Physics* **19**, 287 (1962).
- [5] C. Mahaux and H. A. Weidenmüller, *Shell-Model Approach to Nuclear Reactions*. (Amsterdam: North-Holland, 1969).
- [6] H. Barz, I. Rotter, and J. Höhn, *Nuclear Physics A* **275**, 111 (1977).
- [7] K. Ikeda, N. Takigawa, and H. Horiuchi, *Progress of Theoretical Physics Supplement* **68**, 464 (1968).
- [8] J. Okołowicz, M. Płoszajczak, and W. Nazarewicz, *Progress of Theoretical Physics Supplement* **196**, 230 (2012).
- [9] J. Okołowicz, W. Nazarewicz, and M. Płoszajczak, *Fortschritte der Physik* **61**, 66 (2012).
- [10] J. Okołowicz, M. Płoszajczak, and I. Rotter, *Physics Reports* **374**, 271 (2003).
- [11] R. Id Betan, R. J. Liotta, N. Sandulescu, and T. Vertse, *Physical Review Letters* **89**, 042501 (2002).
- [12] N. Michel, W. Nazarewicz, M. Płoszajczak, and K. Bennaceur, *Physical Review Letters* **89**, 042502 (2002).
- [13] N. Michel, W. Nazarewicz, M. Płoszajczak, and J. Okołowicz, *Physical Review C* **67**, 054311 (2003).
- [14] N. Michel, W. Nazarewicz, M. Płoszajczak, and T. Vertse, *Journal of Physics G: Nuclear and Particle Physics* **36**, 013101 (2008).
- [15] N. Michel and M. Płoszajczak, *Gamow Shell Model, The Unified Theory of Nuclear Structure and Reactions*, Vol. 983 (Lectures Notes in Physics, Springer, 2021).
- [16] Y. Jaganathen, N. Michel, and M. Płoszajczak, *Physical Review C* **89**, 034624 (2014).
- [17] K. Fossez, N. Michel, M. Płoszajczak, Y. Jaganathen, and R. M. Id Betan, *Physical Review C* **91**, 034609 (2015).
- [18] S. Quaglioni and P. Navrátil, *Physical Review Letters* **101**, 092501 (2008).

- [19] S. Quaglioni and P. Navrátil, *Physical Review C* **79**, 044606 (2009).
- [20] S. Baroni, P. Navrátil, and S. Quaglioni, *Physical Review Letters* **110**, 022505 (2013).
- [21] S. Baroni, P. Navrátil, and S. Quaglioni, *Physical Review C* **87**, 034326 (2013).
- [22] P. Navrátil, S. Quaglioni, G. Hupin, C. Romero-Redondo, and A. Calci, *Physica Scripta* **91**, 053002 (2016).
- [23] G. Papadimitriou, J. Rotureau, N. Michel, M. Płoszajczak, and B. R. Barrett, *Physical Review C* **88**, 044318 (2013).
- [24] A. M. Shirokov, G. Papadimitriou, A. I. Mazur, I. A. Mazur, R. Roth, and J. P. Vary, *Physical Review Letters* **117**, 182502 (2016).
- [25] N. Michel, W. Nazarewicz, and M. Płoszajczak, arXiv:2306.05192 (2023).
- [26] G. Gamow, *Zeitschrift für Physik* **51**, 204 (1928).
- [27] W. Heisenberg, in *Original scientific papers / Wissenschaftliche Originalarbeiten* (Springer Berlin Heidelberg, 1989), pp. 611–636.
- [28] J. Humblet and L. Rosenfeld, *Nuclear Physics* **26**, 529 (1961).
- [29] T. Berggren, *Nuclear Physics A* **109**, 265 (1968).
- [30] T. Berggren, *Physics Letters B* **73**, 389 (1978).
- [31] T. Berggren, *Physics Letters B* **373**, 1 (1996).
- [32] K. Maurin, Lecture Notes, ICTP, Trieste, preprint IC/66/12 (1966).
- [33] A. Böhm and J. D. Dollard, *The Rigged Hilbert Space and Quantum Mechanics: Lectures in Mathematical Physics at the University of Texas at Austin* (Springer Berlin Heidelberg, 1978).
- [34] R. de la Madrid, *European Journal of Physics* **26**, 287 (2005).
- [35] A. Mercenne, N. Michel, and M. Płoszajczak, *Physical Review C* **99**, 044606 (2019).
- [36] A. Mercenne, N. Michel, J. P. Linares Fernández, and M. Płoszajczak, *Physical Review C* **107**, L011603 (2023).
- [37] E. P. Wigner, *Physical Review* **73**, 1002 (1948).
- [38] N. Michel, W. Nazarewicz, and M. Płoszajczak, *Physical Review C* **75**, 031301 (2007).
- [39] N. Michel, W. Nazarewicz, and M. Płoszajczak, *Nuclear Physics A* **794**, 29 (2007).
- [40] A. J. F. Siegert, *Physical Review* **56**, 750 (1939).
- [41] J. A. Wheeler, *Physical Review* **52**, 1107 (1937).
- [42] Y. B. Zel'dovich, *Sov. Phys. JETP* **12**, 542 (1961).
- [43] I. M. Gel'fand and N. Y. Vilenkin, *Generalized Functions: Applications of Harmonic Analysis*, Vol. 4 (Academic press, New York, 1964).
- [44] A. B. Migdal, A. M. Perelomov, and V. S. Popov, *Yadernaya Fizika* **14**, 874 (1971).
- [45] A. B. Migdal, A. M. Perelomov, and V. S. Popov, *Soviet Journal of Nuclear Physics* **14**, 488 (1972).
- [46] J. R. Taylor, *Scattering Theory: the Quantum Theory of Nonrelativistic Collisions* (Courier Corporation, 2006).

- [47] L. Dubé and A. Herzenberg, *Physical Review Letters* **38**, 820 (1977).
- [48] M. A. Morrison, *Physical Review A* **25**, 1445 (1982).
- [49] L. A. Morgan, *Physical Review Letters* **80**, 1873 (1998).
- [50] O. I. Tolstikhin, V. N. Ostrovsky, and H. Nakamura, *Physical Review Letters* **79**, 2026 (1997).
- [51] R. G. Newton, *Journal of Mathematical Physics* **1**, 319 (2004).
- [52] A. Bohm, M. Gadella, and S. Maxson, *Computers and Mathematics with Applications* **34**, 427 (1997).
- [53] M. Abramowitz, I. A. Stegun, and R. H. Romer, *Handbook of Mathematical Functions with Formulas, Graphs, and Mathematical Tables*, Vol. 56, 10 (American Association of Physics Teachers (AAPT), 1988).
- [54] W. Blum, H.-P. Dürr, and H. Rechenberg, eds., *Original scientific papers / Wissenschaftliche Originalarbeiten* (Springer Berlin Heidelberg, 1989).
- [55] R. Jost, *Helvetica Physica Acta* **20**, 256 (1947).
- [56] P. Lind, *Physical Review C* **47**, 1903 (1993).
- [57] N. Michel, *Journal of Mathematical Physics* **49**, 022109 (2008).
- [58] J. Bang, F. Gareev, M. Gizzatkulov, and S. Goncharov, *Nuclear Physics A* **309**, 381 (1978).
- [59] B. Gyarmati, F. Krisztinkovics, and T. Vertse, *Physics Letters B* **41**, 110 (1972).
- [60] B. F. Samsonov, *Journal of Physics A: Mathematical and General* **38**, L571 (2005).
- [61] T. Katö, *Perturbation Theory for Linear Operators, Vol. 132 of Classics in Mathematics* (Springer, Berlin, Germany, 1995).
- [62] M. Zirnbauer, J. Verbaarschot, and H. Weidenmüller, *Nuclear Physics A* **411**, 161 (1983).
- [63] W. D. Heiss and W.-H. Steeb, *Journal of Mathematical Physics* **32**, 3003 (1991).
- [64] W. D. Heiss and A. L. Sannino, *Physical Review A* **43**, 4159 (1991).
- [65] M. V. Nikolayev and V. S. Olkhovskiy, *Lettere Al Nuovo Cimento Series 2* **8**, 703 (1973).
- [66] B. Gyarmati and T. Vertse, *Nuclear Physics A* **160**, 523 (1971).
- [67] V. I. Kukulin, V. M. Krasnopol'skiy, and J. Horáček, *Theory of Resonances* (Springer Netherlands, 1989).
- [68] I. Talmi, *Helvetica Physica Acta* **26**, 185 (1952).
- [69] M. Moshinsky, *Nuclear Physics* **13**, 104 (1959).
- [70] G. Hagen, M. Hjorth-Jensen, and N. Michel, *Physical Review C* **73**, 064307 (2006).
- [71] K. Maurin, *Generalized Eigenfunctions Expansions and Unitarity Representations of Topological Groups* (Polish Scientific Publishers, Warsaw, 1968).
- [72] K. Maurin, *Analysis, Part II* (Polish Scientific Publishers, Warsaw, 1980).
- [73] R. de la Madrid, *Journal of Physics A: Mathematical and General* **39**, 3949 (2006).
- [74] R. de la Madrid, *Journal of Physics A: Mathematical and General* **39**, 3981 (2006).
- [75] R. de la Madrid, *Journal of Mathematical Physics* **53**, 102113 (2012).

- [76] G. Ludwig, *Foundations of Quantum Mechanics*, Vol. 1,2 (Springer, New York, 1983).
- [77] G. Ludwig, *An Axiomatic Basis of Quantum Mechanics*, Vol. 1,2 (Springer Verlag, Berlin, 1983).
- [78] P. A. M. Dirac, *The Principles of Quantum Mechanics*, 27 (Oxford university press, 1981).
- [79] J. Von Neumann, *Mathematical Foundations of Quantum Mechanics*, Vol. 53 (Princeton university press, 2018).
- [80] U. Fano, [Physical Review **124**, 1866 \(1961\)](#).
- [81] P. Navrátil and B. R. Barrett, [Physical Review C **57**, 562 \(1998\)](#).
- [82] P. Navrátil and B. R. Barrett, [Physical Review C **59**, 1906 \(1999\)](#).
- [83] P. Navrátil, G. P. Kamuntavičius, and B. R. Barrett, [Physical Review C **61**, 044001 \(2000\)](#).
- [84] K. Bennaceur, F. Nowacki, J. Okołowicz, and M. Płoszajczak, [Journal of Physics G: Nuclear and Particle Physics **24**, 1631 \(1998\)](#).
- [85] K. Bennaceur, F. Nowacki, J. Okołowicz, and M. Płoszajczak, [Nuclear Physics A **651**, 289 \(1999\)](#).
- [86] K. Bennaceur, J. Dobaczewski, and M. Płoszajczak, [Physics Letters B **496**, 154 \(2000\)](#).
- [87] N. Michel, J. Okołowicz, F. Nowacki, and M. Płoszajczak, [Nuclear Physics A **703**, 202 \(2002\)](#).
- [88] J. Rotureau, J. Okołowicz, and M. Płoszajczak, [Physical Review Letters **95**, 042503 \(2005\)](#).
- [89] J. Rotureau, J. Okołowicz, and M. Płoszajczak, [Nuclear Physics A **767**, 13 \(2006\)](#).
- [90] A. Poves, J. Sánchez-Solano, E. Caurier, and F. Nowacki, [Nuclear Physics A **694**, 157 \(2001\)](#).
- [91] J. P. Elliott, [Proceedings of the Royal Society of London. Series A, Mathematical and Physical Sciences **245**, 562 \(1958\)](#).
- [92] M. Dufour and A. P. Zuker, [Physical Review C **54**, 1641 \(1996\)](#).
- [93] P. F. A. Klinkenberg, [Reviews of Modern Physics **24**, 63 \(1952\)](#).
- [94] C. Lanczos, [Journal of Research of the National Bureau of Standards **45**, 255 \(1950\)](#).
- [95] E. Caurier, G. Martínez-Pinedo, F. Nowacki, A. Poves, and A. P. Zuker, [Reviews of Modern Physics **77**, 427 \(2005\)](#).
- [96] J. M. Arias and M. Lozano, eds., *An Advanced Course in Modern Nuclear Physics* (Springer Berlin Heidelberg, 2001).
- [97] B. R. Barrett, P. Navrátil, and J. P. Vary, [Progress in Particle and Nuclear Physics **69**, 131 \(2013\)](#).
- [98] P. Navrátil, S. Quaglioni, I. Stetcu, and B. R. Barrett, [Journal of Physics G: Nuclear and Particle Physics **36**, 083101 \(2009\)](#).
- [99] S. Ôkubo, [Progress of Theoretical Physics **12**, 603 \(1954\)](#).

- [100] K. Suzuki and S. Y. Lee, *Progress of Theoretical Physics* **64**, 2091 (1980).
- [101] K. Suzuki and R. Okamoto, *Progress of Theoretical Physics* **92**, 1045 (1994).
- [102] S. K. Bogner, R. J. Furnstahl, and R. J. Perry, *Physical Review C* **75**, 061001 (2007).
- [103] J. Draayer, T. Dytrych, K. Launey, and D. Langr, *Progress in Particle and Nuclear Physics* **67**, 516 (2012).
- [104] J. P. Draayer, T. Dytrych, and K. D. Launey, in *Journal of Physics: Conference Series*, Vol. 322 (2011), p. 012001.
- [105] K. D. Launey, T. Dytrych, G. H. Sargsyan, R. B. Baker, and J. P. Draayer, *The European Physical Journal Special Topics* **229**, 2429 (2020).
- [106] T. Dytrych, K. D. Sviratcheva, J. P. Draayer, C. Bahri, and J. P. Vary, *Journal of Physics G: Nuclear and Particle Physics* **35**, 123101 (2008).
- [107] M. Honma, T. Mizusaki, and T. Otsuka, *Physical Review Letters* **75**, 1284 (1995).
- [108] M. Honma, T. Mizusaki, and T. Otsuka, *Physical Review Letters* **77**, 3315 (1996).
- [109] T. Otsuka, M. Honma, T. Mizusaki, N. Shimizu, and Y. Utsuno, *Progress in Particle and Nuclear Physics* **47**, 319 (2001).
- [110] J. Carlson, *Physical Review C* **36**, 2026 (1987).
- [111] J. Carlson, S. Gandolfi, F. Pederiva, S. C. Pieper, R. Schiavilla, K. E. Schmidt, and R. B. Wiringa, *Reviews of Modern Physics* **87**, 1067 (2015).
- [112] K. Wildermuth and Y. C. Tang, *A Unified Theory of the Nucleus* (Vieweg+Teubner Verlag, 1977).
- [113] Y. Tang, M. LeMere, and D. Thompson, *Physics Reports* **47**, 167 (1978).
- [114] T. Fliessbach and H. Walliser, *Nuclear Physics A* **377**, 84 (1982).
- [115] R. Lovas, R. Liotta, A. Insolia, K. Varga, and D. Delion, *Physics Reports* **294**, 265 (1998).
- [116] H. M. Hofmann and G. M. Hale, *Physical Review C* **77**, 044002 (2008).
- [117] I. Rotter, H. Barz, and J. Höhn, *Nuclear Physics A* **297**, 237 (1978).
- [118] W. Wang and C. Shakin, *Physics Letters B* **32**, 421 (1970).
- [119] J. Faes and M. Płoszajczak, *Nuclear Physics A* **800**, 21 (2008).
- [120] J. Dobaczewski, N. Michel, W. Nazarewicz, M. Płoszajczak, and M. Stoitsov, in *A New Era of Nuclear Structure Physics* (2004), pp. 162–171.
- [121] T. Otsuka, A. Gade, O. Sorlin, T. Suzuki, and Y. Utsuno, *Reviews of Modern Physics* **92**, 015002 (2020).
- [122] F. Stancu, D. Brink, and H. Flocard, *Physics Letters B* **68**, 108 (1977).
- [123] T. Otsuka, T. Suzuki, R. Fujimoto, H. Grawe, and Y. Akaishi, *Physical Review Letters* **95**, 232502 (2005).
- [124] G. L. G. Sleijpen, A. G. L. Booten, D. R. Fokkema, and H. A. van der Vorst, *BIT Numerical Mathematics* **36**, 595 (1996).
- [125] R. D. Lawson, *Theory of the Nuclear Shell Model* (Clarendon, NY, 1980).
- [126] Y. Suzuki and K. Ikeda, *Physical Review C* **38**, 410 (1988).

- [127] Y. Jaganathen, R. M. I. Betan, N. Michel, W. Nazarewicz, and M. Płoszajczak, *Physical Review C* **96**, 054316 (2017).
- [128] N. Michel, W. Nazarewicz, and M. Płoszajczak, *Physical Review C* **70**, 064313 (2004).
- [129] N. Michel, *The European Physical Journal A* **42**, 523 (2009).
- [130] D. Vautherin and M. Vénéroni, *Physics Letters B* **25**, 175 (1967).
- [131] F. Palumbo, *Nuclear Physics A* **99**, 100 (1967).
- [132] G. Hagen, T. Papenbrock, and D. J. Dean, *Physical Review Letters* **103**, 062503 (2009).
- [133] J. G. Li, N. Michel, W. Zuo, and F. R. Xu, *Physical Review C* **103**, 034305 (2021).
- [134] K. Fosse, J. Rotureau, N. Michel, and W. Nazarewicz, *Physical Review C* **96**, 024308 (2017).
- [135] R. Id Betan, R. J. Liotta, N. Sandulescu, and T. Vertse, *Physical Review C* **67**, 014322 (2003).
- [136] N. Michel, W. Nazarewicz, M. Płoszajczak, and J. Rotureau, *Revista Mexicana de Física* **50**, 74 (2004).
- [137] X. Mao, J. Rotureau, W. Nazarewicz, N. Michel, R. M. Id Betan, and Y. Jaganathen, *Physical Review C* **102**, 024309 (2020).
- [138] J. G. Li, B. S. Hu, Q. Wu, Y. Gao, S. J. Dai, and F. R. Xu, *Physical Review C* **102**, 034302 (2020).
- [139] N. Michel, J. G. Li, F. R. Xu, and W. Zuo, *Physical Review C* **100**, 064303 (2019).
- [140] J. Rotureau, N. Michel, W. Nazarewicz, M. Płoszajczak, and J. Dukelsky, *Physical Review Letters* **97**, 110603 (2006).
- [141] J. Rotureau, N. Michel, W. Nazarewicz, M. Płoszajczak, and J. Dukelsky, *Physical Review C* **79**, 014304 (2009).
- [142] S. R. White, *Physical Review Letters* **69**, 2863 (1992).
- [143] S. R. White, *Physical Review B* **48**, 10345 (1993).
- [144] N. Michel, W. Nazarewicz, M. Płoszajczak, and J. Rotureau, *Physical Review C* **74**, 054305 (2006).
- [145] R. Id Betan, R. J. Liotta, N. Sandulescu, T. Vertse, and R. Wyss, *Physical Review C* **72**, 054322 (2005).
- [146] N. Michel, J. G. Li, F. R. Xu, and W. Zuo, *Physical Review C* **103**, 044319 (2021).
- [147] J. Li, N. Michel, H. Li, and W. Zuo, *Physics Letters B* **832**, 137225 (2022).
- [148] N. Michel, J. G. Li, F. R. Xu, and W. Zuo, *Physical Review C* **101**, 031301 (2020).
- [149] J. Okołowicz, N. Michel, W. Nazarewicz, and M. Płoszajczak, *Physical Review C* **85**, 064320 (2012).
- [150] G. Papadimitriou, A. T. Kruppa, N. Michel, W. Nazarewicz, M. Płoszajczak, and J. Rotureau, *Physical Review C* **84**, 051304 (2011).
- [151] G. Hagen, M. Hjorth-Jensen, and J. S. Vaagen, *Physical Review C* **71**, 044314 (2005).

- [152] G. Hagen, M. Hjorth-Jensen, and J. S. Vaagen, *Journal of Physics G: Nuclear and Particle Physics* **31**, S1337 (2005).
- [153] Y. Ma, F. Xu, L. Coraggio, B. Hu, J. Li, T. Fukui, L. D. Angelis, N. Itaco, and A. Gargano, *Physics Letters B* **802**, 135257 (2020).
- [154] E. Epelbaum, *Few-Body Systems* **43**, 57 (2008).
- [155] K. Fossez, J. Rotureau, N. Michel, and M. Płoszajczak, *Physical Review Letters* **119**, 032501 (2017).
- [156] J. G. Li, N. Michel, B. S. Hu, W. Zuo, and F. R. Xu, *Physical Review C* **100**, 054313 (2019).
- [157] B. R. Barrett, G. Papadimitriou, N. Michel, and M. Płoszajczak, in *14th International Conference on Nuclear Reaction Mechanisms* (2015), pp. 49–56.
- [158] I. J. Shin, Y. Kim, P. Maris, J. P. Vary, C. Forssén, J. Rotureau, and N. Michel, *Journal of Physics G: Nuclear and Particle Physics* **44**, 075103 (2017).
- [159] I. M. Green and S. A. Moszkowski, *Physical Review* **139**, B790 (1965).
- [160] H. Furutani, H. Horiuchi, and R. Tamagaki, *Progress of Theoretical Physics* **62**, 981 (1979).
- [161] H. Furutani, H. Kanada, T. Kaneko, S. Nagata, H. Nishioka, S. Okabe, S. Saito, T. Sakuda, and M. Seya, *Progress of Theoretical Physics Supplement* **68**, 193 (1980).
- [162] L. Eisenbud and E. P. Wigner, *Proceedings of the National Academy of Sciences* **27**, 281 (1941).
- [163] R. Tamagaki and W. Watari, *Progress of Theoretical Physics Supplement* **39**, 23 (1967).
- [164] A. De Shalit and H. Feshbach, *Theoretical Nuclear Physics*, Wiley Classics Library vol. 1 (Wiley, 1974).
- [165] P. Ring and P. Schuck, *The Nuclear Many-Body Problem* (Springer Berlin Heidelberg, 1980).
- [166] N. Michel, W. Nazarewicz, and M. Płoszajczak, *Physical Review C* **82**, 044315 (2010).
- [167] J. Dobaczewski, W. Nazarewicz, and P.-G. Reinhard, *Journal of Physics G: Nuclear and Particle Physics* **41**, 074001 (2014).
- [168] R. T. Birge, *Physical Review* **40**, 207 (1932).
- [169] D. Sivia and J. Skilling, *Data Analysis: a Bayesian Tutorial* (OUP Oxford, 2006).
- [170] G. Satchler, *Direct Nuclear Reactions* (Clarendon, 1983).
- [171] N. Glendenning, in *Direct nuclear reactions* (Academic Press, 1983), pp. 45–60.
- [172] P. Fröbrich and R. Lipperheide, *Theory of Nuclear Reactions*, Vol. 18 (Courier Corporation, 1996).
- [173] A. Messiah, *Quantum Mechanics* (Courier Corporation, 2014).
- [174] N. Michel, J. G. Li, L. H. Ru, and W. Zuo, *Physical Review C* **106**, L011301 (2022).
- [175] G. X. Dong, N. Michel, K. Fossez, M. Płoszajczak, Y. Jaganathen, and R. M. I. Betan, *Journal of Physics G: Nuclear and Particle Physics* **44**, 045201 (2017).
- [176] G. X. Dong, X. B. Wang, N. Michel, and M. Płoszajczak, *Physical Review C* **105**, 064608 (2022).

- [177] G. X. Dong, X. B. Wang, N. Michel, and M. Płoszajczak, *Physical Review C* **107**, 044613 (2023).
- [178] J. P. Linares Fernandez, N. Michel, M. Płoszajczak, and A. Mercenne, *Physical Review C* **108**, 044616 (2023).
- [179] P. Descouvemont and D. Baye, *Reports on progress in physics* **73**, 036301 (2010).
- [180] J. Dohet-Eraly, P. Navrátil, S. Quaglioni, W. Horiuchi, G. Hupin, and F. Raimondi, *Physics Letters B* **757**, 430 (2016).
- [181] M. Vorabbi, P. Navrátil, S. Quaglioni, and G. Hupin, *Physical Review C* **100**, 024304 (2019).
- [182] P. Navratil, K. Kravvaris, P. Gysbers, C. Hebborn, G. Hupin, and S. Quaglioni, arXiv:2212.00160 (2022).
- [183] M. H. Macfarlane and J. B. French, *Reviews of Modern Physics* **32**, 567 (1960).
- [184] P. Endt, *Atomic Data and Nuclear Data Tables* **19**, 23 (1977).
- [185] M. B. Tsang, J. Lee, and W. G. Lynch, *Physical Review Letters* **95**, 222501 (2005).
- [186] G. Kramer, H. Blok, and L. Lapikás, *Nuclear Physics A* **679**, 267 (2001).
- [187] B. A. Brown, P. G. Hansen, B. M. Sherrill, and J. A. Tostevin, *Physical Review C* **65**, 061601 (2002).
- [188] P. Hansen and J. Tostevin, *Annual Review of Nuclear and Particle Science* **53**, 219 (2003).
- [189] R. Furnstahl and H.-W. Hammer, *Physics Letters B* **531**, 203 (2002).
- [190] T. Duguet, H. Hergert, J. D. Holt, and V. Somà, *Physical Review C* **92**, 034313 (2015).
- [191] A. M. Mukhamedzhanov and R. E. Tribble, *Physical Review C* **59**, 3418 (1999).
- [192] A. M. Mukhamedzhanov and F. M. Nunes, *Physical Review C* **72**, 017602 (2005).
- [193] K. Jedamzik, *Physical Review Letters* **84**, 3248 (2000).
- [194] E. Vangioni-Flam, M. Cassé, R. Cayrel, J. Audouze, M. Spite, and F. Spite, *New Astronomy* **4**, 245 (1999).
- [195] E. G. Adelberger, S. M. Austin, J. N. Bahcall, A. B. Balantekin, G. Bogaert, L. S. Brown, L. Buchmann, F. E. Cecil, A. E. Champagne, L. de Braekeleer, C. A. Duba, S. R. Elliott, S. J. Freedman, M. Gai, G. Goldring, C. R. Gould, A. Gruzinov, W. C. Haxton, K. M. Heeger, E. Henley, C. W. Johnson, M. Kamionkowski, R. W. Kavanagh, S. E. Koonin, K. Kubodera, K. Langanke, T. Motobayashi, V. Pandharipande, P. Parker, R. G. H. Robertson, C. Rolfs, R. F. Sawyer, N. Shaviv, T. D. Shoppa, K. A. Snover, E. Swanson, R. E. Tribble, S. Turck-Chièze, and J. F. Wilkerson, *Reviews of Modern Physics* **70**, 1265 (1998).
- [196] E. G. Adelberger, A. García, R. G. H. Robertson, K. A. Snover, A. B. Balantekin, K. Heeger, M. J. Ramsey-Musolf, D. Bemmerer, A. Junghans, C. A. Bertulani, J.-W. Chen, H. Costantini, P. Prati, M. Couder, E. Uberseder, M. Wiescher, R. Cyburt, B. Davids, S. J. Freedman, M. Gai, D. Gazit, L. Gialanella, G. Imbriani, U. Greife, M. Hass, W. C. Haxton, T. Itahashi, K. Kubodera, K. Langanke, D. Leitner, M. Leitner, P. Vetter, L. Winslow, L. E. Marcucci, T. Motobayashi, A. Mukhamedzhanov, R. E. Tribble, K. M. Nollett, F. M. Nunes, T.-S. Park, P. D. Parker, R. Schiavilla, E. C. Simpson, C. Spitaleri, F. Strieder, H.-P. Trautvetter, K. Suemmerer, and S. Typel, *Reviews of Modern Physics* **83**, 195 (2011).

- [197] J. He, S. Chen, C. Rolfs, S. Xu, J. Hu, X. Ma, M. Wiescher, R. deBoer, T. Kajino, M. Kusakabe, L. Zhang, S. Hou, X. Yu, N. Zhang, G. Lian, Y. Zhang, X. Zhou, H. Xu, G. Xiao, and W. Zhan, *Physics Letters B* **725**, 287 (2013).
- [198] D. Entem and R. Machleidt, *Physical Review C* **68**, 041001 (2003).
- [199] R. J. Spiger and T. A. Tombrello, *Physical Review* **163**, 964 (1967).
- [200] J. A. McCray, *Physical Review* **130**, 2034 (1963).
- [201] D. Bardayan, *Journal of Physics G: Nuclear and Particle Physics* **43**, 043001 (2016).
- [202] F. Nunes, G. Potel, T. Poxon-Pearson, and J. Cizewski, *Annual Review of Nuclear and Particle Science* **70**, 147 (2020).
- [203] J. Thomas, D. Bardayan, J. Blackmon, J. Cizewski, U. Greife, C. Gross, M. Johnson, K. Jones, R. Kozub, J. Liang, et al., *Physical Review C* **71**, 021302 (2005).
- [204] R. L. Kozub, D. W. Bardayan, J. C. Batchelder, J. C. Blackmon, C. R. Brune, A. E. Champagne, J. A. Cizewski, T. Davinson, U. Greife, C. J. Gross, C. C. Jewett, R. J. Livesay, Z. Ma, B. H. Moazen, C. D. Nesaraja, L. Sahin, J. P. Scott, D. Shapira, M. S. Smith, J. S. Thomas, and P. J. Woods, *Physical Review C* **71**, 032801 (2005).
- [205] J. S. Thomas, G. Arbanas, D. W. Bardayan, J. C. Blackmon, J. A. Cizewski, D. J. Dean, R. P. Fitzgerald, U. Greife, C. J. Gross, M. S. Johnson, K. L. Jones, R. L. Kozub, J. F. Liang, R. J. Livesay, Z. Ma, B. H. Moazen, C. D. Nesaraja, D. Shapira, M. S. Smith, and D. W. Visser, *Physical Review C* **76**, 044302 (2007).
- [206] R. L. Kozub, G. Arbanas, A. S. Adekola, D. W. Bardayan, J. C. Blackmon, K. Y. Chae, K. A. Chipps, J. A. Cizewski, L. Erikson, R. Hatarik, W. R. Hix, K. L. Jones, W. Krolas, J. F. Liang, Z. Ma, C. Matei, B. H. Moazen, C. D. Nesaraja, S. D. Pain, D. Shapira, J. F. Shriner, M. S. Smith, and T. P. Swan, *Physical Review Letters* **109**, 172501 (2012).
- [207] B. Manning, G. Arbanas, J. A. Cizewski, R. L. Kozub, S. Ahn, J. M. Allmond, D. W. Bardayan, K. Y. Chae, K. A. Chipps, M. E. Howard, K. L. Jones, J. F. Liang, M. Matos, C. D. Nesaraja, F. M. Nunes, P. D. O'Malley, S. D. Pain, W. A. Peters, S. T. Pittman, A. Ratkiewicz, K. T. Schmitt, D. Shapira, M. S. Smith, and L. Titus, *Physical Review C* **99**, 041302 (2019).
- [208] <http://www.nndc.bnl.gov/ensdf>.
- [209] J. F. Dicello, G. Igo, W. T. Leland, and F. G. Perey, *Physical Review C* **4**, 1130 (1971).
- [210] D. Winterhalter, *Zeitschrift für Physik* **200**, 487 (1967).
- [211] I. Fodor, I. Szentpétery, and J. Zimányi, *Nuclear Physics* **73**, 155 (1965).
- [212] G. Brown, A. Denning, and A. Macgregor, *Nuclear Physics A* **153**, 145 (1970).
- [213] F. Barker, *Proceedings of the Physical Society* **84**, 681 (1964).
- [214] S. N. Abramovich, *Bulletin of the Russian Academy of Sciences: Physics* **79**, 823 (2015).
- [215] C. F. Moore, C. E. Watson, S. A. A. Zaidi, J. J. Kent, and J. G. Kulleck, *Physical Review Letters* **17**, 926 (1966).
- [216] Z. E. Switkowski, J. C. P. Heggie, and F. M. Mann, *Physical Review C* **17**, 392 (1978).

- [217] Z. Kohley, T. Baumann, D. Bazin, G. Christian, P. A. DeYoung, J. E. Finck, N. Frank, M. Jones, E. Lunderberg, B. Luther, S. Mosby, T. Nagi, J. K. Smith, J. Snyder, A. Spyrou, and M. Thoennessen, *Physical Review Letters* **110**, 152501 (2013).
- [218] B. Blank and M. Płoszajczak, *Reports on Progress in Physics* **71**, 046301 (2008).
- [219] M. Pfützner, I. Mukha, and S. M. Wang, *Progress in Particle and Nuclear Physics* **132**, 104050 (2023).
- [220] V. Girard-Alcindor, A. Mercenne, I. Stefan, F. de Oliveira Santos, N. Michel, M. Płoszajczak, M. Assié, A. Lemasson, E. Clément, F. Flavigny, A. Matta, D. Ramos, M. Rejmund, J. Dudouet, D. Ackermann, P. Adsley, M. Assunção, B. Bastin, D. Beaumel, G. Benzoni, R. Borcea, A. J. Boston, D. Brugnara, L. Cáceres, B. Cederwall, I. Celikovic, V. Chudoba, M. Ciemala, J. Collado, F. C. L. Crespi, G. D'Agata, G. De France, F. Delaunay, C. Diget, C. Domingo-Pardo, J. Eberth, C. Fougères, S. Franchoo, F. Galtarossa, A. Georgiadou, J. Gibelin, S. Giraud, V. González, N. Goyal, A. Gottardo, J. Goupil, S. Grévy, V. Guimaraes, F. Hammache, L. J. Harkness-Brennan, H. Hess, N. Jovančević, D. S. Judson Oliver, O. Kamalou, A. Kamenyero, J. Kiener, W. Korten, S. Koyama, M. Labiche, L. Lalanne, V. Lapoux, S. Leblond, A. Lefevre, C. Lenain, S. Leoni, H. Li, A. Lopez-Martens, A. Maj, I. Matea, R. Menegazzo, D. Mengoni, A. Meyer, B. Million, B. Monteagudo, P. Morfouace, J. Mrazek, M. Niikura, J. Piot, Z. Podolyak, C. Portail, A. Pullia, B. Quintana, F. Recchia, P. Reiter, K. Rezyunkina, T. Roger, J. S. Rojo, F. Rotaru, M. D. Salsac, A. M. Sánchez Benítez, E. Sanchis, M. Şenyigit, N. de Séréville, M. Siciliano, J. Simpson, D. Soehler, O. Sorlin, M. Stanoiu, C. Stodel, D. Suzuki, C. Theisen, D. Thisse, J. C. Thomas, P. Ujic, J. J. Valiente-Dobón, and M. Zielińska, *Physical Review C* **105**, L051301 (2022).
- [221] M. Freer, H. Horiuchi, Y. Kanada-En'yo, D. Lee, and U.-G. Meißner, *Reviews of Modern Physics* **90**, 035004 (2018).
- [222] J. Okołowicz and M. Płoszajczak, *International Journal of Modern Physics E* **15**, 529 (2006).
- [223] J. Okołowicz, M. Płoszajczak, and Y. Luo, *Acta Physical Polonica B* **39**, 389 (2007).
- [224] J. Okołowicz and M. Płoszajczak, *Physica Polonica B* **40**, 409 (2008).
- [225] N. Michel, W. Nazarewicz, J. Okołowicz, and M. Płoszajczak, *Journal of Physics G: Nuclear and Particle Physics* **37**, 064042 (2010).
- [226] J. Okołowicz, W. Nazarewicz, and M. Płoszajczak, *Acta Physical Polonica B* **45**, 331 (2014).
- [227] J. Okołowicz, M. Płoszajczak, R. J. Charity, and L. G. Sobotka, *Phys. Rev. C* **97**, 044303 (2018).
- [228] R. J. Charity, K. W. Brown, J. Okołowicz, M. Płoszajczak, J. M. Elson, W. Reviol, L. G. Sobotka, W. W. Buhro, Z. Chajecki, W. G. Lynch, J. Manfredi, R. Shane, R. H. Showalter, M. B. Tsang, D. Weisshaar, J. R. Winkelbauer, S. Bedoor, and A. H. Wuosmaa, *Phys. Rev. C* **97**, 054318 (2018).
- [229] J. Okołowicz, M. Płoszajczak, and W. Nazarewicz, *Physical Review Letters* **124**, 042502 (2020).
- [230] J. Wylie, J. Okołowicz, W. Nazarewicz, M. Płoszajczak, S. M. Wang, X. Mao, and N. Michel, *Physical Review C* **104**, L061301 (2021).

- [231] G. Breit, *Physical Review* **107**, 1612 (1957).
- [232] A. Baz, *Soviet Physics JETP* **6**, 709 (1958).
- [233] R. G. Newton, *Annals of Physics* **4**, 29 (1958).
- [234] L. Fonda, *Il Nuovo Cimento* **20**, 116 (1961).
- [235] W. E. Meyerhof, *Physical Review* **129**, 692 (1963).
- [236] A. I. Baz, I. B. Zeldovich, and A. M. Perelomov, *Scattering, Reactions and Decay in Nonrelativistic Quantum Mechanics*, Vol. 510 (Israel Program for Scientific Translations, 1969).
- [237] A. Lane, *Physics Letters B* **33**, 274 (1970).
- [238] E. Amaldi, O. D'Agostino, E. Fermi, B. Pontecorvo, F. Rasetti, and E. Segrè, *Proceedings of the Royal Society of London. Series A - Mathematical and Physical Sciences* **149**, 522 (1935).
- [239] H. A. Bethe, *Physical Review* **47**, 747 (1935).
- [240] F. Petrin and W. M. Elsasser, *Journal de Physique et le Radium* **6**, 194 (1935).
- [241] M. Ishigami, B. Blue, R. Tsuchikawa, A. Ahmadi, D. Heligman, Z. Zhang, J. Hone, and E. Mucciolo, in *Aps march meeting abstracts*, Vol. 2018 (2018), H40–014.
- [242] B. Blue, R. Tsuchikawa, A. Ahmadi, Z. Zhang, D. Heligman, S. D. Lough, J. Hone, E. R. Mucciolo, and M. Ishigami, *Solid State Communications* **353**, 114834 (2022).
- [243] P. Caradonna, C. Makochekanwa, A. Jones, J. R. Machacek, J. P. Sullivan, and S. J. Buckman, in *Journal of Physics: Conference Series*, Vol. 388, 7 (IOP Publishing, 2012), p. 072012.
- [244] H. R. Sadeghpour, J. L. Bohn, M. J. Cavagnero, B. D. Esry, I. I. Fabrikant, J. H. Macek, and A. R. P. Rau, *Journal of Physics B: Atomic, Molecular and Optical Physics* **33**, R93 (2000).
- [245] R. Bilodeau, I. Dumitriu, N. Gibson, C. Walter, and N. Berrah, in *Journal of Physics: Conference Series*, Vol. 194, 2 (IOP Publishing, 2009), p. 022095.
- [246] A. Starostin, S. Prakhov, B. M. K. Nefkens, V. V. Abaev, C. E. Allgower, V. S. Bekrenev, W. J. Briscoe, M. Clajus, J. R. Comfort, K. Craig, D. Grosnick, D. Isenhower, N. Knecht, D. D. Koetke, N. G. Kozlenko, S. P. Kruglov, A. A. Kulbardis, G. Lolos, I. V. Lopatin, D. M. Manley, R. Manweiler, A. Maru ši é, S. McDonald, J. Olmsted, Z. Papandreou, D. C. Peaslee, N. Phaisangittisakul, J. W. Price, A. F. Ramirez, M. Sadler, A. Shafi, H. Spinka, T. D. S. Stanislaus, H. M. Staudenmaier, I. Supek, and W. B. Tippens (Crystal Ball Collaboration), *Physical Review C* **72**, 015205 (2005).
- [247] J. Batley, C. Lazzeroni, D. Munday, M. Slater, S. Wotton, R. Arcidiacono, G. Bocquet, N. Cabibbo, A. Ceccucci, D. Cundy, V. Falaleev, M. Fidecaro, L. Gatignon, A. Gonidec, W. Kubischta, A. Norton, M. Patel, A. Peters, S. Balev, P. Frabetti, E. Goudzovski, P. Hristov, V. Kekelidze, V. Kozhuharov, L. Litov, D. Madigozhin, E. Marinova, N. Molokanova, I. Polenkevich, Y. Potrebenikov, S. Stoynev, A. Zinchenko, E. Monnier, E. Swallow, R. Winston, P. Rubin, A. Walker, W. Baldini, A. Cotta Ramusino, P. Dalpiaz, C. Damiani, M. Fiorini, A. Gianoli, M. Martini, F. Petrucci, M. Savrié, M. Scarpa, H. Wahl, A. Bizzeti, M. Calvetti, E. Celeghini, E. Iacopini, M. Lenti, F. Martelli, G. Ruggiero, M. Veltri, M. Behler, K. Eppard, K. Kleinknecht, P. Marouelli, L. Masetti, U. Moosbrugger, C. Morales Morales, B.

- Renk, M. Wache, R. Wanke, A. Winhart, D. Coward, A. Dabrowski, T. Fonseca Martin, M. Shieh, M. Szleper, M. Velasco, M. Wood, G. Anzivino, P. Cenci, E. Imbergamo, M. Pepe, M. Petrucci, M. Piccini, M. Raggi, M. Valdata-Nappi, C. Cerri, G. Collazuol, F. Costantini, L. DiLella, N. Doble, R. Fantechi, L. Fiorini, S. Giudici, G. Lamanna, I. Mannelli, A. Michetti, G. Pierazzini, M. Sozzi, B. Bloch-Devauux, C. Cheshkov, J. Chèze, M. De Beer, J. Derré, G. Marel, E. Mazzucato, B. Peyaud, B. Vallage, M. Holder, A. Maier, M. Ziolkowski, S. Bifani, C. Biino, N. Cartiglia, M. Clemencic, S. Goy Lopez, F. Marchetto, H. Dibon, M. Jeitler, M. Markytan, I. Mikulec, G. Neuhofer, and L. Widhalm, [Physics Letters B **633**, 173 \(2006\)](#).
- [248] R. K. Adair, [Physical Review **111**, 632 \(1958\)](#).
- [249] S. Abramovich, B. Y. Guzhovskij, A. Zvenigorodskij, and S. Trusillo, *Yadernaya Fizika* **30**, 1276 (1979).
- [250] S. N. Abramovich, G. B. Ya., and L. L. M., *Fiz. Elem. Chastits At. Yadra* **23**, 179 (1992).
- [251] S. Abramovich, A. Baz, and B. Y. Guzhovskij, *Yadernaya Fizika* **32**, 402 (1980).
- [252] C. Hategan, [Physics Letters B **46**, 23 \(1973\)](#).
- [253] J. T. Wells, A. B. Tucker, and W. E. Meyerhof, [Physical Review **131**, 1644 \(1963\)](#).
- [254] P. E. Hodgson, [Nature **259**, 364 \(1976\)](#).
- [255] P. R. Malmberg, [Physical Review **101**, 114 \(1956\)](#).
- [256] H. Comisel, C. Hategan, and H. H. Wolter, [Physics of Particles and Nuclei **41**, 574 \(2010\)](#).
- [257] L. Lapikás, [Nuclear Physics A **553**, 297 \(1993\)](#).
- [258] W. Dickhoff and C. Barbieri, [Progress in Particle and Nuclear Physics **52**, 377 \(2004\)](#).
- [259] W. Dickhoff, [Journal of Physics G: Nuclear and Particle Physics **37**, 064007 \(2010\)](#).
- [260] S. Paschalis, M. Petri, A. Macchiavelli, O. Hen, and E. Piasetzky, [Physics Letters B **800**, 135110 \(2020\)](#).
- [261] T. Aumann, C. Barbieri, D. Bazin, C. Bertulani, A. Bonaccorso, W. Dickhoff, A. Gade, M. Gómez-Ramos, B. Kay, A. Moro, T. Nakamura, A. Obertelli, K. Ogata, S. Paschalis, and T. Uesaka, [Progress in Particle and Nuclear Physics **118**, 103847 \(2021\)](#).
- [262] A. Gade, D. Bazin, B. A. Brown, C. M. Campbell, J. A. Church, D. C. Dinca, J. Enders, T. Glasmacher, P. G. Hansen, Z. Hu, K. W. Kemper, W. F. Mueller, H. Olliver, B. C. Perry, L. A. Riley, B. T. Roeder, B. M. Sherrill, J. R. Terry, J. A. Tostevin, and K. L. Yurkewicz, [Physical Review Letters **93**, 042501 \(2004\)](#).
- [263] A. Gade, P. Adrich, D. Bazin, M. D. Bowen, B. A. Brown, C. M. Campbell, J. M. Cook, T. Glasmacher, P. G. Hansen, K. Hosier, S. McDaniel, D. McGlinchery, A. Obertelli, K. Siwek, L. A. Riley, J. A. Tostevin, and D. Weisshaar, [Physical Review C **77**, 044306 \(2008\)](#).
- [264] J. A. Tostevin and A. Gade, [Physical Review C **103**, 054610 \(2021\)](#).
- [265] C. Barbieri and W. H. Dickhoff, [International Journal of Modern Physics A **24**, 2060 \(2009\)](#).

- [266] F. Flavigny, A. Obertelli, A. Bonaccorso, G. Grinyer, C. Louchart, L. Nalpas, and A. Signoracci, [Physical Review Letters](#) **108**, 252501 (2012).
- [267] G. Grinyer, D. Bazin, A. Gade, J. Tostevin, P. Adrich, M. Bowen, B. Brown, C. Campbell, J. Cook, T. Glasmacher, et al., [Physical Review C](#) **86**, 024315 (2012).
- [268] B. Kay, J. Schiffer, and S. Freeman, [Physical Review Letters](#) **111**, 042502 (2013).
- [269] N. Timofeyuk, [Physical Review C](#) **88**, 044315 (2013).
- [270] J. Tostevin and A. Gade, [Physical Review C](#) **90**, 057602 (2014).
- [271] J. Lee, H. Liu, P. Doornenbal, M. Kimura, K. Minomo, K. Ogata, Y. Utsuno, N. Aoi, K. Li, M. Matsushita, H. Scheit, D. Steppenbeck, S. Takeuchi, H. Wang, H. Baba, E. Ideguchi, N. Kobayashi, Y. Kondo, S. Michimasa, T. Motobayashi, H. Sakurai, M. Takechi, and Y. Togano, [Progress of Theoretical and Experimental Physics](#) **2016**, 083D01 (2016).
- [272] S. Wang, Y. Xu, and D. Pang, [Physica Scripta](#) **94**, 015302 (2018).
- [273] L. Atar, S. Paschalis, C. Barbieri, C. A. Bertulani, P. Díaz Fernández, M. Holl, M. A. Najafi, V. Panin, H. Alvarez-Pol, T. Aumann, V. Avdeichikov, S. Beceiro-Novo, D. Bemmerer, J. Benlliure, J. M. Boillos, K. Boretzky, M. J. G. Borge, M. Caamaño, C. Caesar, E. Casarejos, W. Catford, J. Cederkall, M. Chartier, L. Chulkov, D. Cortina-Gil, E. Cravo, R. Crespo, I. Dillmann, Z. Elekes, J. Enders, O. Ershova, A. Estrade, F. Farinon, L. M. Fraile, M. Freer, D. Galaviz Redondo, H. Geissel, R. Gernhäuser, P. Golubev, K. Göbel, J. Hagdahl, T. Heftrich, M. Heil, M. Heine, A. Heinz, A. Henriques, A. Hufnagel, A. Ignatov, H. T. Johansson, B. Jonsson, J. Kahlbow, N. Kalantar-Nayestanaki, R. Kanungo, A. Kelic-Heil, A. Knyazev, T. Kröll, N. Kurz, M. Labiche, C. Langer, T. Le Bleis, R. Lemmon, S. Lindberg, J. Machado, J. Marganיע-Gałązka, A. Movsesyan, E. Nacher, E. Y. Nikolskii, T. Nilsson, C. Nociforo, A. Perea, M. Petri, S. Pietri, R. Plag, R. Reifarth, G. Ribeiro, C. Rigollet, D. M. Rossi, M. Röder, D. Savran, H. Scheit, H. Simon, O. Sorlin, I. Syndikus, J. T. Taylor, O. Tengblad, R. Thies, Y. Togano, M. Vandebrouck, P. Velho, V. Volkov, A. Wagner, F. Wamers, H. Weick, C. Wheldon, G. L. Wilson, J. S. Winfield, P. Woods, D. Yakorev, M. Zhukov, A. Zilges, and K. Zuber, [Physical Review Letters](#) **120**, 052501 (2018).
- [274] M. Gómez-Ramos and A. Moro, [Physics Letters B](#) **785**, 511 (2018).
- [275] N. T. T. Phuc, K. Yoshida, and K. Ogata, [Physical Review C](#) **100**, 064604 (2019).
- [276] W. von Oertzen, [The European Physical Journal A](#) **11**, 403 (2001).
- [277] W. von Oertzen, M. Freer, and Y. Kanada-En'yo, [Physics Reports](#) **432**, 43 (2006).
- [278] W. von Oertzen, M. Milin, T. Dorsch, H. G. Bohlen, R. Krücken, T. Faestermann, R. Hertenberger, T. Kokalova, M. Mahgoub, C. Wheldon, and H. F. Wirth, [The European Physical Journal A](#) **46**, 345 (2010).
- [279] W. von Oertzen and M. Milin, [Clusters in Nuclei, Volume 3](#), 147 (2014).
- [280] J. A. Wheeler, [Physical Review](#) **52**, 1083 (1937).
- [281] C. F. von Weizsäcker, [Naturwissenschaften](#) **26**, 209 (1938).
- [282] W. Wefelmeier, [Zeitschrift für Physik](#) **107**, 332 (1937).
- [283] E. Garrido, D. Fedorov, and A. Jensen, [Nuclear Physics A](#) **617**, 153 (1997).

- [284] T. Webb, S. Wang, K. Brown, R. Charity, J. Elson, J. Barney, G. Cerizza, Z. Chajacki, J. Estee, D. Hoff, S. Kuvin, W. Lynch, J. Manfredi, D. McNeel, P. Morfouace, W. Nazarewicz, C. Pruitt, C. Santamaria, J. Smith, L. Sobotka, S. Sweany, C. Tsang, M. Tsang, A. Wuosmaa, Y. Zhang, and K. Zhu, *Physical Review Letters* **122**, 122501 (2019).
- [285] I. Tanihata, H. Hamagaki, O. Hashimoto, Y. Shida, N. Yoshikawa, K. Sugimoto, O. Yamakawa, T. Kobayashi, and N. Takahashi, *Physical Review Letters* **55**, 2676 (1985).
- [286] C. Thibault, R. Klapisch, C. Rigaud, A. M. Poskanzer, R. Prieels, L. Lessard, and W. Reisdorf, *Physical Review C* **12**, 644 (1975).
- [287] I. Tanihata, *Journal of Physics G: Nuclear and Particle Physics* **22**, 157 (1996).
- [288] E. M. Burbidge, G. R. Burbidge, W. A. Fowler, and F. Hoyle, *Reviews of Modern Physics* **29**, 547 (1957).
- [289] D. Inglis, *Nuclear Physics* **30**, 1 (1962).
- [290] E. Beth and G. E. Uhlenbeck, *Physica* **4**, 915 (1937).
- [291] A. T. Kruppa and K. Arai, *Physical Review A* **59**, 3556 (1999).
- [292] H. C. Ohanian and C. G. Ginsburg, *American Journal of Physics* **42**, 310 (1974).
- [293] P. Kleinwachter and I. Rotter, *Physical Review C* **32**, 1742 (1985).
- [294] I. Rotter, *Reports on Progress in Physics* **54**, 635 (1991).
- [295] V. Sokolov and V. Zelevinsky, *Physics Letters B* **202**, 10 (1988).
- [296] V. Sokolov and V. Zelevinsky, *Nuclear Physics A* **504**, 562 (1989).
- [297] S. Drożdż, J. Okołowicz, M. Płoszajczak, and I. Rotter, *Physical Review C* **62**, 024313 (2000).
- [298] R. H. Dicke, *Physical Review* **93**, 99 (1954).
- [299] N. Auerbach and V. Zelevinsky, *Reports on Progress in Physics* **74**, 106301 (2011).
- [300] Y. V. Fyodorov and B. A. Khoruzhenko, *Physical Review Letters* **83**, 65 (1999).
- [301] J. Okołowicz and M. Płoszajczak, *Physical Review C* **80**, 034619 (2009).
- [302] Y. Luo, J. Okołowicz, M. Płoszajczak, and N. Michel, arXiv:nucl-th/0211068 (2002).
- [303] J. Okołowicz, M. Płoszajczak, and W. Nazarewicz, *Journal of Physics G: Nuclear and Particle Physics* **49**, 10LT01 (2022).
- [304] A. N. Bohr and B. R. Mottelson, *Nuclear Structure*, Vol. 2 (Reading, MA: Benjamin, 1975).
- [305] B. Barmore, A. T. Kruppa, W. Nazarewicz, and T. Vertse, *Physical Review C* **62**, 054315 (2000).
- [306] A. T. Kruppa and W. Nazarewicz, *Physical Review C* **69**, 054311 (2004).

Title: Collective phenomena at the particle emission thresholds

Most of the nuclear chart consists of unstable nuclei, which are subject to various decay modes. Therefore, it is more appropriate to describe these nuclei in the open quantum system formalism. Natural formulation of this problem is given by the Gamow Shell Model in the Coupled Channels representation (GSM-CC), that allows to unify nuclear structure and reactions.

In the first part, the multiple mass-partition GSM-CC has been developed. In this unifying approach, we have calculated spectra of ${}^7,8\text{Be}$, ${}^7\text{Li}$, and low-energy cross-sections: ${}^4\text{He}({}^3\text{He},{}^3\text{He})$, ${}^4\text{He}({}^3\text{He},{}^3\text{He})$, and ${}^6\text{Li}(p,p)$. Inclusion of different mass partitions in the GSM-CC proved to be crucial for describing the structure of low-energy states in these nuclei. α -correlations in the 0_1^+ , 2_1^+ , 4_1^+ resonances of ${}^8\text{Be}$ emerged naturally as the near-threshold open quantum system phenomenon. Deuteron correlations turned out to be important in all low-energy states of ${}^8\text{Be}$. In heavier nuclei, the GSM-CC has been applied to calculate the spectra of ${}^{42}\text{Ca}$, ${}^{42}\text{Ti}$, ${}^{42}\text{Sc}$, and cross-sections of direct reactions, with a special focus on the transfer reaction ${}^{40}\text{Ca}(d,p){}^{41}\text{Ca}$.

The second part has been devoted for understanding how the clustering appears in the near-threshold states. The GSM-CC studies were carried out by looking at the evolution of reaction channel probabilities, spectroscopic factors and continuum-coupling correlation energy as a function of the distance to various particle emission thresholds. This has given insight into the origin of near-threshold clustering as a consequence of an alignment of the collective GSM-CC state with the decay channel.

Keywords: Nuclear physics, nuclear structure, nuclear reactions, clustering, near-threshold effects, direct reactions.

Titre: Phénomènes collectifs aux seuils d'émission de particules

La majeure partie de la carte de nucléides est composée de noyaux instables soumis à divers modes de désintégration. Il est donc plus approprié de décrire ces noyaux dans le formalisme des systèmes quantiques ouverts. La formulation naturelle de ce problème est donnée par le Modèle en Couches Gamow en représentation des Canaux Couplés (GSM-CC), qui permet d'unifier la structure nucléaire et les réactions.

Dans la première partie, le GSM-CC à partitions de masse multiples a été développé. Dans cette approche unificatrice, nous avons calculé les spectres de ${}^7,8\text{Be}$, ${}^7\text{Li}$, et les sections efficaces à basse énergie : ${}^4\text{He}({}^3\text{He},{}^3\text{He})$, ${}^4\text{He}({}^3\text{He},{}^3\text{He})$, et ${}^6\text{Li}(p,p)$. L'inclusion de différentes partitions de masse dans le GSM-CC s'est avérée cruciale pour décrire la structure des états à basse énergie de ces noyaux. Les corrélations α dans les résonances 0_1^+ , 2_1^+ , 4_1^+ de ${}^8\text{Be}$ ont émergé naturellement en tant que phénomène du système quantique ouvert proche du seuil. Les corrélations de deutons se sont révélées importantes dans tous les états à basse énergie de ${}^8\text{Be}$. Dans les noyaux plus lourds, le GSM-CC a été appliqué pour calculer les spectres de ${}^{42}\text{Ca}$, ${}^{42}\text{Ti}$, ${}^{42}\text{Sc}$, et les sections efficaces des réactions directes, avec un accent particulier sur la réaction de transfert ${}^{40}\text{Ca}(d,p){}^{41}\text{Ca}$.

La deuxième partie a été consacrée à comprendre comment le clustering apparaît dans les états proches du seuil. Les études GSM-CC ont été réalisées en examinant l'évolution des probabilités de canaux de réaction, des facteurs spectroscopiques et de l'énergie de corrélation de couplage au continuum en fonction de la distance par rapport aux différents seuils d'émission de particules. Cela a permis de mieux comprendre l'origine de la clusterisation proche du seuil en tant que conséquence de l'alignement de l'état du GSM-CC collectif avec le canal de désintégration.

Mots-clé: Physique nucléaire, structure nucléaire, réactions nucléaires, clustering, effets proches du seuil, réactions directes.